Understanding atomic interactions in an optical lattice clock and using them to study many-body physics

by

Michael N. Bishof

B.A., Physics, University of Chicago, 2007

B.S., Mathematics, University of Chicago, 2007

M.S., Physics, University of Colorado at Boulder, 2011

A thesis submitted to the
Faculty of the Graduate School of the
University of Colorado in partial fulfillment
of the requirements for the degree of
Doctor of Philosophy
Department of Physics
2014

This thesis entitled:
Understanding atomic interactions in an optical lattice clock and using them to study many-body physics
written by Michael N. Bishof
has been approved for the Department of Physics

Jun Ye

Ana Maria Rey

Date

The final copy of this thesis has been examined by the signatories, and we find that both the content and the form meet acceptable presentation standards of scholarly work in the above mentioned discipline.

Bishof, Michael N. (Ph.D., Physics)

Understanding atomic interactions in an optical lattice clock and using them to study many-body physics

Thesis directed by Prof. Jun Ye

Strontium optical lattice clocks at JILA recently demonstrated record-high accuracy and stability. These advances were enabled by an ultrastable laser with fractional frequency stability of 1×10^{-16} at 1 second. This laser allows us to study systematic shifts of the $^1S_0$ to $^3P_0$ clock transition with unprecedented precision. Density-dependent frequency shifts represent an unavoidable perturbation for clocks based on many atoms. Our studies of atomic interactions in an optical lattice clock system uncover the nature of these interactions and reveal important many-body atomic correlation effects in this open quantum system. By extending our measurements to all ten nuclear-spin sublevels of the clock states, we observe the first direct evidence of SU(N) symmetric interactions in alkaline earth(-like) atoms. Using the techniques we developed in these studies, we also demonstrate a novel technique for measuring the frequency noise spectrum of an ultrastable laser. We discuss designs for the future direction of our experiment which will place ^{87}Sr atoms within a high finesse cavity that is resonant on the $^1S_0$ to $^3P_1$ transition. We will use this system to study collective effects in cavity quantum electrodynamics. Most notably, strong atom-cavity coupling can enhance the spectroscopic sensitivity of our clock by creating spin-squeezed states via quantum non-demolition measurements. As a precursor to future work studying cavity-mediated collective behavior, we use the unique atomic structure of ^{88}Sr to investigate free-space retarded dipolar coupling in an optically thick sample of atoms.

Dedication

This thesis is dedicated to Cynthia.

Acknowledgements

To successfully acknowledge every person who has contributed to my doctoral research would be an impossible task, so I apologize in advance to those I forget to mention below.

After competing high school, I knew that I wanted to study physics due to the influence of my passionate math and science teachers, including Virginia Highstone, Steve Sample, Bob Blous, and Mr. Tieman. At the University of Chicago, I was again able to connect with professors who were similarly committed to education. Prof. Don York got me started in scientific research where I investigated diffuse interstellar bands and quasar-galaxy pairs. As a mentor, he was great at pointing me in the right direction, while still allowing me to figure things out for myself. Perhaps the most influential person in making my graduate career a reality was Prof. Zheng-Tian Lu of Argonne National Laboratory and the University of Chicago. After taking his atomic physics course, I knew that atomic physics was the field that interested me most. However, had he not given me the opportunity to work for him the year after I graduated college, I probably would have needed to get a job outside science and my academic career would have ended. I was extremely lucky to have Lu as a mentor. He has been a role-model as both a scientist and a teacher through his kind and thoughtful approach to everything he does.

I have had an incredible experience working on the strontium team for Prof. Jun Ye. Jun may be one of the busiest people at JILA (although there is plenty of competition for this title) yet he always makes time to remain intimately involved our team's work and it is clear that he is very passionate about every one of his projects. Furthermore, despite his demanding schedule, he is always willing to make time for his students and postdocs. Working with Jun has been a great experience because I have been able to learn so much from him. While he expects great things from his students and postdocs, he is also a very understanding and kind person. I believe that Jun is so effective as an advisor because he learned from the best. Having Jun's former advisor Jan Hall around the lab has been immensely beneficial. Jan is always willing to lend an ear or a few words of wisdom.

Working in Jun's lab is a unique and greatly fruitful experience. He has been extremely successful in continuing to supplement his own extensive knowledge with an army of extremely talented and knowledgeable scientists with a broad knowledge base. Working on the strontium project I have overlapped with many great researchers. Every one of our projects has been a team effort and every one of my colleges has contributed greatly to our work. At the start of my career, Dr. Gretchen Campbell taught me the basics of the strontium experiment. Every time I hear a soda can open I think of the angry look she would give to anyone who dared unlock the clock laser. I overlapped much more extensively with Dr. Matthew Swallows whose encyclopedic knowledge of pretty much everything was both a blessing and a curse. I got in the bad habit of always asking Matt every question I had about science instead of looking something up in a book or figuring it out for myself. Matt was undeniably a great asset to our experiment and my development as a scientist. Another cornerstone of the strontium experiment with whom I overlapped significantly was Michael Martin. Michael's knowledge of lasers and atomic physics rivals even Jun's. He was also a very patient teacher and a great person to work with. To this day, the clock laser he built is still the linchpin for all of our strontium work. When Dr. Xibo Zhang first came to our lab, it was his karaoke skills that impressed me most. I soon learned that his talent in the laboratory is even more impressive. He learned the entire strontium experiment with blinding speed and his attention to detail has been essential to the success of our work. His enthusiasm for physics is unmatched and it has been a joy to work with him. I also had the pleasure of working with Yige Lin while he visited our lab for a couple years. During his relatively short time working with strontium he became valuable member of the team and we could not have completed our two-dimensional lattice work without him. Craig Benko spent a brief time working with strontium before eventually shifting gears to Jun's extreme ultraviolet frequency comb project. Craig was a great asset to our team while he was involved in strontium and a great person to work with. Prof. Jan Thomsen of the Niels Bohr Institute has also lent a helping hand to the strontium team on his frequent visits to our lab. Additionally, I have been very fortunate work with Sebastian Blatt, Travis Nicholson, Dr. Jason Wlliams, Ben Bloom, Sara Campbell, Dr. Wei Zhang, Sarah Bromley, Ross Hutson, and Toby Bothwell. I know that Xibo, Travis, Sara, Wei, Sarah, Ross, and Toby will continue to produce great scientific results with strontium. Outside of strontium, I have had the great opportunity to work alongside and have fruitful discussions with Dylan Yost, Marcio Miranda (Oh Yeah!), Brian Sawyer, Dr. Florian Adler, Dr. Thomas Allison, Dr. Arman Cingoz, Benjamin Stuhl, Michael Thorpe, Bryce Bjork, Alejandra Collopy, Kevin Cossel, Jacob Covey, Dan Gresh, Steven Moses, David Reens, Mark Yeo, Dr. Bryce Gadway, Dr. Matthew Hummon, Dr. Francois Labaye, and Prof. Long-Sheng Ma.

One of the most beneficial collaborations for our project has been the close ties between our strontium experiment and the theory work of Prof. Ana Maria Rey. My doctoral research is also the product of very fruitful collaborations with Alexey Gorshkov, Goulven Quéméner, Javier von-Stecher, Andrew Ludlow, Nathan Lemke, Christina Kraus, Marianna Safronova, Peter Zoller, Peter Kómár, Eric Kessler, Liang Jiang, Anders Sørensen and Mikhail Lukin. The electronics shop, the computing group, and the instrument shop at JILA have also been, well, instrumental in the success of our research, especially Tracy Keep, Hans Green, and J. R. Raith.

I would finally like to acknowledge my family for their love and support over the past years. They have always been supportive of my education, even when they knew it would take me 1000 miles (1609 km) away. Most especially, I would like to thank my wife Cynthia for putting up with all the long hours and late nights. I'd like to thank her for maintaining strong interactions even at long-range through frequent phone calls and text messages. Over the past few months she has done an extremely impressive job extending our interactions to the many-body regime by convincing our 1-year-old son Ronan to stand in front of a cell phone without grabbing it and inadvertently ending the video call. She has been a true partner. My son Ronan has also greatly contributed to my work by giving me additional motivation to complete my PhD with his constant refrain, ”Da-da home?”

Contents

Chapter

Appendix

Tables

Table

Figures

Figure

Chapter 1

A brief introduction to the strontium clock

Starting with solid chunks of metallic strontium sitting in a steel tube, we are able to create the most stable and accurate clock [1, 2], a novel optical spectrum analyzer for ultrastable lasers [3], and an incredible laboratory for exploring many-body physics [4] and quantum magnetism [5]. This chapter tells the story of how the above results are possible: how we cool, trap, prepare, probe, and detect in our optical lattice clock experiments. This topic has previously been discussed in great detail [6, 7, 8, 9, 10, 11] and, with that in mind, we aim to introduce unfamiliar readers with the general operation of our experiment, rather than give an exhaustive account of every experimental detail.

1.1 The strontium apparatus

Figure 1.1 shows a drawing or our experimental vacuum chamber. The vacuum chamber itself is composed of two parts that can be physically separated with a gate valve. The oven side of the chamber consists of the effusive atomic oven, transverse cooling, and atomic beam shutter. Differential pumping apertures ensure that the oven side of the chamber has a minimal effect on the background pressure in the science side of the chamber. Within the oven, a reservoir of several grams of solid strontium is heated to ~ 400 °C where the vapor pressure of strontium is sufficient to provide enough gaseous strontium to feed our atom traps, though they always hunger for more atoms. Strontium exits the oven through a millimeter sized nozzle which we heat to ~ 600 °C to avoid buildup of strontium within the nozzle.

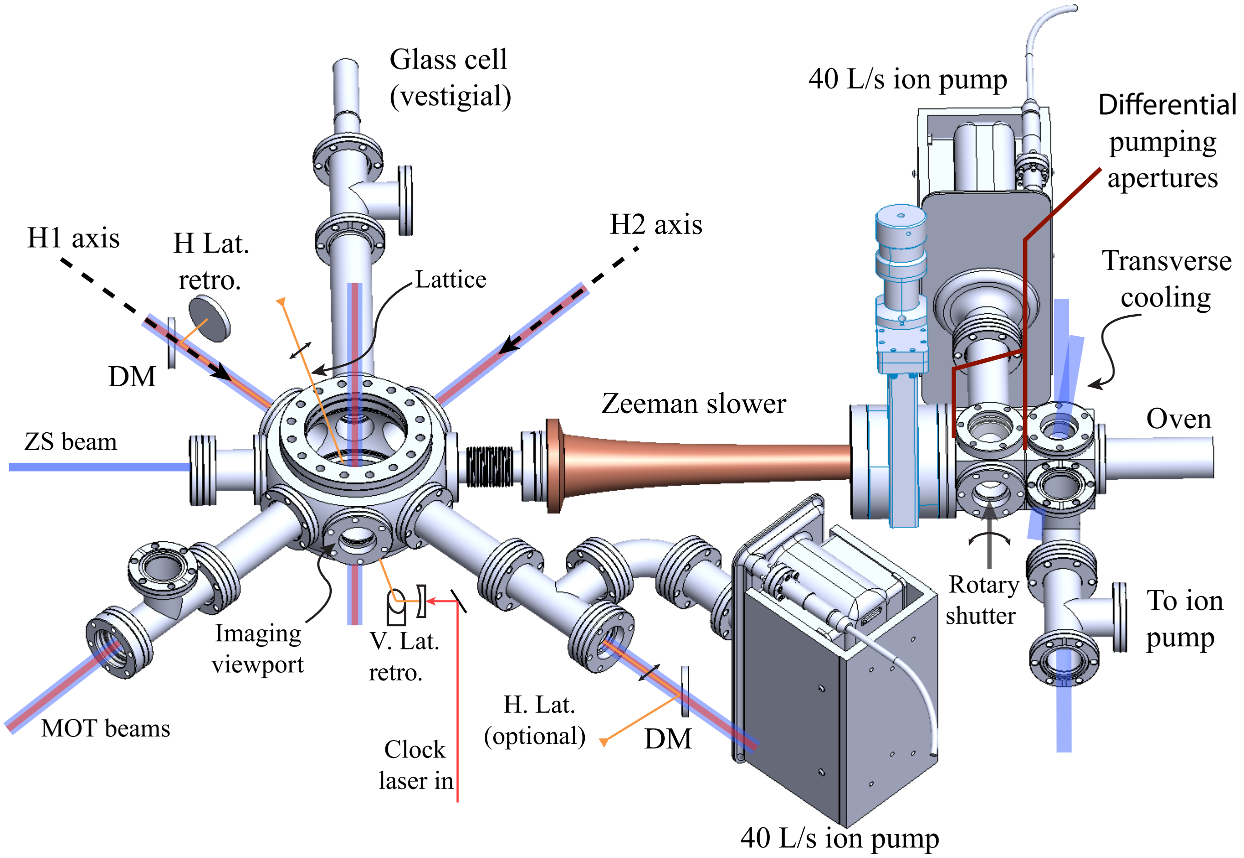

Figure 1.1: An annotated drawing of our experimental vacuum chamber showing where various lasers and other technical components are integrated into our experiment. Thick blue and red lines represent laser light used for magneto-optical trapping at 461 nm and 689 nm, respectively. The thin red line represents the path of the clock laser, which is overlapped with the lattice light, drawn here as a thin orange line. The horizontal lattice that is used in some of our work is represented by the thin orange line along the H1 axis.

Upon exiting the oven, the atoms experience their first interaction with laser light. For the initial cooling and trapping of strontium, we use the $^1S_0$ to $^1P_1$ (blue) transition at 461 nm (Fig. 1.2) because the 32 MHz natural linewidth of this transition allows us to apply a large force on the atoms. Counter-propagating transverse cooling beams containing ~ 10 mW of power and tuned 10 MHz below resonance are directed perpendicular to the atomic beam in two orthogonal directions to collimate the rapidly expanding beam of atoms. Transverse cooling results in a atom number gain of ~ 4 in the magneto-optical trap (MOT) based on the blue transition (blue MOT), which we describe in the following section. The atom beam then passes through a differential pumping aperture, after which it encounters an atomic beam shutter that can be used to block the beam during interrogation of the clock transition.[a] Next, the atoms pass through an additional differential pumping aperture and gate valve, which can be closed to physically separate the oven side of our chamber from the science side.

The science portion of our chamber begins with a Zeeman slower where 50 mW of laser light tuned ~ 1 GHz below the unperturbed transition resonance is kept on resonance with the moving atoms by balancing the change in Doppler shift as the atoms slow down with a variable Zeeman shift along the slower, created by a solenoid of variable winding number. Light scattering from the Zeeman slower laser brings the atoms to rest (along the slowing axis) at the center of our main science chamber. Figure 1.1 shows how the subsequent components of our experiment (e.g. MOT, optical lattice, clock laser) are introduced to the atoms.

1.2 One MOT two MOT red MOT blue MOT

To cool the atoms to the μK temperatures that are necessary for loading into our ^{87}Sr optical lattice and for achieving the most optically thick sample of ^{88}Sr atoms, we employ two separate MOTs based on the blue and ^{1}S$_0$ to ^{3}P$_1$ (red) transitions (Fig. 1.2). As demonstrated in Fig. 1.3, fermionic ^{87}Sr has hyperfine structure resulting from its nuclear spin, $I = 9/2$, whereas bosonic ^{88}Sr with $I = 0$ lacks hyperfine structure. Due to the different hyperfine splittings and linewidths involved, we will see that the presence of hyperfine structure affects the blue and red MOTs differently. For ^{88}Sr , both MOTs are relatively simple, with the only complication being the re-pumping lasers that are necessary in the blue MOT due to decay from ^{1}P$_1$ to ^{1}D$_2$. In the absence of nuclear spin, both MOTs operate on total angular momentum $J = 0$ to $J = 1$ transitions. For these values, the MOT operation is simple to describe. Three orthogonally oriented pairs of circularly polarized, counter-propagating laser beams are overlapped at the atoms and detuned one linewidth below the transition they operate on. Each beam has a polarization that is orthogonal to

---

[a] We have never observed a frequency shift of the clock transition resulting from the atomic beam

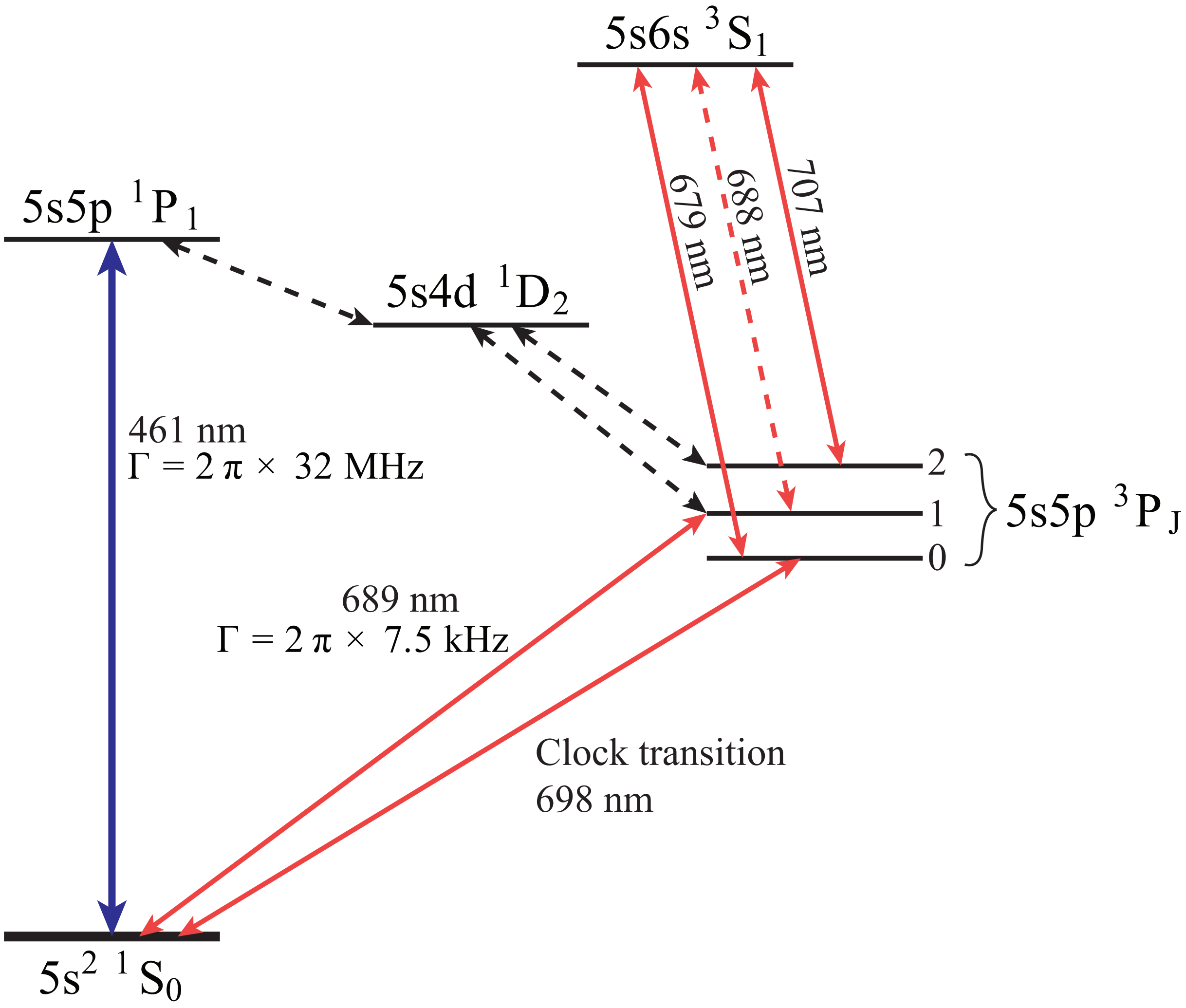

Figure 1.2: A strontium level diagram. Solid lines indicate all the laser driven transitions involved in operating and optical lattice clock. Dashed black lines indicated population leaks that create the need for re-pumping lasers in the blue MOT. The dashed red line indicates the decay pathway that allows the re-pumping lasers to transfer atoms back to the ground state via $^3P_1$ decay. The hyperfine structure present in ^{87}Sr is neglected in this diagram.

its counter-propagating partner ($\hat{\sigma}^+$ or $\hat{\sigma}^-$). Field gradients are matched with the beams such that when an atom travels too far in a given direction, the magnetic field shifts the proper transition closer to resonance with the corresponding laser beam to push the atom back towards trap center. Adding a large nuclear spin of $^9/_2$ to this formula can complicate MOT operation, or, with exactly the same quantum numbers, it can matter very little, as we will see below.

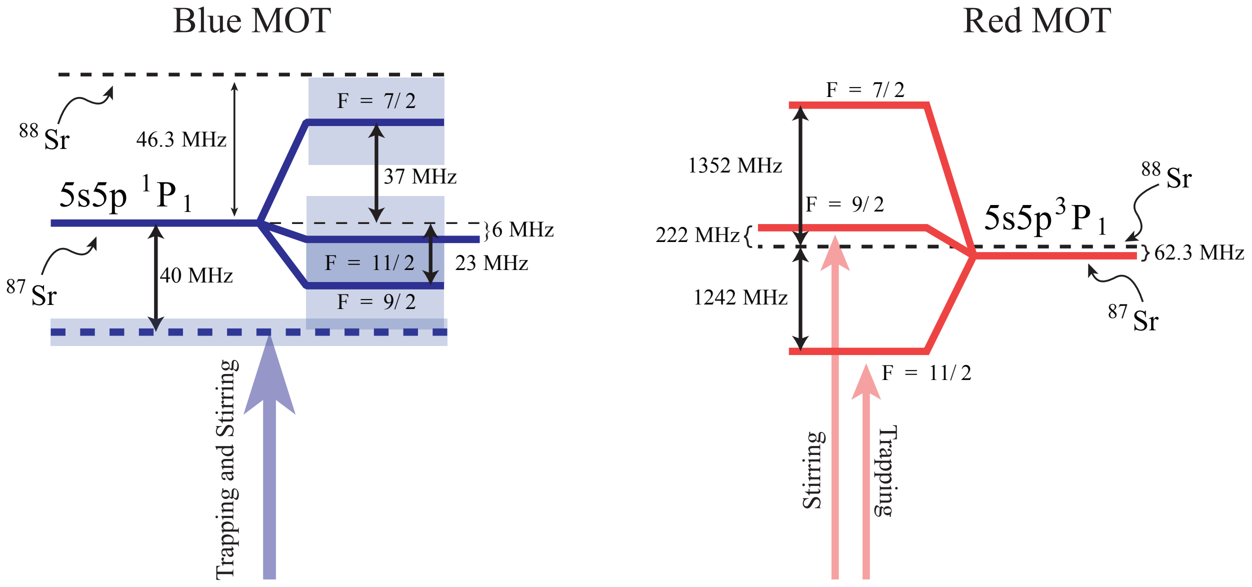

Figure 1.3: A level diagram for the hyperfine splitting in the $^1P_1$ and $^3P_1$ states used for MOT trapping. For the $^1P_1$ state, the hyperfine splitting between ^{87}Sr energy levels is drawn to scale and the natural linewidth of the transitions and trapping laser linewidth are represented by translucent blue rectangles. For the $^3P_1$ state, the natural linewidths are much narrower than the solid lines used to draw the center frequencies. The trapping and stirring lasers necessary for ^{87}Sr blue and red MOT operation are represented with pale blue and red arrows, respectively.

1.2.1 The red MOT

To gain a greater insight into both ^{87}Sr MOTs, we begin by describing the red MOT. There are three factors that couple together to make the red MOT more difficult to achieve in ^{87}Sr than in ^{88}Sr . **(i)** The Landé g-factor of the ground state is effectively zero compared to that of the excited state since the ground state has total electronic angular momentum $J = 0$ and the nuclear g-factor is smaller than the electronic g-factor by the ratio of the electron mass to proton mass. **(ii)** the nuclear spin of 9/2 is large enough (> 1) such that we have $\sigma^{\pm}$ transitions that do not change the sign of the total angular momentum projection along the quantization axis. **(iii)** The hyperfine splitting is large compared to the transition natural linewidth. For the MOT operation we still require that we operate on a J to $J' = J + 1$ transition so that the $\hat{\sigma}^{\pm}$ polarized light can excite any of the ground nuclear-spin magnetic sublevels. Figure 1.4(a) demonstrates how

(i-iii) contribute to make some of the ground sublevels not trappable. We see that in the example shown, the atom has traveled away from the trap center in the $\hat{x}$ direction such that the field has shifted excited state levels with $m_F \leq -1/2$ down in energy and states with $m_F \geq 1/2$ up in energy. For σ^- transitions from ground states with $m_F \leq 1/2$, the MOT transition shifts lower in frequency, bringing the transition closer to resonance with the σ^- polarized laser beam such that it pushes the atoms back to the trap center. However, for ground state $m_F > 1/2$ the red MOT transition actually increases in frequency, meaning that these states are not trapped by the MOT laser beams. In the example illustrated by Fig. 1.4(a), one might also worry that for ground states with $m_f < -1/2$, both σ^- and σ^+ transitions are brought closer to resonance with the magnetic field. However, as the atom moves away from trap center, σ^- transitions are shifted into resonance before σ^+ resonances for these states due to the m_F dependent g-factor. Additionally, Fig. 1.4(b) shows that the Clebsch-Gordan coefficients favor the σ^- transitions in these sublevels.

To circumvent the problem of non-trapped states, we also apply light tuned to the $^1\mathrm{S}_0$ to $^3\mathrm{P}_1$, $F = 9/2$ state (Fig. 1.3) with identical polarization and geometry to the MOT beams. The g-factor for this state is smaller than that of the $F = 11/2$ state, which allows atoms to scatter light on the $F = 9/2$ transition over a larger distance from trap center. The Clebsh-Gordan coefficients further show that the scattering rates for $\sigma^{\pm}$ light is near unity and slightly favors the opposite transitions as the $F = 11/2$ MOT light (Fig. 1.4(b)). These factors combine to make the $F = 9/2$ light efficient at randomizing or "stirring" the value of m_F for the atoms, allowing the MOT to operate efficiently on all atoms.

1.2.2 The blue MOT

Although the blue MOT operates with all the same quantum numbers as the red MOT, it does not demonstrate the same complication, and we are able to use a single frequency to create a MOT just as with ^{88}Sr . The reason for this fortuitous simplification is that condition **(iii)** is no longer satisfied. When the MOT light is tuned one linewidth below the $F = 11/2$ MOT transition, the $F = 9/2$ stirring transition is actually only 17 MHz above the frequency of the MOT light (Fig.

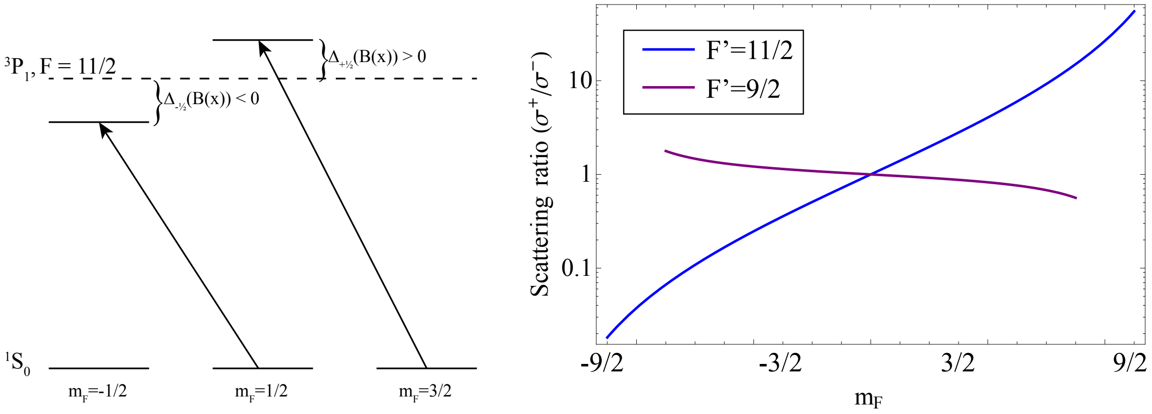

(a) Non-trapped states in the ^{87}Sr red MOT

(b) Ratio of σ^+ to σ^- transition strengths for the ^{87}Sr red MOT

Figure 1.4: (a) An illustration demonstrating the non-trapped states in the ^{87}Sr red MOT. (b) Ratio of σ^+ to σ^- transition strengths calculated from Clebsch-Gordan coefficients for the $^1S_0$ to $^3P_1$ transition with excited total angular momenta of $F' = 11/2$ (blue) and $F' = 9/2$ (purple).

1.3). Thus, the single MOT frequency acts as both stirring and trapping light.

The main vice of the blue transition is that it has a small probability to decay to the $^1D_2$ state, which can decay to the metastable $^3P_2$. To pump all the atoms out of $^3P_2$ and back to the ground state through $^3P_1$, two re-pumping lasers are required that act on the $^3P_2$ to $^3S_1$ transition at 707 nm and the $^3P_0$ to $^3S_1$ transition at 679 nm. The $^3P_0$ state is populated by decay from $^3S_1$. For ^{87}Sr , the $^3S_1$ state has hyperfine structure so we modulate the re-pumping lasers over several GHz to address all hyperfine states. This technique also allows us to address the ^{88}Sr resonances over a long period of time without actively controlling the frequency of the re-pumping lasers.

1.2.3 Putting it all together

Both the blue and red MOTs are incredible tools for cooling and trapping strontium atoms. The strong blue MOT is able to capture large numbers of atoms (See [9] for in-depth analysis of blue MOT trapping and cooling) and the narrow red MOT is able to cool them to a final temperature of $\sim 1\ \mu$K (The many regimes in which this MOT can operate are explored in [10]). However, putting

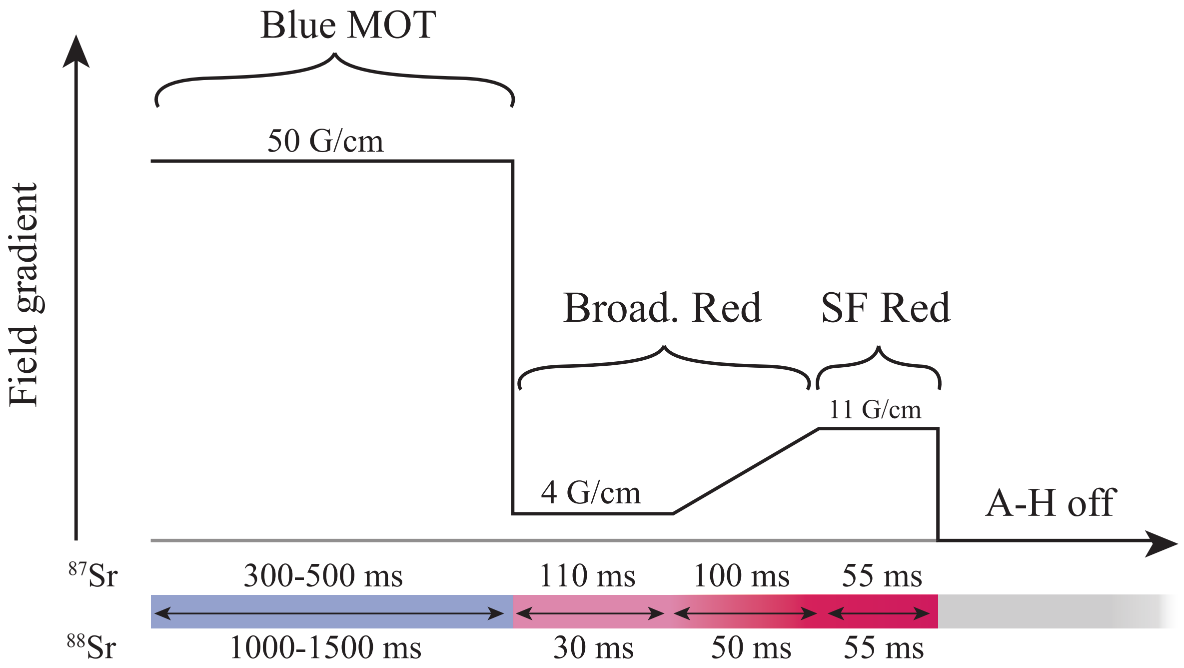

Figure 1.5: A timing diagram of the different magnetic field gradient strengths that are used for the magneto-optical trapping of ^{87}Sr and ^{88}Sr .

these two tools together is a non-trivial task, owing to their vastly different natural linewidths. After initially loading atoms in the blue MOT , we extinguish the blue MOT light, greatly decrease the magnetic field gradient and modulate the frequencies of the red MOT light to broaden their linewidth by about 1 MHz. The use of this "broadband" red MOT achieves spatial mode-matching with the blue MOT. At this point, the few mK temperature of the blue MOT has been reduced to $\sim$ 100 μK. Next, the magnetic field gradient is increased to compress the MOT cloud, after which, we cease the broadband modulation of the red MOT lasers. The red mot lasers have a linewidth below 1 kHz so that we can determine the final temperature and atomic density of the "single frequency" red mot with the intensity and frequency of the MOT lasers [10]. For ^{87}Sr clock operation we optimize these parameters to maximize the number of atoms loaded into our optical lattice. In our work with ^{88}Sr , it is advantageous for us to maximize the optical thickness of the red MOT cloud, which does not necessarily maximize the atom number. Figure 1.5 demonstrates the exact timing and field gradients used in our MOT trapping of ^{87}Sr and ^{88}Sr .

1.3 A magic wavelength optical lattice

For the final preparation of ^{87}Sr atoms before spectroscopy, we transfer the atoms into an optical trap where the atoms are attracted to the intensity maximum of the trapping light due to the interaction between the light and the dipoles induced in the atoms (See [12] for an overview of this effect). The attractive force we use to trap our atoms is intimately related to a shift of the potential energy of the atomic state. Obviously, this could have disastrous consequences for clock operation, but, for our trap we choose the wavelength such that the energy shifts for both clock states are identical. The wavelength at which this occurs is known as the magic wavelength and for ^{87}Sr it is 813.4 nm. Of course, it is often the case that science dispels magic and for our "magic" wavelength this is true at some level. First, the atomic energy level shifts depend on not only the intensity of the trapping light, but also the polarization of this light and its orientation relative to the atom's quantization axis (determined by an applied magnetic field). We can separate the shift of the clock transition proportional to lattice intensity into three components [13, 14]

$$\Delta\nu_{\text{Latt}}(\omega_{\text{Latt}}) = I_0(\kappa_s(\omega_{\text{Latt}}) + \kappa_v(\omega_{\text{Latt}})m_F\xi\hat{e}_k \cdot \hat{e}_B + \kappa_t(\omega_{\text{Latt}})\beta), \tag{1.1}$$

where ω_{Latt} is the frequency of the light, $\xi\hat{e}_k = -i\hat{\epsilon} \times \hat{\epsilon}^*$ is the degree of circularity, and $\beta = (3|\hat{\epsilon} \cdot \hat{e}_B|^2 - 1)[3m_F^2 - F(F+1)]$, with $\hat{\epsilon}$ the polarization vector for the light and $\hat{e}_B$ a unit vector in the direction of the applied magnetic field. $\kappa_s(\omega_{\text{Latt}})$ determines the scalar portion of the shift, which only depends on the light intensity. $\kappa_v(\omega_{\text{Latt}})$ determines the the vector component of the shift, which depends on the polarization of the light and its orientation relative to the magnetic field, as well as the m_F level of the atom. $\kappa_t(\omega_{\text{Latt}})$ determines the tensor component of the shift, which depends on the magnitude of the light polarization vector along the magnetic field as well as the magnitude of m_F. Thus, we see that there is no one magic wavelength for ^{87}Sr , but that the magic wavelength depends both on the atomic structure and the experimental setup of the applied magnetic and light fields. Second, higher order contributions to the intensity shift contribute with a different dependence on intensity. For example, hyperpolarizability, proportional to the square of intensity has been measured at extremely high lattice depths [15]. Additionally, magnetic dipole (M1) and electric quadrapole (E2) shifts are proportional to the square root of intensity [14]. For our current clock accuracy and operating conditions, these higher order effects do not contribute at the 10^{-18} fractional frequency level and our lattice is still magical.

For our ^{87}Sr optical lattice clock, the single frequency red MOT is overlapped with a one-dimensional (1D) optical lattice created by the interference pattern of a retro-reflected 813.4 nm laser beam. Although the lattice light creates a conservative potential, the stark shift of the red MOT transition caused by the lattice light allows the MOT to efficiently load atoms into the lattice. The beam focus is centered on the atoms and the Rayleigh range of the beam is much longer than the ~ 30 μm standard deviation of the MOT cloud so that the individual lattice sites can be treated as identical. The number of atoms in each site is determined using a Poissonian probability distribution with a mean value corresponding to the Gaussian density profile of the MOT. The lattice is about 19° from vertical, traveling along the plane made by the vertical and H1 axes of our vacuum chamber (Fig. 1.1). The lattice is polarized along H2. When we use a two-dimensional (2D) lattice, a second lattice along H1, also linearly polarized along H2, is ramped on after the red MOT is extinguished. The first lattice is then ramped off and back on to ensure that all atoms are trapped at the intersection of the two beams.

1.4 Spectroscopy in an optical lattice

We can operate with trap depths between 5 and 30 μK and with atom temperatures between 1 and 7 μK, but typically the atom temperature is much lower than the trap depth so that we can approximate our trap as a harmonic oscillator. In this approximation we can use our lattice to characterize both the trap and the atom temperature. From the expressions for trap frequencies derived in Appendix A, $\Omega_x = \Omega_y = \frac{1}{w}\sqrt{\frac{4V_0}{m}}$ and $\Omega_z = \frac{2\pi}{\lambda}\sqrt{\frac{2V_0}{m}}$, we get an expression for the trap

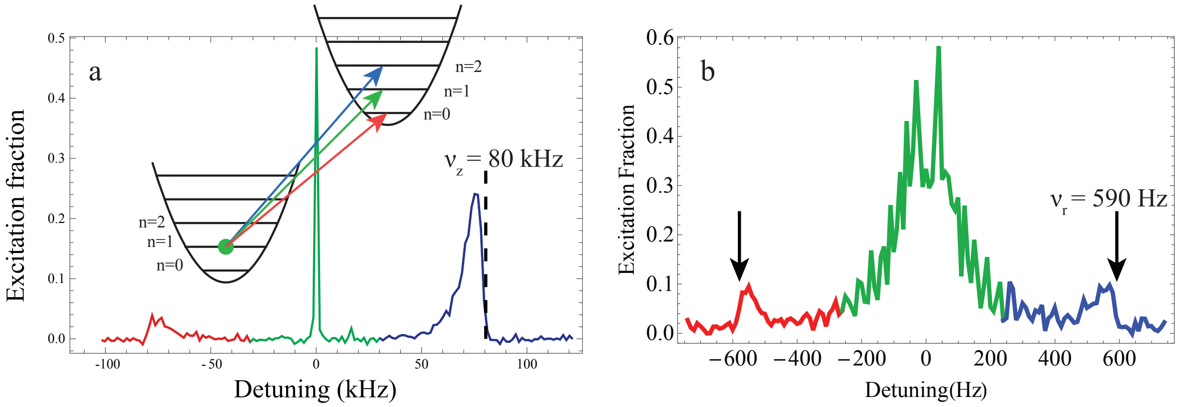

Figure 1.6: (a) The drawing overlaid on the plot depicts the process of exciting atoms in oscillator level n to oscillator levels $n-1$, n, and $n+1$. The plotted excitation fraction versus detuning, which uses a high intensity 80 ms clock laser pulse, shows a measurement of the longitudinal trap frequency. Below the n to n carrier transition frequency (green points) we excite atoms from n to $n-1$ in the longitudinal direction (red sideband). Above the carrier frequency, we excite atoms from n to $n+1$ (blue sideband). The steep edges of these features occur at the longitudinal trap frequency and excitation closer to the carrier results from trap anharmonicity. (b) A measurement of the radial trap frequency. We intentionally misalign the clock laser beam so that we may excite the radial sidebands. The measured excitation fraction versus detuning shows small peaks above and below the carrier (green) at the radial trap frequency corresponding to the blue and red sidebands, respectively.

depth in terms of the measured trap frequency along the longitudinal axis of the lattice,

$$V_0 = \nu_z^2 \frac{m^2 \lambda^4}{h^2} E_{\text{rec}}, \tag{1.2}$$

where $\nu_i = \Omega_i/(2\pi)$, m is mass of an atom, λ is the lattice wavelength, h is Planck's constant, and $E_{\text{rec}} = h^2/(2m\lambda^2)$ is the recoil energy of a lattice photon. We also get an expression for the lattice beam waist in terms of the ratio of longitudinal trap frequency to radial trap frequency,

$$w_0 = \frac{\nu_z}{\nu_r} \frac{\lambda}{\sqrt{2}\pi}. \tag{1.3}$$

We can measure the trap frequencies directly owing to the strong confinement along the longitudinal axis of the lattice provided by the $\cos^2 kz$ modulation of light intensity. Since ν_z is much larger than the recoil frequency, $\nu_{\text{rec}} = E_{\text{rec}}/h$, and the transition linewidth, we are operating in the Lamb-Dicke and resolved sideband regime where the ${}^1\mathrm{S}_0$ to ${}^3\mathrm{P}_0$ (clock) transition is free

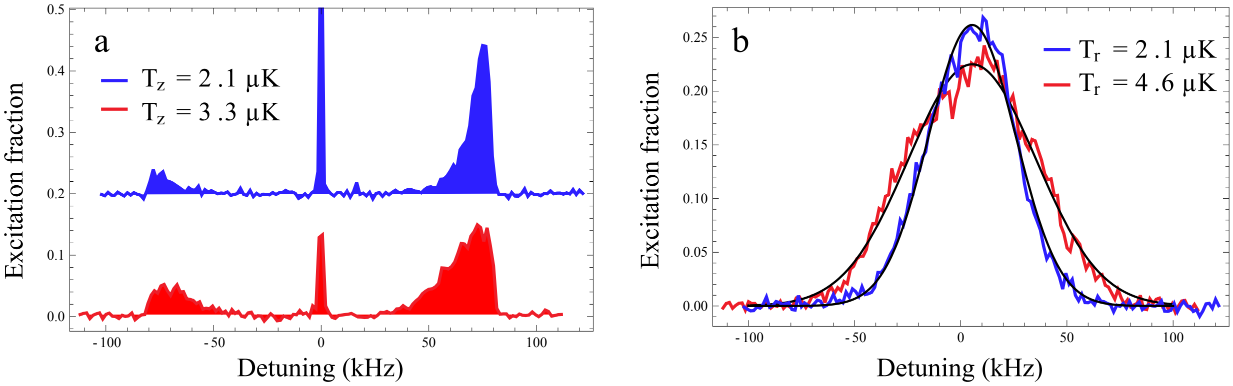

Figure 1.7: (a) The two plotted excitation fraction versus detuning curves demonstrate the temperature dependence of the area underneath the sidebands. The blue curve corresponds to $T_z = 2.1$ μK and the red curve corresponds to $T_z = 3.3$ μK. The area underneath the curves is filled in and the blue curve is offset by 0.2 for clarity. (b) The measured excitation fraction versus detuning for probing the clock transition along the radial direction. The radial temperature determines the width of this resonance via Doppler broadening.

from Doppler and recoil effects. The motional effects manifest as sideband transitions that drive an atom in the n^{th} oscillator level to the $(n \pm 1)$ level. Figure 1.6 demonstrates our measurements of the trap frequencies. With the clock laser aligned to the lattice laser, we subject the atoms to an intense 80 ms pulse of clock laser light. Atoms in $^1\text{S}_0$ $(|g\rangle)$ are excited to $^3\text{P}_0$ $(|e\rangle)$ at the clock transition frequency and at $\sim \nu_z$ below(above) the transition frequency, corresponding to the red(blue) sideband. The sideband excitation extends toward the carrier for several kHz since trap anharmonicity makes longitudinal sideband frequencies depend on the atom's oscillator level in the radial direction. We can also observe the radial sideband frequency by adding an intentional misalignment between our clock and lattice lasers. We can operate with ν_z between 40 and 100 kHz, limited by atom loss at low trap frequencies and laser power at large trap frequencies. For a reference ν_z of 80 kHz, we have measured ν_r to be between 450 and 600 Hz, indicating that over the past 6 years our lattice spot size has varied between 24 and 32 μm.

The measured longitudinal sidebands can also tell us about atom temperature in this dimension, T_z. It was shown that the ratio of the area underneath the red and blue sidebands is related to temperature by [16],

$$\frac{A_{\text{red}}}{A_{\text{blue}}} = 1 - \frac{e^{-E_0/k_B T}}{\sum_{n_z=0} e^{-E_{n_z}/k_B T}}, \tag{1.4}$$

where the sum should go over the number of levels that exist in the trap ($\sim$ 6 for 80 kHz) and $E_{n_z} = h\nu_z(n_z + \frac{1}{2}) - \frac{\nu_{\text{rec}}}{2}(n_z^2 + n_z + 1)$ is the energy of the n_z oscillator level including the effect of anharmonicity, modeled as a quartic distortion. Figure 1.7(a) shows measurements of the sidebands at two different temperatures. We can also extract the radial temperature from the shape of the blue sideband [16, 17], however, a much simpler method is to probe the clock transition in one of the radial dimensions. In this case, we fit the measured resonance to a Gaussian of the form,

$$P_e(\nu) = Ae^{\frac{-(\nu_0-\nu)}{2\sigma_d^2}}, \quad where \quad \sigma_d = \nu_0\sqrt{\frac{k_B T_r}{mc^2}}, \tag{1.5}$$

with k_B being the Boltzmann constant and c being the speed of light. Figure 1.7 shows two example measurements of T_r, which were obtained by fitting a Gaussian of the form in Eqn. 1.5 to the measured excitation fraction versus detuning.

1.5 State preparation

Often we wish to prepare a specific nuclear spin state or mixture of nuclear spin states at a particular temperature. To accomplish this we apply a small magnetic field of $\sim$ 100 mG along the H2 axis of our vacuum chamber (Fig. 1.1) to establish a quantization axis. Using a beam of $\sigma^{+(-)}$ light resonant on the $^1S_0$ to $^3P_1$, $F = 9/2$ transition and propagating along H2, we can populate all the atoms in the $m_F = +(-)9/2$ state. We can also reduce the power or duration of this polarizing light in order to vary the $m_F = +(-)9/2$ population between 10% and 100% of the total atom number, leaving the remaining atoms mostly in $m_F = +(-)7/2$ with a smaller number of $m_F = +(-)5/2$ atoms. We can also address the atoms with light resonant on the $^1S_0$ to $^3P_1$, $F = 7/2$ transition and linearly polarized along H2. This prepares all the atoms in the $m_F = \pm 9/2$ states and we can adjust the imbalance between the two populations by adjusting the polarizing laser frequency.

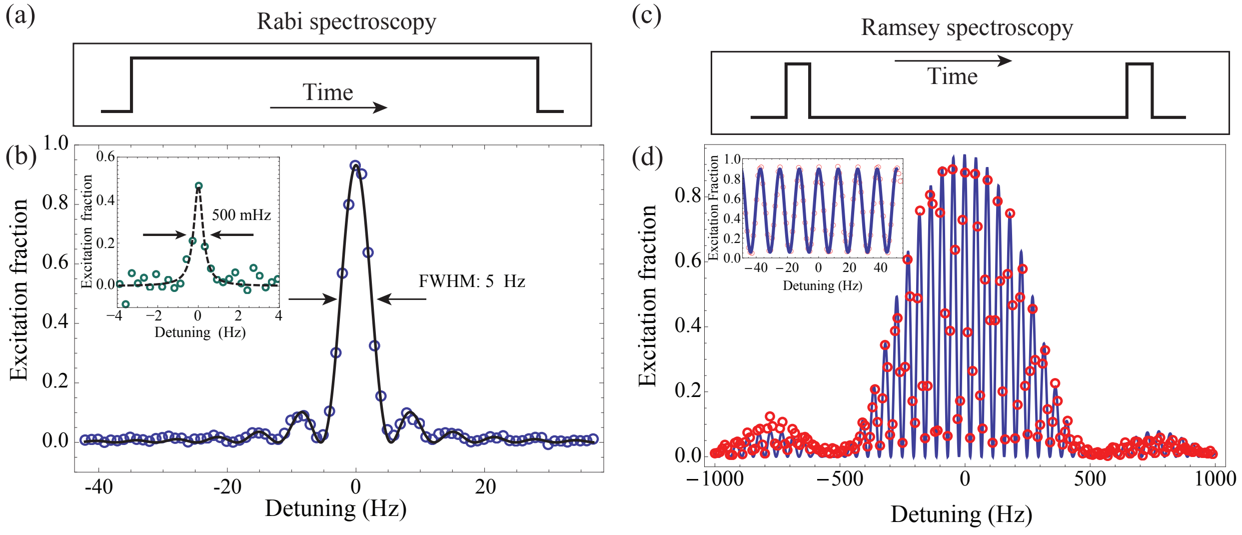

Figure 1.8: (a) A timing diagram demonstrating when the clock laser is on during Rabi spectroscopy. (b) The measured $|e\rangle$ state fraction versus detuning for Rabi spectroscopy with an 80 ms π-pulse. The black line is the calculated line shape from Eqn. 1.7 with an amplitude that is fit to the data. The inset demonstrates the probe time dependence of the measured linewidth as well as the onset of decoherence. It shows the measured excitation fraction versus detuning for a 3 s excitation pulse. (c) A timing diagram demonstrating when the clock laser is on during Ramsey Spectroscopy. (d) The measured excitation fraction versus detuning for Ramsey spectroscopy where detuning is scanned over a large range such that we can see the complicated structure predicted in Eqn. 1.8. The blue line represents the prediction of Eqn. 1.8 with an amplitude that is fit to the data. The inset shows the measured excitation fraction versus detuning using Ramsey spectroscopy for $\pi/2$-pulse times of 750 μs and a free evolution time of 80 ms that is scanned ±50 Hz from resonance. Here, we can neglect the the complicated structure predicted by Eqn. 1.8 and fit the data to a $\cos^2$ function.

Any in-lattice cooling is performed during the first half of polarization preparation because the cooling light generally depolarizes the atoms. We apply sideband cooling of T_z and Doppler cooling of T_r using the $^1\mathrm{S}_0$ to $^3\mathrm{P}_1$, $F = 11/2$ transition. When we work with a completely unpolarized sample, the $F = 9/2$ transition is more effective for cooling although it pushes the atoms toward the $m_F = -9/2$ state, increasing this state's population from 10% to 13% of the total population.

1.6 Clock spectroscopy

With the atoms prepared in the desired nuclear-spin sublevels, we are ready to measure the frequency of their $^1\mathrm{S}_0$ to $^3\mathrm{P}_0$ transition. Before spectroscopy we increase the applied magnetic field so that spectroscopic features from different nuclear spin states are well separated (~ 0.5 to 2 G). The clock laser is linearly polarized along H2 such that we only drive $\Delta m_F = 0$ (π) transitions. The lifetime of the $^3\mathrm{P}_0$ state is $\sim$ 150 s, corresponding to a $\sim$ 1 mHz natural linewidth. The first consequence of this long lifetime is that we do not need to consider the effect of spontaneous emission on the time scales that we probe our atoms (≤ 3 s). The second is that the linewidth we measure is Fourier-limited by the timing of our spectroscopy sequence. The interaction between atoms and clock laser can be modeled with the Hamiltonian

$$\hat{H} = \frac{1}{2}\hbar\Omega(\mathbf{r},t)\hat{\sigma}_\phi(t) - \frac{1}{2}\hbar\Delta(t)\hat{\sigma}_z, \tag{1.6}$$

where $\Omega(\mathbf{r},t) \equiv \langle g|\,\hat{\mathbf{d}}\cdot\mathbf{E_0}(\mathbf{r},t)\,|e\rangle/\hbar$ is the Rabi frequency with $\hat{\mathbf{d}}$ being the dipole operator and $\mathbf{E_0}$ the amplitude of the electric field, $\Delta(t) = \omega_L - \omega_a$ is the detuning of the clock laser frequency ω_L from the atomic transition frequency ω_a, and $\hat{\sigma}_\phi(t) = \cos\phi(t)\hat{\sigma}_x + \sin\phi(t)\hat{\sigma}_y$ with $\hat{\sigma}_i$ being the Pauli spin matrices.

Let us first consider the simple case of Rabi spectroscopy where the clock laser is applied to the atoms for a time $t = 0$ to T with uniform Rabi frequency $\Omega(\mathbf{r},t) = \Omega_0$, detuning $\Delta(t) = \Delta_0$, and phase of the clock laser $\hat{\sigma}_\phi(t) = \hat{\sigma}_x$. In this case, the probability for an atom to be in $|e\rangle$ is given by

$$p_e^{\mathrm{Rabi}}(T,\Delta_0) = \frac{\Omega_0^2}{\Omega_{\Delta_0}^2}\sin^2\frac{\Omega_{\Delta_0}T}{2}, \tag{1.7}$$

where $\Omega_{\Delta_0} = \sqrt{\Omega_0^2 + \Delta_0^2}$. We typically operate the clock with $T\Omega_0 = \pi$ (a π-pulse), such that the fracion of atoms in $|e\rangle$ is maximized at $\Delta_0 = 0$. The full width at half-maximum (FWHM) of Eqn. 1.7 for a π-pulse is given by $\delta\omega/(2\pi) \approx 0.799/T$. Figure 1.8(b) shows measured Rabi line shapes for an 80 ms π-pulse and a 3 s π-pulse. While the 80 ms pulse demonstrates the line shape predicted in Eqn. 1.7, the 3 s π-pulse shows that the onset of decoherence makes the measured resonance feature deviate from this prediction. Decoherence can occur from laser frequency noise or from atomic interactions, as we will see in Chapters 2 and 3, respectively. In principle, photon scattering from the lattice laser can also cause decoherence, however, under typical experimental conditions calculations of lattice photon scattering predict less than 0.1 scattering events per second [8].

In addition to Rabi spectroscopy, our work makes extensive use of Ramsey spectroscopy, where two laser pulses are applied to the atoms, separated in time. The most common implementation of this is to have two pulses of time $t = \pi/(2\Omega_0)$ (a $\pi/2$-pulse) separated by a time τ. Once again we assume a uniform Rabi frequency during the pulses and a constant detuning and phase of the clock laser. Then using Eqn. 1.6 we get that the probability to be in $|e\rangle$ after the final pulse is

$$p_e^{\mathrm{Ramsey}}(\tau,\Delta_0) = \frac{\Omega_0^2}{\Omega_{\Delta_0}^4}\left[\Omega_{\Delta_0}\cos\left(\frac{\Delta_0\tau}{2}\right)\sin\left(\frac{\pi\Omega_{\Delta_0}}{2\Omega_0}\right) - 2\Delta\sin\left(\frac{\Delta_0\tau}{2}\right)\sin^2\left(\frac{\pi\Omega_{\Delta_0}}{4\Omega_0}\right)\right]^2. \quad (1.8)$$

Figure 1.8(a) displays the pulse timing for this implementation of Ramsey spectroscopy and Fig. 1.8(b) demonstrates two experimental implementations of Ramsey spectroscopy. The first shows that when Δ_0 is stepped across a range that is comparable to Ω_0 we observe the complicated structure predicted in Eqn. 1.8. In a second example (Fig. 1.8(b) inset), the Rabi frequency $\Omega_0 = 2\pi \times 333$ Hz, is large compared to the scan range of detuning $\Delta_0 = \pm 2\pi \times 50$ Hz. Here, we see that the observed fraction of atoms in $|e\rangle$ versus detuning fits well to the limit of Eqn. 1.8 for $\Delta_0 \ll \Omega_0$, $\cos^2(\frac{\Delta_0\tau}{2})$. This simple case has a FWHM of $\delta\omega/(2\pi) = 1/(2T)$. To account for decoherence, we add an amplitude and vertical offset that is allowed to fit to the data.

In the subsequent work described in this thesis, we use many variations on this prototypical example of Ramsey spectroscopy. One variation that we commonly use is to change the time of the first Ramsey pulse. This allows us to examine the effects of interactions during the free evolution time, τ, with different superpositions of $|g\rangle$ and $|e\rangle$ (See Chapters 3 and 4). We also have the ability to change the phase of the second Ramsey pulse relative to that of the first pulse. Furthermore, by adding a π-pulse in the middle of the free evolution time we can cancel certain decoherence mechanisms (Chapter 4). Adding a train of π-pulses that are equally spaced throughout τ can be used to either avoid or focus on noise processes with a specific frequency dependence (See Chapter

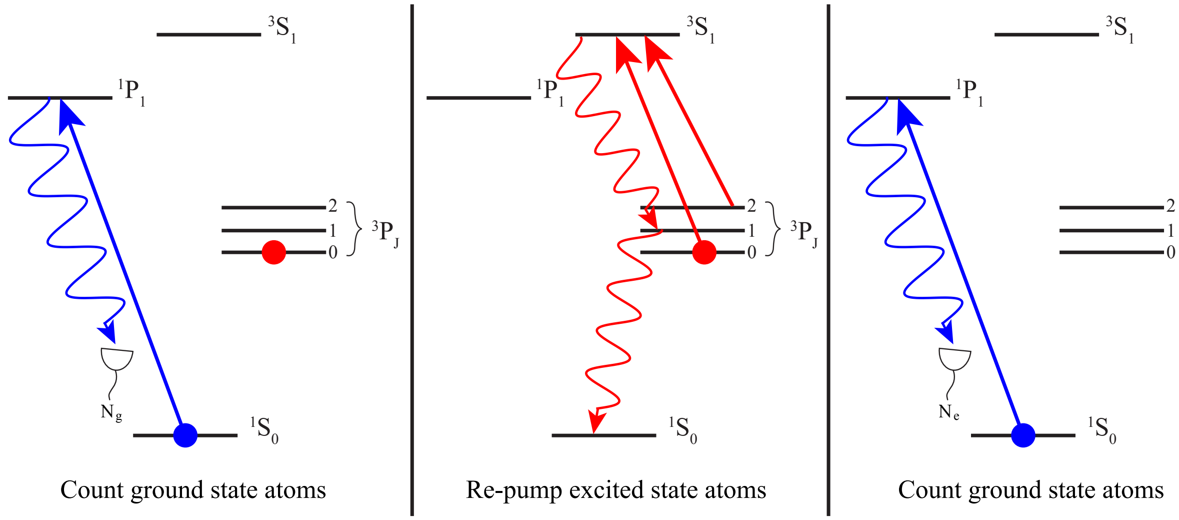

Figure 1.9: This diagram demonstrates the electron shelving technique for counting the number of $|g\rangle$ (N_g) and $|e\rangle(N_e)$ atoms after clock laser excitation. First, the $|g\rangle$ atoms are counted by fluorescence from the $|g\rangle$ to $^1P_1$ transition. This measurement heats $|g\rangle$ atoms out of the trap but leaves $|e\rangle$ atoms unperturbed. Next, $|e\rangle$ atoms are re-pumped to $|g\rangle$ via decay through the $^3P_1$ state using 707 nm and 679 nm light resonant on the $^3P_2$ to $^3S_1$ and $|e\rangle$ to $^3S_1$ transitions. Finally, the atoms in $|g\rangle$ are counted again to measure the number of atoms originally in $|e\rangle$.

2). We can even cancel the accumulation of pulse timing errors by changing the phase of our laser such that each applied π-pulse has a phase opposite that of the preceding π-pulse.

1.7 Atomic state Detection

To measure the final populations in $|g\rangle$ and $|e\rangle$ we employ the electron shelving technique (Fig. 1.9). First we count the number of $|g\rangle$ atoms by probing the atoms with a retro-reflected laser beam resonant on the $|g\rangle$ to $^1P_1$ transition. We detect 461 nm fluorescence with a photomultiplier tube (PMT). The large scattering rate from this transition heats atoms out of the lattice. After all the $|g\rangle$ atoms are removed from the trap, we re-pump the $|e\rangle$ atoms to $|g\rangle$ by exciting transitions from both $|e\rangle$ and $^3P_2$ to $^3S_1$ with the blue MOT re-pumping lasers. Atoms decay back to $|g\rangle$ via $^3P_1$ decay. Finally, we count the number of atoms originally in $|e\rangle$ by counting the number of $|g\rangle$ atoms again. For N_g atoms measured in $|g\rangle$ and N_e atoms in $|e\rangle$ the fraction of atoms in $|e\rangle$, or excitation fraction, is given by $n_e = \frac{N_e}{N_e+N_g} \equiv n$.

Since the measured excitation fraction is so central to our work, an understanding of the noise processes that affect this measurement is extremely useful. There are two fundamental noise sources that contribute to the noise we observe. Quantum projection noise (QPN) arises from the fact that our measurements of N_g and N_e deterministically project an atom in state $|\psi\rangle = \alpha |g\rangle + \beta |e\rangle$ into either $|g\rangle$ or $|e\rangle$ with probabilities α^2 or β^2, respectively. The variance in our measurements of N_g and N_e arising from QPN is given by $\Delta N^2_{g,e_{QPN}} = N n_{g,e}(1 - n_{g,e})$ [18], where $n_g = \frac{N_g}{N_e+N_g}$ is the fraction of atoms in $|g\rangle$. Propagating the error while accounting for the correlation between the two measurements (if an atom is projected into $|g\rangle$ by our measurement, it is expressly not projected into $|e\rangle$ and vice versa) gives that the variance in n due to QPN is given by,

$$\Delta n^2_{QPN} = \frac{n(1-n)}{N}. \tag{1.9}$$

Photon shot noise (PSN) of the scattered light we collect from our atoms is another fundamental process that arises due to the particle nature of light. For measurements of N_g and N_e we collect $\eta_{g,e} = N_{ph} N_{g,e}$ photons where N_{ph} is the average number of photons collected per atom. The variance in the number of photons collected due to PSN is $\Delta \eta^2_{g,e} = \eta_{g,e}$ which gives that the variance in a measurement of $N_{g,e}$ arising from PSN is given by $\Delta N^2_{g,e_{PSN}} = N_{g,e}/N_{ph}$. Unlike with QPN, the variance of N_g arising from PSN is uncorrelated with that of N_e because PSN only depends on the number of photons collected. Therefore, the variance of n arising from PSN is given by,

$$\Delta n^2_{PSN} = \frac{n(1-n)}{N_{ph} N}. \tag{1.10}$$

Combining the scattering rate of the $^1\mathrm{S}_0$ to $^1\mathrm{P}_1$ transition, the average scattering lifetime of atoms in the lattice before they are heated out of the trap, our detection geometry, and the quantum efficiency of our PMT, we estimate that we detect ~ 100 photons per atom such that PSN is always much lower than QPN in our system.

In addition to these fundamental noise processes, technical noise can also affect our measurement of n arising from our detection electronics, fluctuations in the atom number [19], and noise in the ultrastable laser used to excite the clock transition (the Dick effect) [20, 21, 22]. The variance

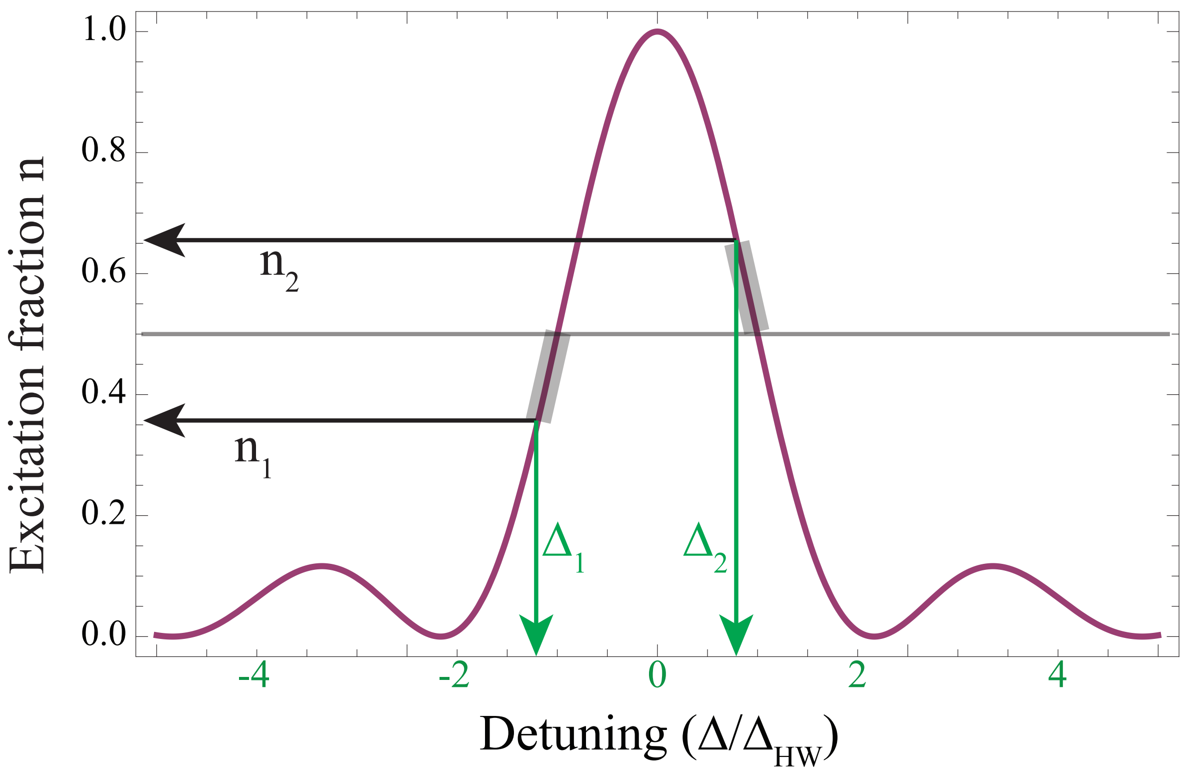

Figure 1.10: A diagram demonstrating the relationship between the excitation fractions n_1 and n_2 measured at $\Delta_1 = \omega_{\text{old}} - \Delta_{\text{HW}} - \omega_a$ and $\Delta_2 = \omega_{\text{old}} + \Delta_{\text{HW}} - \omega_a$, respectively, to the detuning of the clock laser $\omega_{\text{old}} - \omega_{\text{new}} = \frac{(n_2 - n_1)}{2} \left.\frac{\delta n}{\delta \Delta}\right|_{\Delta=\Delta_{\text{HW}}}$.

in n due to electronic noise ant atom number fluctuations scales at $1/N^2$. In our system, these are only important if our atom number is very low ($N < 100$). For typical clock operation where we interrogate 1000 atoms with an ultrastable laser having a 1 s fractional frequency stability of 1×10^{-16}, the Dick effect is the dominant source of noise. We demonstrate clock stability about a factor of 2 worse than what we expect from QPN alone [1].

1.8 Feedback from the atomic signal

During clock operation, the measured value of excitation fraction is used to feed back upon the clock laser, so that it remains at the clock transition frequency. Our clock laser is initially set to our best estimate of the clock transition frequency, $\omega_L = \omega_{\text{old}}$. We add in an offset of $\pm\Delta_{\text{HW}}$

to ω_L such that we probe the atoms at $\Delta_1 = \omega_{\text{old}} - \Delta_{\text{HW}} - \omega_a$ and $\Delta_2 = \omega_{\text{old}} + \Delta_{\text{HW}} - \omega_a$ where we measure the excitation fractions n_1 and n_2, respectively. Here, $\pm\Delta_{\text{HW}}$ is the detuning where the excitation fraction is equal to half its maximum value. For small deviations of ω_L from ω_a, the slope of $n(\Delta)$ at Δ_{HW} relates the difference between n_2 and n_1 to the true detuning of the clock laser such that $\omega_{\text{old}} - \omega_{\text{new}} = \frac{(n_2 - n_1)}{2} \left.\frac{\delta n}{\delta \Delta}\right|_{\Delta = \Delta_{\text{HW}}}$. The clock laser is tuned to new best estimate for the clock transition frequency, ω_{new}, and the measurement is repeated. For clock operation, these measurements are made for atoms prepared in the $m_F = +9/2$ and the $m_F = -9/2$ states to infer the field-free transition frequency.

We can also use this procedure to measure systematic shifts of the clock transition. Between two subsequent measurements, we modulate an experimental condition such that the difference between even numbered measurements and odd numbered measurements will resolve the frequency shift associated with the changed condition. For example, we may perform all odd measurements at a high density and all even measurements at a low density to extract the density dependent shift of the clock transition. On such short time scales, the effect of laser drift is negligible on our measurements since we are able to cancel laser drift to below 1 mHz/s. However, we can also remove a polynomial drift of order $N - 2$ from any N-measurement sequence by using the analysis technique described in [23].

1.9 Clock Performance

There are two measures of clock performance, accuracy and stability. Stability measures the mean deviation in the clock's frequency over a particular period of time whereas accuracy measures the clock's mean offset from an ideal value. To demonstrate a clock's stability one can compare it to a more stable reference. For a clock with state-of the art stability this is no longer an option so one can compare two clocks of similar stability and then the single clock stability can be found by dividing the stability of the comparison by $\sqrt{2}$. True accuracy below the 10^{-16} fractional frequency level is not possible because the second is defined in terms of the ground hyperfine splitting of the caesium-133 atom, which is only known with a fractional systematic uncertainty of 1×10^{-16}

Table 1.1: Total Systematic Uncertainties for the Sr1 and Sr2 clocks. The quantities below are in fractional frequency units multiplied by 10^{-18}. The reported uncertainties are 1σ standard errors, determined by the square root of the quadrature sum of systematic and statistical standard errors. Reproduced from [2].

Source of Shift	Δ_{Sr1}	σ_{Sr1}	Δ_{Sr2}	σ_{Sr2}
BBR Static	-4832	45	-4962.9	1.8
BBR Dynamic	-332	6	-345.7	3.7
Density Shift	-84	12	-4.7	0.6
Lattice Stark	-279	11	-461.5	3.7
Probe Beam AC stark	8	4	0.8	1.3
First-order Zeeman	0	< 0.1	-0.2	1.1
Second-order Zeeman	-175	1	-144.5	1.2
Residual Lattice Vector	0	< 0.1	0	< 0.1
Line Pulling and Tunneling	0	< 0.1	0	< 0.1
DC Stark	-4	4	-3.5	2.1
Background Gas Collisions	0	0.07	0	0.6
AOM Phase Chirp	-7	20	0.6	0.4
Second-order Doppler	0	< 0.1	0	< 0.1
Servo Error	1	4	0.4	0.6
Totals	-5704	53	-5921.2	6.4

[24]. What we *can* measure is the total systematic uncertainty of our clock, which is the difference between the mean frequency of our clock and an ideal unperturbed ^{87}Sr atom.

Recently, another ^{87}Sr clock has been constructed at JILA and we are able to compare with this clock to determine the stability of our clocks and confirm the validity of our total systematic uncertainty evaluations. Henceforth, we will refer to our clock as Sr1 and the newly constructed clock as Sr2. While Sr1 has not implemented any major changes to reduce its systematic uncertainty since it was last evaluated to be 1.4×10^{-16} [25], Sr2 was constructed to perform at the lowest total systematic uncertainty of any clock. One major change implemented in Sr2 is a large volume optical lattice, which greatly reduces the density of atoms and its associated systematic shift[b] . Sr2 also uses an in-vacuum thermometer, which measures the temperature of the radiative environment at the atoms and allows for a factor of 10 reduction in the uncertainty of the systematic frequency shift caused by blackbody radiation. Finally, Sr2 uses a titanium-sapphire based lattice laser

---

[b] Of course, if Sr1 switched to a similar lattice, we would not be able to study the interactions that make up the bulk of this thesis.

which demonstrates a much more reliable frequency spectrum compared to a lattice based on a semiconductor amplifier. The amplifier has a broad spontaneous emission pedestal which can alter the associated stark shift of the laser at the 10^{-15} level from day to day. Even after filtering the amplified light with an interference filter and a Fabry-Pérot cavity, we observed a lattice stark shift that changed by 3×10^{-18} per day for our comparison operating conditions [2]. Table 1.1 shows the measured systematic effects for Sr1 and Sr2 along with the total systematic uncertainties of these systems. A detailed description of each one of these effects is the topic of another thesis [26], although it is worth noting that the improvements implemented in Sr2 allowed them to achieve the lowest total systematic uncertainty of any clock to date: 6.4×10^{-18} in fractional frequency units. Meanwhile, Sr1 was able to reduce their total systematic uncertainty to 5.3×10^{-17}, more than a factor of 2 below previous evaluations [25, 27]. Two factors contributed to the improvement. First, we improved our measurement of the blackbody environment surrounding our atoms by using more accurate (0.1 K uncertainty) temperature sensors and measuring the temperature of our chamber in more locations. These measurements were paired with a model of our system using the emissivities and solid angles of the components that have a direct line-of-sight view of the atoms. Second, our clock laser with 1×10^{-16} fractional frequency stability at 1 s allows us to evaluate systematic frequency shifts faster and more precisely compared to the laser with 1×10^{-15} stability at 1 s [28] that was used in previous evaluations. In fact, we will see that this laser also enables much of the work in the following chapters.

Figure 1.11 displays the frequency difference record and the Allan deviation of that record for the comparison between Sr1 and Sr2. We see that the measured frequency difference is less than 3×10^{-17} which is consistent with the stated systematic uncertainty of Sr1. The comparison also demonstrates the stability of our clocks through the plotted Allan deviation in Fig. 1.11(a). The Allan deviation [29] is defined as

$$\sigma_y(\tau) = \sqrt{\frac{1}{2}\left\langle(\overline{y}_{n+1} - \overline{y}_n)^2\right\rangle}, \tag{1.11}$$

where $\overline{y}_n$ is the n^{th} fractional frequency average over time τ and the angled brackets signify a time average. The Allan deviation measures the stability of a clock over different time periods τ. At short times, the Allan deviation represents the stability of our clock laser, since the atom feedback servo take about ~ 20 s to acquire a lock. After this time, the Allan deviation decreases proportional to $1/\sqrt{\tau}$, consistent with random noise from uncorrelated measurements. This long term trend represents the stability of our clock and fits to $3.4 \times 10^{-16}/\sqrt{\tau}$. The best reported stability for our system is $3.1 \times 10^{-16}/\sqrt{\tau}$ [1]. Similar stability was also reported in a Yb optical lattice clock and they were able to average for a longer time to reach an ultimate stability of 1.6×10^{-18} after 7 hours of averaging time [30]. These results represent nearly a factor of 10 improvement over the previous best reported stability from a comparison between Al^{+} ion clocks [31].

1.10 Conclusion

As we see from the proceeding discussion, the stability of our clock laser has led to an incredible improvement in clock stability, which, in turn, has enabled the evaluation of systematic effects in a ^{87}Sr clock with a total uncertainty of 6.4×10^{-18} [2]. The stability of this laser is also essential to the research reported in the remainder of this thesis. Chapter 2 describes a method of analyzing a laser's frequency noise spectrum using the clock transition in ^{87}Sr as an ultrastable reference. This work was born out of necessity because our laser was so much more stable than our previous clock laser that traditional methods of analyzing laser noise spectra with an optical heterodyne beat between two or more lasers [32, 33, 28, 34, 35, 36] were not possible. The ability to use this method with our clock laser shows that even state-of-the-art lasers can be characterized directly with atoms. Chapter 3 describes how measurements using our clock laser were able to identify the nature of interactions in ^{87}Sr as well as the importance of many-body atomic correlation effects. Similarly, Chapter 4 leverages our clock laser to provide the first direct evidence for SU(N) symmetry[c] in the interactions between all 10 nuclear-spin sublevels of the clock transition. The clock laser not only allows us to rapidly measure density-dependent frequency shifts

---

[c] Here, N is equal to the number of populated nuclear-spin sublevels, having a maximum value of $2I+1$ where I is the nuclear spin of the atom. For ^{87}Sr , $I = 9/2$.

with high precision, but it also allows us to observe the dynamics of these nuclear-spin polarized and nuclear-spin-mixed systems over longer time periods. We will see that this is essential for demonstrating the failure of a mean-field description of our system in Chapter 3 and verifying our ability to model the evolution of orbital coherence in Chapter 4. The final chapter (Chapter 5) describes our measurements of broadening in ^{88}Sr resulting from retarded dipolar coupling in an optically thick sample of atoms as well as future work in ^{87}Sr that will place atoms within a high finesse cavity to achieve strong atom-cavity coupling on the $^1S_0$ to $^3P_1$ transition. While the other chapters demonstrate the utility of our clock laser, this chapter shows that it will soon be inadequate. We show that we can achieve significant gains in the spectroscopic sensitivity of our atoms by creating spin-squeezed states via quantum non-demolition measurements, highlighting the need for lasers with even greater stability.

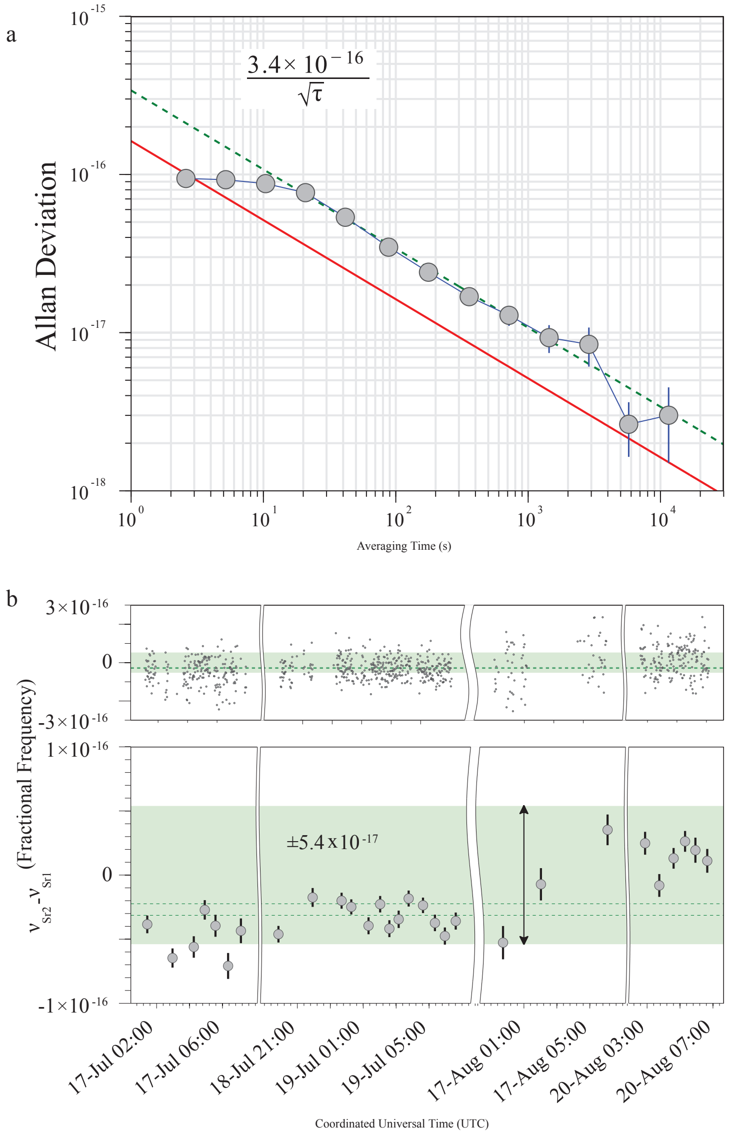

Figure 1.11: Sr2 - Sr1 Frequency Comparison. **a)** Allan deviation of the Sr1 and Sr2 comparison divided by $\sqrt{2}$ to reflect the performance of a single clock. The red solid line is the calculated quantum projection noise for this comparison. The green dashed line is a fit to the data, showing the worst case scenario for the averaging of a single clock of 3.4×10^{-16} at one second. **b)** The absolute agreement between Sr1 and Sr2 recorded at the indicated Coordinated Universal Time. The light-green region denotes the 1σ combined systematic uncertainty for the two clocks under the running conditions at that time. The top panel shows the frequency record binned at 60 s; in the bottom panel each solid circle represents 30 min of averaged data. The green dashed lines represent the 1σ standard error inflated by the square root of the reduced chi-squared, $\sqrt{\chi^2_\nu}$, for the weighted mean of these binned comparison data. The final comparison over 52,000 s of data showed agreement at $-2.7(5) \times 10^{-17}$ ($\sqrt{\chi^2_\nu}$ =10.5) for the 30-min averaging time and $-2.8(2) \times 10^{-17}$ ($\sqrt{\chi^2_\nu}$ =3.5) for the 60-s averaging time. Reproduced from [2].

Chapter 2

Laser spectral analysis using an optical lattice clock

2.1 Introduction

The development of ultrastable frequency sources has paved the way for advances in fundamental tests of physics, primary frequency standards, precision spectroscopy, and quantum many-body systems. However, the utility of a precision frequency source is limited by its instability. In our experiments, laser stability determines how precisely we can manipulate and measure the clock transition in ^{87}Sr. Because of the intimate connection between oscillator stability and measurement precision, many methods to rigorously characterize these instabilities have been developed [37]. Ultrastable lasers pose a unique challenge to characterizing frequency instabilities because, until now, measurements of their performance required an optical herterodyne beat between two or more lasers with similar stability [32, 33, 28, 34, 35, 36]. Single laser performance can be inferred from a three-cornered hat measurement [38, 39], but valuable information about a laser's frequency noise power spectral density (PSD) [40] is limited in an optical beat by the less stable laser.

Optical lattice-trapped ^{87}Sr atoms are uniquely suited for laser noise spectral analysis due to the ultranarrow linewidth and field insensitivity of the $^1S_0$ ($|g\rangle$) to $^3P_0$ ($|e\rangle$) clock transition as well as the low quantum projection noise (QPN) achievable with ensembles of many atoms. To accomplish this, we adopt a technique similar to radio-frequency-based dynamical decoupling [41] to manipulate the frequency noise sensitivity of this transition. Previous implementations of dynamical decoupling manipulated radio-frequency transitions in quantum systems to eliminate [42, 43] or analyze [44] environmental noise. Here, the ^{87}Sr clock transition is so insensitive to perturbations that we are able to measure the noise spectrum of the ultrastable laser used to excited it. To guide and interpret our experimental measurements, we develop a simple and robust theoretical framework that combines concepts from [37] with a model for atomic sensitivity to frequency fluctuations [20, 21, 22][a] . We compare experimentally measured fluctuations in atomic population to our theory and accurately determine the PSD of our laser. As laser stability advances, we can continue to leverage the QPN-limited noise floor of this technique to analyze lasers with greater stability.

2.2 Theoretical model

2.2.1 Derivation of the detuning-dressed basis Hamiltonian

To model the frequency of our laser, we start with the Schrödinger equation for a two-level atom driven by a laser field with a frequency that can vary in time. This is most simply treated using the instantaneous phase of the laser, $\phi_L(t) = \int_0^t \omega_L(t)dt$, where $\omega_L(t)$ is the instantaneous frequency of the laser. For a general state $|\psi\rangle = c_g(t)\,|g\rangle + c_e(t)\,|e\rangle$, we get the coupled differential equations:

$$\begin{aligned} i\dot{c}_e(t) &= \tfrac{\omega_a}{2} c_e(t) - \tfrac{\Omega(t)}{2}\left(e^{i\phi_L(t)} + e^{-i\phi_L(t)}\right) c_g(t), \\ i\dot{c}_g(t) &= -\tfrac{\omega_a}{2} c_g(t) - \tfrac{\Omega(t)}{2}\left(e^{i\phi_L(t)} + e^{-i\phi_L(t)}\right) c_e(t). \end{aligned} \tag{2.1}$$

Here, $\Omega(t)$ is the Rabi frequency and ω_a is the frequency of the $|g\rangle$ to $|e\rangle$ transition.

To simplify the solutions to these equations, we substitute the complex state coefficients with

$$\tilde{c}_e(t) \equiv e^{i\omega_a t/2} c_e(t) \quad \text{and} \quad \tilde{c}_g(t) \equiv e^{-i\omega_a t/2} c_g(t). \tag{2.2}$$

---

[a] We note that our treatment is consistent with that in [45].

Using this substitution, (2.1) becomes

$$\begin{aligned}
&\tfrac{\omega_a}{2} e^{-i\omega_a t/2}\tilde{c}_e(t) + i e^{-i\omega_a t/2}\dot{\tilde{c}}_e(t) \\
&= \tfrac{\omega_a}{2} e^{-i\omega_a t/2}\tilde{c}_e(t) - \tfrac{\Omega(t)}{2}\left(e^{i\phi(t)} + e^{-i\phi(t)}\right) e^{i\omega_a t/2}\tilde{c}_g(t), \\
& \\
&-\tfrac{\omega_a}{2} e^{i\omega_a t/2}\tilde{c}_g(t) + i e^{i\omega_a t/2}\dot{\tilde{c}}_g(t) \\
&= -\tfrac{\omega_a}{2} e^{i\omega_a t/2}\tilde{c}_g(t) - \tfrac{\Omega(t)}{2}\left(e^{i\phi(t)} + e^{-i\phi(t)}\right) e^{-i\omega_a t/2}\tilde{c}_e(t).
\end{aligned} \tag{2.3}$$

We can cancel an overall phase factor of $e^{-(+)i\omega_a t/2}$ from the top(bottom) equation in (2.3) and simplify to get

$$\begin{aligned}
i\dot{\tilde{c}}_e(t) &= -\tfrac{\Omega(t)}{2}\left(e^{i(\phi_L(t)+\omega_a t)} + e^{-i(\phi_L(t)-\omega_a t)}\right)\tilde{c}_g(t), \\
& \\
i\dot{\tilde{c}}_g(t) &= -\tfrac{\Omega(t)}{2}\left(e^{i(\phi_L(t)-\omega_a t)} + e^{-(i\phi_L(t)+\omega_a t)}\right)\tilde{c}_e(t).
\end{aligned} \tag{2.4}$$

In order to proceed, we assume that the instantaneous laser frequency is the sum of a constant frequency and a small noise term that varies in time, $\omega_L(t) = \omega_{L_0} + \delta\omega(t)$. Then we can write the instantaneous phase of the laser as $\phi_L(t) = \omega_{L_0} t + \int_0^t \delta\omega(t')dt' \equiv \omega_{L_0} t + \delta\phi(t)$. Substituting this into (2.4), we get:

$$\begin{aligned}
i\dot{\tilde{c}}_e(t) &= -\tfrac{\Omega(t)}{2}\times \\
&\quad \left(e^{i(\omega_{L_0} t+\delta\phi(t)+\omega_a t)} + e^{-i(\omega_{L_0} t+\delta\phi(t)-\omega_a t)}\right)\tilde{c}_g(t), \\
& \\
i\dot{\tilde{c}}_g(t) &= -\tfrac{\Omega(t)}{2}\times \\
&\quad \left(e^{i(\omega_{L_0} t+\delta\phi(t)-\omega_a t)} + e^{-i(\omega_{L_0} t+\delta\phi(t)+\omega_a t)}\right)\tilde{c}_e(t).
\end{aligned} \tag{2.5}$$

Since, $\delta\phi(t)$ is assumed to be small, we can make the usual rotating wave approximation where we neglect terms that rotate at the sum of ω_{L_0} and ω_a. The resulting equations are

$$\begin{aligned}
i\dot{\tilde{c}}_e(t) &= -\tfrac{\Omega(t)}{2} e^{-i(\overline{\Delta} t+\delta\phi(t))}\tilde{c}_g(t), \\
& \\
i\dot{\tilde{c}}_g(t) &= -\tfrac{\Omega(t)}{2} e^{i(\overline{\Delta} t+\delta\phi(t))}\tilde{c}_e(t).
\end{aligned} \tag{2.6}$$

where, $\overline{\Delta} \equiv \omega_{L_0} - \omega_a$.

Another basis change is necessary before arriving at the final result, so we express (2.6) in terms of new state coefficients defined as

$$b_e(t) \equiv e^{-i\overline{\Delta}t/2}\tilde{c}_e(t) \quad \text{and} \quad b_g(t) \equiv e^{i\overline{\Delta}t/2}\tilde{c}_g(t). \tag{2.7}$$

After canceling overall phase factors we get the following differential equations.

$$\begin{aligned} i\dot{b}_e(t) &= -\tfrac{\Omega(t)}{2}e^{-i\delta\phi(t)}b_g(t) + \tfrac{\overline{\Delta}}{2}b_e(t), \\ i\dot{b}_g(t) &= -\tfrac{\Omega(t)}{2}e^{i\delta\phi(t)}b_e(t) - \tfrac{\overline{\Delta}}{2}b_g(t). \end{aligned} \tag{2.8}$$

The Hamiltonian in this basis is

$$\frac{\hat{H}}{\hbar} = -\frac{\Omega(t)}{2}\begin{pmatrix} 0 & e^{i\delta\phi(t)} \\ e^{-i\delta\phi(t)} & 0 \end{pmatrix} - \frac{\overline{\Delta}}{2}\hat{\sigma}_z, \tag{2.9}$$

where $\hat{\sigma}_z$ is a pauli spin matrix. The chosen spectroscopy sequence determines the time dependence of $\Omega(t)$. In the absence of other perturbations, the atom-light interaction can be engineered to filter laser noise. For example, random fluctuations that occur on time scales that are fast compared to the atomic state evolution will average to zero.

2.2.2 Calculation of the sensitivity function

To measure the effect of laser frequency fluctuation on the atoms, we observe fluctuations in the population imbalance between $|g\rangle$ and $|e\rangle$. For a general state $|\psi\rangle = a\,|g\rangle + b\,|e\rangle$, the population imbalance is defined as $\mathbb{P} \equiv bb^* - aa^*$. We can express $\mathbb{P}$ in terms of the time-dependent laser detuning as

$$\mathbb{P}(\tau) = \mathbb{P}_0 + \int_0^\tau dt\, r(t)\, \Delta(t), \tag{2.10}$$

where $\mathbb{P}_0$ is the initial imbalance, τ is the total spectroscopy time, $\Delta(t) \equiv \overline{\Delta} + \delta\omega(t)$, and $r(t)$ is the impulse response [37], commonly referred to as the sensitivity function [21, 22]. The sensitivity function, and its Fourier transform $R(f)$, are determined by the chosen spectroscopy sequence. As we apply different spectroscopy sequences, fluctuations in $\mathbb{P}$ correspondingly reveal laser instabilities at different Fourier frequencies, as illustrated by the shifting spectral response of $|R(f)|^2$ in Fig. 2.1(c) and 1(e).

Equation (2.10) rigorously connects $\mathbb{P}$ to $\Delta(t)$ and, to quantify fluctuations in $\mathbb{P}$, we consider its variance, $I^2 \equiv \langle \mathbb{P}^2 \rangle - \langle \mathbb{P} \rangle^2$. To calculate the variance of $\mathbb{P}$, we first need to calculate the sensitivity function, r(t), for a given spectroscopy sequence. This quantity describes the atomic response to frequency deviations of the form $\delta\omega(t, t_0) = \Delta\phi\, \delta(t - t_0)$, where $\delta(t)$ is the Dirac delta function and $\Delta\phi$ is infinitesimally small. Using the definition of $\delta\phi(t)$ from above, we see that frequency fluctuations of this form are equivalent to instantaneous steps in $\delta\phi(t)$ at time t_0. Adding finite steps in $\delta\phi(t)$ can also account for deliberate phase shifts of the laser which we implement during spectroscopy.

Inserting the above form of $\delta\omega(t, t_0)$ into Eqn. 2.10 and differentiating with respect to $\Delta\phi$, we get

$$\left.\frac{\partial \mathbb{P}}{\partial \Delta\phi}\right|_{\Delta\phi=0} = \int_0^{\tau} dt\, r(t)\, \delta(t - t_0) = r(t_0). \tag{2.11}$$

We calculate $\mathbb{P}$ using Eqn. 2.9 for a particular spectroscopy sequence, $\Omega(t)$, and with an added phase step of $\Delta\phi$ occurring at time t_0. Finally, $r(t)$ is calculated by allowing t_0 to vary throughout the spectroscopy sequence.

2.2.3 Calculating the variance of $\mathbb{P}$

To derive the variance of $\mathbb{P}$, we assume that all measurements are made near $\mathbb{P} = 0$ so it will be sufficient to calculate the quantity

$$\left\langle \mathbb{P}^2 \right\rangle = \left\langle \int_{-\infty}^{\infty} \int_{-\infty}^{\infty} dt_1\, dt_2\, \Delta(t_1)\, r(t_1)\, \Delta(t_2)\, r(t_2) \right\rangle. \tag{2.12}$$

This expression can be simplified using the definition of the convolution operation along with the definition of the autocorrelation function,

$$\mathcal{R}_f(t_1 - t_2) = \langle f(t_1) f^*(t_2) \rangle\,, \tag{2.13}$$

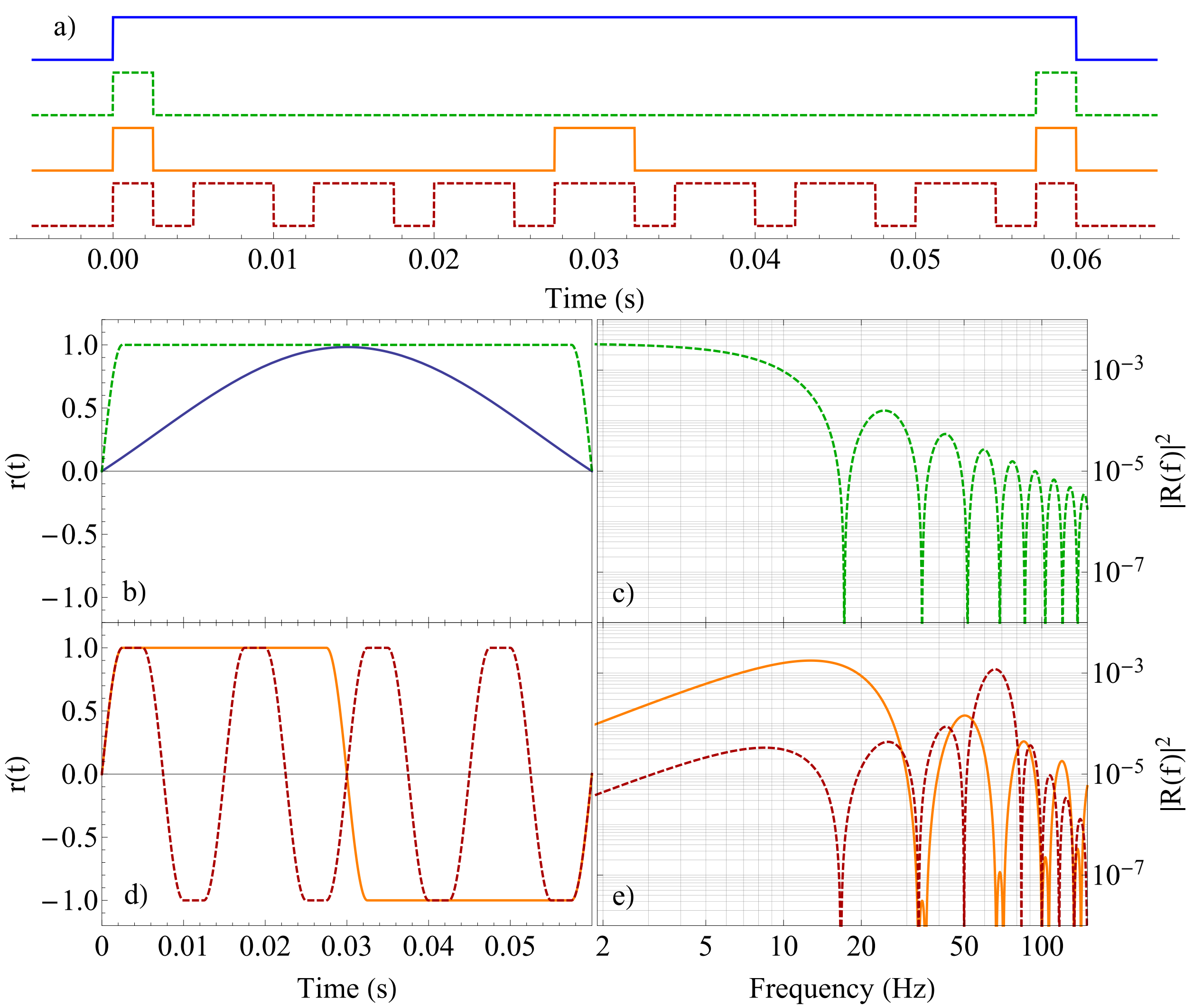

Figure 2.1: An example total spectroscopy time of 60 ms is shown. The schematic diagrams shown in (a) signify when $\Omega(t)$ is nonzero by their “high” value. For Rabi spectroscopy, the nonzero Ω is selected so the total pulse area is π (π pulse). For the other spectroscopy sequences, the nonzero value of Ω is $\pi/(0.005)$ rad/s. The diagrams are offset in height for clarity and are ordered top to bottom: Rabi, Ramsey, one-echo, and seven-echo.. Plots of $|R(f)|^2$ in (c) and (e) are calculated from the corresponding $r(t)$ curves plotted in (b) and (d). In (a), (b) and (c) solid blue (dashed green) lines correspond to Rabi (Ramsey) spectroscopy sequences. In (a), (d) and (e) solid orange (dashed red) lines correspond to one-echo (seven-echo) spectroscopy sequences. Reproduced from [3].

where R_f is the autocorrelation function of f. Then, equation (2.12) simplifies to,

$$\left\langle \mathbb{P}^2 \right\rangle = \int_{-\infty}^{\infty} dt\, (\mathcal{R}_\Delta \star r)(t)\, r(t), \tag{2.14}$$

where "$\star$" represents convolution. Since an oscillator's noise properties are typically characterized in frequency space via a power spectral density, we employ Parseval's theorem, which relates the integral of two complex valued functions of time $x(t)$ and $y(t)$ to the integral of their Fourier transforms $X(f)$ and $Y(f)$ as follows

$$\int_{-\infty}^{\infty} dt\, x(t)\, y^*(t) = \int_{-\infty}^{\infty} df\, X(f)\, Y^*(f). \tag{2.15}$$

Here, f^* denotes the complex conjugate of f. Since r(t) is real valued, we get that

$$\int_{-\infty}^{\infty} dt\, (\mathcal{R}_\Delta \star r)(t)\, r(t) = \int_{-\infty}^{\infty} df\, \mathcal{F}\left[(\mathcal{R}_\Delta \star r) \right](f)\, R^*(f), \tag{2.16}$$

where $\mathcal{F}$ is the fourier transform operation and $R(f)$ is the Fourier transform of $r(t)$. The convolution theorem states that the Fourier transform of a convolution of two functions is equal to the product of the Fourier transforms of the two functions. Additionally, the Wiener-Khinchin theorem states that the power spectral density (PSD) of a function, f, is equal to the Fourier transform of the autocorrelation function of f. Thus, we get that

$$\left\langle \mathbb{P}^2 \right\rangle = \int_{-\infty}^{\infty} df\, S_\Delta(f)\, \left| R(f) \right|^2, \tag{2.17}$$

where $S_\Delta(f)$ is the double sided PSD of the laser in units of (rad/s)^2/Hz. We can express the variance in terms of the more commonly used single sided PSD with units of Hz^2/Hz, $S_\nu(f)$, to obtain the final result

$$I^2 = \left\langle \mathbb{P}^2 \right\rangle = (2\pi)^2 \int_{0}^{\infty} df\, S_\nu(f)\, \left| R(f) \right|^2. \tag{2.18}$$

Here, we have used the relationship, $S_\Delta(f) = (2\pi)^2 S_\nu(f)/2$ for $f \geq 0$. Figure 2.1 shows a schematic diagram for the spectroscopy sequences we use along with their corresponding sensitivity functions, $r(t)$ and $|R(f)|^2$.

2.2.4 Calculating the two sample Allan variance of $\mathbb{P}$

For Rabi and Ramsey spectroscopy, the calculated value for I diverges since thermal noise, a fundamental limit to $S_\nu(f)$ at low frequency, has an f^{-1} character. For these measurements, we use the Allan variance [29] to characterize fluctuations in $\mathbb{P}$. In particular, we consider the two-sample Allan variance, defined as

$$I_{(2)}^2 \equiv \frac{1}{2}\left\langle (\mathbb{P}_{i+1} - \mathbb{P}_i)^2 \right\rangle , \tag{2.19}$$

where the index i signifies the i^{th} measurement of $\mathbb{P}$. In the treatment of multiple measurements we consider the sensitivity function as periodic with a period equal to the experimental cycle time T_c. For this work, T_c is approximately $1 + \tau$ s. Then the expression for the two-sample Allan variance is completely analogous to (2.12) under the substitution,

$$r(t) \rightarrow r_{(2)}(t) \equiv r(t) - r(t - T_c). \tag{2.20}$$

Since the Fourier transform operation is linear and a shift in time of T_c simply adds a phase factor of $e^{-2\pi\, i\, T_c\, f}$ to the Fourier transform of $r(t)$, we get that

$$\begin{aligned} \mathcal{F}\left[r_{(2)}(t)\right] &= \mathcal{F}\left[r(t)\right] - \mathcal{F}\left[r(t - T_c)\right] \\ &= 2ie^{-\pi\, i\, T_c\, f}\ \sin\left(\pi\, T_c\, f\right) R(f). \end{aligned} \tag{2.21}$$

This shows that $I_{(2)}^2$ can be expressed in terms of $R(f)$ as

$$I_{(2)}^2 = (2\pi)^2 \int_0^\infty df\, S_\nu(f)\, 2\sin^2(\pi f T_c)\, |R(f)|^2 . \tag{2.22}$$

Although the calculated value of $I_{(2)}$ remains finite for all experimental conditions, it does not properly account for coherent vibrational or electronic noise that exists on our laser at frequencies above 20 Hz. This noise is aliased onto our measurements and leads to regular, slow oscillations of the measured $\mathbb{P}$. To capture the effect of coherent noise, we use I to characterize echo pulse sequences. Rabi and Ramsey sequences do not suffer from this aliasing because they do not have significant sensitivity to noise above 20 Hz for the spectroscopy times we use.

2.3 Experimental Design

Our experimental setup follows that of our Sr clock [46, 47]. Between 2000 and 3000 ^{87}Sr atoms are cooled to about 2 μK in a one-dimensional optical lattice and nuclear spin polarized into the ground $^1S_0$ $m_F = 9/2$ state. The optical lattice is kept near the magic wavelength [48] for the $|g\rangle$ to $|e\rangle$ clock transition. Lattice-trapped atoms are excited with 698 nm light according to the spectroscopy sequences shown in Fig. 2.1(a). The clock light propagates along the strongly confined axis of the lattice so that it probes the atoms in the well-resolved sideband regime [49, 16], free from Doppler and recoil effects. Finally, the numbers of atoms in $|g\rangle$ and $|e\rangle$ are measured to determine $\mathbb{P}$.

Using this setup, we have resolved 0.5 Hz spectral features [27, 4] and demonstrated the most stable [1] and most accurate [2] optical clock . These results are enabled by the ultrastable laser that addresses the clock transition (hereafter termed "α laser"). The stability of the α laser is at its thermal noise limit of 1×10^{-16} fractional frequency units for ∼1 to 1000 s. We can look for noise features at higher frequencies using an optical beat with a second laser (hereafter termed "β laser"). The β laser has demonstrated thermal noise-limited stability at the 10^{-15} fractional frequency level [28]. The PSD of the optical beat (Fig. 2.2(a)) is limited by thermal noise in the β laser out to Fourier frequencies of 10 Hz, beyond which it becomes limited by the noise floor of the detector; however, discrete features exist above this floor. Pairs of narrow noise peaks are visible near 22 and 30 Hz. Additionally, noise peaks are consistently measured at 24 and 60 Hz. The 60 Hz peak is dominated by detector noise and the 24 Hz peak is visible in previous beat measurements between two β lasers [28].

Spectroscopy sequences are designed such that the measured $\mathbb{P}$ is sensitive to laser noise. For Rabi spectroscopy, we detune the α laser from resonance by the half width at half maximum (HWHM) of the Rabi line shape and apply a π pulse. For Ramsey spectroscopy, we tune the laser exactly on resonance and apply two $\pi/2$ pulses separated in time. We shift the phase of the final $\pi/2$ pulse by $\pi/2$ radians relative to the initial $\pi/2$ pulse, which is equivalent to detuning by the

HWHM of the central Ramsey fringe in the absence of phase shifts. The echo pulse sequences add to the Ramsey sequence a number of π pulses such that the free evolution times between pulses are equal. We switch the phase of the laser by π rad between adjacent echo pulses so that pulse area errors cancel. The echo pulse sequences act as a bandpass filter peaked at $(n+1)/(2\tau)$ Hz, where n is the number of echo pulses. One can intuitively understand this behavior from the sensitivity functions in Fig. 2.1(d), which are periodic at this frequency. Figure 2.1(e) explicitly demonstrates this frequency sensitivity.

2.4 Measurement Results

2.4.1 The unaltered laser

We use 80 consecutive measurements of $\mathbb{P}$ to estimate the raw standard(pair) deviation and its statistical uncertainty, then divide this raw deviation by the measured contrast to get $I(I_{(2)})$. The contrast is determined by a fit to the measured excitation versus detuning for Rabi spectroscopy or a fit to measured oscillations in excitation as the phase of the final pulse is scanned for other sequences. Figure 2.2(b) shows measured values of I or $I_{(2)}$ for different spectroscopy sequences as a function of total spectroscopy time. Each data point represents a weighted mean of at least four measurements and error bars are estimated from the variance of the weighted mean. Spectroscopy times are investigated in a random order to avoid systematic drifts. Each data point consists of measurements separated by several hours to ensure consistency of the data.

The spectroscopy sequences we use are chosen to measure different Fourier components of $S_\nu(f)$ and demonstrate the utility of dynamical decoupling. The peak frequency sensitivity of the one-echo pulse data ranges between 5 and 50 Hz; however, individual noise components cannot be identified. By increasing the number of echo pulses to seven, we clearly resolve three peaks in the measured values of I, centered at 0.070, 0.135, and 0.180 s of total spectroscopy time. The peak centered at 0.135 s originates from alternating current motors in our lab operating near 30 Hz. The peak at 0.180 s corresponds to an acoustic resonance of the lab at 22 Hz. The width of the peak

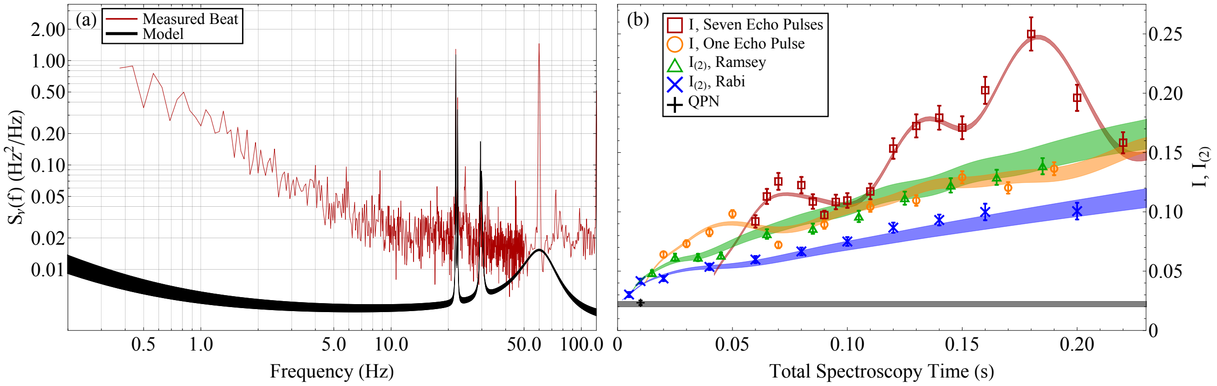

Figure 2.2: (a) $S_\nu(f)$ measured from a beat between the α and β lasers is plotted in red. An estimate of $S_\nu(f)$ for the α laser is plotted as a black band. This estimate is based on our measurements of I and $I_{(2)}$. (b) Measured values of I or $I_{(2)}$ are plotted as a function of total spectroscopy time for the spectroscopy sequences shown in Fig. 2.1. Colored bands represent calculated values of I or $I_{(2)}$ using the estimated $S_\nu(f)$ in (a) with QPN added in quadrature. A gray band indicates the mean calculated QPN for all experimental data. The black cross represents a measurement of the QPN (see the text). Reproduced from [3].

at 0.070 s corresponds to a frequency width that is broader than the resolution of the seven-echo pulse sequence (roughly τ^{-1}). It contains multiple unresolved noise components corresponding to electrical noise at 60 Hz and acoustic noise near 40 and 80 Hz, which was previously observable in the optical heterodyne beat prior to the installation of an acoustic isolation box around the α laser [8]. Lasers are also subject to white noise (no dependence on Fourier frequency) and noise proportional to $1/f$ originating from electronic and thermal noise, respectively. At the magnitudes we extract from the experimental data, these noise components have a negligible effect on the calculated values of I for seven-echo pulse sequences. In contrast, calculated values of $I_{(2)}$ for Rabi and Ramsey pulse sequences depend primarily on the magnitudes of white and $1/f$ noise since their $|R(f)|^2$ decreases with increasing f. The agreement between these two sequences is used to bound the uncertainty in the magnitudes of white and $1/f$ noise.

To determine $S_\nu(f)$ for the α laser we fit measured values of I and $I_{(2)}$ to theoretical calculations using a single model $S_\nu(f)$ in Eqs. (2.18) and (2.22). The functional form of the model is

$$S_\nu(f) = h_{\text{white}} + \frac{h_{\text{thermal}}}{f} + \sum_{i=1}^{N} \frac{h_i}{1 + \left(\frac{f-f_i}{\Gamma_i/2}\right)^2}, \tag{2.23}$$

where h_i, f_i, and Γ_i are the magnitude, frequency, and full width at half maximum (FWHM) for the i^{th} noise resonance. All h_i are fit to the seven-echo pulse data and the Rabi and Ramsey data are used to simultaneously fit h_{white} and h_{thermal}. We determine $h_{\text{thermal}} = 1.5(4)\times10^{-3}$ Hz^2, consistent with predicted thermal noise [27], and $h_{\text{white}} = 3.3(3) \times 10^{-3}$ Hz^2/Hz. Widths and frequencies of discrete noise peaks are chosen to be consistent with the optical beat. The parameters for these resonances are given in Table 2.1. We note that widths and frequencies could be identified without the aid of the optical beat, as demonstrated by the distinct peaks in Fig. 2.2(b), but the resolution would be limited to $\sim 1/\tau$.

For each data point, the QPN is calculated for the measured number of atoms and the mean excitation fraction. The mean QPN for each sequence is added in quadrature with the calculated I and $I_{(2)}$ to more accurately represent experimental data. These quantities are plotted as colored bands in Fig. 2.2(b) where the extent of the band corresponds to the uncertainty of the model $S_\nu(f)$. The mean and standard deviations of all calculated QPN values are represented in Fig. 2.2(b) as a gray band. QPN is experimentally measured by the standard deviation of $\mathbb{P}$ following a 5 ms, resonant, $\pi/2$ pulse. The measured and calculated QPN are consistent.

Table 2.1: $S_\nu(f)$ Resonant Features

Index	f_i (Hz)	h_i (Hz^2/Hz)	Γ_i (Hz)
1	21.87	1.2[b]	0.03
2	22.39	0.6[b]	0.03
3	29.45	0.15	0.1
4	29.90	0.08	0.4
5	60	0.012	27
Added Noise			
6	46.6	0.07	2
7	93.2	0.25	2

---

[b] We note that an overall 17% reduction in the strength of these features was necessary for the data plotted in figure 3(d), corresponding to daily variation in the acoustic environment. A further 60% reduction was necessary for the condition with feedback active

2.4.2 Calculating the minimum observable laser linewidth

Although an exact relationship between $S_\nu(f)$ and a FWHM linewidth exists [50], an analytic expression for this relationship does not exist with $1/f$ frequency noise. Here, the observed linewidth depends on the measurement time [51]. By accounting for a finite measurement time, we numerically calculate the minimum observable α laser linewidth to be 26(4) mHz. To determine the linewidth of the α laser, we express the autocorrelation function for the laser's electric field, $R_E(\tau)$, in terms of the frequency noise PSD, $S_\nu(f)$, and take the Fourier transform of $R_E(\tau)$ to get the laser line shape function [50, 51]. We consider an electric field of the form

$$E(t) = E_0 e^{i(2\pi\nu_{L_0}t+\delta\phi(t))}, \tag{2.24}$$

where $\nu_{L_0} \equiv \omega_{L_0}/2\pi$. Then, $R_E(\tau)$ can be expressed in terms of $S_\nu(f)$ as follows: [51]

$$R_E(\tau) = E_0^2 e^{i2\pi\nu_{L_0}\tau} e^{-2\int_0^\infty S_\nu(f)\frac{\sin^2(\pi f\tau)}{f^2}df}. \tag{2.25}$$

Since the model $S_\nu(f)$ that we deduce from our measurements contains a component proportional to $1/f$, the integral in the exponent diverges and we must take into account the measurement time over which the laser is observed. A measurement lasting T_0 s is insensitive to frequency noise below $1/T_0$ Hz. This dictates that the lower bound of the integral in Eqn. (2.25) should be set to $1/T_0$, thereby making the integral finite. The finite observation time also scales $R_E(\tau)$ by a triangle bump function since the measurement is windowed by a flat rectangle function between $t = 0$ and $t = T_0$. Therefore, the line shape observed over a finite time T_0 will depart from a simple Fourier transform of $R_E(\tau)$ and take the form

$$S_E(\nu) = 2\int_{-T_0}^{T_0}\left(1-\frac{|\tau|}{T_0}\right)e^{-i2\pi\nu\tau}R_E(\tau)d\tau, \tag{2.26}$$

which can be simplified to

$$\begin{aligned} S_E(\delta\nu) = {} & 4E_0^2\int_0^{T_0}\left(1-\frac{|\tau|}{T_0}\right)\cos(2\pi\,\delta\nu\,\tau) \\ & \times\ e^{-2\int_{1/T_0}^\infty S_\nu(f)\frac{\sin^2(\pi f\tau)}{f^2}df}d\tau, \end{aligned} \tag{2.27}$$

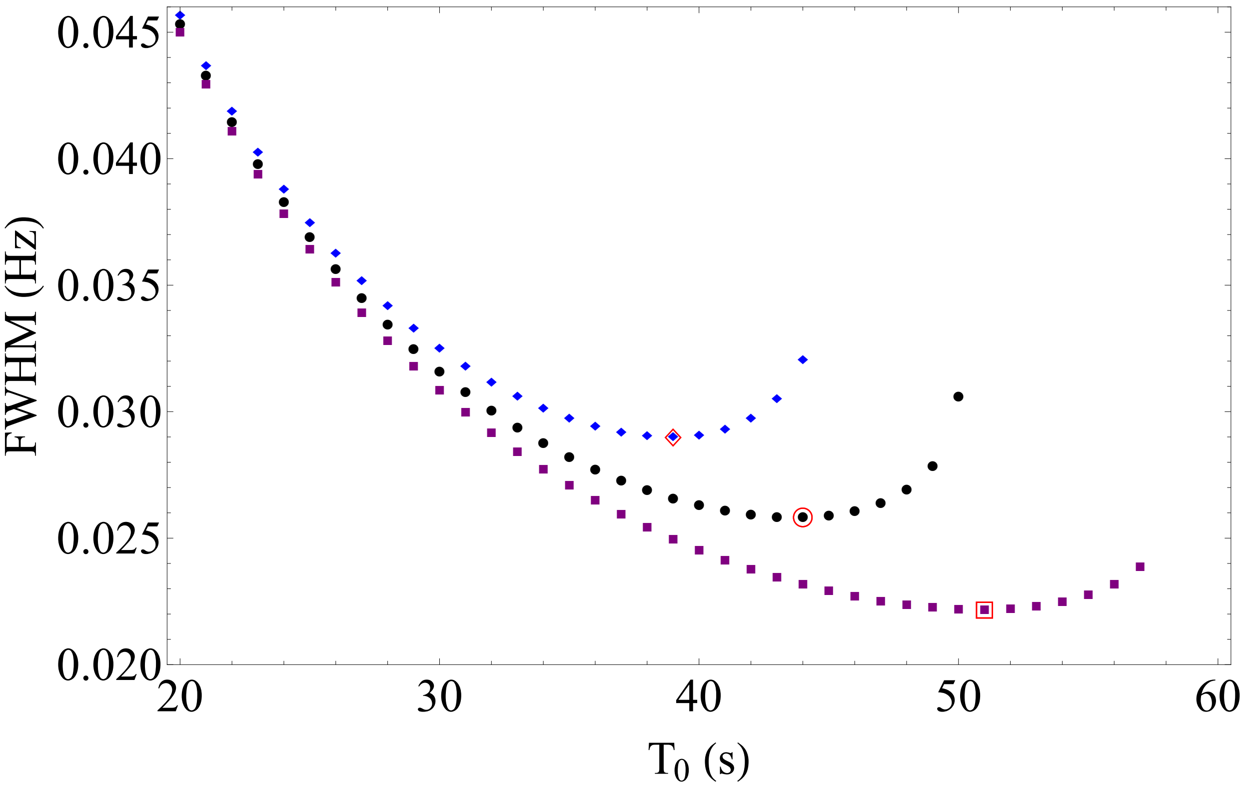

Figure 2.3: The numerically calculated FWHM of the α laser as a function of observation time. Black circles represent calculations using the model $S_\nu(f)$ that is quoted in the main text, excluding narrow resonance features that do not contribute to the FWHM. Blue diamonds(purple squares) represent calculations using the upper(lower) limit quoted for $S_\nu(f)$. The minimum value for each condition is outlined in red. These values determine the minimum observable linewidth for the α laser: 26(4) mHz. Reproduced from [3].

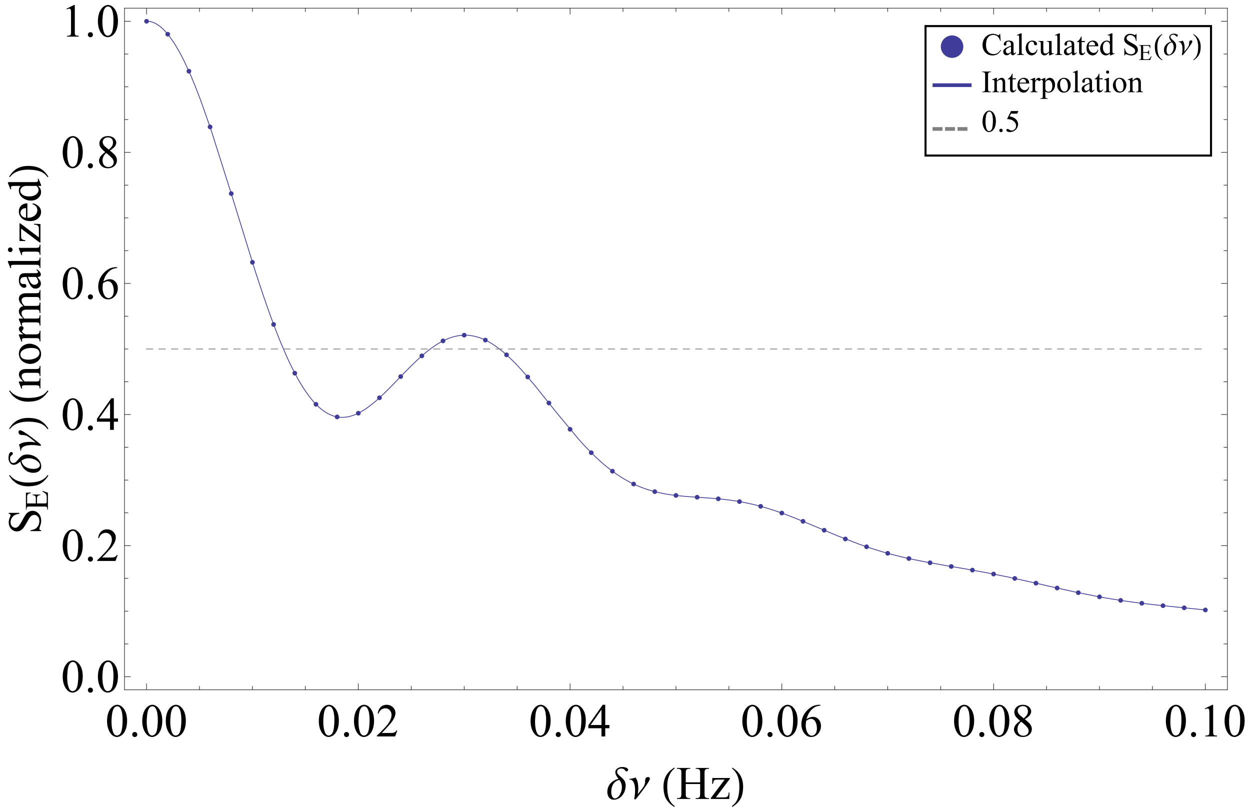

Figure 2.4: The calculated line shape, $S_E(\delta\nu)$, using $h_{\text{white}} = 0.0033$ Hz^2/Hz, $h_{\text{thermal}} = 0.0015$ Hz^2, and $T_0 = 44$ s. This measurement time corresponds to the minimum FWHM of $S_E(\nu)$ for these values of $S_\nu(f)$. A dashed gray line signifies the half maximum to guide the eye. Reproduced from [3].

where $\delta\nu \equiv \nu - \nu_{L_0}$.

To calculate the minimum observable FWHM, we compute the FWHM of $S_E(\delta\nu)$ as a function of T_0 for the model $S_\nu(f)$ (Fig. 2.2(a)) and its upper and lower bounds. The three conditions lead to three minimum linewidths, observable at three different measurement times (Fig. 2.3) and determine the minimum observable linewidth of the α laser to be 26(4) mHz. The calculated line shape, $S_E(\delta\nu)$, using $\mathrm{h_{white}} = 0.0033\ \mathrm{Hz^2/Hz}$ and $\mathrm{h_{thermal}} = 0.0015\ \mathrm{Hz^2}$ is plotted in Fig. 2.4 for the measurement time that gives the minimum FWHM, $T_0 = 44$ s. In practice we only include the white, 1/f, and broad acoustic resonance #5 contributions to $S_\nu(f)$ for this calculation because the narrow peaks increase computation time and we have confirmed that these peaks do not significantly affect the calculated FWHM ($< 0.1\%$ effect for tested times). For $T_0 < 30$ s, the FWHM is dominated by the Fourier limit of the triangular windowing function ($\mathrm{FWHM} = 0.8859/T_0$ for $S_\nu(f) = 0$) with a small contribution from white noise ($h_{\mathrm{white}} = 0.0033(3)\ \mathrm{Hz^2/Hz}$ leads to a Lorentzian linewidth of 10(1) mHz). Between $T_0 \cong 40$ s and $T_0 \cong 60$ s, the line shape can cross 50% of its peak value multiple times: a result of side bumps in the line shape arising from the windowing function and from the increasing contribution of 1/f noise as T_0 increases. We always calculate the FWHM from the lowest frequency half maximum crossing.

2.4.3 External modulation and noise cancellation via feedback

To further test our theory we intentionally add noise to the α laser. White noise is passed through a bandpass filter at 46.6 Hz with 2 Hz bandwidth and used to frequency modulate the α laser with an acoustic optical modulator (AOM). Figure 2.5(a) demonstrates the effect of the modulation on the optical beat between the α and β lasers. By adding noise into our model $S_\nu(f)$, corresponding to the 1st and 2nd order contributions of the modulation, we can fully account for measured values of I with modulation. Figure 2.5(b) shows calculated and measured values of I for seven-echo pulse spectroscopy with and without 46.6 Hz modulation. In addition to using the optical beat to validate atomic measurements, we also harness the information within the beat to reduce discrete noise features in the α laser. We filter the beat with a bandpass at 22 Hz having

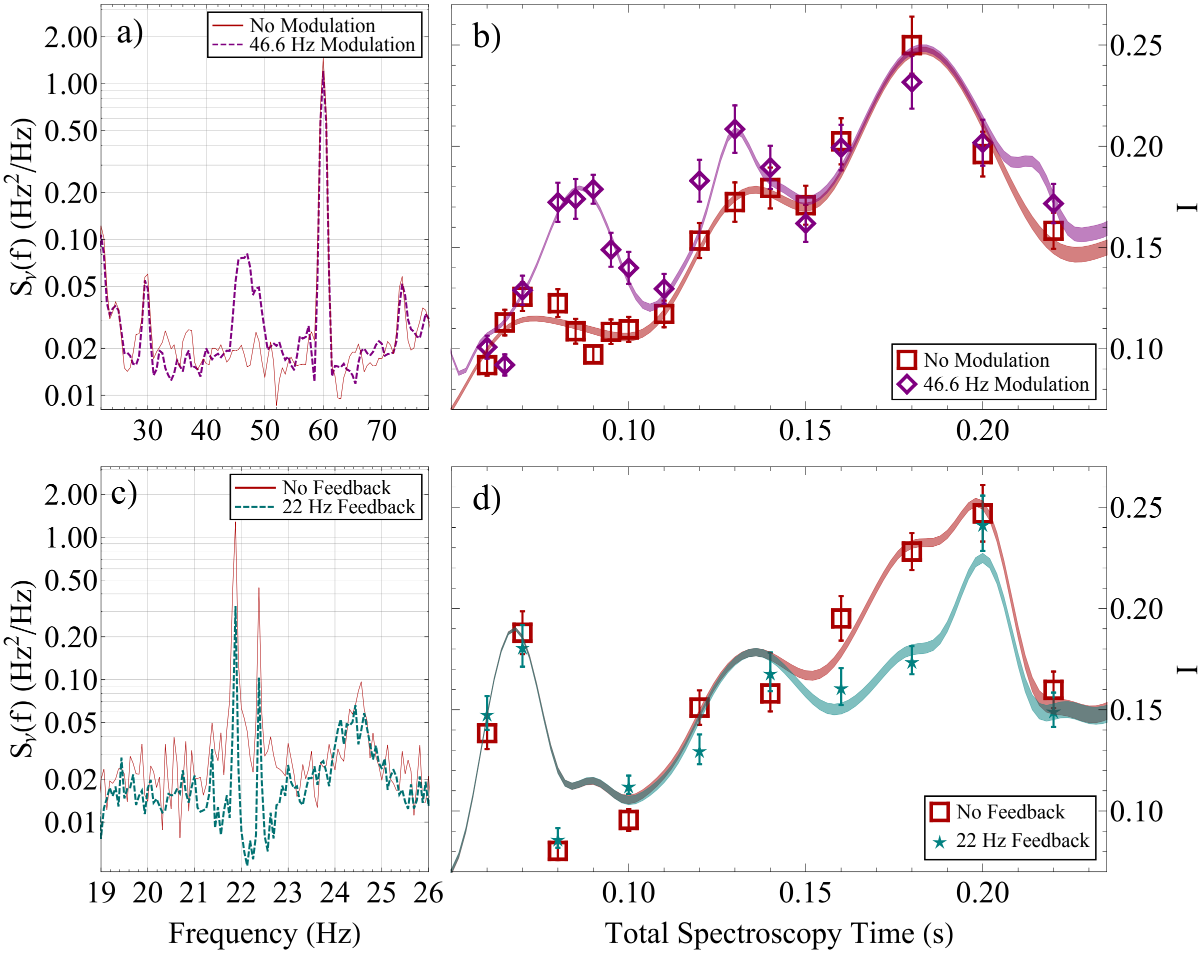

Figure 2.5: (a) Measured $S_\nu(f)$ of an optical beat between the α and β lasers and (b) measured and calculated I for seven-echo pulse sequences with and without modulation at 46.6 Hz. (c) Measured $S_\nu(f)$ of an optical beat between the α and β lasers and (d) measured and calculated I for seven-echo pulse sequences with and without feedback cancellation of 22 Hz noise. (d) Also demonstrated is the appearance of 60 Hz noise due to a malfunctioning signal generator that increases the measured I at 0.06 and 0.2 s of total spectroscopy time. Reproduced from [3].

subhertz bandwidth. This signal is inverted and fed back onto the α laser with an AOM. We can observe the effect of feedback on the beat (Fig. 2.5(c)), although we truly demonstrate the effectiveness of this technique by observing a reduction in I for τ between 0.15 and 0.20 s when feedback is active (Fig. 2.5(d)). To reproduce the measured I with feedback, the magnitude of 22 Hz noise needed to be reduced by 60% in the model $S_\nu(f)$ compared to the condition without feedback modulation.

2.5 Technical comments

In this work, we have used an optical heterodyne beat to verify the optical origin of noise observed in the excitation of an atomic system. Any process that shifts the frequency of the atomic resonance will degrade the sensitivity of our measurement over the frequency range that it occurs, but distinguishing between laser and atomic noise processes is possible even without comparison to an optical beat. For example, inhomogeneous atomic noise will be associated with reduced contrast in the spectroscopic signal. Furthermore, noise that affects the atomic coherence will depend on the internal state of the atom. For example, magnetic field noise will affect different nuclear spin states proportional to the projection of the nuclear spin along the quantization axis, whereas laser noise will affect all nuclear spin states equally. Known processes that could lead to atomic noise, such as magnetic field noise, are limited to the 10^{-16} fractional frequency level at Fourier frequencies below a few hertz using the monitored central frequency and Zeeman splitting between nuclear spin levels during normal clock operations.

The fundamental limit to the accuracy of our spectrum analysis technique combines both the timing accuracy of the pulse sequences we use and our ability to reproducibly measure the amplitude of PSD for a given source of noise. For the current work, the accuracy of our pulse sequences is limited by the reference oscillator of our experimental timing card which is at the 100 parts per million level. When using longer total spectroscopy times, and thereby more precisely determining the frequency of measured noise peaks, we can use a more precise external reference to improve the accuracy of our pulse timing. The accuracy of our measured PSD amplitude is determined by several factors: fluctuations in the actual noise present in our laser, uncertainty in the determination of the spectroscopic contrast, and the statistical uncertainty of our measurement. Our measurements are generally repeatable at the level of 5% over the course of a few days, after which both the optical beat measurements and atomic spectral analysis measurements show larger fluctuations in the amplitude of the discrete noise resonances. However, further work is needed to rigorously access the accuracy of our technique using a known noise source over a long period of time.

We note that stabilized frequency combs have demonstrated that the inherent noise associated with the mode locking process leads to relative noise between comb teeth at the μHz level or below [52]. Furthermore, transfer of optical coherence between 1.5 μm and 698 nm has been demonstrated with 10^{-16} fractional frequency instability, limited only by the 1.5 μm laser [53]. Therefore, there is no fundamental limit to the sensitivity of our method of spectrum analysis arising from the transfer of phase coherence from lasers at other wavelengths to 698 nm using a frequency comb and our technique should be immediately applicable to sources at other wavelengths using standard phase lock techniques.

While we have proposed causes of the measured noise peaks, we do not have conclusive evidence as to their origin and it is possible that the 30 Hz and 22 Hz noise peaks are related due to their shared doublet structure. For noise near 30 Hz we have proposed that alternating current motors, which exist in the building that houses our lab, are the cause. Vibrations from these motors commonly put noise to our lasers even after several layers of heavily mechanically stabilized platforms. Each alternating current motor will have a slightly different operating frequency due to the varying lag of different motors. This could explain the doublet. In reference to the 22 Hz noise peaks, we note that this frequency is near the acoustic resonance frequency of the room that houses the α laser, although this does not immediately explain the doublet structure. We also note that since not all noise features exhibit this doublet structure, we believe that this structure does not arise from a flaw or limitation in our optical heterodyne measurement. The strongest evidence lies in a direct and independent experimental measurement: the 22 Hz and 30 Hz doublets are present

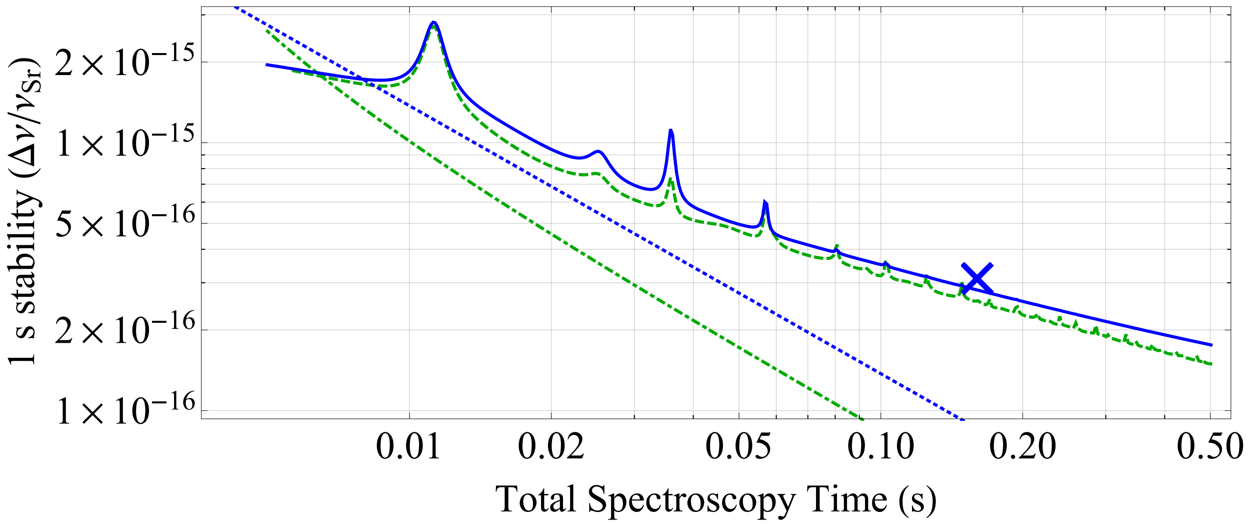

Figure 2.6: The solid blue (dashed green) line represents the 1 s stability limit for an optical clock due to the Dick effect using Rabi (Ramsey) spectroscopy. The blue dotted (green dot-dashed) line represents the QPN stability limit at 1 s for Rabi (Ramsey) spectroscopy assuming a collection of 2000 uncorrelated atoms. Ramsey spectroscopy assumes 2.5 ms $\pi/2$ pulses. The blue "x" denotes the single clock 1 s stability from Ref. [1]. Reproduced from [3].

in vibration noise PSD measured on the table that supports the α laser, which is actively vibration isolated, as well as in acoustic PSD measured inside the acoustic isolation box that houses our laser system. The 24 Hz resonance observed in the optical heterodyne beat between the α and β lasers is believed to be a mechanical resonance of the support structure on which the reference cavity for the β laser is mounted.

2.6 Conclusion

Having developed an accurate model for the α laser's $S_\nu(f)$, we can predict the stability this laser can achieve when used in an optical atomic clock. Here, the laser's frequency is slaved to the clock transition by periodic interrogation. The stability is limited by the Dick effect [20, 21, 22], whereby periodic interrogation creates sensitivity to laser noise at harmonics of $1/T_c$. Figure 2.6 plots the 1 s stability limit due to the Dick effect for Rabi and Ramsey spectroscopy as a function of τ, using the lower limit of the model $S_\nu(f)$. We assume a typical T_c of $857.5 + \tau$ ms, where the 857.5 ms includes laser cooling, MOT trapping, lattice loading, state preparation, and state readout. We find that for Rabi spectroscopy with $\tau = 160$ ms, the Dick effect limits clock stability to $2.8 \times 10^{-16}/\sqrt{\tau}$ in fractional frequency units. For a comparison of two uncorrelated clocks, one operating with 1000 atoms and one operating with 2000 atoms, we predict a stability of $4.6 \times 10^{-16}/\sqrt{\tau}$ which is within 5% of the achieved stability in Ref. [1].

Chapter 3

Strong interactions and many body physics

3.1 Introduction

Strongly correlated quantum many-body systems have become a major focus of modern science. Researchers are using quantum-degenerate atomic gases[54, 55, 56, 57, 58, 59], ultracold polar molecules[60, 61, 62], and ensembles of trapped ions[63, 64] to realize novel quantum phases of matter and simulate complex condensed matter systems. This chapter describes the road that our ^{87}Sr optical lattice clock has taken from the initial discovery of density dependent frequency shifts to demonstrating the importance of many-body effects in our system and observing the onset of quantum correlations between many atoms.

It is important to emphasize that this work would not be possible without recent advances in ultrastable laser performance [8, 27, 36] that have achieved fractional frequency stability of 1 part in 10^{16} at 1 second and drift rates below 1 mHz/s. The experimental results presented later in this chapter rely on the unprecedented stability that these lasers enable in clock systems [1, 30]. In addition to providing improved measurement precisions, the increased atom-light coherence allows us to explore operating regimes that were not previously possible, where perturbations of the clock transition of 1 part in 10^{16} can dominate the system dynamics.

Another critically important piece of this scientific puzzle has been the incredible theoretical work that has been done to explain our experiments [65, 66, 67]. While we will describe the basic structure of the theory and describe results that are pertinent to our measurements, those seeking a more rigorous and complete description should seek out Refs. [65, 66] as well as Refs. [17, 4] and their supplementary on-line material.

3.2 A many-body spin model for interactions

We wish to model the dynamics during clock spectroscopy so we consider a nuclear-spin-polarized ensemble of fermionic atoms with two electronic states: $^1\mathrm{S}_0$ ($|g\rangle$) and $^3\mathrm{P}_0$ ($|e\rangle$). The atoms are trapped in a magic wavelength [48] (also, see Ch. 1) external potential V_{ext} and are illuminated by a linearly polarized laser beam with bare Rabi frequency $\Omega_0 \equiv \langle g|\,\hat{\mathbf{d}}\cdot\mathbf{E_0}\,|e\rangle/\hbar$, where $\hat{\mathbf{d}}$ is the dipole operator and $\mathbf{E_0}$ is the amplitude of the electric field. This system is governed by the following Hamiltonian:

$$
\begin{aligned}
\hat{H} &= \hat{H}_0 + \hat{H}_1, \qquad (3.1)\\
\hat{H}_0 &= \sum_{\alpha}\int d^3\mathbf{R}\ \hat{\Psi}^{\dagger}_{\alpha}(\mathbf{R})\left(-\frac{\hbar^2}{2m}\nabla^2 + V_{\text{ext}}(\mathbf{R})\right)\hat{\Psi}_{\alpha}(\mathbf{R})\\
&\quad + \frac{4\pi\hbar^2 a^{-}_{eg}}{m}\int d^3\mathbf{R}\ \hat{\Psi}^{\dagger}_{e}(\mathbf{R})\hat{\Psi}_{e}(\mathbf{R})\hat{\Psi}^{\dagger}_{g}(\mathbf{R})\hat{\Psi}_{g}(\mathbf{R})\\
&\quad + \frac{3\pi\hbar^2}{m}\sum_{\alpha,\beta} b^3_{\alpha\beta}\int d^3\mathbf{R}\ \left[\left(\vec{\vec{\nabla}}\hat{\Psi}^{\dagger}_{\alpha}(\mathbf{R})\right)\hat{\Psi}^{\dagger}_{\beta}(\mathbf{R}) - \hat{\Psi}^{\dagger}_{\alpha}(\mathbf{R})\left(\vec{\vec{\nabla}}\hat{\Psi}^{\dagger}_{\beta}(\mathbf{R})\right)\right]\\
&\quad \times\left[\hat{\Psi}_{\beta}(\mathbf{R})\left(\vec{\vec{\nabla}}\hat{\Psi}_{\alpha}(\mathbf{R})\right) - \left(\vec{\vec{\nabla}}\hat{\Psi}_{\beta}(\mathbf{R})\right)\hat{\Psi}_{\alpha}(\mathbf{R})\right] + \frac{1}{2}\hbar\omega_a\int d^3\mathbf{R}\ \left[\hat{\rho}_e(\mathbf{R}) - \hat{\rho}_g(\mathbf{R})\right],\\
\hat{H}_1 &= -\frac{\hbar\Omega_0}{2}\int d^3\mathbf{R}\ \left[\hat{\Psi}^{\dagger}_{e}(\mathbf{R})e^{-i(\omega_L t - \mathbf{k}\cdot\mathbf{R})}\hat{\Psi}_{g}(\mathbf{R}) + h.c\right].
\end{aligned}
$$

Here, $\hat{\Psi}_{\alpha}(\mathbf{R})$ is the fermionic field operator at position $\mathbf{R}$ for the electronic state $\alpha = g$ or e and $\hat{\rho}_{\alpha}(\mathbf{R}) = \hat{\Psi}^{\dagger}_{\alpha}(\mathbf{R})\hat{\Psi}_{\alpha}(\mathbf{R})$ is the corresponding density operator. Interactions occur between pairs of atoms via two channels due to the requirement of overall wavefunction anti-symmetry under exchange. Symmetric electronic states $|gg\rangle$, $\frac{1}{\sqrt{2}}(|eg\rangle + |ge\rangle)$, and $|ee\rangle$ result in p-wave interactions governed by the scattering volumes b^3_{gg}, $b^3_{eg^+}$, and b^3_{ee}, respectively. The anti-symmetric electronic state $\frac{1}{\sqrt{2}}(|eg\rangle - |ge\rangle)$ results in s-wave interactions described by the scattering length a_{eg^-}. $\hat{H}_1$ describes the atom-laser interaction, which only applies when the atoms are being interrogated by the clock laser, with frequency ω_L and wavevector $\mathbf{k}$. In the rotating frame of the laser, its frequency will be characterized by its detuning from the atomic transition ω_a, defined as $\delta = \omega_L - \omega_a$.

To make this Hamiltonian tractable, we approximate the one-dimensional (1D) optical lattice trapping potential as a harmonic oscillator with trap frequencies ω_x, ω_y, and ω_z. This is a good approximation for the $\sim 2\ \mu$K atoms in an optical potential of $\sim 20\ \mu$K depth that we use for this work. The atoms are strongly confined along $\hat{z}$ due to the interference pattern of the retro-reflected laser beam and weakly confined in the radial directions, $\hat{x}$ and $\hat{y}$, due to the Gaussian beam profile. For $T = 2\ \mu$K and $\omega_z = 80$ kHz, most atoms are in the ground oscillator level in this dimension so we can neglect higher oscillator levels and consider our system as two-dimensional (2D). In the two weakly confined dimensions, $k_B T \gg \hbar\omega_{x,y}$ (k_B being the Boltzmann constant) so we consider the thermal occupation of oscillator levels in the trap. We refer to the j^{th} atom's oscillator level in these dimensions with the vector $\mathbf{n_j} = n_{xj}\hat{x} + n_{y_j}\hat{y}$, where j varies from 1 to N, the number of atoms in a specific trap site. The slight anharmonicity of the traps allows us to neglect collisions which change the oscillator mode of the atoms, whereas in a truly harmonic trap, transitions that preserve $\mathbf{n}_j + \mathbf{n}_{j'}$ would be energetically allowed [66]. Now, we can expand the fermionic field operator in a non-interacting atom basis, $\hat{\Psi}_\alpha(\mathbf{R}) = \phi_0^z(z)\sum_{\mathbf{n}} \hat{c}_{\alpha\mathbf{n}}\phi_{n_x}(x)\phi_{n_y}(y)$, where ϕ_0^z is the ground mode in the $\hat{z}$ direction, ϕ_{n_i} are harmonic oscillator eigenmodes in the i^{th} dimension, and $\hat{c}^\dagger_{\alpha\mathbf{n}}$ creates a fermion in mode $\mathbf{n}$ and electronic state α.

Although the $|g\rangle$ to $|e\rangle$ transition frequency is free from Doppler and recoil effects when probed along the strongly confined axis of the trap (see Ch. 1), the effective Rabi frequency depends on the oscillator level in the weakly confined dimensions, arising from slight misalignments between the clock laser and trapping laser k-vectors. For a trapping laser along the $\hat{z}$ dimension we can model this with a small component of the clock laser along the $\hat{x}$ dimension such that $\mathbf{k} = k(\sin\phi\hat{x} + \cos\phi\hat{z})$ where ϕ is the small angle between the lattice and clock lasers. Then the effective Rabi frequency is given by [68],

$$\Omega_{\mathbf{n}} = \Omega_0 L_{n_x}(\eta_x^2) L_0(\eta_z^2) e^{-(\eta_z^2+\eta_x^2)/2}, \tag{3.2}$$

where $\eta_{x,z} = k_{x,z} a_{\text{ho}}^{x,z}$ are Lamb-Dicke parameters, $a_{\text{ho}}^i = \sqrt{\frac{\hbar}{\omega_i m}}$, and L_n are Laguerre polynomials.

A central feature of this theory model is that we approximate the two clock states as a spin-

1/2 system. This is a good approximation for our system because the atoms are polarized in the $m_F = 9/2$ state. Since the lifetime of the excited state is ~ 150 s, no other sub-levels are populated via spontaneous emission. Furthermore, the clock light is polarized along the magnetic field that defines the quantization axis so it only drives m_F maintaining π transitions. Therefore, we can treat the two $m_F = 9/2$ states that we populate as a spin-1/2 system and the Hamiltonian can be written as

$$\begin{aligned}\hat{H}/\hbar = -\delta \sum_{j=1}^{N} \hat{S}^z_{\mathbf{n}_j} - \sum_{j=1}^{N} \Omega_{\mathbf{n}_j} \hat{S}^x_{\mathbf{n}_j} + \sum_{j\neq j'}^{N} \left[J^{\perp}_{\mathbf{n}_j,\mathbf{n}_{j'}} (\overrightarrow{S}_{\mathbf{n}_j} \cdot \overrightarrow{S}_{\mathbf{n}_{j'}}) + \chi_{\mathbf{n}_j,\mathbf{n}_{j'}} \hat{S}^z_{\mathbf{n}_j} \hat{S}^z_{\mathbf{n}_{j'}} \right] \\ + \sum_{j\neq j'}^{N} \left[\frac{C_{\mathbf{n}_j,\mathbf{n}_{j'}}}{2} (\hat{S}^z_{\mathbf{n}_j} I_{\mathbf{n}_{j'}} + \hat{S}_{\mathbf{n}_{j'}} I_{\mathbf{n}_j}) + \frac{K_{\mathbf{n}_j,\mathbf{n}_{j'}}}{4} I_{\mathbf{n}_j} I_{\mathbf{n}_{j'}} \right].\end{aligned} \tag{3.3}$$

Here, $\overrightarrow{S}_{\mathbf{n}_j} = \frac{1}{2}\sum_{\alpha,\beta} \hat{c}^{\dagger}_{\alpha\mathbf{n}_j} \overrightarrow{\sigma}_{\alpha\beta} \hat{c}_{\beta\mathbf{n_j}}$, with $\sigma^{x,y,z}_{\alpha\beta}$ being Pauli matricies and $I_{\mathbf{n}_j}$ is the identity matrix. The mode-dependent coupling constants are defined as:

$$J^{\perp}_{\mathbf{n}_j,\mathbf{n}_{j'}} = \frac{V^{eg^+}_{\mathbf{n}_j,\mathbf{n}_{j'}} - U^{eg^-}_{\mathbf{n}_j,\mathbf{n}_{j'}}}{2}, \tag{3.4}$$

$$\chi_{\mathbf{n}_j,\mathbf{n}_{j'}} = \frac{V^{ee}_{\mathbf{n}_j,\mathbf{n}_{j'}} + V^{gg}_{\mathbf{n}_j,\mathbf{n}_{j'}} - 2V^{eg^+}_{\mathbf{n}_j,\mathbf{n}_{j'}}}{2}, \tag{3.5}$$

$$C_{\mathbf{n}_j,\mathbf{n}_{j'}} = \frac{V^{ee}_{\mathbf{n}_j,\mathbf{n}_{j'}} - V^{gg}_{\mathbf{n}_j,\mathbf{n}_{j'}}}{2}, \quad \textit{and} \tag{3.6}$$

$$K_{\mathbf{n}_j,\mathbf{n}_{j'}} = \frac{V^{ee}_{\mathbf{n}_j,\mathbf{n}_{j'}} + V^{gg}_{\mathbf{n}_j,\mathbf{n}_{j'}} + V^{eg^+}_{\mathbf{n}_j,\mathbf{n}_{j'}} + U^{eg^-}_{\mathbf{n}_j,\mathbf{n}_{j'}}}{2}, \tag{3.7}$$

where $V^{gg}_{\mathbf{n}_j,\mathbf{n}_{j'}}$, $V^{eg^+}_{\mathbf{n}_j,\mathbf{n}_{j'}}$, $V^{ee}_{\mathbf{n}_j,\mathbf{n}_{j'}}$, and $U^{eg^-}_{\mathbf{n}_j,\mathbf{n}_{j'}}$ are related to the fundamental scattering parameters b^3_{gg}, $b^3_{eg^+}$, b^3_{ee}, and a_{eg^-}, respectively, as described in Appendix B. Equation 3.3 serves as the basis for the theoretical understanding of our many-body clock system. Although this Hamiltonian can be exactly solved numerically, the problem quickly becomes intractable with increasing N since the size of the Hilbert space scales exponentially with N. The average value of N for a single lattice site in our experimental system is about 20. Furthermore, additional complications to our system, such as two-body loss from $|e\rangle$ and collisions that modify the oscillator level of the atoms greatly complicate the theoretical treatment of our system.

To further simplify the Hamiltonian in Eqn. 3.3 we assume that the atoms are prepared in the $S = N/2$ Dicke manifold [69], which is true for our experiments where atoms are all prepared in $|g\rangle$ or

$|e\rangle$ corresponding to $S = N/2$, $m_S = \pm N/2$. This allows us to restate Eqn. 3.3 in terms of collective spin operators $\hat{S}^{\tau=x,y,z} = \sum_{j=1}^{N} \hat{S}^{\tau}_{\mathbf{n}_j}$, mean Rabi frequency $\bar{\Omega} = \frac{1}{N}\sum_{j=1}^{N} \Omega_{\mathbf{n}_j}$, and mean interaction parameters $\chi = \frac{1}{N(N-1)}\sum_{j\neq j'} \chi_{\mathbf{n}_j,\mathbf{n}_{j'}}$, $C = \frac{1}{N(N-1)}\sum_{j\neq j'} C_{\mathbf{n}_j,\mathbf{n}_{j'}}$, and $J^{\perp} = \frac{1}{N(N-1)}\sum_{j\neq j'} J^{\perp}_{\mathbf{n}_j,\mathbf{n}_{j'}}$. We depend on the fact that our system remains in the $S = N/2$ manifold which occurs for three reasons: (1) the interaction parameters depend weakly on the thermally occupied modes, $\mathbf{n}_j$, so that they are peaked around their mean values, (2) $J^{\perp}$ is much greater than the standard deviations of $\chi_{\mathbf{n}_j,\mathbf{n}_{j'}}$ and $C_{\mathbf{n}_j,\mathbf{n}_{j'}}$, $\Delta\chi$ and ΔC, (3) the standard deviation of $\Omega_{\mathbf{n}}$, $\Delta\bar{\Omega}$, is much smaller than $\bar{\Omega}$. Thus, Eqn. 3.3 becomes,

$$\hat{H}/\hbar = -\delta\hat{S}^z - \bar{\Omega}\hat{S}^x + \chi(\hat{S}^z)^2 + C(N-1)\hat{S}^z + J^{\perp}\overrightarrow{S}\cdot\overrightarrow{S} + \mathcal{O}(\hat{S}^z)^3. \tag{3.8}$$

An alternative situation, where $\frac{\Delta\bar{\Omega}}{\bar{\Omega}} \ll 1$ does not hold and the p-wave interaction parameters $V^{\alpha\beta(+)}_{\mathbf{n}_j,\mathbf{n}_{j'}}$ are small compared to $U^{eg^-}_{\mathbf{n}_j,\mathbf{n}_{j'}}$, leads to dominantly s-wave interactions enabled by inhomogeneous excitation. A theoretical model based on these assumptions was originally used to explain the observed density shifts in one- and 2D optical lattice trapped ^{87}Sr atoms [70, 17]. Although the data showed good agreement with this model, we will see that our later work described in Ch. 4 has ruled out the possibility of the observed density shifts arising solely from s-wave interactions and we must also consider p-wave interactions for a complete description of our system.

3.3 First observation of density dependent frequency shifts

Before describing our most recent work that benefits from the enhanced stability of our new clock laser, we will first look at the original observation of density dependent frequency shifts, attempts to describe them theoretically, and also our fist attempt to exploit a strongly-interacting system for the benefit of clock accuracy.

Fermionic optical lattice clocks were first thought to be free from interaction effects due to the ~ μK temperature of the atoms, the requirement of overall wavefunction anti-symmetry from the Pauli exclusion principle, and the ~ 20 μK centrifugal barrier to p-wave interactions [71]. Initial evaluations of radio-frequency clocks based on alkali atoms seemed to support this claim [72, 73]

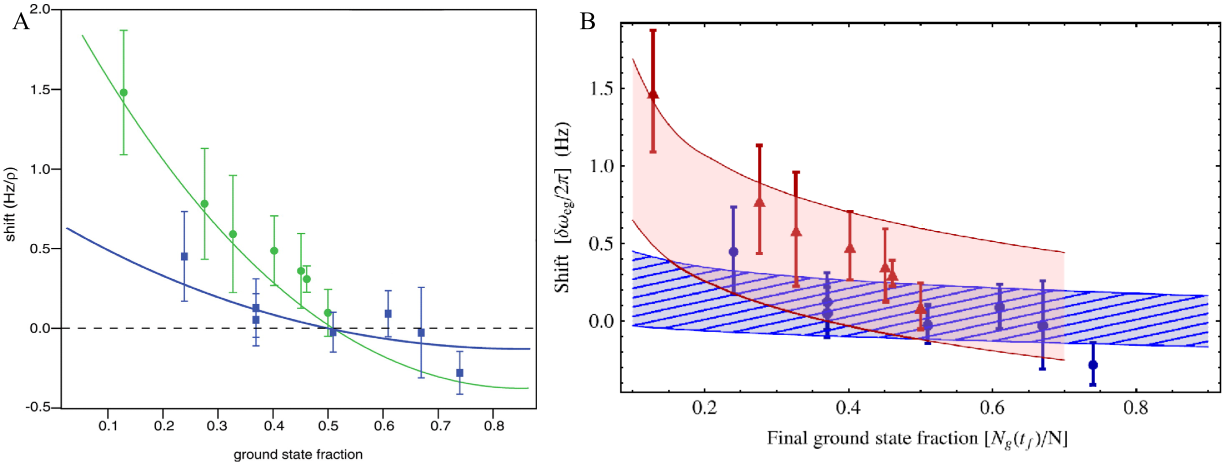

Figure 3.1: Density shift data for nuclear-spin polarized atoms at two different temperatures compared to two different theory models based on s-wave interactions enabled by inhomogeneous excitation. The data points are from [70] where the atoms are prepared in $|e\rangle$ and transfered down to $|g\rangle$ with an 80 ms π pulse. The final ground state population is varied by changing the detuning from the center of the clock transition. Green circles in (a) and red triangles in (b) correspond to data taken at 3 μK. Blue squares in (a) and blue circles in (b) correspond to data taken at 1 μK. The change in temperature varies the excitation inhomogeneity. Theory lines in (a) correspond to a simple, two-particle model used in [70] whereas the theory bands in (b) correspond to the many-body model in [65]. (a) and (b) reproduced from [70] and [65], respectively.

however, these evaluations were not performed with sufficient precision to be relevant to the best frequency standards.

The great improvements to clock precision brought on by the first generation of ultra-stable lasers and optical clocks allowed for evaluations of density dependent clock shifts in our ^{87}Sr lattice clock system at the 10^{-16} fractional frequency level and revealed their existence [70]. These frequency shifts were attributed to s-wave collisions allowed by inhomogeneous excitation [70, 65, 74, 75]; p-wave interactions were assumed to be suppressed because of the ~ 1 μK sample temperature. Fig. 3.1 shows figures from [70] and [65] where the data from [70] is compared to both a two-particle theory model (Fig. 3.1(a)) and a many-body theory model (Fig. 3.1(b)). Immediately, we see that the effects of interactions are weak. The measured density shifts are a ~ 1 Hz perturbation of a 429 THz transition. Furthermore, the differences between the many-body theory and the two-particle theories are subtle and the experimental precision of the data is not

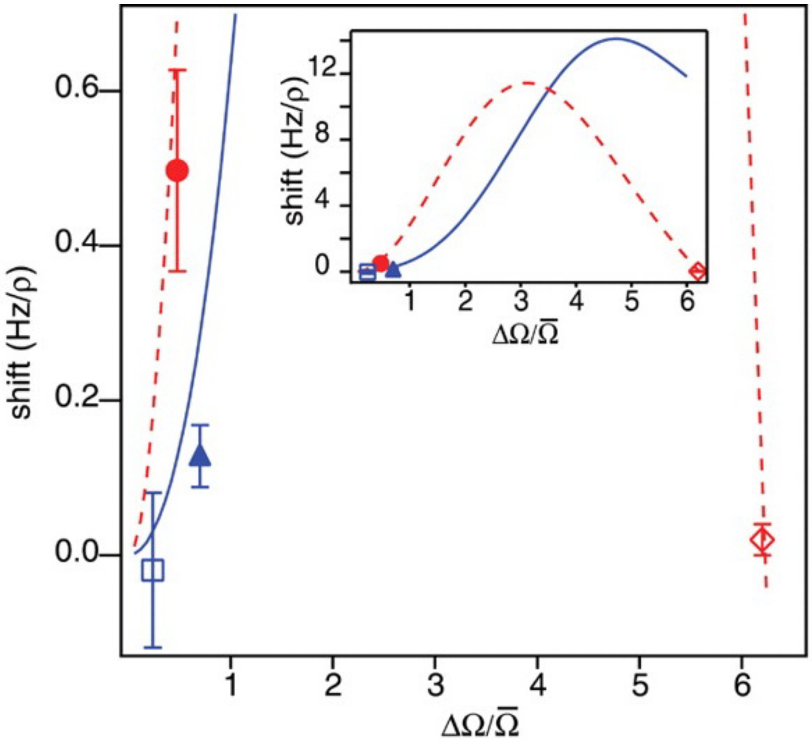

Figure 3.2: Observed density shifts versus excitation inhomogeneity as measured by $\Delta\bar{\Omega}/\bar{\Omega}$. The blue points represent data taken at 1 μK and red points represent data at 3 μK. Blue solid and red dashed lines represent predictions of the theoretical model based on s-wave interactions. Reproduced from [70].

sufficient to confirm the importance of many-body effects.

The central assumption of the s-wave interaction theory that was used to describe the observed density shift is that the inhomogeneous excitation, characterized by the spread in Rabi frequencies $\Delta\bar{\Omega}$ drives atoms into the anti-symmetric electronic state, $(|ge\rangle - |eg\rangle)/\sqrt{2}$, where s-wave interactions are allowed. A convincing way to confirm this effect is to vary $\Delta\bar{\Omega}$ and show that the observed shift obeys the predicted behavior from the model. Although the data presented in Fig. 3.2 (or lack there of) is consistent with the predicted behavior, in order to convincingly confirm the predicted behavior a much more systematic variation of $\Delta\bar{\Omega}$ with many more points along the theoretical curves is necessary.

3.4 Entering the strongly interacting regime

Motivated by further confirmation of the s-wave theoretical model and one of its intriguing predictions at large interaction energies, we set out to investigate density dependent frequency shifts where interactions are more dominant over other relevant energy scales. For our optical lattice clock system, there are two relevant energy scales other than interactions. Since we are always in the regime where $\bar{\Omega}$ is much greater than Γ, the natural linewidth of the clock transition, $\bar{\Omega}$ determines the spectroscopic resolution for Rabi spectroscopy. Since $\Delta\Omega$ drives the atoms into the anti-symmetric electronic state, this energy scale is also relevant especially for the situation where $V^{\alpha\beta(+)}_{\mathbf{n}_j,\mathbf{n}_{j'}}$ are small compared to $U^{eg^-}_{\mathbf{n}_j,\mathbf{n}_{j'}}$. It is important to note that the temperature of the atoms does not significantly effect atom dynamics since we operate in the resolved sideband regime. Temperature only enters indirectly through it's effect on $\Delta\Omega$, atomic density, and the mode dependence of interaction parameters. When the interaction energy dominates over the other relevant energy scales, we say that our system is in the strongly interacting regime.

Strongly interacting quantum systems can exhibit counterintuitive behaviors. For example, frequency shifts of a microwave transition in a quantum gas remains finite close to a Feshbach resonance [72, 76, 77]. In particular, the effective interaction strength is significantly enhanced in low dimensions, resulting in particles avoiding each other in order to minimize their total energy. This tendency can lead to behavior that in many aspects resembles that of non-interacting systems. One such example is the Tonks–Girardeau regime of an ultracold Bose gas, in which the strong repulsion between particles mimics the Pauli exclusion principle, causing the bosons to behave like non-interacting fermions [78, 79, 80, 81]. Here, we demonstrate that the enhancement of atomic interactions in a strongly interacting, effectively 1D fermionic system suppresses collisional frequency shifts in an optical atomic clock.

To gain insight into the originally proposed origin of the collisional frequency shift and the interaction-induced suppression, we consider a two-atom model system confined in a harmonic oscillator potential. The collective-pseudospin states of these two identical fermions can be expressed using a basis comprised of three pseudospin-symmetric triplet states and an antisymmetric singlet state [74, 65]. Because the atoms are initially prepared in the same internal state ($|g\rangle$), with their internal degrees of freedom symmetric with respect to exchange, the Pauli exclusion principle requires that their spatial wave function be antisymmetric and they experience no s-wave interactions. If the atoms are coherently driven with the same Rabi frequency ($\bar{\Omega} = (\Omega_{\mathbf{n}_1} + \Omega_{\mathbf{n}_2})/2 = \Omega_{\mathbf{n}_1}$, their electronic degrees of freedom remain symmetric under exchange. Here, $\mathbf{n}_i$ represents the oscillator level of the i^{th} atom, and $\Omega_{\mathbf{n}_i}$ is the mode-dependent Rabi frequency (Eqn. 3.2) proportional to the bare Rabi frequency Ω_0^B. Consequently, these atoms will not experience any s–wave interactions during the excitation of the clock transition. However, if $\Delta\Omega = (|\Omega_{\mathbf{n}_1}$ - $\Omega_{\mathbf{n}_2}|)/2$ is not zero, the optical excitation inhomogeneity can transfer atoms with a certain probability to the antisymmetric spin state (singlet) that is separated from the triplet states by an interaction energy U, as in the singlet state the atoms do interact. U, which is inversely proportional to the atomic confinement volume, gives rise to a frequency shift during clock interrogation [74, 65].

Figure 3.3 contrasts the 2D lattice experiment with prior studies carried out in a 1D lattice [65, 82]. In a 1D lattice, U is typically smaller than $2\bar{\Omega}$ (the energy spread of the driven triplet states at zero detuning). Consequently, any small excitation inhomogeneity $\Delta\Omega$ can efficiently populate the singlet state. By tightly confining atoms in a 2D lattice, one can reach the limit where $U \gg \bar{\Omega}$, inhibiting the evolution into the singlet state; as a result, the collisional frequency shift of the clock transition is suppressed. In this regime, the singlet state can only participate as a "virtual" state in second-order excitation processes and the frequency shift scales as $\Delta\Omega^2/U$. In this limit, the energy-carrying singlet resonance has been shifted so far from the triplet resonances that it is completely resolved from them, and the remaining line-pulling effect can be negligible. Such behavior is reminiscent of the dipolar blockade mechanism in a Rydberg atom gas [83].

For this work, our current clock laser with 10^{-16} stability at 1 second was not yet completed, so the option of increasing the importance of interactions by decreasing $\bar{\Omega}$ was not available. Our only option was to increase the interaction strength through stronger confinement of the atoms. We achieve stronger interactions by confining the atoms in a 2D optical lattice. The 2D lattice

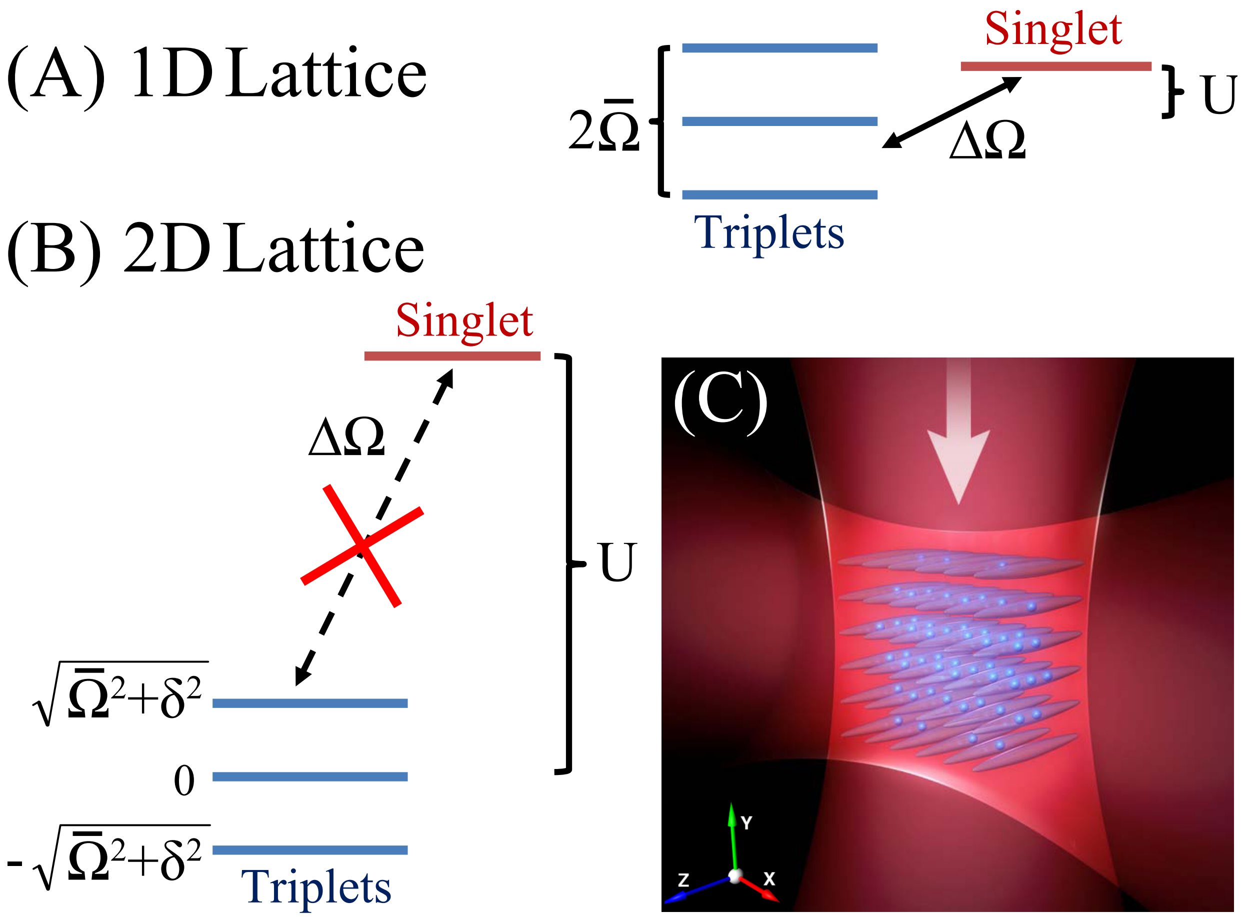

Figure 3.3: A schematic of the s-wave interaction blockade mechanism proposed for the suppression of collisional frequency shifts. (A) In a 1D optical lattice, the interaction energy of the singlet state lies within the energies of the dressed triplet states (characterized by an energy spread of the order of $\bar{\Omega}$). A weak excitation inhomogeneity characterized by $\Delta\Omega$ is capable of producing triplet-singlet mixtures, causing a collisional frequency shift proportional to the interaction strength U. (B) In a 2D optical lattice, the interaction energy exceeds the atom-light Rabi frequency, creating an energy gap between the spin triplet and singlet states. Evolution into the singlet state is inhibited and the collisional frequency shift is suppressed. (C) Quasi-1D tube-like optical potentials formed by two intersecting optical lattices. The laser which interrogates the clock transition propagates along $\hat{y}$, the vertical axis. Reproduced from [17].

provides strong confinement along two directions ($\hat{x}$ and $\hat{y}$), and relatively weak confinement along the remaining dimension ($\hat{z}$). It is important to note that this axis labeling convention is different from that of our 1D optical lattice. Using Doppler and sideband spectroscopy we determine that the lattice confined atoms are sufficiently cold ($T_x \simeq T_y \simeq 2\ \mu$K) that they primarily occupy the ground state of the potentials along the tightly confined directions, with trap frequencies $\omega_x/2\pi$ ∼75-100 kHz and $\omega_y/2\pi$ ∼45-65 kHz. This creates a 2D array of isolated tube-shaped potentials oriented along $\hat{z}$, which have trap frequencies $\omega_z/2\pi$ ∼0.55-0.75 kHz. We estimate that approximately 20%-30% of the occupied lattice sites have more than one atom. At a typical axial temperature T_z of a few μK, various axial vibrational modes n are populated in each tube. In our clock experiment, the $|g\rangle \rightarrow |e\rangle$ transition is interrogated via Rabi spectroscopy using an ultrastable laser propagating along $\hat{y}$. The clock laser and both lattice beams are linearly polarized along $\hat{z}$. As described in Refs. [70, 16] and above, any small projection of the probe beam along $\hat{z}$ leads to a slightly different Rabi frequency Ω_n for each mode $\Omega_n(\eta_z^2)$. Here $\eta_z = k_z a_{ho}/\sqrt{2}$ is the Lamb-Dicke parameter and k_z represents a small component of the probe laser wave vector along $\hat{z}$, resulting in a typical $\eta_z \sim 0.05$.

The spectroscopy of the clock transition is performed with an 80-ms pulse, resulting in a Fourier-limited linewidth of ∼ 10 Hz. The laser power is adjusted to produce a π pulse on resonance, and the clock laser is locked to the atomic resonance by probing two points on either side of the resonance, with a frequency separation corresponding to the resonance FWHM. The high–finesse Fabry–Perot cavity [28] used to narrow the clock laser's linewidth is sufficiently stable over short time scales that it can be used as a frequency reference in a differential measurement scheme [84]. A single experimental cycle (e.g., cooling and trapping atoms, preparing the 2D lattice, and interrogating the clock transition) requires about 1.5 s, and we modulate the sample density every two cycles. The corresponding modulation of the atomic resonance frequency relative to the cavity reference is a measurement of the density shift.

We perform measurements at several trap depths to directly observe the interaction-induced suppression of the collisional frequency shift. To access different interaction energies, we vary the intensity of the horizontal lattice beam (I_x), which results in the change of mainly ω_x but also ω_y and ω_z. The change in ω_y arises from the fact that the laser beams that create the two lattices are not orthogonal but instead at an angle of 71°. The change in ω_z results from the Gaussian profile of the beams. Since the experimentally measured shift was originally understood in terms of s-wave interactions, the interaction strength of our system is parameterized by the s-wave energy scale for the effectively 1D system, $u = 4\sqrt{\omega_x \omega_y} \frac{a_{eg^-}}{a^z_{\text{ho}}}$. Because $u \propto \sqrt{\omega_x \omega_y \omega_z}$, an increase of the horizontal beam power leads to a monotonic increase of u. We observe a significant decrease of the collisional shift with increasing horizontal lattice power, as shown by the data points (filled black squares and blue triangles) in Fig. 3.4 (inset). Squares and triangles indicate data taken with slightly different beam waists. We have also studied the dependence of the collisional shift on the Rabi frequency used to drive the clock transition. Ω_0^B was increased by a factor of two, and the interrogation time was decreased by 2, yielding a constant Rabi pulse area. Under these conditions, we observe that the collisional shift under similar temperature and trapping conditions increases sharply (green open square and green open triangle in the inset to Fig. 3.4), confirming that the shift suppression mechanism will not operate effectively for short, higher Rabi frequency pulses.

Also shown in the inset of Fig. 3.4 is the shift predicted by the spin model, assuming two atoms per lattice site. The theoretical points are scaled by the fraction of the atomic population in doubly occupied lattice sites. The pink rectangles are the theory results, $\Delta\nu^T(\omega_z^i, T_z^i, u, \Omega_0^{B\,i})$ with $i = 1, \ldots, 9$, obtained at different temperatures, trapping frequencies, and Rabi frequencies corresponding to the actual experiment conditions under which the data were taken. The spread of theory results (indicated by the vertical extent of the pink rectangles) corresponds to a range of scattering lengths $a_{eg^-} = -(35\text{–}50)\ a_0$ (where a_0 is the Bohr radius), $\eta_z = 0.046$, and $\omega_z = 2\pi \times 0.7$ kHz at the point with the smallest collisional shift.

Because the temperature and trapping conditions substantially varied for different experimental data points, some scaling is required to make direct comparisons between data in Fig. 3.4 (inset). To help visualize the comparison between experiment and theory, we rescaled the measured experimental values of the shift by a factor extracted from the theoretical model $\frac{\Delta\nu^T(\omega_z^{\text{fix}}, T_z^{\text{fix}}, u, \Omega_0^{B\,fix})}{\Delta\nu^T(\omega_z^i, T_z^i, u, \Omega_0^{B\,i})}$.

Figure 3.4 shows that after rescaling all data points lie very close to the theoretical curve of fractional frequency shift *vs.* u at constant $\omega_z^{\mathrm{fix}} = 2\pi \times 0.7$ kHz, $T_z^{\mathrm{fix}} = 3.5$ μK, and $\Omega_0^{B\,fix} = \Omega_0^B$. The data confirm three trends in the prediction: the collisional shift $\Delta\nu$ decreases with increasing u at similar T_Z and trapping conditions, $\Delta\nu$ increases with increasing Ω_0^B at similar T_Z and trapping conditions, and $\Delta\nu$ decreases with smaller T_Z. The sign of the observed shift is negative, i.e., an increased sample density shifts the atomic resonance to lower frequencies. Previous studies of the collisional shift in a 1D optical lattice [25, 70] are consistent with this observation.

We have made an extensive series of collisional shift measurements at the largest trap depths available to us. The first-generation clock laser has a stability of about 1.5×10^{-15} at time scales of 1–10 seconds [28]. Therefore, a substantial integration time is required to determine the collisional shift with an uncertainty of 1×10^{-17}. Frequency drifts are minimized by measuring the long-term drift in the resonance frequency (relative to the ultrastable reference cavity) and applying a feed-forward correction to the clock laser. The correlation between the atomic resonance frequencies and the density of trapped atoms was calculated by analyzing overlapping sequences of four consecutive measurements and eliminating frequency drifts of up to second order [23]. Approximately 60 hours of data were acquired at $T_z = 7$ μK over a ~ 2 month time period for the record shown in Fig. 3.5A. Each data point represents a period during which the clock was continuously locked, with error bars determined from the standard error of the measurements in that data set. At an axial temperature $T_z \simeq 7$ μK, the collisional shift in our 2D lattice clock was measured to be $(5.6 \pm 1.3) \times 10^{-17}$ in fractional units, with $\sqrt{\chi^2_{\mathrm{red}}} \simeq 0.84$. At a lower T_z of 3.5 μK, the collisional shift is reduced to $(0.5 \pm 1.7) \times 10^{-17}$, with $\sqrt{\chi^2_{\mathrm{red}}} \simeq 0.73$ (the record in Fig. 3.5C). The corresponding Allan deviations of both data sets are shown in Fig. 3.5B and D.

We note that, relative to previous measurements of collisional shifts in a 1D optical lattice [25, 70], the atomic density in a 2D lattice is an order of magnitude higher. Hence, if the collisional shift in a 2D lattice were not suppressed, we would expect a larger shift than earlier results, even after assuming that only $20 - 30\%$ of lattice sites are contributing.

Our more recent work has shown that a_{eg^-} is positive (see Ch. 4), indicating that the pre-

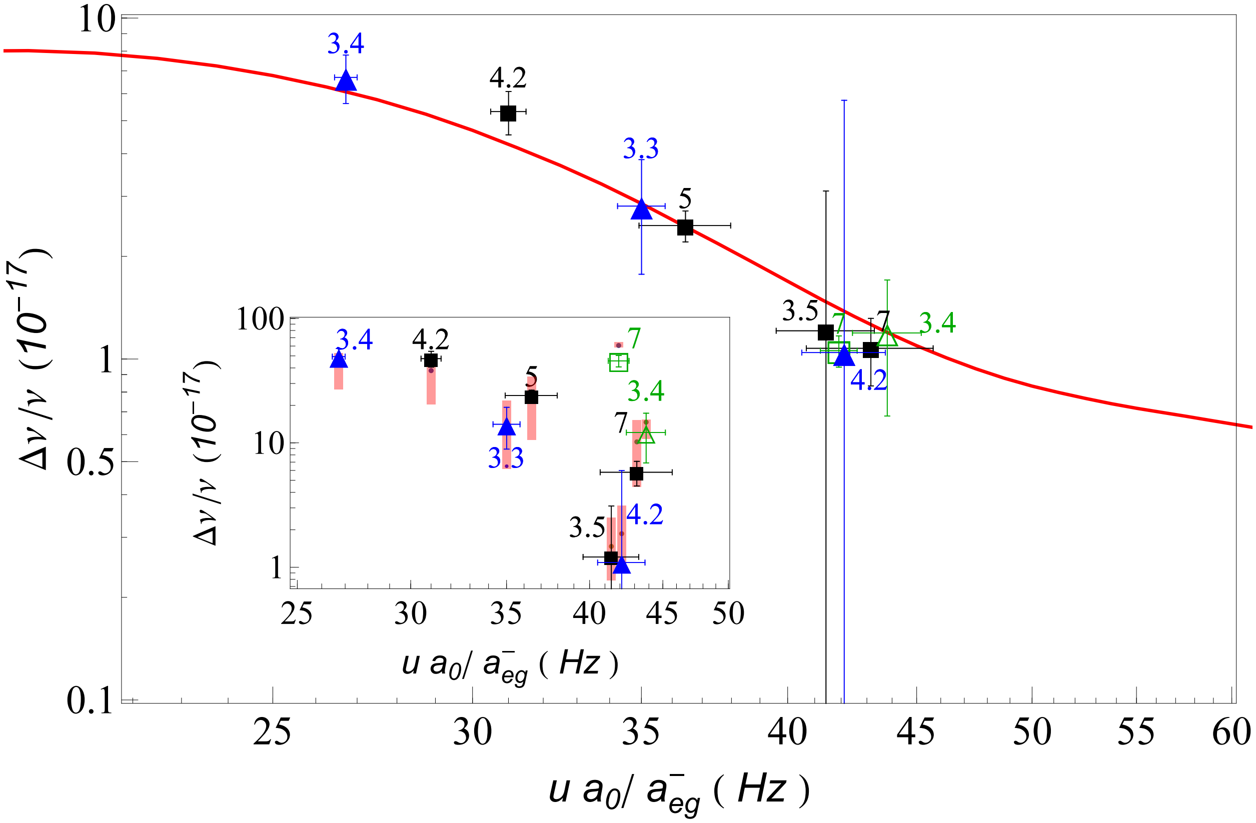

Figure 3.4: Experimental observation of the suppression of the collisional frequency shift with increasing interaction energy u. We scale $u = 4\omega_\perp \frac{a_{eg}^-}{a_{ho}}$ by a_0/a_{eg}^- with a_0 the Bohr radius. The value of u was varied by changing three important parameters: I_x, T_z, and Ω_0^B. To better compare the shift at different experimental conditions we rescale the experimental data by a factor $\Delta\nu^T(\omega_z^{fix}, T_z^{fix}, u, \Omega_0^{B\,fix})/\Delta\nu^T(\omega_z^i, T_z^i, u, \Omega_0^{B\,i})$, with $\omega_z^{fix} = 2\pi \times 0.7$ kHz, $T_z^{fix} = 4.2$ μK, and $\Omega_0^{B\,fix} = \Omega_0^B$. The $\Delta\nu^T(\omega_z^i, T_z^i, u, \Omega_0^{B\,i})$ are calculated values using the spin model for $N = 2$ with actual experimental parameters and a scattering length of $|a_{eg}^-| = (35\text{-}50)\ a_0$ (see inset). The calculations are scaled by the fraction of the atomic population in doubly occupied lattice sites. A theoretical curve of $\Delta\nu^T(\omega_z^{fix}, T_z^{fix}, u, \Omega_0^{B\,fix})$ is shown with a solid red line at $|a_{eg}^-| = 40\ a_0$. Inset: unscaled experimental data with T_z indicated for each point. The black and blue colored symbols were taken at Ω_0^B and the green colored symbols at $2\Omega_0^B$ and half the interrogation time. Squares and triangles distinguish between two sets of data points measured under different lattice configurations. The vertical extent of pink rectangles indicate the corresponding spin model predictions for the range of $|a_{eg}^-| = (35\text{-}50)\ a_0$. The variation of ω_z and u with I_x was explicitly taken into account in theory which used $\eta_z = 0.046$ and $\omega_z = 2\pi \times 0.7$ kHz at the point with the smallest collisional shift. Reproduced from [17].

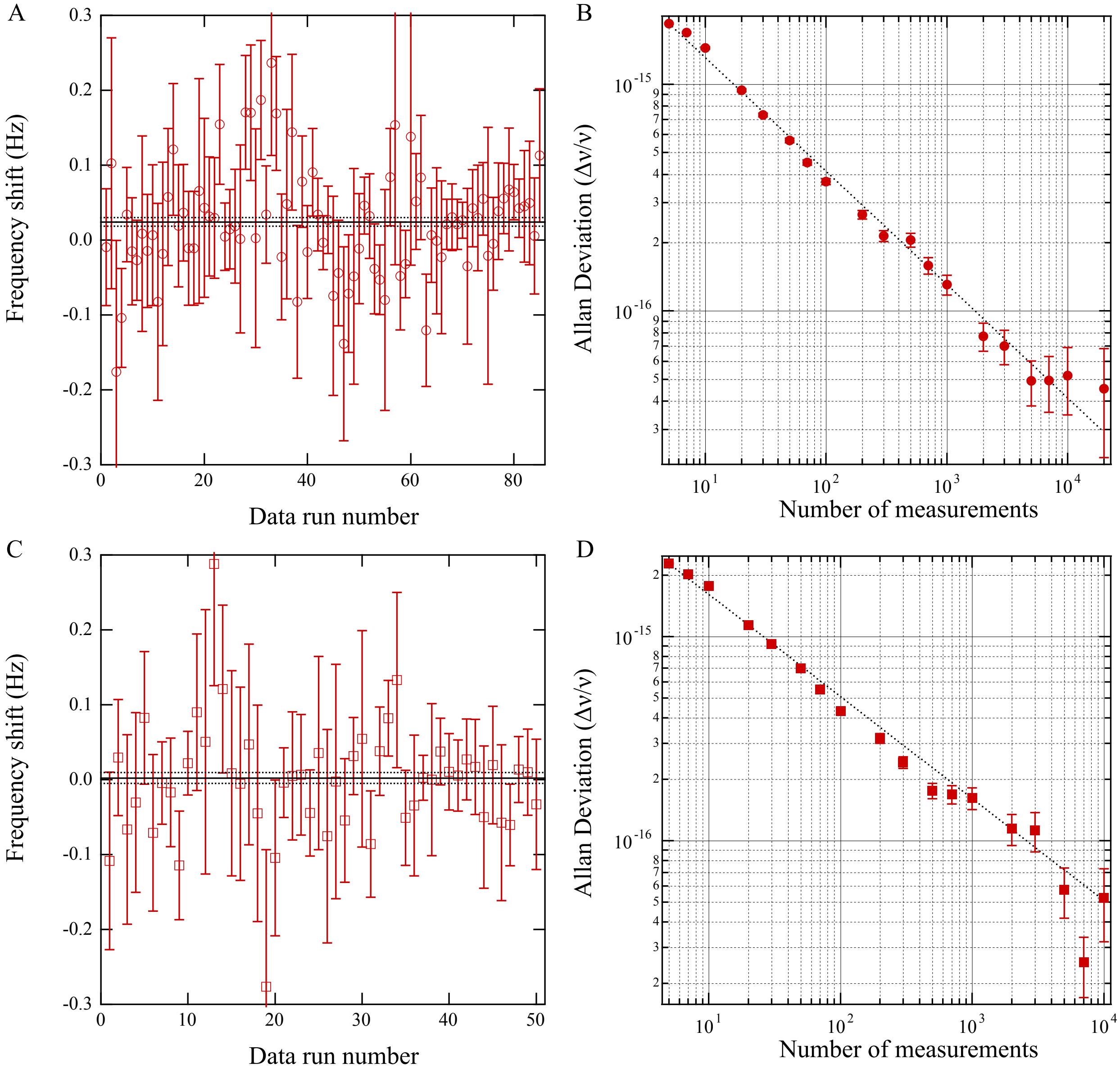

Figure 3.5: Data records of collision-induced frequency shift measurements for ^{87}Sr atoms confined in a 2D optical lattice. Each point represents a data set collected from a continuous operation of the Sr clock, with error bars determined from the standard error of that data set. The weighted mean and weighted error of all the data are determined from the shift and error values of each data set, and the weighted error is scaled by the square-root of the reduced chi-square, $\sqrt{\chi^2_{\mathrm{red}}}$. These are shown as the solid and dashed horizontal lines in panels (A) and (C). Panels (B) and (D) show the corresponding Allan deviations (ignoring dead time between data runs) of the frequency shift records displayed in (A) and (C), respectively. Each measurement represents a differential comparison between two density conditions. Under typical clock operating conditions ($N \simeq 2000$), the weighted mean and the weighted standard error of the fractional frequency shift are $(5.6 \pm 1.3) \times 10^{-17}$ at $T_Z = 7$ μK ((A) and (B)) and $(0.5 \pm 1.7) \times 10^{-17}$ at $T_Z = 3.5$ μK ((C) and (D)). For the 7 μK data the reduced chi-square was $\sqrt{\chi^2_{\mathrm{red}}} = 0.84$, and for the 3.5 μK data $\sqrt{\chi^2_{\mathrm{red}}} = 0.73$. Reproduced from [17].

vious picture with s-wave interactions is incomplete. As we will see later in this chapter, p-wave interactions dominate the dynamics in our 1D optical lattice, even at higher radial temperatures. Certainly, a hand-waving argument can be made that p-wave interactions could also lead to a suppression of density dependent frequency shifts if the mean p-wave interaction energy is much larger than $\bar{\Omega}$. In this case, the sites with two or more particles are shifted away from the interaction-free peak created by the dominant single-particle occupied tubes. The main difference between this mechanism and the s-wave shift suppression is that while U prevents atoms from ever populating an interacting electronic state, p-wave interactions merely shift already interacting atoms from the non-interacting signal. As a result, s-wave shift suppression actually becomes stronger with more atoms in the trap, while p-wave shift suppression depends on the fact that most atoms exist in single-occupancy trap sites. Certainly further theoretical and experimental work could greatly help to place the observed density shift suppression on more solid theoretical ground.

3.5 Evidence for p-wave interactions: two-body $|e\rangle$-$|e\rangle$ loss

As stated above, our more recent work shows that p-wave interactions are actually dominant for the most common configuration of operating our clock: atoms trapped in a 1D optical lattice. The first clue that interactions in our ^{87}Sr system had a p-wave nature, however, did not come from investigations of density dependent frequency shifts. At ~ 1 μK, inelastic $|ee\rangle$ losses observed in the ^{87}Sr system [46] must be p-wave because the $|ee\rangle$ two-atom state is symmetric under exchange. At the same time, in an optical clock based on ^{171}Yb atoms at ~ 10 μK, p-wave interactions were reported to lead to two-body losses and density shifts [85, 86].

To measure atom loss from $|e\rangle$, atoms are excited on the $|g\rangle$ to $|e\rangle$ transition prior to lattice hold time with a resonant π pulse from an ultrastable laser co-propagating with the lattice beam. The ultrastable laser is polarized along the quantization axis made by an applied magnetic field (π-polarized). The remaining $|g\rangle$ atoms are removed with a 5 ms pulse of 461 nm light.

Measured loss from $|g\rangle$ is well represented by exponential decay with a lifetime of $7 - 8$ s, consistent with loss due to collisions with background gas. In contrast, we measure a rapid,

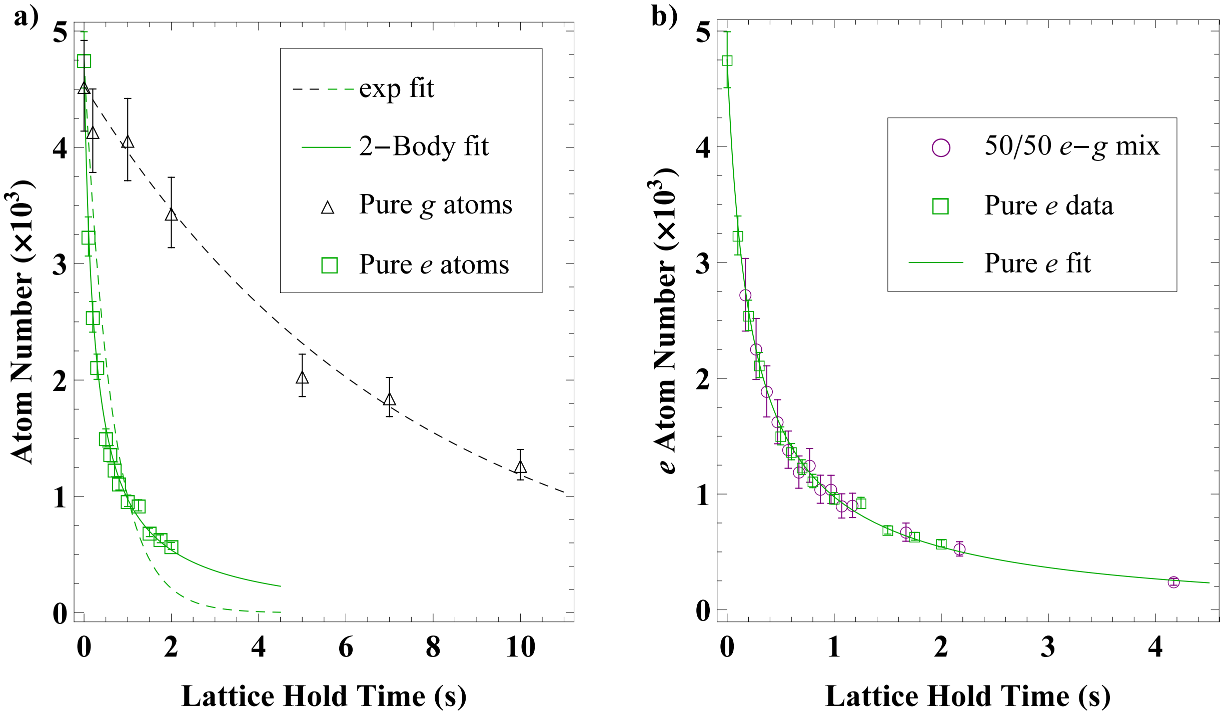

Figure 3.6: a) Atom number as a function of lattice hold time for atoms prepared in $|g\rangle$ (black triangles) and in $|e\rangle$ (green squares). Fits to the decay curves are calculated for the case of exponential decay (dashed lines). The solid line is a fit to the $|e\rangle$ atom decay using a sum over decays in single lattice sites [Eqn. 3.10]. b) Comparison of $|e\rangle$ atom decay in the presence of an equal population of $|g\rangle$ atoms (purple circles) to that of a pure population of $|e\rangle$ atoms (green squares). Here, temperature is 3.5 μK. Reproduced from [46].

density-dependent loss from $|e\rangle$ that is inconsistent with a simple exponential decay law. Fig. 3.6 a) shows measured atom number as a function of lattice hold time for polarized samples of $|g\rangle$ and $|e\rangle$ atoms under similar temperature and trapping conditions. The additional loss from $|e\rangle$ results from inelastic $|e\rangle$-$|e\rangle$ collisions. Fig. 3.6 b) compares $|e\rangle$ atom decay with and without an equal number of $|g\rangle$ atoms present. Agreement between the two curves in Fig. 3.6 b) limits inelastic $|g\rangle$-$|e\rangle$ collisions to below the sensitivity of our experiment and thus, we neglect them. The decay of $|g\rangle$ atoms in the 50/50 mixture is likewise unperturbed by the presence of $|e\rangle$ atoms.

To quantify loss from $|e\rangle$, we adopt a model that includes both one and two-body losses. The atomic density in $|e\rangle$, n_e, is described by

$$\dot{n}_e = -\Gamma n_e - K_{ee} n_e^2. \tag{3.9}$$

Here, Γ is the one-body loss rate due to collisions with background gas, and K_{ee} is the two-body loss rate coefficient. As in Refs. [87, 88], spatial integration of the solution to Eqn. (3.9) yields an expression for the atom number in a single lattice site as a function of time:

$$N(t) = \frac{N_0 \exp(-\Gamma t)}{1 + [N_0 K_{ee}/(\pi^{3/2}\Gamma w_r^2 w_z)][1 - \exp(-\Gamma t)]}. \tag{3.10}$$

Here, N_0 is the initial atom number in a trap site and w_z (w_r) is the $1/e^2$ radius of the atom cloud in the strongly (weakly) confined direction(s).

For polarized atoms, loss occurs dominantly from inelastic p-wave collisions at microkelvin temperatures. This gives that $K_{ee} = K_p^{\mathrm{ind}}(T)$, where $K_p^{\mathrm{ind}}(T)$ is the loss rate coefficient due to inelastic p-wave collisions between indistinguishable $|e\rangle$ atoms, which depends on temperature, T. For dual spin state atoms, loss can occur from intra-spin-state odd partial wave collisions and from inter-spin-state collisions which can be both even and odd partial waves, limited by temperature. Keeping only s and p-wave contributions, the decay of a single spin state, α, in the presence of another spin state, β, can be written as,

$$\dot{n}_\alpha = -\Gamma n_\alpha - K_p^{\mathrm{ind}}(T) n_\alpha^2 - (K_s^{\mathrm{dist}} + K_p^{\mathrm{dist}}(T)) n_\alpha n_\beta, \tag{3.11}$$

where n_α (n_β) is the density of spin state α (β), and K_l^{dist} is the loss rate coefficient due to l-wave inelastic collisions between distinguishable e atoms. In the case where $n_\alpha = n_\beta = 1/2\, n_e$ the differential equation for the total e state density gives that $K_{ee} = 1/2\, K_s^{\mathrm{dist}} + 3/4\, K_p^{\mathrm{ind}}(T)$, since $K_p^{\mathrm{ind}} = 2\, K_p^{\mathrm{dist}}$ [89, 90].

To compare with experiment, we extract K_{ee} from the decay in total atom number using a fit to a sum of single site decays [Eqn. (3.10)] based on the estimated distribution of atoms. The one-body decay rate is set to $1/7.6$ s^{-1}, the measured value from $|g\rangle$ atom decay. Rate coefficients for dual spin state and polarized atoms at different temperatures are shown in Fig. 3.7. One might expect to measure much greater rate coefficients for dual spin state atoms compared to polarized

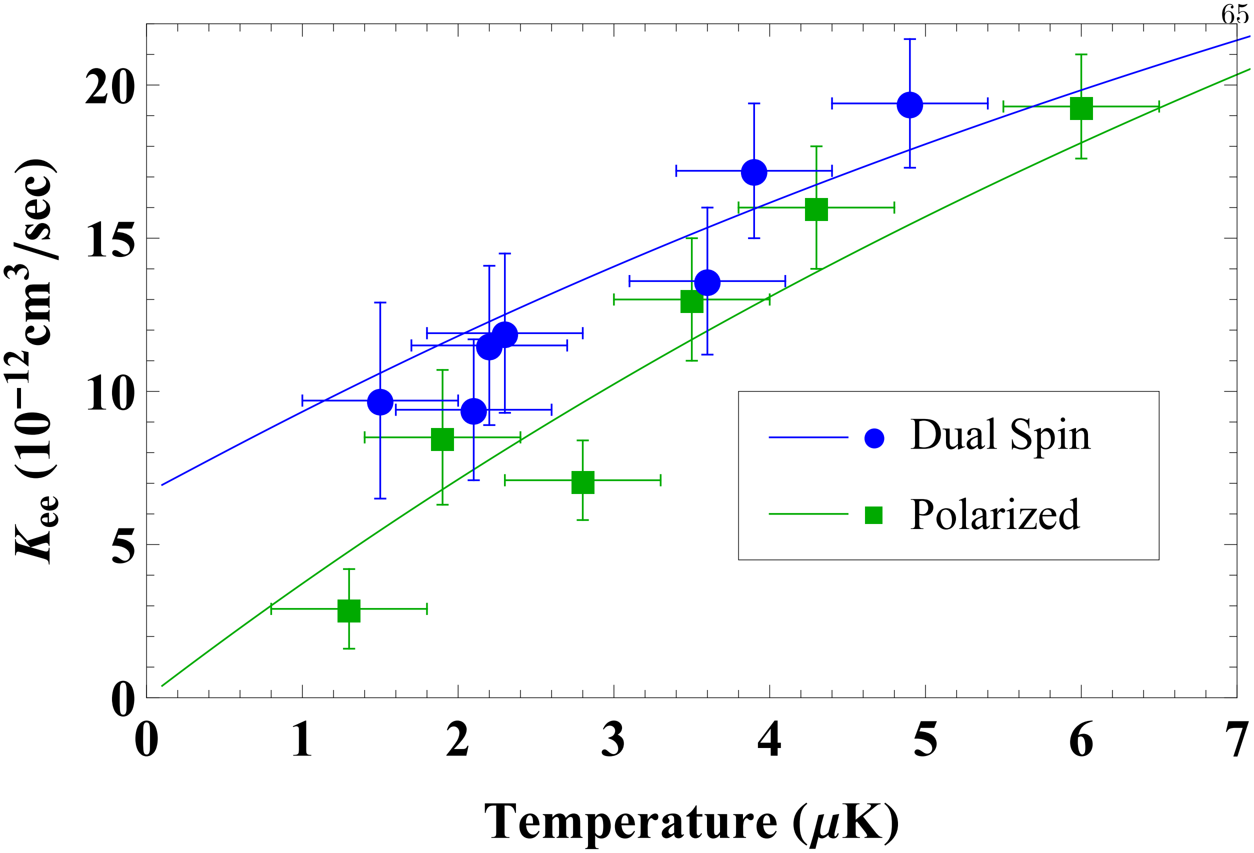

Figure 3.7: Measured two-body loss rate coefficients for polarized and dual spin state atoms as a function of temperature. The vertical error bars are calculated from an uncertainty in atom cloud size associated with a temperature uncertainty of 0.5 μK, a conservative estimation to account for measurement uncertainty and experimental drifts. Solid lines are calculated values for loss rate coefficients (see text). Reproduced from [46].

atoms since p-wave collisions should be suppressed at microkelvin temperatures. Yet, measured loss coefficients for dual spin state atoms are only slightly larger than for polarized atoms at equivalent temperatures.

To understand this result, we perform a time-independent quantum calculation, similar to that in Refs. [91, 92], using a single scattering channel, and a short-range boundary condition at an interatomic separation, $R = R_0$, described by two parameters. A first parameter, δ, represents an accumulated phase-shift from $R = 0$ to $R = R_0$ due to an unknown atom-atom short-range potential of Sr_2. A second parameter, p_{ls}, represents the probability of two atoms to be lost when they encounter at $R = R_0$. These atomic losses are due to couplings that can take place between different electronic potential energy curves of the Sr_2 complex at small R [93, 94, 95, 96]. The release of kinetic energy associated with changes in electronic configurations results in trap loss. The long-range interaction potential between two ^{87}Sr atoms is given by an attractive van der Waals electronic potential. We choose an isotropic C_6 van der Waals coefficient of 5260 a.u. (1 a.u. $= 1\ \mathrm{E_h a_0^6}$, $\mathrm{E_h}$ is the Hartree energy, $\mathrm{a_0}$ is the Bohr radius) for the e-e interaction [97].

The logarithmic-derivative of the scattering wavefunction is computed for each R after giving an initial value at $R = R_0$, which is defined in terms of the two parameters δ and p_{ls}. Using asymptotic boundary conditions at large interatomic distances, we obtain cross sections for a wide range of collision energies. Thermalized loss rate coefficients are calculated by averaging the cross section over a Maxwell-Boltzmann distribution of the relative velocities in three dimensions. Using values of $\delta = 0.9\,\pi$, $p_{\mathrm{ls}} = 0.4$ and $R_0 = 30\ \mathrm{a_0}$ as initial boundary conditions, we were able to simultaneously determine: (i) $K_p^{\mathrm{ind}} = T\times(4 \pm 2)\ 10^{-6}\ \mathrm{cm^3\ s^{-1}\ K^{-1}}$ (ii) and $K_s^{\mathrm{dist}} = (1.4 \pm 0.8)\ 10^{-11}\ \mathrm{cm^3\ s^{-1}}$ for ^{87}Sr atoms, as well as reproduce (iii) K_s^{ind} ($\approx 2 \times 10^{-11}\ \mathrm{cm}^3\ s^{-1}$) and (iv) the elastic cross section ($\approx 7 \times 10^{-12}\ \mathrm{cm}^2$) of indistinguishable bosonic ^{88}Sr e atoms, from previous experimental studies [88]. From a collisional point of view, the loss rate probability at short range $p_{\mathrm{ls}} = 0.4$ indicates that the Sr-Sr system deviates significantly from a high-lossy universal system ($p_{\mathrm{ls}} = 1$) [91, 92] where s-wave collisions are generally two orders of magnitude higher than p-wave collisions [98] at these typical temperatures.

3.6 A new era of precision

After discovering the existence of p-wave two-body loss from the excited state, a new tool in our laboratory allowed us to also uncover a complete picture for the nature of interactions present in our ^{87}Sr clock system. In our previous experiment [17], a strongly interacting regime (*i.e.*, where atom-laser and atom-atom interactions are energetically comparable) was reached by tightly confining the atoms in a 2D optical lattice, at the expense of reducing the occupancy to one or two atoms per site. In our 1D lattice configuration, the average number of atoms per occupied lattice site is ~ 20 and the importance of many-body effects in this system had previously been recognized

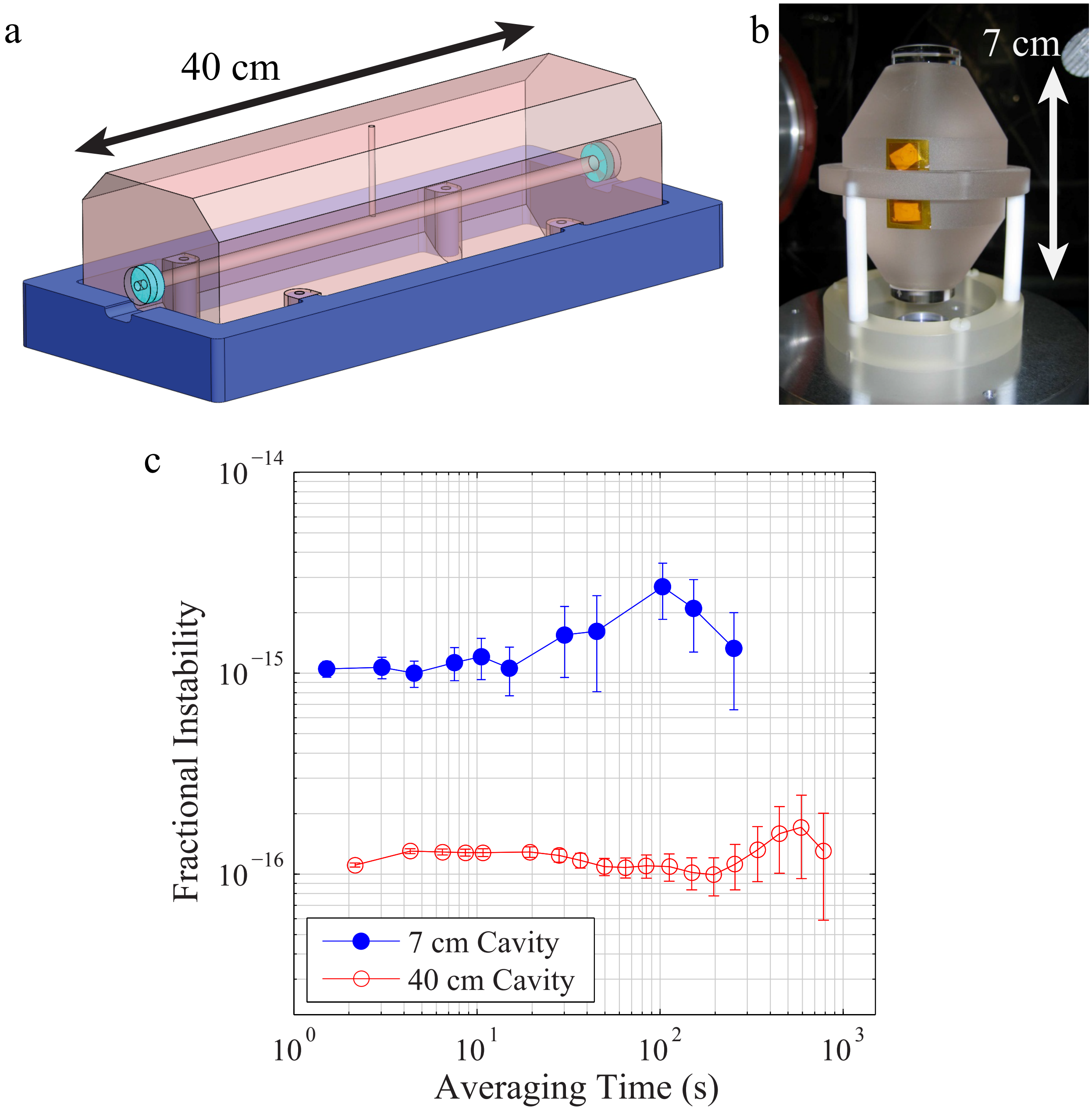

Figure 3.8: (a) a drawing of the new clock laser cavity based on a horizontally mounted 40 cm ULE spacer with fused silica mirrors. (b) a picture of the old clock laser cavity made from a vertically mounted 7 cm ULE spacer with ULE mirrors. (c) The measured thermal noise floor of the two optical reference cavities. The stability of the 7 cm cavity (filled circles) was measured by comparing two cavities of the same design. For the 40 cm cavity (open circles), we determine its frequency stability from a measurement based on the atomic reference. We lock this laser to the ^{87}Sr clock transition and subtract off a residual cavity drift of ~1.4 mHz/s. This data includes contributions from other technical noise and thus represents an upper bound on the thermal noise floor.

theoretically [65, 74, 75]. As we saw earlier, we needed to make interactions more dominant in this system to reveal many-body effects. Since we could not confine the atoms more strongly in a 1D lattice due to the power limitations of our trapping laser, we took a different route.

Instead of making interactions stronger, we are able to make the other relevant energy scale, $\bar{\Omega}$ weaker. In other words, we are able to probe interactions more precisely and over a longer coherence time. This is possible because were are able to extend atom-laser coherence, which was previously limited by laser instability. We will see below that decoherence due to interactions can now limit our system. To improve upon our previous laser, we did not fundamentally change the laser design, rather, current techniques in creating ultrastable lasers were pushed too their limits. The previous laser design (shown in Fig. 3.8b) was limited by thermal noise in the mirrors and optical coating materials (see [8] for a detailed description of thermal noise in optical cavities) to 1×10^{-15} fractional frequency stability at 1 s. Since thermal noise arising from the cavity spacer is much below this limit, by increasing the length of the cavity to 40 cm, the fractional stability should improve proportionally. The limiting factor for this approach is the cavity's sensitivity to vibrations. In order to keep these fluctuations below the thermal noise limit of the cavity, active vibration isolation is used to support the cavity and finite element analysis of the mounting points was used to locate the support points that would lead to the greatest vibration insensitivity [8]. Furthermore, mirrors for the new cavity were made from fused silica glass, which have a thermal noise limit roughly two times lower than the ultra-low-expansion (ULE) glass that was used in the previous design. The final design of the new clock laser is shown in Fig. 3.8a and we find that its stability is near the thermal noise limit of $\sim 1 \times 10^{-16}$ (Fig. 3.8c).

This factor of 10 increase in stability translates into a factor of 100 gain in averaging time for measuring systematic shifts of the clock transition since these measurements average down proportional to the square root of the averaging time for Gaussian noise. Fig. 3.9 simultaneously demonstrates the increased precision of the new laser through the sub Hz lines shapes that we are able to reliably scan with 2 s long π pulses in Rabi spectroscopy as well as the subtle interaction effects that we are able to resolve. Fig. 3.9a clearly shows an asymmetric side-bump on the lower

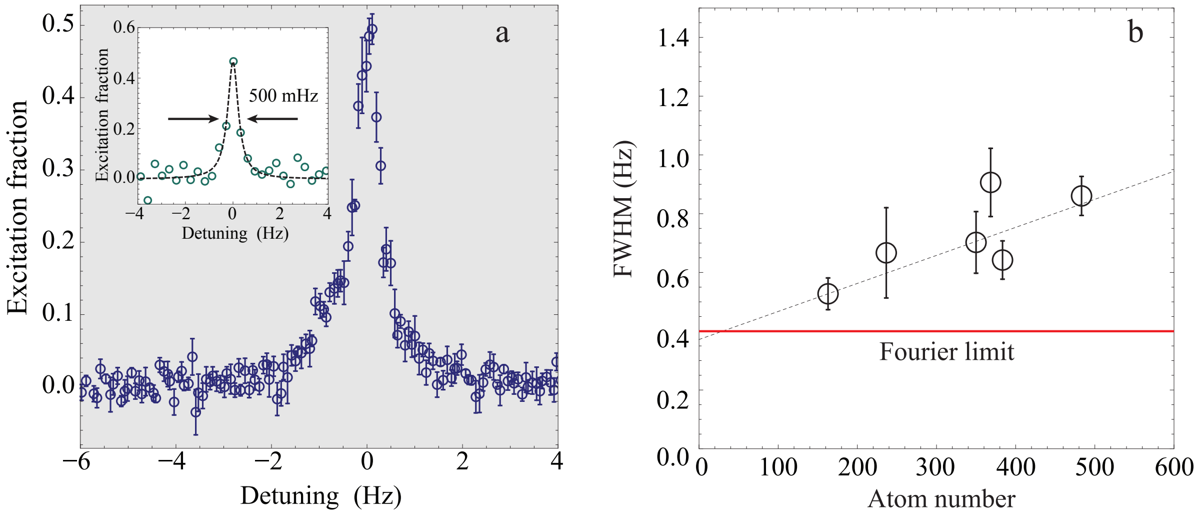

Figure 3.9: Interaction effects visible at the sub-Hz energy scale. (a) Composite lineshape obtained at an operating density of $0.1\rho_0$ with a 2 s π pulse, where ρ_0 is the density obtained for 5×10^3 atoms, and is given by $\rho_0 = 5(2) \times 10^{11}$ cm^{-3}. The line shape shows a clear distortion due to the density-dependent interaction at the sub-Hz energy scale. (Inset) Extremely low density scan ($\rho = 5 \times 10^{-2}\rho_0$) with a 3 s clock probe, demonstrating the ultimate frequency resolution of the system. This is a single scan thus no binning or averaging was applied. (b) measured linewidth as a function of atom number in the low-density regime for the scans compiled to create the figure at left. As seen from the data, the density-dependence of the linewidth extrapolates to the 0.4 Hz Fourier limit for the 2 s Rabi pulse used.

frequency tail of the resonance and we see in Fig. 3.9b that the fitted FWHM approaches the Fourier limit as atom number tends to 0. It is exactly this capability to examine interactions at a new level of precision that enable the following work of this chapter.

3.7 Confirmation of p-wave interactions

To determine the interaction parameters that characterize our spin Hamiltonian, Eqn. 3.8, we measure the density-dependent frequency shift of the clock transition using a modified Ramsey spectroscopy sequence. The initial pulse area $\theta_1 = \Omega T_R$, chosen such that $0 < \theta_1 < \pi$, controls the initial value of $\langle \hat{S}^z_{\text{tot}} \rangle$. Here, $\hat{S}^z_{\text{tot}}$ is the sum of $\hat{S}^z$ over the hundred relevant lattice sites, such that $-N_{\text{tot}}/2 \leq \langle \hat{S}^z_{\text{tot}} \rangle \leq N_{\text{tot}}/2$, where N_{tot} is the total number of atoms loaded into the lattice. In the presence of two-body losses, $\langle \hat{S}^z_{\text{tot}} \rangle$ is not constant, thus we use its time average, $\overline{\langle \hat{S}^z_{\text{tot}} \rangle}$, to compare with theory. Here, we extract $\overline{\langle \hat{S}^z_{\text{tot}} \rangle}$ from independent measurements periodically inserted into the clock sequence. The duration of the dark time, τ_{dark}, is fixed at 80 ms and the final pulse area is set to $\pi/2$. We measure the shift by modulating the density by a factor of ~ 2 (Fig. 3.10).

Simple mean-field analysis of Eqn. 3.8 (neglecting cubic terms and losses), where the time-dependent operators are replaced by their expectation values, reveals that the average interaction experienced by a single atom behaves as an effective magnetic field along $\hat{z}$, $B(N) = NC + 2\chi\langle \hat{S}^z \rangle$, where $\langle \hat{S}^z \rangle = -(N/2)\cos\theta_1$. The mean-field density-dependent frequency shift $\Delta\nu(N) = B(N)/(2\pi)$ scales linearly with the excitation fraction and agrees with experimental observations (Fig. 3.10). Additionally, we fit an exact solution of Eqn. 3.8 to the data. Both fits are shown in Fig. 3.10. To compare with the experiment, we always perform an average over the atom number distribution across the lattice sites. From this measurement we extract $\chi = 2\pi \times 0.20(4)$ Hz and $C = -0.3\chi$. In contrast, predictions based on pure s-wave interactions predict that when the final pulse area is $\pi/2$ the shift is exactly 0 [74].

As a further step, we directly measure the spectrum of the many-body Hamiltonian with sub-Hz spectral resolution as a function of interaction strength in Fig. 3.11A (parameterized by atom number) and as a function of $\bar{\Omega}$ in Fig. 3.11B (parameterized by the π pulse time). We find that for $\Omega \gg N\chi$, the line shapes are perturbatively shifted. However, for $\Omega \sim N\chi$, the line shapes become significantly distorted and the onset of an interaction blockade mechanism is observed, reflecting the dominant effect of strong interactions on the many-body spectrum. The observed Rabi line shapes can be fully reproduced with the mean field treatment using the interaction parameters extracted from the density shift measurements. Here, a full many-body treatment of the master equation agrees with the mean-field predictions.

3.8 Beyond the mean field

To explore the development of many-body correlations during the full many-body dynamical evolution, we measure the Ramsey fringe contrast, which can undergo a periodic series of collapses and revivals, reflecting the quantized structure of the many-body spectrum. The results require a

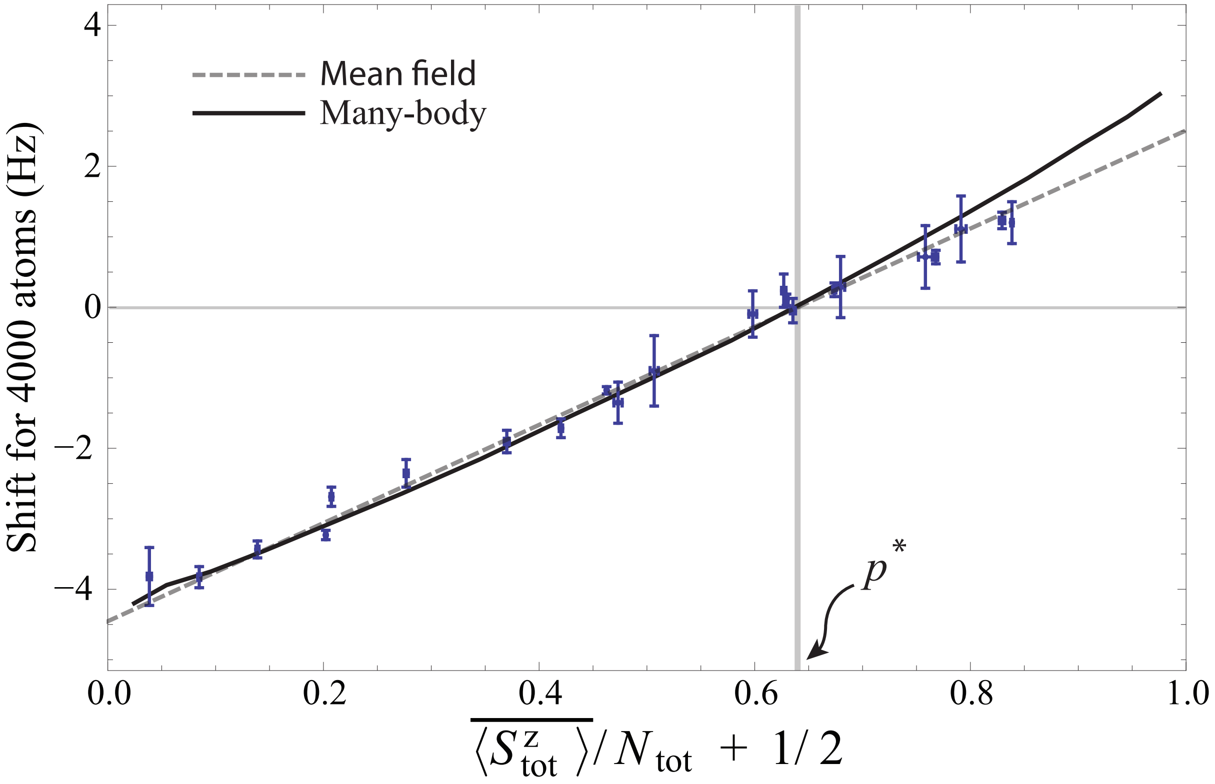

Figure 3.10: Density shifts versus excitation fraction in Ramsey spectroscopy fit with the full many-body solution. Because of the perturbative nature of this measurement, the mean-field approximation (dashed line) to the many-body theory agrees well with the data. The exact many-body solution in the absence of losses (solid curve) agrees best with the data only for lower values of total average spin $\overline{\langle \hat{S}^{z}_{\mathrm{tot}} \rangle}/N_{\mathrm{tot}}$ because of the nonlinear $\overline{(S^z)^3}$ term in the Hamiltonian. The zero crossing occurs at an average excitation fraction, given by $\overline{\langle \hat{S}^{z}_{\mathrm{tot}} \rangle}/N_{\mathrm{tot}} + 1/2$, of $p^* = 0.64(1)$. From the zero crossing and the measured slope we extract χ and C. Reproduced from [4].

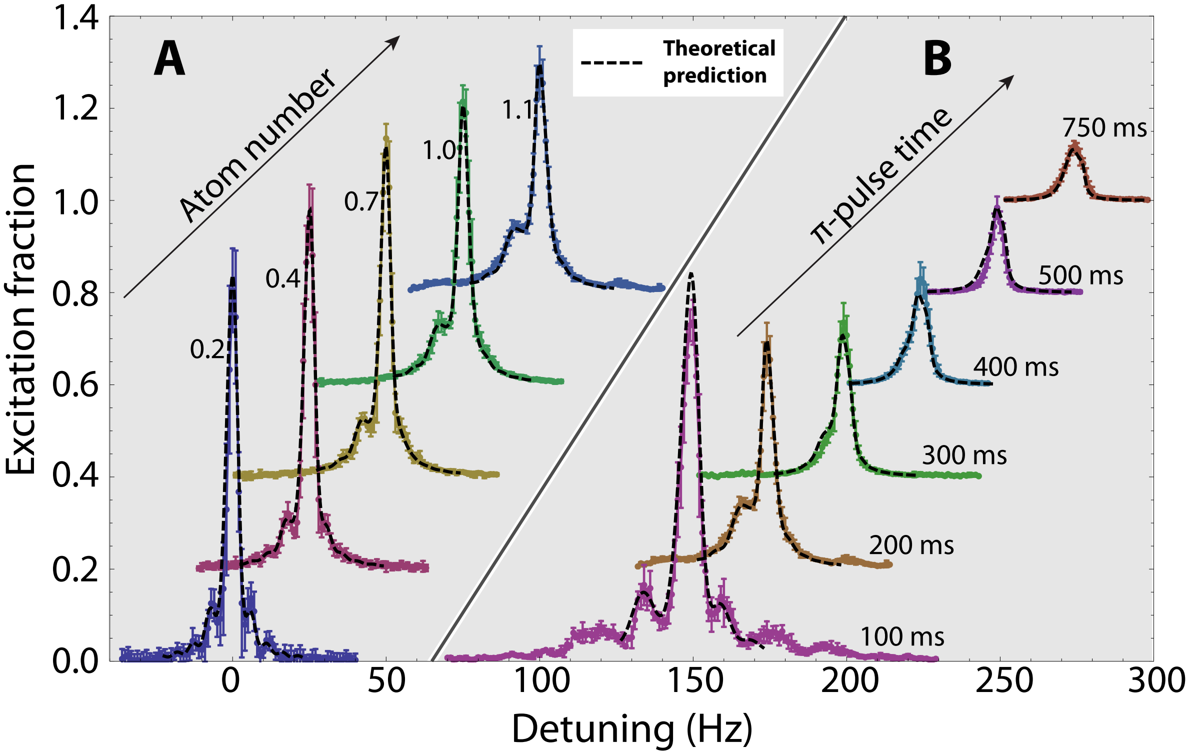

Figure 3.11: Measured line shapes compared to theory as a function of density and Rabi frequency. Each curve is a composite of multiple scans that have been centered atop one another and the data subsequently binned. The curves are offset in both the vertical and horizontal directions for visual clarity. (A) Line shape as a function of density (normalized by $\rho_0 = 5(2) \times 10^{11}$ cm^{-3} the density obtained for 5×10^3 atoms), with a π pulse time of 200 ms. (B) Lineshape for $\rho \simeq \rho_0$ as a function of π pulse time. In both (A) and (B), theoretical curves, obtained with the mean-field treatment including loss, are shown as dashed black lines and agree well with the measurements. Reproduced from [4].

beyond-mean field treatment. The mean-field model at the single-site level (with fixed N) predicts no decay of the Ramsey fringe contrast because, when correlations are neglected, the interactions lead only to a pure precession of the collective Bloch vector [4]. By taking the average over atom distributions among lattice sites and properly treating two-body loss during the Ramsey dark time, the mean-field model does show a decay of the contrast. However, this decay is associated mainly with dephasing arising from different precession rates exhibited by sites with different N.

For the Ramsey sequence designed to measure the fringe contrast effects, the pulse durations are < 6 ms, satisfying $\Omega \gg N\chi$, to suppress interaction effects during the pulses. We apply the final $\pi/2$ readout pulse with a variable relative optical phase of $0^\circ - 360^\circ$ and record the fraction of excited atoms as a function of the readout phase. The contrast of the resulting fringe is extracted in a manner that is insensitive to the frequency noise of the ultrastable clock laser. For a first pulse of area θ_1, we allow the system to evolve for time τ. We then apply a final pulse of area $\pi/2$ and measure the resulting excitation fraction as a function of the optical phase of the second pulse relative to the first pulse. For $\tau \gtrsim 100$ ms, there is a significant additional random phase added due to the frequency fluctuations of the ultrastable clock laser. A given excitation fraction (p_i) measurement will yield $p_i = \mathcal{C}\sin^2(\Delta\phi_i)$, where $\mathcal{C}$ is the contrast and $\Delta\phi_i$ is the ith realization of the both deterministically and randomly varied phase. By analyzing $\mathrm{Var}(p) = \mathcal{C}^2/8$, and assuming a uniform distribution of $\Delta\phi_i$, we obtain the contrast in a way that is insensitive to the laser noise.

We explore three distinct experimental conditions to rule out single-particle decoherence mechanisms and thoroughly test the model. The first condition represents the typical operating parameters of the lattice clock, with $N_{\text{tot}} = 4 \times 10^3$ and $\nu_Z = 80$ kHz. In the second case, we reduce the lattice intensity such that $\nu_Z = 65$ kHz, which results in a reduction of the density by a factor of ~1.8. Finally, we maintain $\nu_Z = 80$ kHz but reduce the atom number to $N_{\text{tot}} = 1 \times 10^3$. Under all conditions, the full many-body density matrix model reproduces the experimental observations well (Figs. 3.12A, 3.12C, and 3.12E). The inclusion of the $(\hat{S}^z)^3$ correction improves the theory-experiment agreement, especially for pulse areas $\theta_1 > \pi/2$ and for the high-density conditions [4]. We also observe a striking breakdown of the mean-field model for $\theta_1 > \pi/2$ where many-body corrections are dominant (Figs. 3.12B, 3.12D, and 3.12F).

3.9 Observing quantum correlations

The frequency shift, lineshape, and Ramsey fringe contrast are quantities that all depend on the first-order expectation values of the spin operators $\langle \hat{S}^{x,y,z} \rangle$. We now turn our attention to the distribution of quantum noise, which depends on the second-order moments of the spin operators, *e.g.*, $\langle \left(\hat{S}^x\right)^2 \rangle - \langle \hat{S}^x \rangle^2$, $\langle \hat{S}^x\hat{S}^z + \hat{S}^z\hat{S}^x \rangle - 2\langle \hat{S}^x \rangle \langle \hat{S}^z \rangle$, etc. Given that the form of the Hamiltonian in

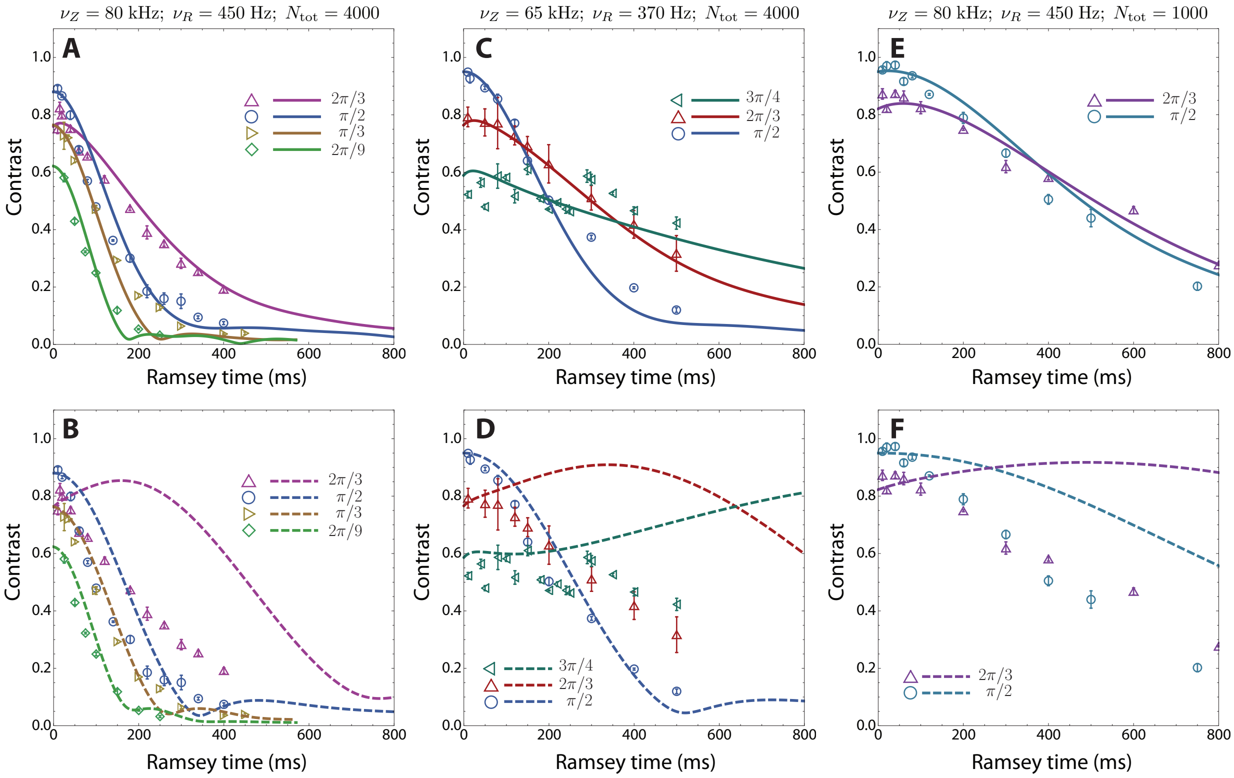

Figure 3.12: Ramsey fringe contrast decay for varying initial pulse areas and experimental conditions. The pulse area values for the data and corresponding theory are given in the legends of the plots. Error bars represent the statistical error of each contrast measurement, and thus do not account for systematic drifts that occur over the course of the experiment. The solid lines (top panels) are the many-body calculations, while the dashed lines (bottom panels) are using the mean-field approximation of the theory. The many-body model and the mean-field approximation agree in the limit of small initial pulse area (*i.e.*, Bloch vector polar angle), but disagree for pulse areas $> \pi/2$. This is an important confirmation of the dominance of many-body effects in this parameter regime. (A, B) $\nu_Z = 80$ kHz, $\nu_R = 450$ Hz, and $N_{\rm tot} = 4000$; (C, D) $\nu_Z = 65$ kHz, $\nu_R = 370$ Hz, and $N_{\rm tot} = 4000$; and (E, F) $\nu_Z = 80$ kHz, $\nu_R = 450$ Hz, and $N_{\rm tot} = 1000$. Reproduced from [4].

Eqn. 3.8 is known to produce squeezed and entangled states [99], the distribution of the spin noise becomes a compelling measurement to probe many-body correlations beyond the mean field.

To minimize single particle dephasing effects (for example, arising from the distribution of site occupancies), we add a spin-echo pulse to the Ramsey sequence. As a result, the sensitivity to low-frequency laser noise is reduced at the expense of increased sensitivity to high-frequency laser noise. With atoms initialized in $|g\rangle$, we follow the pulse sequence (Fig. 3.13) to manipulate and measure the spin noise of the many-body state. For each value of the final rotation angle, representing a specific quadrature in which we measure the spin noise, we repeatedly record $\langle\hat{S}^z_{\text{tot}}\rangle/N_{\text{tot}}$ via measurements of the final atomic excitation fraction after the Ramsey sequence. From the data, we determine $\sigma^2 \equiv \langle\left(\hat{S}^z_{\text{tot}}\right)^2\rangle/N^2_{\text{tot}} - \langle\hat{S}^z_{\text{tot}}\rangle^2/N^2_{\text{tot}}$ by analyzing the pair variance for successive measurement of $\langle\hat{S}^z_{\text{tot}}\rangle/N_{\text{tot}}$. We note that the quantum limit of σ^2 is important for defining the ultimate stability of lattice clocks [1]. For an ideal coherent spin state of the entire ensemble, the standard quantum limit (SQL) of σ^2 is given by $\sigma^2_{\text{sql}} = p\left(1-p\right)/N_{\text{tot}}$, where p is the probability of finding an atom in the excited state, and can be estimated as $p = \langle\hat{S}^z\rangle/N_{\text{tot}} + 1/2$.

We perform measurements for different N_{tot} and τ_{dark}, the total atom number and Ramsey free evolution time, respectively, to probe the time evolution of the spin noise distribution. Long π pulses are used to reduce the sensitivity to spurious high-frequency components of laser noise. For $N_{\text{tot}} = 1 \times 10^3$, the quantum noise contribution to the spin noise is comparable to that of the laser noise (Fig 3.13). However, with $N_{\text{tot}} = 4 \times 10^3$, the laser noise is responsible for a larger fraction of the noise in repeated measurements of $\langle\hat{S}^z\rangle$.

There are qualitative differences between the low and high atom number cases; for example, for $N_{\text{tot}} = 4 \times 10^3$ with $\tau_{\text{dark}} = 20$ ms and 40 ms, we observe a phase shift for the minimum of the spin noise. To compare the predictions of the full many-body master equation with the experiment, we add the effect of laser noise in quadrature with the calculated spin quantum noise. In the absence of laser noise, the theory predicts a small degree of sub-SQL squeezing. This effect is masked by laser noise in both the theoretical prediction for the total spin noise and in our experimental observations, but gives rise to a shift of the spin noise minimum with respect

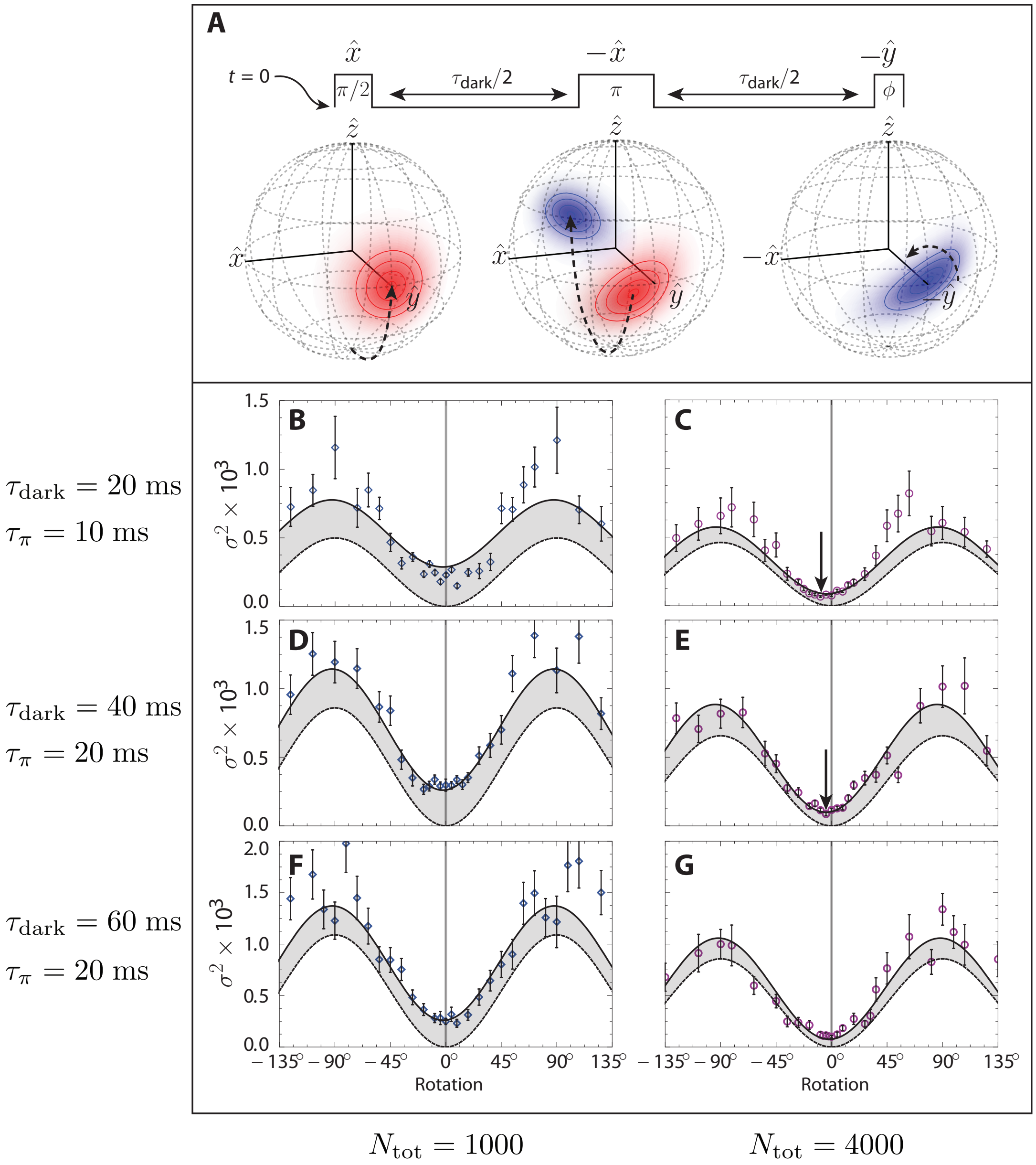

Figure 3.13: Spin noise vs. quadrature. (A) An initial pulse prepares a coherent state along $\hat{y}$, which then evolves for $\tau_{\text{dark}}/2$. An echo pulse then rotates the many-body state 180° about $-\hat{x}$. After an additional evolution time of $\tau_{\text{dark}}/2$, a final pulse rotates the state about $-\hat{y}$ and the spin noise is measured. The π pulse has duration τ_{π}. The many-body state depicted here represents the spin evolution of a 20 atom ensemble in a single trap site with $\tau_{\text{dark}} = 40$ ms. To remove spurious effects due to slow drifts in atom number, the data is processed as detailed in Appendix C, in order to remove the potential bias. For panels (B–G), the dashed line is the pure laser noise extracted from a fit to the data. The solid line is the laser noise plus the full many-body prediction of the spin noise. This full theory is simultaneously fit to both the low and high atom number curves to extract the laser noise for a given dark time. Vertical arrows indicate significantly phase-shifted minima in the experimentally measured spin noise, consistent with the predictions of the many-body theory. π pulse times and τ_{dark} values are indicated at left, and total atom number is indicated at bottom. Reproduced from [4].

to measurement quadrature. We additionally treat the effects of interactions during the laser pulses. The theory predicts the direction and magnitude of the phase shift of the noise minimum in agreement with the experimental observations (Fig. 3.13), in addition to significantly enhanced spin noise for rotations near ±90°. Despite the presence of laser noise, the measurements of the total spin noise are consistent with the many-body spin model.

3.10 Conclusions

In this chapter we introduced the theoretical model that serves as the basis for modeling our open many-body quantum system. We showed how the extreme precision provided by our new clock laser allowed us to confirm the validity of this model and the *p*-wave nature of interactions by measuring the density-dependent frequency shift of the ^{87}Sr clock transition under various experimental conditions with Ramsey spectroscopy. We demonstrated the importance of the many-body behavior of our system through the decay of contrast in Ramsey spectroscopy and found evidence for interaction induced quantum correlations by examining the quadrature dependence of noise. We also detailed the long road we took to reach these results, with several experimental results that were originally explained in terms of only *s*-wave interactions. In the following chapter we further expand upon these experimental investigations and the theoretical model used to describe them by using different combinations of nuclear spin states to explore quantum magnetism in a system with $SU(N)$ symmetry.

Chapter 4

Exploring two-orbital SU(N) magnetism with ^{87}Sr atoms

4.1 Introduction

Symmetries play a fundamental role in physical systems. A very prominent theme in recent theoretical and experimental investigations is the role of SU(N) symmetry as the source of the defining features of rich quantum systems. The archetypical example of this is how the SU(3) symmetry of quantum chromodynamics governs the behavior of quarks and gluons. Generalizing this symmetry to large N is expected to generate exotic many-body behaviors emerging from the increased degeneracy and strict conservation laws. Alkaline-earth(-like) atoms prepared in the two lowest electronic states (clock states with zero electronic angular momenta) are predicted to exhibit nuclear spin (I) independent inter-atomic collisions, owing to strong decoupling between the electronic-orbital and nuclear-spin degrees of freedom [100, 84]. This property directly leads to a SU($N \leq 2I+1$) symmetry for the interaction physics [101, 102, 103, 104]. This symmetry, along with their use as ideal time keepers [2] and quantum information processors [105, 106, 107], is responsible for alkaline earth atoms emerging as a unique platform for the investigation of high-energy lattice gauge theories [108], for testing iconic orbital models used to describe transition metal oxides, heavy fermion compounds, and spin liquid phases [109], and for the observation of exotic topological phases [104, 110]. Progress towards these goals includes the production of quantum degenerate gases for calcium [111] and all stable isotopes of strontium and ytterbium [112, 113], the capability of imaging individual spin components via optical Stern-Gerlach methods [114], and control of interactions with optical Feshbach resonances [112, 115, 116]. Furthermore, we have just described how many-body spin dynamics have been studied directly in our ^{87}Sr system in the previous chapter (also, see Ref. [4]).

However, thus far evidence for the existence of SU(N) symmetry in alkaline-earth(-like) atoms has been indirect, including inference from suppressed nuclear spin-relaxation rates [114], reduced temperatures in a Mott insulator for increased number of spin states [117], and the changing character of a strongly-interacting one-dimensional fermionic system as a function of N [118]. Moreover, these observations are limited to the electronic ground state. The corresponding ground-state s-wave scattering parameter, a_{gg}, has been determined from photo-association [119] and ro-vibrational spectroscopy [120], but the excited state-related scattering parameters remain unknown.

In this chapter, we describe the first spectroscopic observation of SU(N) symmetric interactions and two-orbital SU(N) magnetism in an ensemble of fermionic ^{87}Sr atoms at μK temperatures. For this work, our ^{87}Sr atoms confined in an array of two-dimensional (2D) disc-shaped, state-insensitive optical traps created by a one-dimensional(1D) optical lattice (See Ch. 1 or Ref. [25]). The axial ($\hat{z}$) trapping frequency ω_z is $\sim 2\pi \times 80$ kHz and the radial ($\hat{x}$ and $\hat{y}$) frequency $\omega_x = \omega_y \equiv \omega_r$ is $\sim 2\pi \times 600$ Hz. Axial and radial degrees of freedom are decoupled during the initial lattice loading and cooling. Under typical temperatures ($1\ \mu\text{K} < T_r < 7\ \mu\text{K}$, $T_z \sim 2\ \mu$K), atoms are cooled to the motional ground state along the $\hat{z}$ direction. On the contrary, the radial modes are thermally populated. The SU(N) symmetric spin degree of freedom is encoded in the 10 nuclear spin states with quantum number m_i (Fig. 4.1A), and the pseudo-spin $1/2$ orbital degree of freedom in the two lowest electronic (clock) states ^{1}S$_0$ ($|g\rangle$) and ^{3}P$_0$ ($|e\rangle$). Under typical atomic occupancies (≤ 20 atoms per disc), temperatures and trap volume ($\propto T_r$), the mean interaction energy per particle is at least two orders of magnitude smaller than the single-particle vibrational spacing along any direction. The unprecedented spectral resolution available with an ultra-stable laser of 1×10^{-16} fractional frequency stability [1] enables us to accurately probe these interactions while addressing individual nuclear spin levels.

4.2 Expanding the spin model: an SU(N) symmetric spin-orbital Hamiltonian

Under our operating conditions the atomic interactions are insufficiently energetic to transfer atoms between the initially populated, slightly anharmonic motional eigenmodes. To the first order approximation, atoms remain frozen in these quantized motional levels and the quantum dynamics takes place only in the internal degrees of freedom (spin and orbital angular momenta) [4, 66, 67], in a way analogous to localized atoms in real-space lattice trapping potentials. This approximation greatly simplifies the modeling of our system. Here, the large energy gap between the interaction energy and the single-particle vibrational spacing, along with the anharmonicity and non-separability of the optical trapping potential provided by the Gaussian laser beam profile, lead to an energetic suppression of mode-changing collisions [66, 5]. Moreover, the s-wave and p-wave (Fig. 4.1B) interactions, which are responsible for the dynamics, provide nonlocal interactions when viewed within the energy-space lattice as they couple atoms without being overly sensitive to the thermally populated motional levels. The decoupling between motional and internal degrees of freedom combined with the sub-Hertz spectral resolution of the stable laser allows us to probe spin lattice models with effective long-range couplings in a non-degenerate Fermi gas, as schematically illustrated in Fig. 4.1C. This system thus paves the way for study of quantum orbital magnetism beyond the ultra-cold regime.

Spin models with long-range interactions have been implemented in dipolar gases [121] or trapped ionic systems [122], but our system is further enriched by SU(N) symmetry and holds potential for addressing important open questions on many-body dynamics in spin-orbital models [109, 123] under the co-presence of large degeneracy [124] and long-range interactions. By performing Ramsey spectroscopy with various nuclear spin mixtures, we determine the nuclear spin independence of the s-wave and p-wave interactions. Furthermore, we probe the non-equilibrium dynamics of the orbital coherence, and the results are well reproduced by a two-orbital SU(N) spin lattice model in quantized motional eigenenergy space.

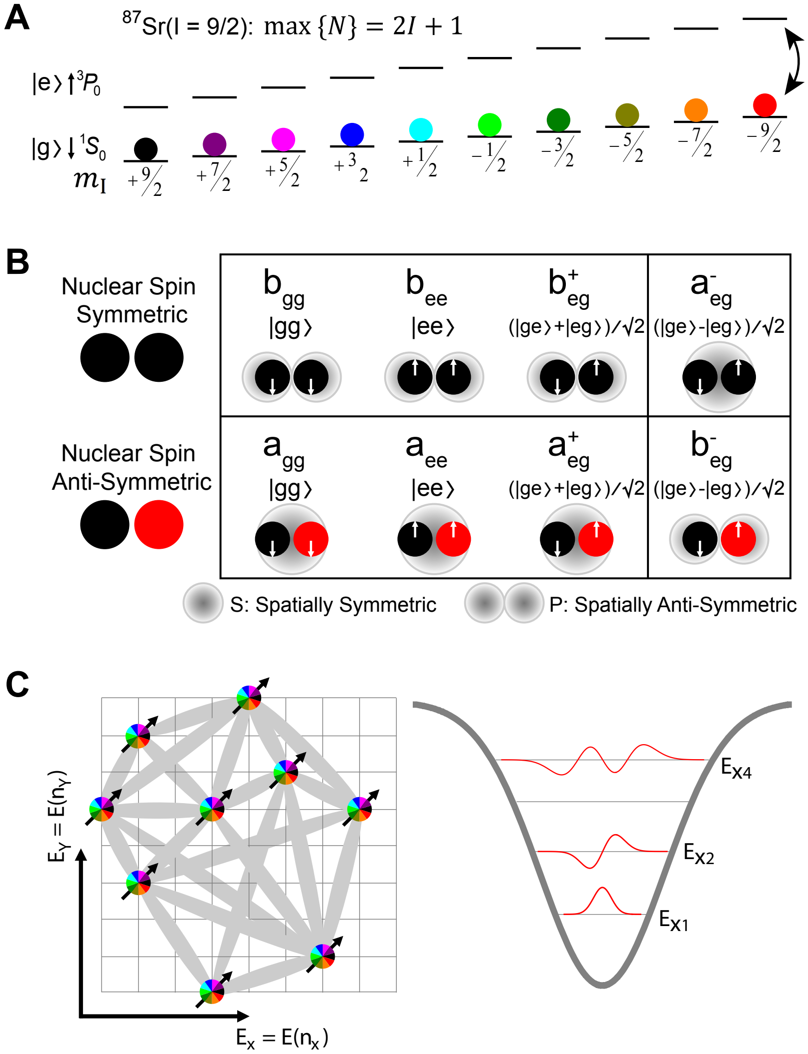

Figure 4.1: Diagram of the interacting spin lattice. (A) Energy levels for the two lowest electronic states ($^1S_0$ and $^3P_0$) of ^{87}Sr atoms in a magnetic field, each with ten nuclear spin states, depicted by colors. This color scheme is used throughout the chapter to denote the interrogated state. (B) Interactions between two fermionic atoms characterized by four s-wave ("a") and four p-wave ("b") elastic scattering parameters. The interactions are governed by symmetries in motional states (bottom labels), nuclear spins (left labels), and electronic orbitals (white arrows). (C) (Left panel) Schematics of the interacting electronic orbitals (spin-$1/2$ arrows) distributed over a lattice spanned by motional eigenenergies; the energy levels are populated according to a Boltzmann distribution. In our system the energy spacings are slightly anharmonic, which is crucial for energetically suppressing the mode-changing collisions and freezing atoms in their initially populated motional modes; for simplicity neither the anharmonic lattice spacing, nor the Boltzmann population of modes are reflected in the schematic representation of the energy space lattice. The gray connections signify the long-range nature of the interactions in energy space. Those interactions are calculated according to the matrix element overlap of the corresponding modes [66, 5]. To the first order approximation, p-wave interactions can be treated collectively and can be assumed to be of all-to-all type. Thus we can replace the values of the coupling constants with their thermal averages [66]. Colored circles show the possibility of preparing statistical mixtures of N nuclear spin states. (Right panel) Illustration of a few occupied eigenmodes in our optical trap formed by a Gaussian beam. Reproduced from [5].

Interactions between two ^{87}Sr atoms are governed by Fermi statistics that require overall wavefunction anti-symmetrization under exchange in the motional, electronic, and nuclear spin degrees of freedom (Fig. 4.1B). Consider a pair of interacting atoms (j and k) occupying two eigenmodes of the trapping potential, $\mathbf{n}_j$ and $\mathbf{n}_k$. Atoms in a nuclear spin symmetric state experience s-wave interactions only if their electronic state is anti-symmetric: $(|eg\rangle - |ge\rangle)/\sqrt{2}$. The elastic scattering length characterizing these collisions is a_{eg^-}. Atoms collide via p-wave interactions in the three possible electronically symmetric configurations $\{|gg\rangle, |ee\rangle, (|eg\rangle + |ge\rangle)/\sqrt{2}\}$, corresponding to the p-wave elastic scattering volumes b^3_{gg}, b^3_{ee} , and $b^3_{eg^+}$, respectively. In contrast, atoms in an anti-symmetric nuclear spin configuration experience s-wave collisions in the three electronically symmetric configurations, with the corresponding scattering lengths a_{gg}, a_{ee} , and a_{eg^+}, respectively. Accordingly, p-wave interactions occur in $(|eg\rangle - |ge\rangle)/\sqrt{2}$, corresponding to the scattering volume $b^3_{eg^-}$. These eight parameters characterize elastic collisions at ultracold temperatures, and SU(N) symmetry predicts them to be independent of the nuclear spin configuration.

The Hamiltonian that governs these interactions can be written in terms of orbital-spin 1/2 operators $\hat{T}^{x,y,z}_{\mathbf{n}_j}$ acting on the j^{th} atoms electronic state, $\{|g\rangle, |e\rangle\}$, and in terms of nuclear-spin permutation operators $\hat{S}^{\beta}_{\alpha}(\mathbf{n}_j)$, acting on the j^{th} atoms nuclear spin levels, $\alpha, \beta \in \{1, 2, ..., N\}$ as:

$$\hat{H} = (\hat{\mathcal{P}}^{+}\hat{H}^{+} + \hat{\mathcal{P}}^{-}\hat{H}^{-}), \qquad \text{and} \tag{4.1}$$

$$\hat{H}^{\pm} = J^{\pm}_{\mathbf{n}_j,\mathbf{n}_k}\vec{T}_{\mathbf{n}_j} \cdot \vec{T}_{\mathbf{n}_k} + \chi^{\pm}_{\mathbf{n}_j,\mathbf{n}_k}\hat{T}^{z}_{\mathbf{n}_j}\hat{T}^{z}_{\mathbf{n}_k} + C^{\pm}_{\mathbf{n}_j,\mathbf{n}_k}\left(\frac{\hat{T}^{z}_{\mathbf{n}_j} + \hat{T}^{z}_{\mathbf{n}_k}}{2}\right) + K^{\pm}_{\mathbf{n}_j,\mathbf{n}_k}\hat{\mathbb{I}}. \tag{4.2}$$

Here, $\hat{\mathbb{I}}$ is the identity matrix, $\hat{\mathcal{P}}^{\pm} = \frac{\left[\hat{\mathbb{I}} \pm \sum_{\alpha,\beta} \hat{S}^{\alpha}_{\beta}(j)\hat{S}^{\beta}_{\alpha}(k)\right]}{2}$ are nuclear spin projector operators into the symmetric triplets (+) and anti-symmetric singlet (−) nuclear spin states, respectively. Eq. 4.2 states that if the nuclear spin of the atoms is in (+) or (−), then they interact according to $\hat{H}^{+}$ or $\hat{H}^{-}$, respectively. The coupling constants $J^{\pm}_{\mathbf{n}_j,\mathbf{n}_k}$, $\chi^{\pm}_{\mathbf{n}_j,\mathbf{n}_k}$, $C^{\pm}_{\mathbf{n}_j,\mathbf{n}_k}$, and $K^{\pm}_{\mathbf{n}_j,\mathbf{n}_k}$ depend on the interaction matrix elements $U^{\eta}_{\mathbf{n}_j,\mathbf{n}_k}$ and $V^{\eta}_{\mathbf{n}_j,\mathbf{n}_k}$, which are determined from the fundamental scattering parameters, a_{η} and b_{η}, $\eta \in \{ee, gg, eg^{+}$ and $eg^{-}\}$, and the wavefunction overlap of the j and k^{th} atoms radial vibrational modes (See Appendix B) in the 2D traps. The Hamiltonian commutes with all the SU(N) generators, $\hat{S}^{\beta}_{\alpha}(j)$, and is thus invariant under transformations from the SU(N) group (i.e., SU(N) symmetric). This implies that the number of atoms in each of the nuclear spin sublevels is conserved. Here, N is chosen by the initial state preparation of the nuclear spin distribution and can vary from 1 to 10 in ^{87}Sr ($I = 9/2$). In this experiment we control N via optical pumping through another electronic state. It is useful to note that in the previous chapter, the orbital-spin $1/2$ operators were represented by the character "S" while in this chapter, they are represented by "T" and "S" is reserved for the nuclear-spin permutation operators.

In addition to elastic interactions, ^{87}Sr atoms also exhibit inelastic collisions. Among those however, only two-body $|e\rangle$-$|e\rangle$ loss has been observed [46]; we denote these two inelastic scattering lengths as γ_{ee} and β_{ee} for s-wave and p-wave, respectively. We set other inelastic parameters to zero based on their negligible contributions in measurements [46].

4.3 Confirming SU(10) symmetry with density-dependent frequency shifts in nuclear-spin mixtures

We first test SU(N) symmetry in a two-orbital system by measuring the density-dependent frequency shift of the clock transition under various nuclear-spin population distributions. We use a Ramsey sequence to measure interactions [4] under an external magnetic field that produces Zeeman splittings much larger than the interaction energy. As shown in Fig. 4.2A, the sequence starts with all atoms in $|g\rangle$. Only atoms in a particular nuclear spin state are coherently excited and interrogated, while atoms in other states (spectators) remain in $|g\rangle$. We denote ${\mathcal{N}_{\mathcal{I}}}^{\mathrm{tot}}$ the number of interrogated atoms, ${\mathcal{N}_{\mathcal{S}}}^{\mathrm{tot}}$ the number of spectator atoms, and define a population ratio $f = {\mathcal{N}_{\mathcal{S}}}^{\mathrm{tot}}/{\mathcal{N}_{\mathcal{I}}}^{\mathrm{tot}}$ and the interrogated fraction $x_{\mathcal{I}} = {\mathcal{N}_{\mathcal{I}}}^{\mathrm{tot}}/({\mathcal{N}_{\mathcal{I}}}^{\mathrm{tot}} + {\mathcal{N}_{\mathcal{S}}}^{\mathrm{tot}})$. We control orbital excitation, p_e, by varying the initial pulse area, θ_1, where $0 < \theta_1 < \pi$. After a free evolution time, $\tau_{\mathrm{Free}} = 80$ ms, a second pulse of area $\pi/2$ is applied for subsequent readout of the electronic orbital distributions. The resonance frequency shift is recorded as a function of the atomic number in the trap, which can be varied in a controlled manner. We operate with highly homogeneous atom-laser coupling such that the orbital excitation is the same for all interrogated atoms. Consequently, in a fully spin-polarized sample, the s-wave interactions are suppressed and the p-wave interactions

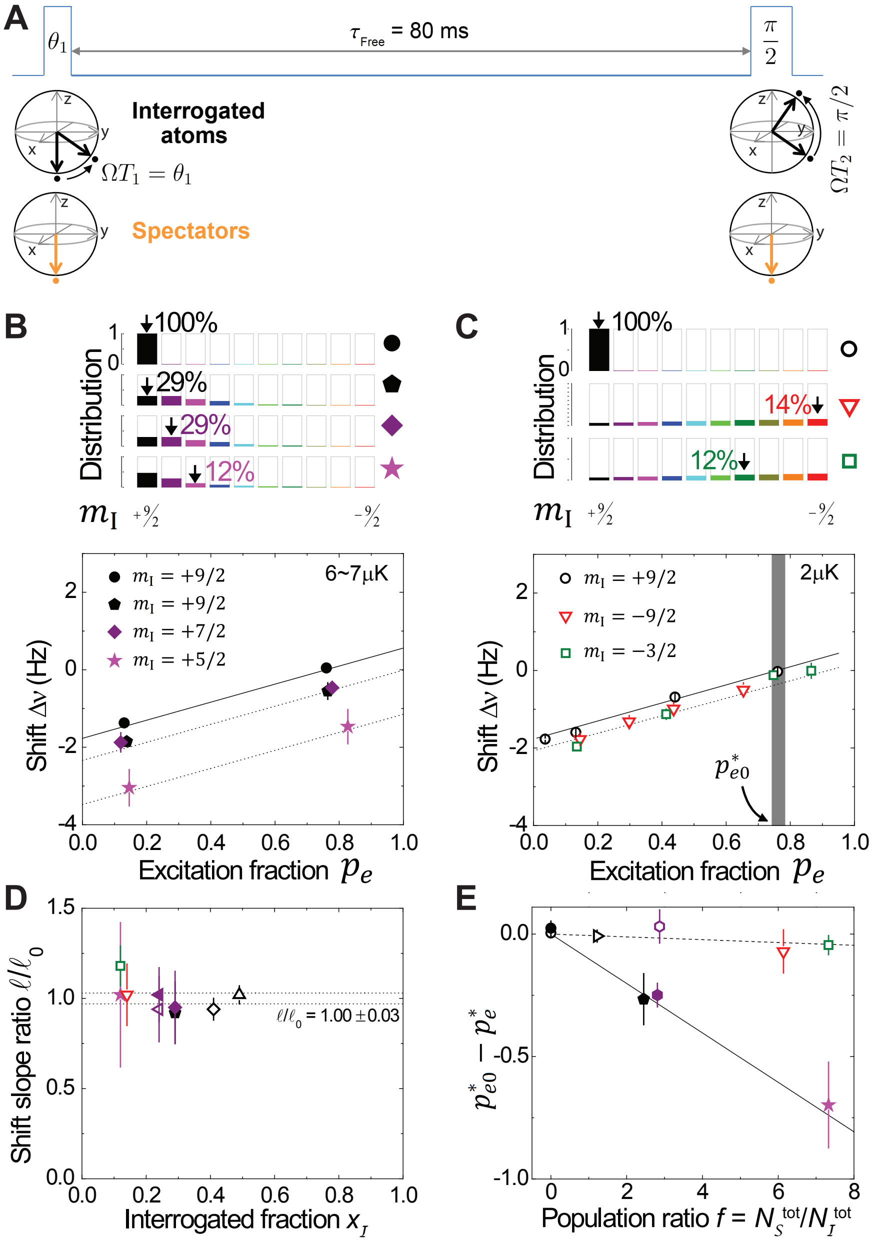

Figure 4.2: Nuclear spin independence of interaction effects. (A) Ramsey sequence with an initial pulse of area θ_1, a final $\pi/2$ pulse, and a free evolution period $\tau_{\text{Free}} = 80$ ms. The spectator atoms remain in $|g\rangle$. (B) and (C) (Upper panel) Illustration of the interrogated states (black arrows) and population distributions among various nuclear spin states. (Lower panel) Measured density shifts (in symbols) for different nuclear spin configurations at $T_r = 6 - 7$ μK and ~ 2 μK, respectively. For consistency, the shifts are scaled for $\mathcal{N}_{\mathcal{I}}{}^{\text{tot}} = 4000$. The solid and dotted lines show theory calculations for the corresponding $x_{\mathcal{I}}$ and T_r as indicated in the plots. The gray band in (C) corresponds to p^*_{e0}, the excitation fraction for zero density shift in a polarized sample. (D) Ratio of the slope of the frequency shift between the spin mixed and polarized samples. The dotted lines represent the standard error. (E) The difference in the zero-shift excitation fraction between the spin-mixed and polarized samples. The solid and dashed lines are theory fits used to determine b_{eg^-}. In D and E, two values of T_r are used: 2.3(2) μK (open symbols) and 6.5(4) μK (filled symbols). In addition to conditions used for B and C, other spin configurations are studied: open up triangles ($x_{\mathcal{I}} = 49\%$), open diamond (41%), open right triangles (46%), open and filled hexagons (26%), open and filled left triangles (24%), filled pentagons (29%), and filled stars (12%). Reproduced from [5].

dominate the free evolution dynamics [4].

In Fig. 4.2B, we compare the fully spin-polarized case ($m_I = +^9\!/\!_2$) against three other scenarios with different spin mixtures under $T_r = 6 - 7\ \mu$K. The observed density shifts as a linear function of p_e, when scaled to the same number of interrogated atoms (${\mathcal{N}_\mathcal{I}}^{\text{tot}} = 4000$), show three features: (*i*) the linear slope, l, depends only on ${\mathcal{N}_\mathcal{I}}^{\text{tot}}$, (*ii*) the offset with respect to the polarized case linearly increases with f, and (*iii*) both l and the offset are independent of how the atoms are distributed in the nuclear spin levels. The last point is verified, for example, by measuring the same shifts when interrogating 29% of the total population in either $+^9\!/\!_2$ or $+^7\!/\!_2$.

To determine the temperature dependence for the density shift and for additional confirmation of the observed nuclear spin independence, we interrogate other nuclear spin states, $-^9\!/\!_2$ or $-^3\!/\!_2$, at a lower $T_r \sim 2\ \mu$K, when the distribution across all spin states is nearly even (Fig. 4.2C). The measured density shifts scaled to ${\mathcal{N}_\mathcal{I}}^{\text{tot}} = 4000$ are again similar to each other, providing further direct experimental evidences for SU($N = 10$) symmetry. At this lower T_r, while the slope still depends only on ${\mathcal{N}_\mathcal{I}}^{\text{tot}}$, there is a smaller offset of the density shift relative to the polarized case when $x_\mathcal{I}$ varies. To quantify the T_r dependence, we plot together all measured ratios, l/l_0, with l_0 the linear slope for the polarized case. We see that (*iv*) the ratios collapse into a single value independently of f and T_r for fixed ${\mathcal{N}_\mathcal{I}}^{\text{tot}}$, yielding $l/l_0 = 1.00 \pm 0.03$ (Fig. 4.2D). This result agrees well with the SU(N)-predicted ratio of unity and verifies this symmetry to the 3% level. Further reduction in our experimental uncertainty can be achieved by enhancing the measurement precision with improved laser stability. We observe that l decreases only by 10% when T_r is raised from 2 μK to 6 μK, verifying its insensitivity to T_r.

We emphasize that the test of SU(N) symmetry (at the 3% level) is based directly on the measured interactions that are independent of nuclear spin configurations, and it does not require accurate knowledge of some common-mode system calibrations. For quantum simulations of SU(N) physics, it is important to precisely test this symmetry to a level much below all relevant energy scales. While our measurement uncertainty (3%) has not reached the ultimate theoretical prediction (0.1%) [103], it is already sufficient for realizing a SU(N)-symmetric, unity-filling spin lattice system.

To demonstrate this point, we follow the analysis presented in Ref. [103]. SU(N) symmetry will be intact if the important energy scales (E_{rel}) are substantially greater than the relevant SU(N)-breaking energy scale (ΔE_{rel}): $\Delta E_{\mathrm{rel}}/E_{\mathrm{rel}} \ll 1$. We consider the implication of our measurement precision for two experimental cases of quantum simulation.

The SU(N)-breaking energy scale for spin models with one atom per site is $\Delta E_{\mathrm{rel}} = \Delta(J^2/U) = (J/U)^2 U$, with U being the on-site interaction energy, J the tunneling energy, and $E_{\mathrm{rel}} = J^2/U$ the super-exchange energy, the key energy scale that controls the spin model spectrum. In this case, the condition for the physics to be unaffected by SU(N) breaking, $\Delta E_{\mathrm{rel}} = E_{\mathrm{rel}} \ll 1$, reduces to $\Delta U/U \ll 1$. This is already satisfied under our current 3% measurement precision. In more contemporary lattice experiments such as in Ref. [117], the typical achieved thermal energy scale, $k_B T$, is in the range of $J \ll kBT \ll U$, and the experiments are limited to mainly access the Mott insulator physics. In this scenario, the relevant energy scale is $E_{\mathrm{rel}} = U$, and the criterion to probe SU(N) symmetry of atomic interaction is $\Delta E_{\mathrm{rel}}/E_{\mathrm{rel}} = \Delta U/U \ll 1$, which is also satisfied with our current precision.

We also determine the excitation fraction where the shift is zero for a spin mixture, p_e^*, and compare it to that of a polarized sample, p_{e0}^* (gray bands, Fig. 4.2C), under various interrogated spin states (colors in Fig. 4.2E). The difference shows the following features: (v) it collapses onto a single line (for a given T_r of either 2.3 or 6.5 μK) as a function of f, which provides a further evidence for spin-independence of the interactions; (vi) at ${\mathcal{N}_{\mathcal{S}}}^{\mathrm{tot}} = 0$ (fully polarized), the two lines cross each other at the origin, as expected from the T_r-insensitivity of the p-wave interactions. The proportionality constant of $(p_{e0}^* - p_e^*)$ to f is finite for 6.5 μK (lower line), and decreases to almost zero for $T_r \sim 2.3$ μK (upper line). This near zero proportionality constant for $T_r \sim 2.3$ μK indicates an accidental cancellation of the spectators' s- and p-wave interaction effects at this temperature.

4.4 Experiment-theory agreement and determination of the scattering parameters

In the presence of a large external magnetic field that produces differential Zeeman splittings much larger than the interaction energy, those terms in the Hamiltonian that exchange the population between the occupied spin-orbital levels are energetically suppressed and the populations of different spin-orbital levels are conserved. Hence, the Hamiltonian is dominated by Ising-type interactions that preserve the spin-orbital population. In this regime the many-body dynamics for a single trap with $\mathcal{N}$ atoms can be captured under a collective approximation that replaces the coupling constants with their corresponding thermal averages, $O_{\mathbf{n}_j,\mathbf{n}_k} \to \overline{O^{\pm}}$ [66]. For the experimental relevant case where only $\mathcal{N}_{\mathcal{I}}$ atoms in spin m_I are interrogated and where $\mathcal{N}_{\mathcal{S}}$ atoms in the other spin components remain in $|g\rangle$, the effective many-body Hamiltonian during τ_{Free} simplifies substantially. It consists of two parts, $\hat{H}_{\mathcal{I}} + \hat{H}_{\mathcal{S}}$. The first part, $\hat{H}_{\mathcal{I}} = \overline{\chi^+}(\hat{\mathbb{T}}^z)^2 + \overline{C^+}\hat{\mathbb{T}}^z\mathcal{N}_{\mathcal{I}}$, describes the p-wave interactions between the interrogated atoms [4, 66], where $\hat{\mathbb{T}}^{\alpha=x,y,z} = \sum_j^{\mathcal{N}} \hat{S}^{m_I}_{m_I}(\mathbf{n}_j)\hat{T}^{\alpha}_{\mathbf{n}_j}$ are collective orbital operators acting on the $\mathcal{N}_{\mathcal{I}}$ interrogated atoms. The density shift induced by these interactions, $\Delta\nu^{\mathcal{I}} = \mathcal{N}_{\mathcal{I}}(\overline{C^+} - \cos\theta_1\overline{\chi^+})$, with $\overline{\chi^+} = \frac{\left[b^3_{ee} - b^3_{gg}\right]}{2}\langle P\rangle_{T_r}$ and $\overline{C^+} = \frac{\left[b^3_{ee} + b^3_{gg} - 2b^3_{eg^+}\right]}{2}\langle P\rangle_{T_r}$, depends linearly on the number of excited atoms $\mathcal{N}_{\mathcal{I}}p_e$. Here $\langle P_{T_r}\rangle$ corresponds to the thermal average of the p-wave mode overlap coefficients. Assuming a Boltzmann distribution of initially populated radial motional modes, we have that $\langle P_{T_r}\rangle$ is insensitive to T_R [4, 66]. For a spin polarized sample, the observed density shifts are well reproduced by theory (solid black lines in Figs. 4.2B and 4.2C) based on the same p-wave parameters as determined in Ref. [4]. The second part, $\hat{H}_{\mathcal{S}} = \mathcal{N}_{\mathcal{S}}\overline{\Lambda}\hat{\mathbb{T}}^z$, describes the interactions between the interrogated and spectator atoms with both p- and s-wave contributions. The related density shift is $\Delta\nu^{\mathcal{S}} = \overline{\Lambda}\mathcal{N}_{\mathcal{S}}$, with $\overline{\Lambda} = \frac{\overline{C^+} + \overline{C^-} - \overline{J^+} - \overline{J^-} - \overline{\chi^+} - \overline{\chi^-}}{2} = \frac{(a_{eg^+} + a_{eg^-} - 2a_{gg})}{4}\langle S_{T_r}\rangle + \frac{(b^3_{eg^+} + b^3_{eg^-} - 2b^3_{gg})}{4}\langle P_{T_r}\rangle$. The s-wave thermal average, $\langle S_{T_r}\rangle$, decreases with T_r as $\langle S_{T_r}\rangle \propto (T_r)^{-1}$.

This model fully reproduces the experimental observations as summarized in points $(i - vi)$ stated in Section 4.3 and shown in Fig. 4.2. To quantitatively compare with the experiment, we perform a Poissonian average of the atom number across the array of 2D traps and use the average excitation fraction to account for the two-body $|e\rangle - |e\rangle$ losses [4, 46] during τ_{Free}. The capability of the SU(N) spin lattice model to reproduce the experimental observations also enables us to determine the remaining s- and p-wave scattering parameters. For each of the four channels, $\eta \in \{ee, gg, eg^+, eg^-\}$, the s-wave and p-wave complex scattering parameters, $A_\eta = a_\eta - i\gamma_e ta$ and $B_\eta^3 = b_\eta^3 - i\beta_e ta^3$, are predicted to relate to each other through the characteristic length, $\overline{a}_\eta = \frac{2\pi}{\Gamma(1/4)^2}\left[\frac{2\mu C_6(\eta)}{\hbar^2}\right]^{1/4}$, of the van der Waals potential, where μ is the reduced mass and $\Gamma(1/4) \approx 3.626$ [91]. This relationship is given by [91]

$$\frac{A_\eta}{\overline{a}_\eta} = 1 + \left(\frac{B_\eta}{\overline{a}_\eta}\right)^3 \left[\left(\frac{B_\eta}{\overline{a}_\eta}\right)^3\right]^{-1}. \tag{4.3}$$

Luckily, the experts in *ab initio* configuration interaction calculations combined with the coupled-cluster all-order approach [125, 126, 127] are able to calculate C_6 coefficients at the few percent level for all channels. They find that $C_6(gg) = 3107(30)$ a.u., $C_6(ee) = 5360(200)$ a.u., and $C_6(eg^+) = C_6(eg^-) \equiv C_6(eg) = 3880(80)$ a.u., where 1 a.u. $= 1E_h a_0^6$ with E_h being the Hartree energy and a_0 the Bohr radius [5].

Thus, after determining $\overline{a}_\eta$ using the van der Waals C_6 coefficients, only four elastic scattering parameters remain independent. Among those, a_{gg}, b_{ee}, and b_{eg^+} (and thus their respective p- or s-wave counterparts) are known [4], leaving only one unknown parameter associated with the eg^- channel. Using the theoretical predictions and a single parameter to fit the data in Fig. 4.2E, we extract a_{eg^-} and b_{eg^-}. Specifically, from the slope and zero-point crossing of the density shift in a polarized sample we determine $[(b_{eg^+})^3 - (b_{gg})^3]\langle P\rangle_{T_r} = -1.65\text{s}^{-1}$ and $[(b_{ee})^3 - (b_{gg})^3] = 0.4[(b_{eg^+})^3 - (b_{gg})^3]$. For our trapping conditions we estimate $a_0^3\langle P\rangle_{T_r} = (3.35 \pm 1)10^{-7}\text{s}^{-1}$ and $a_0\langle S\rangle_{T_r} = (0.08 \pm 0.02)(1\mu\text{K})/[T_r(\mu\text{K})]\text{s}^{-1}$. Those measurements, supplemented by excited state loss measurements [46], allow us to determine the following interaction parameters: $b_{eg^+} \approx (-169 \pm 23)a_0$, $b_{ee} \approx (-119 \pm 18)a_0$ and $\beta_{ee} \approx (121 \pm 13)a_0$.[a] Using Eq. 4.3 we can determine the corresponding s-wave parameters: $a_{eg^+} \approx (169 \pm 8)a_0$, $a_{ee} \approx (176 \pm 11)a_0$ and $\gamma_{ee} \approx (46^{+19}_{-32})a_0$.[b]

---

[a] β_{ee} determined exclusively from this work is in agreement with [46] and both numbers are used to determine the number reported here.

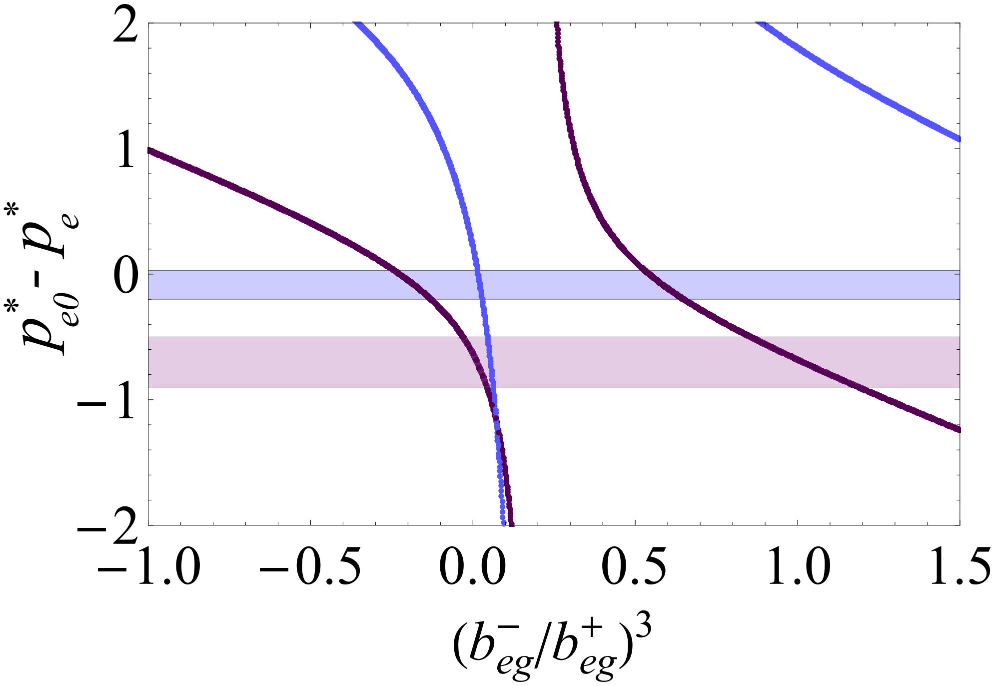

Figure 4.3: Fitting scattering parameters from the density shift data. The figure shows the theoretical predictions of the offset of zero-shift excitation fraction $p^*_{e0} - p^*_e$ in a 13% spin mixture under two temperatures: 2.3(2) μK (blue line) and 6.5(4) μK (purple line) [computed using the expressions for $\Delta\nu^{\mathcal{I}}$ and $\Delta\nu^{\mathcal{S}}$] vs $(b_{eg^-}/b_{eg^+})^3$. The shadowed regions correspond to the values of $p^*_{e0} - p^*_e$ that lie within the experimental error bars for the corresponding temperatures. Reproduced from [5].

Finally, from the density shift measurements in the presence of spectator atoms we determine $|b_{eg^-}| < 60a_0$ (best fit at $-42a_0$), and $a_{eg^-} \approx (68 \pm 22)a_0$. The large variation of b_{eg^-} comes from the fact that the value that best fits the experimental parameters is in a region where it changes sign as shown in Fig. 4.3. Table 4.1 lists all the scattering parameters determined from the prior and current measurements.

---

[b] We determination γ_{ee} from β_{ee} as reported here and Eqn. 4.3. This disagrees with [46] at the 1σ level where σ is the standard error resulting from the analytic relationship. The lower bound for the uncertainty of our analytically determined γ_{ee} has been increased to restore agreement below 1σ.

Table 4.1: s- and p-wave scattering lengths in units of the Bohr radius (a_0). Reproduced from [5].

Channel	s-wave	p-wave	Determination method
gg	96.2(1)	74.6(4)	[s-wave] Two-photon photo-associative spectroscopy [119] and ro-vibrational spectroscopy [120], [p-wave] Analytic relation between s- and p-wave [91]
eg^+	169(8)	-169(23)	[s-wave] Analytic relation [91], [p-wave] Density shift in a polarized sample [4]
eg^-	68(22)	-42^{+103}_{-22}	[s-wave] Density shift in a spin mixtrue at different temperatures (this work)[5], [p-wave] Analytic relation [91]
ee (elastic)	176(11)	-119(18)	[s-wave] Analytic relation [91], [p-wave] Density shift in a polarized sample [4]
ee (inelastic)	46^{+19}_{-32}	121(13)	Two-body loss measurements [46] and analytic relation [91]

4.5 Coherent dynamic spectroscopy

We perform coherent dynamic spectroscopy to explore the development of many-body correlations, in the combined orbital and nuclear spin degrees of freedom, generated by the p-wave and s-wave interactions. This allows us to further validate the SU(N) spin-orbital model (Eq. 4.2) as a description for our system. The many-body correlations that build up during the free evolution manifest as a decay of the $|e\rangle - |g\rangle$ orbital coherence in the form of Ramsey fringe contrast $\mathcal{C}(\tau_{\text{Free}}) = 2/\mathcal{N}_{\mathcal{I}}\sqrt{\langle\hat{\mathbb{T}}^y_{\text{tot}}\rangle^2 + \langle\hat{\mathbb{T}}^x_{\text{tot}}\rangle^2}$ that we measure as a function of τ_{Free}. Here $\hat{\mathbb{T}}^{x,y}_{\text{tot}}$ is the sum of $\hat{\mathbb{T}}^{x,y}$ over the 2D traps. We extract a normalized $\mathcal{C}$ by comparing the high-atom-number raw contrast against that of the low-atom-number. This normalization removes single-particle decoherence effects. The decay of $\mathcal{C}$ during the free-evolution period has been shown to be a particularly suitable observable for characterizing the role of interactions during the dynamics [128]. For example, contrast measurements in an array of polar molecules pinned in a 3D lattice provided clear signatures of dipolar interactions and their description in terms of a spin exchange model [121, 129].

In the presence of a large magnetic field, the decay of $\mathcal{C}$ has two sources. The first arises from within the interrogated atoms: p-wave elastic interactions, two-body $|e\rangle - |e\rangle$ losses, higher-order interaction-induced mode-changing processes, as well as dephasing induced by the variation of atom number across all occupied trap sites. These p-wave effects are taken into account in our theory using the same p-wave parameters determined in Ref. [4]. These parameters are reconfirmed with our density shift measurements here (Fig. 4.2). The second source comes from spectators, which act on the interrogated atoms at a given site as an inhomogeneous and density-dependent effective magnetic field along $\hat{z}$, with both s-and p-wave contributions. The effective magnetic field is static if the atoms are frozen in their motional states, but can vary with time in the presence of higher-order mode-changing processes. For our 2D geometry, p-wave interactions play a dominant role at high $T_r = 5 - 6\ \mu$K, while s-wave interactions, which have stronger dependence on mode distribution, becomes significant at lower T_r. We focus first on the nuclear spin-polarized case (Fig. 4.4) to benchmark our model, and then use various population distributions among nuclear spin states to investigate the interplay between orbital and spin degrees of freedom (Fig. 4.5).

4.6 Two-orbital dynamics in spin-polarized atoms

To understand in detail the orbital dynamics induced by p-wave interactions, we first study a nuclear spin-polarized sample ($x_{\mathcal{I}} = 100\%$) for $T_r = 5 - 6\ \mu$K and $\theta_1 = \pi/4$, as displayed in Fig. 4.4B. To separate the effects of dephasing and many-body correlation in the contrast decay, we apply a π echo pulse in the middle of the Ramsey sequence (Fig. 4.4A, lower panel). The π echo pulse modifies contrast decay dependent on θ_1, due to enhanced $|e\rangle - |e\rangle$ loss after the echo pulse for $\theta_1 < \pi/2$ as well as θ_1-dependent p-wave contributions to contrast decay. The θ_1-dependent contribution is generated by the term $\overline{\chi^+}(\hat{\mathbb{T}}^z)^2$ in the Hamiltonian, and can lead to many-body orbital correlations that are not removable by echo. The echo pulse helps to illuminate these correlations because it removes θ_1-independent contributions generated by the term $\overline{\mathcal{C}^+}\hat{\mathbb{T}}^z\mathcal{N}_{\mathcal{I}}$, responsible for density-dependent dephasing between atoms distributed in different 2D traps, as well as other θ_1-independent technical noise.

As shown in Fig. 4.4B, under $\theta_1 = \pi/4$, the Ramsey contrast decays more slowly with an echo pulse. This effect can be attributed to the suppressed dephasing from inhomogeneous atomic densities across different 2D traps (θ_1-independent contributions) and to the faster number loss with

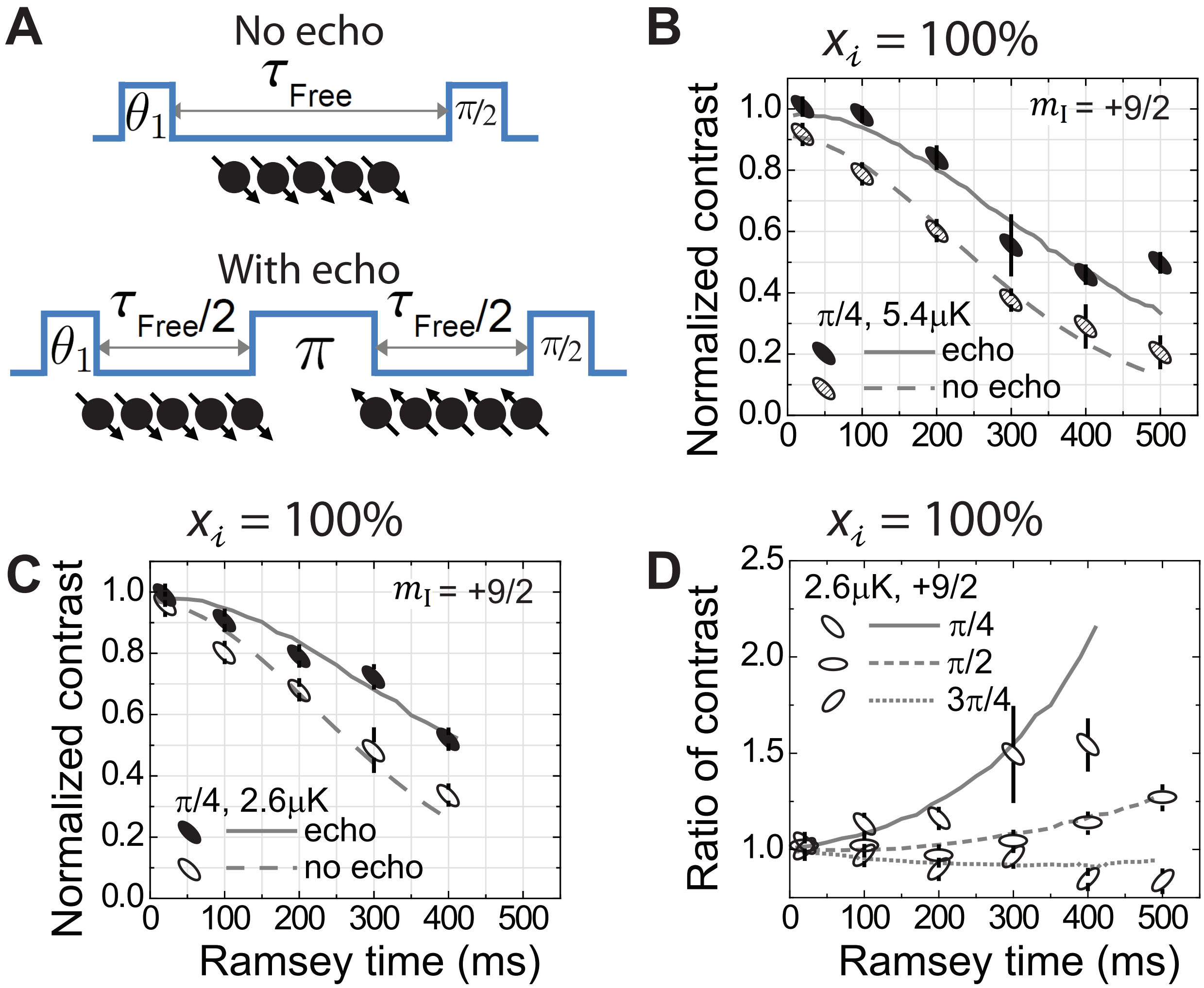

Figure 4.4: Evolution of orbital coherence in nuclear spin-polarized samples. (A) (Upper panel) Ramsey sequence with varying θ_1 and τ_{Free}; (Lower panel) sequence with an echo (π) pulse. The group of circles illustrates the orbital configurations for interrogated atoms (black circles). (B and C) Normalized Ramsey contrasts for $\theta_1 = \pi/4$, $x_{\mathcal{I}} = 100\%$, under two different radial temperatures, $T_r = 5.4$ μK and 2.6 μK, respectively. The contrast is normalized by comparing the high-atom-number raw Ramsey fringe contrast, $\mathcal{C}$ (defined in the main text), against the low-atom-number raw contrast. The high total atom numbers (measured at a very short free evolution time, $\tau_{\text{Free}} = 20$ ms) are in the range of $2200 \sim 3100$ (day-to-day variation over four months). However, for each specific case the data without and with echo were taken on the same day and their atom numbers are matched to within 3 7%. These atom numbers are recorded and serve as inputs to our theory calculation of Ramsey contrast decay. The filled symbols are for echo measurements and the empty symbols without echo. The solid and dashed lines show theory calculations with echo and without echo, respectively, using a two-orbital model with independently determined parameters (based on measurements shown in Fig. 4.2 and previous studies, see Table 4.1). Under the conditions of (B and C), the dominant source for contrast decay arises from p-wave interactions between the interrogated atoms. (D) Effects of echo, characterized by the ratio of contrast with echo to that without echo, for $\theta_1 = \pi/4$ (anti-diagonal ellipse and solid line), $\pi/2$ (horizontal ellipse and short dashed line), and $3\pi/4$ (diagonal ellipse and short dotted line), under $x_{\mathcal{I}} = 100\%$. Reproduced from [5].

echo. In a polarized sample where p-wave interactions dominate, the contrast decay is expected to be insensitive to T_r. This is confirmed with measurements performed at $T_r = 2.6$ μK (Fig. 4.4C) that show similar decay behaviors to those at 5.4 μK (Fig. 4.4B). In addition, we find an excellent agreement between the data and the theoretical model that uses temperature-insensitive p-wave parameters. Figure 4.4D plots the ratio of contrasts with and without echo for different pulse areas and illustrates both the roll of the echo pulse for $\theta_1 = \pi/4$, where it suppresses contrast decay, as well as for $\theta_1 = 3\pi/4$, where the echo pulse enhances contrast decay. This enhancement derives from the development of many-body orbital correlations for $\theta_1 = 3\pi/4$ [4] and the reduced $|e\rangle - |e\rangle$ loss after the echo. All measurements are well reproduced by theory.

4.7 Spin-orbital SU(N) dynamics in spin mixtures

To investigate the interplay between orbital and spin degrees of freedom, we perform similar spectroscopic measurements in spin-mixed samples, as illustrated in Fig. 4.5A. We study the spin-mixed cases at $T_r = 5 - 6$ μK, with $\theta_1 = \pi/4$ and the interrogated fraction $x_{\mathcal{I}} = 14\%$ and 56%, as labeled in Figs. 4.5B and 4.5C, respectively. In the presence of spectator atoms, the data show a similar suppression of contrast decay with the addition of an echo pulse. Since p-wave interactions between interrogated atoms are reduced as the interrogated fraction decreases, the overall contrast decay becomes slower. Based on the determined scattering parameters, our model predicts that spectator atoms cause almost negligible decoherence effects at this high $T_R = 5 - 6$ μK.

When we decrease T_r to ~ 2 μK, the rise of s-wave contributions to contrast decay causes significant decoherence due to the spectator atoms. Figure 4.5D illustrates the influence of spectators for the $x_{\mathcal{I}} = 14\%$ case where contrast decay is faster than in Fig. 4.5B. The inclusion of off-resonant mode-changing collisions as higher order corrections is required for temperatures below 5 μK to accurately reproduce the experimental observations. These mode-changing collisions can be visualized as relocating pairs of atoms in the energy-space lattice shown in Fig. 4.1C, analogous to interaction-induced tunneling processes in a real space lattice. The echo pulse suppresses the part of contrast decay arising from mode-preserving collisions between spectators and interro-

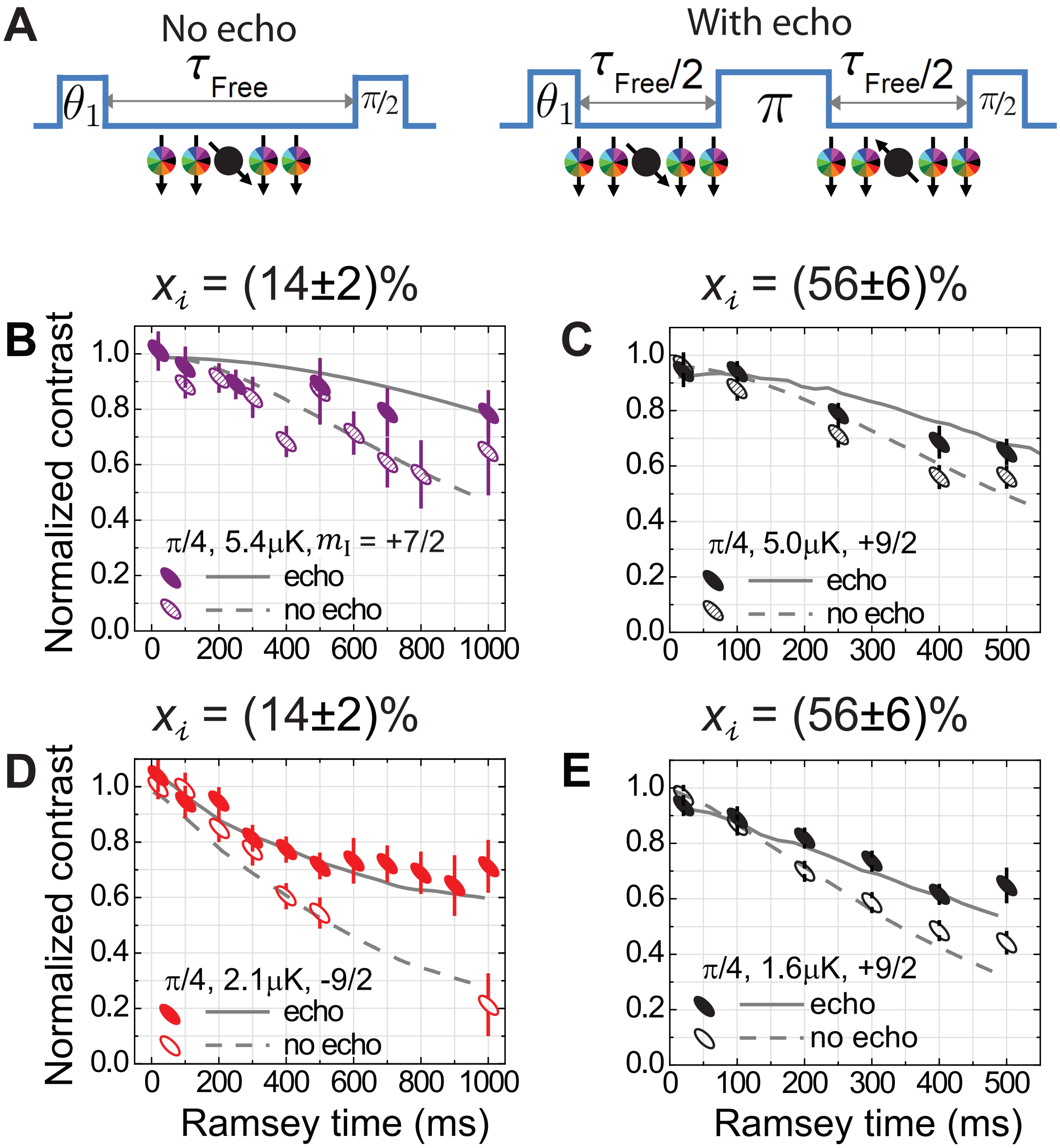

Figure 4.5: Evolution of orbital coherence in nuclear spin-mixed samples. (A) (Left panel) Ramsey sequence with varying θ_1 and τ_{Free}; (Right panel) sequence with an echo (π) pulse. The group of circles illustrates the orbital configurations for interrogated atoms (black circles) and spectator atoms (colored circles). (B and D) Normalized Ramsey contrast for $\theta_1 = \pi/4$, $x_{\mathcal{I}} = (14 \pm 2)\%$, at $T_r = 5.4$ μK and 2.1 μK, respectively: measurements with echo (filled symbols) and without echo (empty symbols). (C and E) Normalized contrast for $\theta_1 = \pi/4$, $x_{\mathcal{I}} = (56 \pm 6)\%$, at $T_r = 5.0$ μK and 1.6 μK, respectively. The solid and dashed lines show theory calculations with echo and without echo, respectively, using a two-orbital model with independently determined parameters (based on measurements shown in Fig. 4.2 and previous studies, see Table 4.1). In this model, the spectators act as an effective inhomogeneous magnetic field causing dephasing to the interrogated atoms. Without mode changing collisions the dephasing is static and removable by echo; with mode changing collisions it is assumed and confirmed experimentally that echo does not remove the time-dependent dephasing. The theory uses a single fitting parameter for the mode-changing processes for all plots. Reproduced from [5].

gated atoms, but it cannot reverse the decay due to mode-changing processes. In Fig. 4.5D, the measured contrast decay with echo enables us to determine a single parameter characterizing the mode-changing processes [5, 66].

For an additional, independent test of our model, we explore another spin mixture with $x_{\mathcal{I}} = 56\%$ and $T_r \sim 2\ \mu$K, so that both the interrogated atoms and spectator atoms have important contributions to the contrast decay. As shown in Fig. 4.5E, the data are well described by the same theory model without any variation of the pre-determined parameters, demonstrating a firm understanding of the system dynamics.

4.8 Looking for interaction-induced spin-orbital exchange

Spin-orbital exchange processes (Fig. 4.6A) are an intriguing feature of two-orbital magnetism, which are responsible for rich physics exhibited by transition metal oxides and heavy fermion materials. In our system, the characteristic exchange energy, J_{ex}, depends on $a_{eg^+} - a_{eg^-}$ and $b^3_{eg^+} - b^3_{eg^-}$. Under an external magnetic field B, those exchange processes can be suppressed by the first-order Zeeman shift (of about -109 m_I Hz/G) [100]. To probe possible exchange processes, we perform a Ramsey sequence with the first pulse $\pi/2$ and the second pulse $-\pi/2$ both interrogating only the $+9/2$ state, while B is reduced to zero during τ_{Free} (Fig. 4.6A). B is raised to a high value during the pulses to provide spectral separation for interrogating a single nuclear spin component. Exchange processes which swap atoms between states such as $|m_{I,1} = 9/2, e\rangle\,|m_{I,2} = 7/2, g\rangle \leftrightarrow |m_{I,1} = 9/2, g\rangle\,|m_{I,2} = 7/2, e\rangle$, manifest as an increased final excitation fraction after the second pulse in the low-B case.

Since single particle depolarization occurs when B is tuned to near zero due to spin procession along stray residual magnetic fields at the mGauss level, we perform the above described measurements at both low- and high-atom-number and look for excess excitation in the high-atom-number condition. This insures that the measured excess total excitation originates from interaction-induced spin exchange. The data reported in Fig. 4.6B for both low and high B represent the difference in excitation between high-atom-number and low-atom-number conditions.

Our measurements at low B, with τ_{Free} as long as 1 s, show no excess excitation compared to the high-B reference case (Fig. 4.6B), indicating a very small J_{ex}. Using the scattering parameters obtained from the density shift measurements, we independently determine the mean exchange energy per particle to be smaller than $h \times 0.35$ Hz, for $2\mu\text{K} < T_r < 6\text{K}$. This value is indeed too small to generate measurable population transfer. Similar measurements performed for multiple spin configurations all show population transfer consistent with zero, suggesting a spin-independent, negligible J_{ex}. For comparison, Fig. 4.6B shows the effect of exchange interaction if J_{ex} is increased tenfold. Enhanced spatial resolution and signal-to-noise for single-site detection of 10 atoms will demonstrate the exchange dynamics more clearly (Fig. 4.6B inset). Spin-exchange could be observed in our system at lower temperatures or even possibly if the initial excitation fraction is kept smaller so that inelastic collisions are less important to the dynamics. Evidence for spin-exchange has been reported in ^{173}Yb trapped in a 3D optical lattice where interaction effects are on the kHz energy scale [130, 131].

Experimental explorations of exotic SU(N) physics are still in their infancy. In the same way that the extreme precision of our ultrastable laser allowed us to explore many-body effects in Ch. 3 it has now enabled us to explore Ising orbital magnetism at relatively high temperatures. Future investigations that employ greater control over atomic density and temperature, the applied magnetic field, and lasers with greater stability will be able to engineer various spin-spin and spin-orbital dynamics, giving experimental access to the full suite of rich behavior predicted in our SU(N) symmetric Hamiltonian. While such advances will undoubtedly lead to ever more exotic emergent many-body quantum physics at relatively high temperatures, future investigation in the quantum gas regime could also study time-resolved dynamics in the SU(N) Kondo lattice and Kugel-Khomskii models [103, 132, 133].

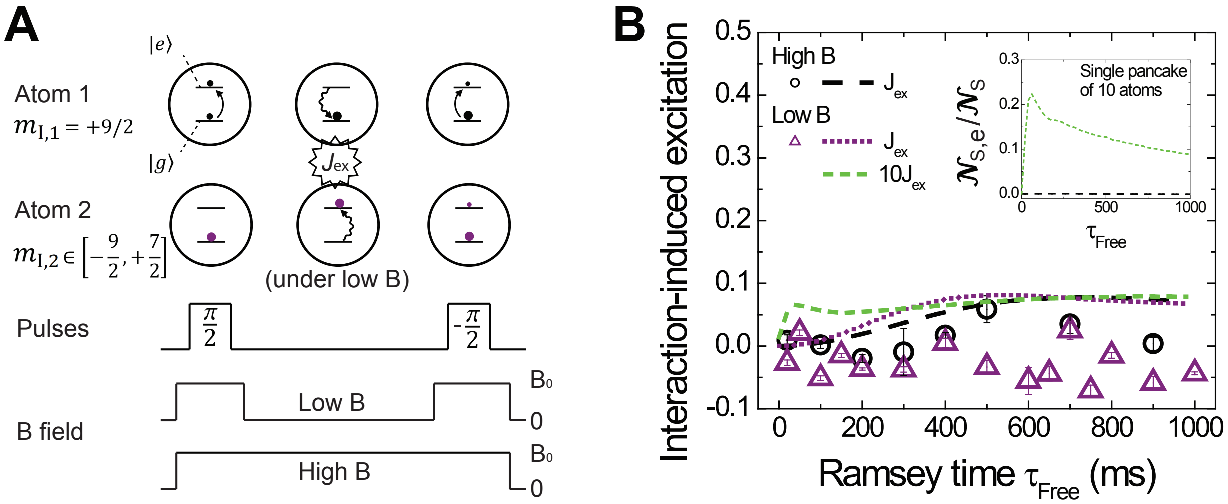

Figure 4.6: Interaction-induced spin exchange. (A) Illustration of spin exchange processes. The Ramsey sequence has $\theta_1 = \pi/2$ and a final $-\pi/2$ pulse, interrogating the $+9/2$ state and leaving the rest as spectators. Exchange processes (wiggled arrows) are suppressed at high magnetic fields, B, and resonant at $B \sim 0$, causing an excess in total excitation fraction after the final pulse. (B) Interaction-induced excitation fraction. Up to $\tau_{\mathrm{Free}} = 1$ s, no excess excitation fraction is observed at low B (purple triangles), similar to the case at high B (black circles). Black dashed and purple dotted lines show independent simulations based on the determined scattering parameters, while the green short dashed line shows a simulation using 10 times larger J_{ex}. Inset shows simulations under the same conditions, but for a single pancake of 10 atoms ($x_{\mathcal{I}} = 50\%$).

Chapter 5

Photon mediated collective effects is strontium: retarded dipolar coupling in free space and future work in cQED

5.1 Introduction

In this chapter we describe both a simple experiment involving ^{88}Sr atoms awaiting theoretical rigor, along with the design and theoretical performance for a new strontium system awaiting construction. They have been grouped together not solely for their incompleteness, rather, they are related at their very core. Both experiments look to uncover a better understanding of the interaction between light and atoms, although, they operate in very different regimes. The former looks to explain the seemingly collective coupling between ^{88}Sr in an optically dense sample that expresses itself through broadening of atomic transitions. The latter is a newly designed optical cavity that will be placed in our ^{87}Sr system to achieve strong atom-cavity coupling. The goal for this system is to explore collective effects in cavity quantum electrodynamic (cQED). While our system will be of immediate utility to advancing clock performance via quantum non-demolition measurement and spin-squeezing, this system could also lead to breakthroughs in quantum information science and advance our understanding of many-body physics by investigating the exotic quantum states that are achievable in cQED systems.

5.2 Collective effects in a freely expanding cloud of strontium atoms

This section will summarize the line broadening measurements we have made in a freely expanding cloud of ^{88}Sr atoms for the ^{1}S$_0$ to ^{1}P$_1$ and ^{1}S$_0$ to ^{3}P$_1$ transitions. The main goal of

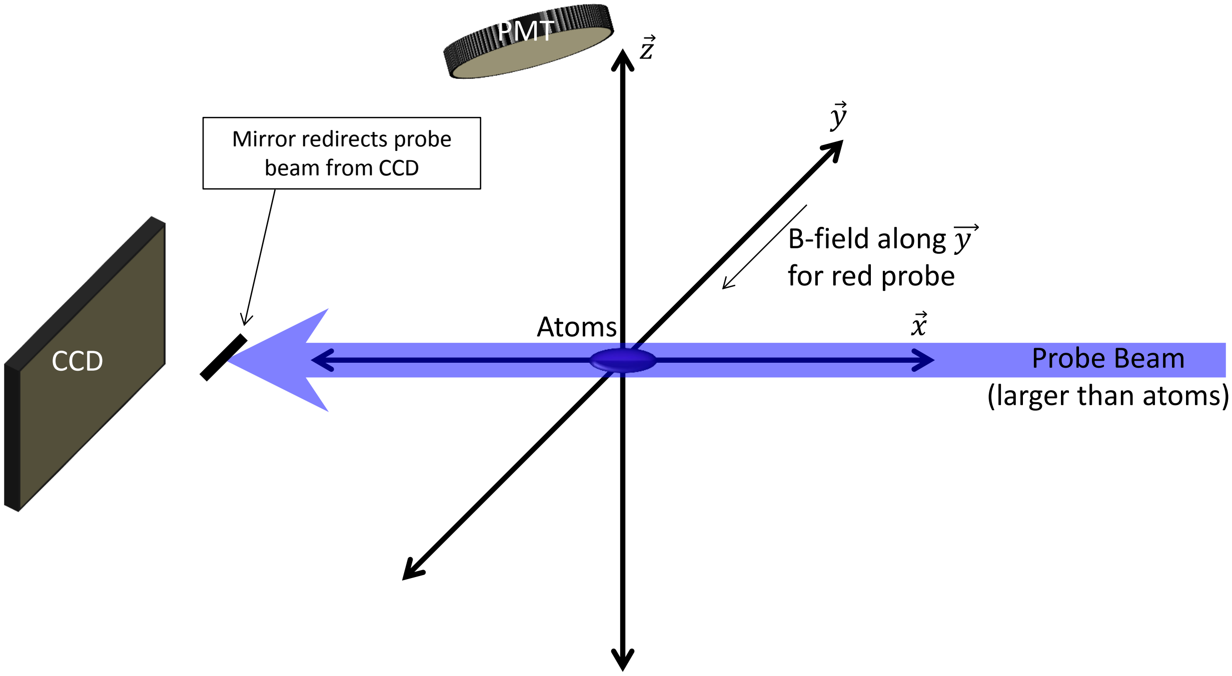

Figure 5.1: A schematic diagram of our detection scheme. Gravity is in the $\hat{z}$ direction. The probe light travels along the $-\hat{x}$ direction for the blue and the $\hat{x}$ direction for the red. For the blue probe, no B-field is applied. For the red probe, a 2 Gauss field is applied in the $\hat{y}$ direction to split transitions to different m_J levels by $\sim$ 1 MHz. The polarization of the probe for this scheme is linear and we take data with $\hat{y}$, $\hat{z}$, and diagonal polarization. The CCD views fluorescence from along the $\hat{x}$ direction and the PMT views fluorescence from nearly along the $\hat{z}$ direction.

these measurements is to study this broadening mechanism in a single system for two very different regimes. Alkaline-earth(-like) atoms offer the unique opportunity to probe a single system using ground state transitions of greatly varying linewidth. For the dipole allowed ^{1}S$_0$ to ^{1}P$_1$ (blue) transition, the natural linewidth is so broad (32 MHz in strontium) that it dominates all motional, finite temperature, and background magnetic field effects. Therefore, broadening of the natural linewidth at high optical depths/densities dominates the observed line shapes. In contrast, the relatively narrow $^1\mathrm{S}_0$ to $^3\mathrm{P}_1$ (red) transition (7.5 kHz in strontium) offers insight into how these broadening mechanisms are modified by Doppler effects (10's of kHz at μK temperatures). Through independent measurements of the atom cloud temperature we are able to precisely determine broadening of the natural linewidth even when the Doppler effect plays a very significant role in the observed linewidth.

5.2.1 Experimental Setup

After the atoms are cooled to between 1 and 2 μK in a magneto-optical trap (MOT), the MOT light and magnetic field are extinguished and the atoms are allowed to freely expand and fall. After a variable amount of time (1 to 25 ms), we interrogate the atoms with probe light resonant on either the blue or red transition. Light is collected with either a photomultiplier tube (PMT) that observes the cloud fluorescence nearly along the $\hat{z}$ direction or a CCD camera that observes the cloud fluorescence along the $\hat{x}$ direction. Fig. 5.1 depicts this detection scheme. Additionally, the CCD images the atom cloud with 20 μm resolution when the cloud is probed with the blue probe. For each time-of-flight (ToF) time, we measure the standard deviation of the Gaussian cloud (cloud radius) in the $\hat{z}$ (σ_z) and $\hat{y}$ (σ_y) directions. The radius along the $\hat{x}$ direction (σ_x) should be equal to σ_y based on the geometry of the MOT anti-Helmholtz coils.

We measure fluorescence versus detuning of the probe and fit the measured fluorescence signals to a Lorentzian function for the blue transition (Fig. 5.2(a)) where the natural linewidth (32 MHz) is much broader than Doppler broadening, or a Voigt profile for the red transition (Fig. 5.2(b)) when the Doppler FWHM (40 kHz) is over four times as large as the unbroadened Lorentzian FWHM (7.5 KHz).

To know the true size of our atom cloud, we precisely calibrate our imaging system by tracking the center of the atom cloud as a function of fall time. The atoms accelerate at 9.8 m/s^2 and we fit out the initial position and velocity of the atoms as well as the real size represented by one pixel. The data and fit for one such calibration is shown in Fig. 5.3. The initial position of the atoms remained constant to within a couple pixels across all data sets. The initial velocity in the

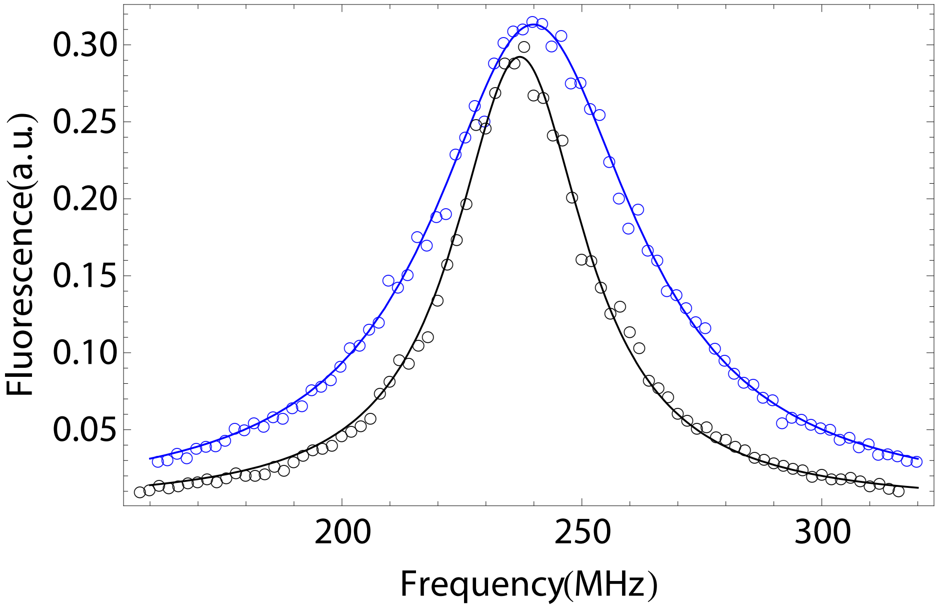

(a) Blue Probe

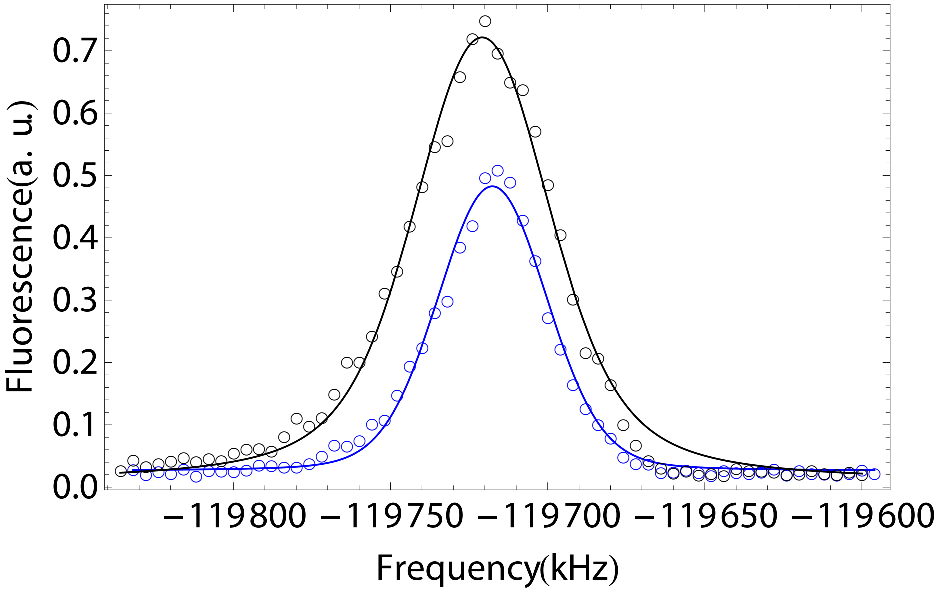

(b) Red Probe

Figure 5.2: Examples of fluorescence measurements using the blue and red probes with fluorescence measured by the PMT. (a) For the blue probe, blue points correspond to 1 ms of ToF and a FWHM of 53 MHz, the black points corespond to 25 ms of ToF and a FWHM of 33 MHz, and the solid lines are fitted Lorentzian functions. (b) For the red probe, the black points are for 5 ms of ToF and the Blue points are for 20 ms of ToF. The red transition data demonstrate a slight asymmetry which is visible when compared with the fitted Voigt profiles (solid lines). The fit lines assume a Doppler temperature of 1.3 μK.

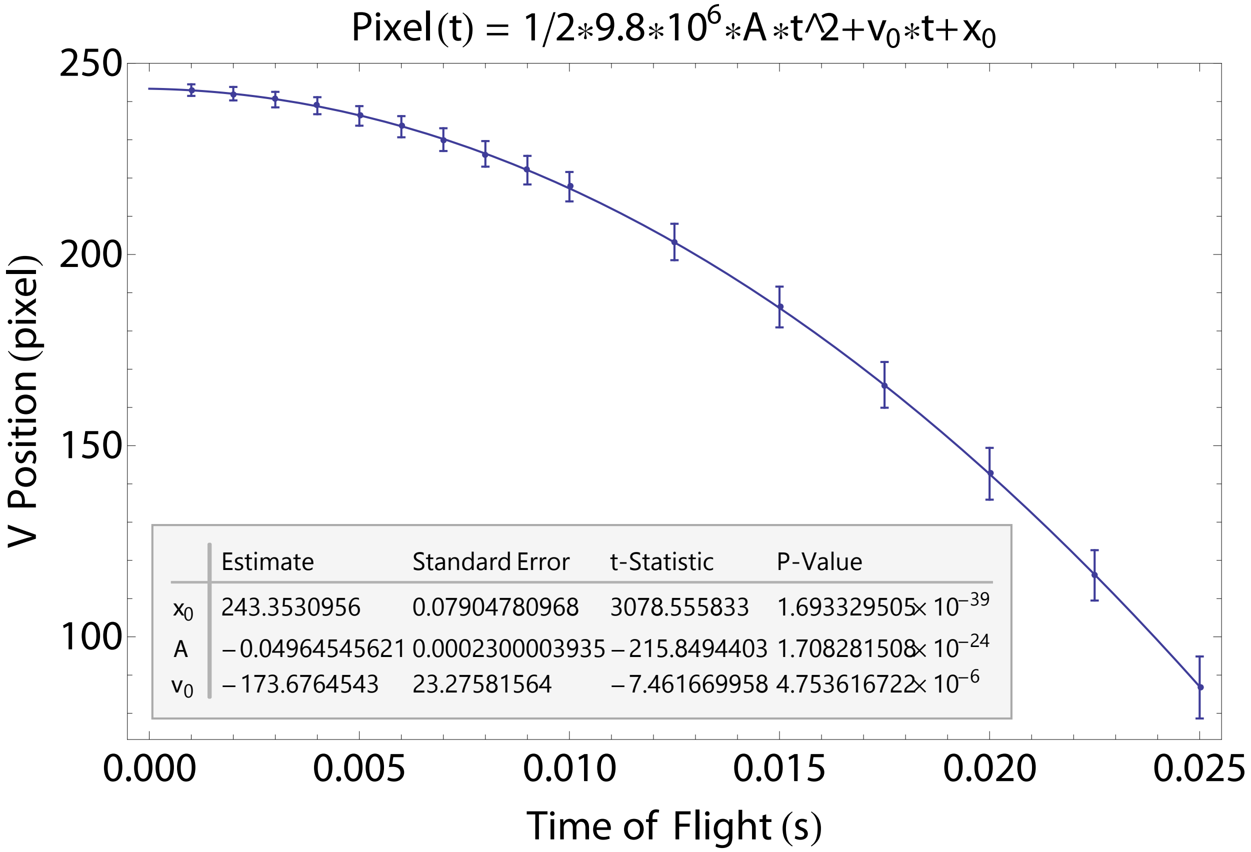

	Estimate	Standard Error	t-Statistic	P-Value
x_0	243.3530956	0.07904780968	3078.555833	$1.693329505 \times 10^{-39}$
A	−0.04964545621	0.0002300003935	−215.8494403	$1.708281508 \times 10^{-24}$
v_0	−173.6764543	23.27581564	−7.461669958	$4.753616722 \times 10^{-6}$

Figure 5.3: The measured vertical position of the cloud center versus time of flight. Used to calibrate length correspondign to one CCD pixel in our atom cloud images.

horizontal direction (perpendicular to the CCD) remained below 1 mm/s while the initial velocity in the vertical direction varied between 3 and 10 mm/s. In the images of our atom clouds, we find that one CCD pixel corresponds to 20.3 ± 0.3 μm. This is consistent with previous measurements [10] and the expected result from our imaging system.

In addition to knowing the size of the atom cloud, we must also know how many atoms it contains. To accomplish this, we calibrate the signal from our PMT at a reference ToF to the true number of atoms. We start by measuring the number of atoms in the blue MOT. We first measure the lifetime of the MOT in the absence of re-pumping lasers to determine the intensity in all six trapping beams, as detailed in [9]. From this intensity and the fluorescence collection geometry we can deduce the atom number in the blue MOT. Next we measure the transfer efficiency to

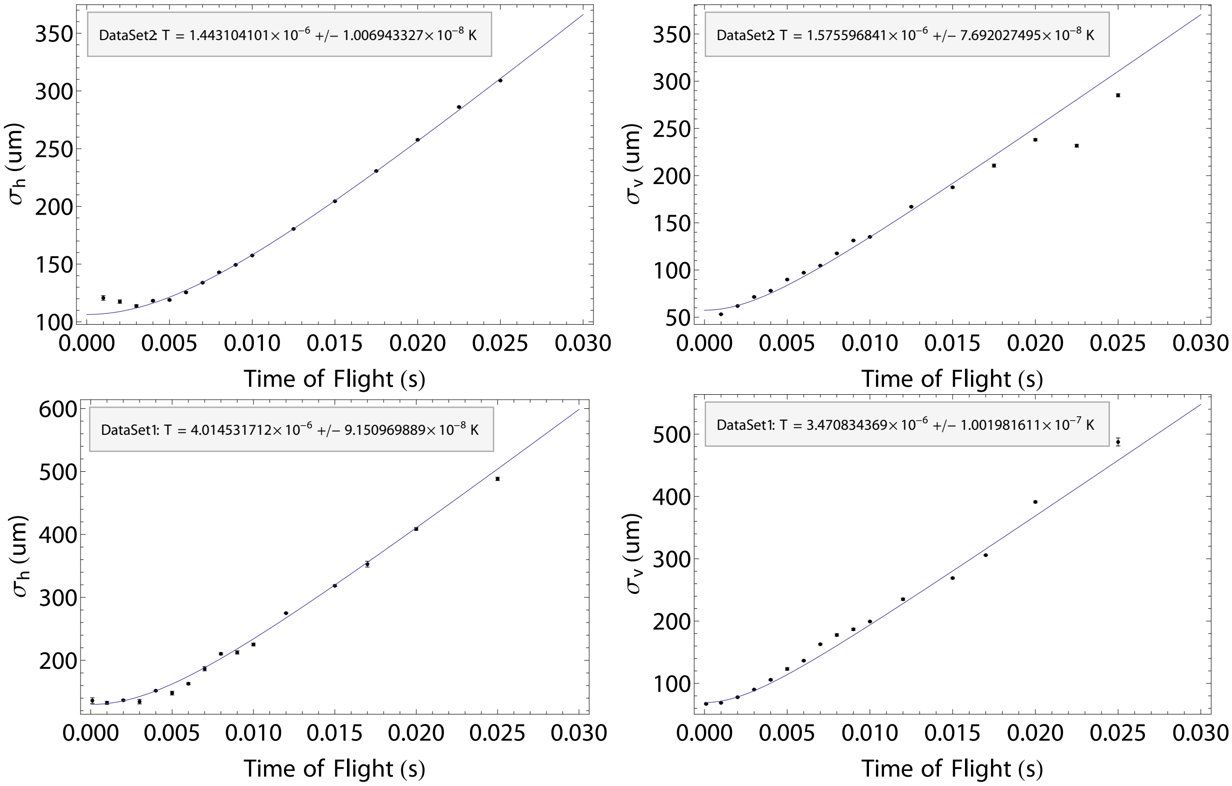

Figure 5.4: Two example measurements of cloud temperature. The plotted cloud radius versus time is fit to the function described in the text to extract cloud temperature. After data set 1 the power of the red MOT beams were adjusted to decrease the cloud temperature, resulting in a more dense sample and greater broadening.

the broadband red MOT and also between the broadband red MOT and the atoms measured in ToF. The two steps are necessary because of the vastly different sizes and scattering rates of atoms in the blue MOT stage and in the ToF stage. We must also take care to measure the atoms after a sufficient amount of ToF time so that density dependent effects do not alter the collected fluorescence but not after so much time that the size of the atom cloud is comparable to the size of the probe beam. We find that for a constant number of atoms, the fluorescence signal decreases if the ToF is less than 5 ms, or greater than 15 ms due to the effects discussed above.

The temperature of the cloud is related to its velocity distribution by $T = \frac{M}{k_B}\sigma_{\mathrm{vel}}^2$ where M is the atomic mass and k_B is the Boltzmann constant. We can fit the velocity distribution from the measured cloud radius versus time. The two quantities are related by the equation, $\sigma(t) =$

$\sqrt{\sigma_0^2 + t^2 * \sigma_{\text{vel}}^2}$, where σ_0 is the initial cloud radius. Fig. 5.4 shows two examples of the measured cloud temperature in the vertical and horizontal dimensions before and after the power of the MOT beams was adjusted to maximize broadening. After this adjustment, the cloud temperature remained between 1.3 and 2.2 μK in both dimensions.

With the atom number and pixel size of our CCD camera both calibrated, we are able to extract quantities such as the optical depth (OD) and density. The mean density of the atomic cloud can be approximated by $n = \frac{N}{(2\pi)^{3/2} * \sigma_x * \sigma_y * \sigma_z}$, where N is the number of atoms, and σ_i is the cloud radius in the i^{th} dimension (see Appendix A). The mean OD for resonant light is given by $b_0 = \frac{3 * N}{2(k * \sigma_\perp)^2}$, where k is the wavenumber of the atomic transition and $\sigma_\perp$ is the geometrical mean of the cloud radii along directions perpendicular to the detection axis. For light collected with the PMT we have $\sigma_\perp = \sigma_y$ and for light collected with the CCD we have $\sigma_\perp = (\sigma_y \sigma_z)^{1/2}$.

5.2.2 A brief theory sketch

The light we detect originates from a cloud of N coupled dipoles being driven by an optical field. This is a difficult problem even for a two level atom and this system has been the topic of recent theoretical [134, 135] and experimental [136] investigations of collective effects. In this case, an analytic expression for the OD dependent linewidth of scattered light has been derived: [135]

$$\Gamma = \Gamma_0(1 + b_0/12). \tag{5.1}$$

At the heart of this broadening is retarded dipolar coupling between atoms. In the case of real atomic transitions, the problem is further complicated by angular momentum since, the excited states we probe have total electronic angular momentum $J = 1$, which provides three magnetic sublevels to populate, each with their own unique polarization dependencies. Nevertheless, while our more complicated situation is being set on solid theoretical ground, we can compare to the two-level prediction to see how well it fairs. Additionally, the question of if this OD dependent broadening is also accompanied by a frequency shift is a hotly debated topic. Cooperative Lamb shifts have been measured in iron atoms implanted in a planer cavity [137] and rubidium atoms in

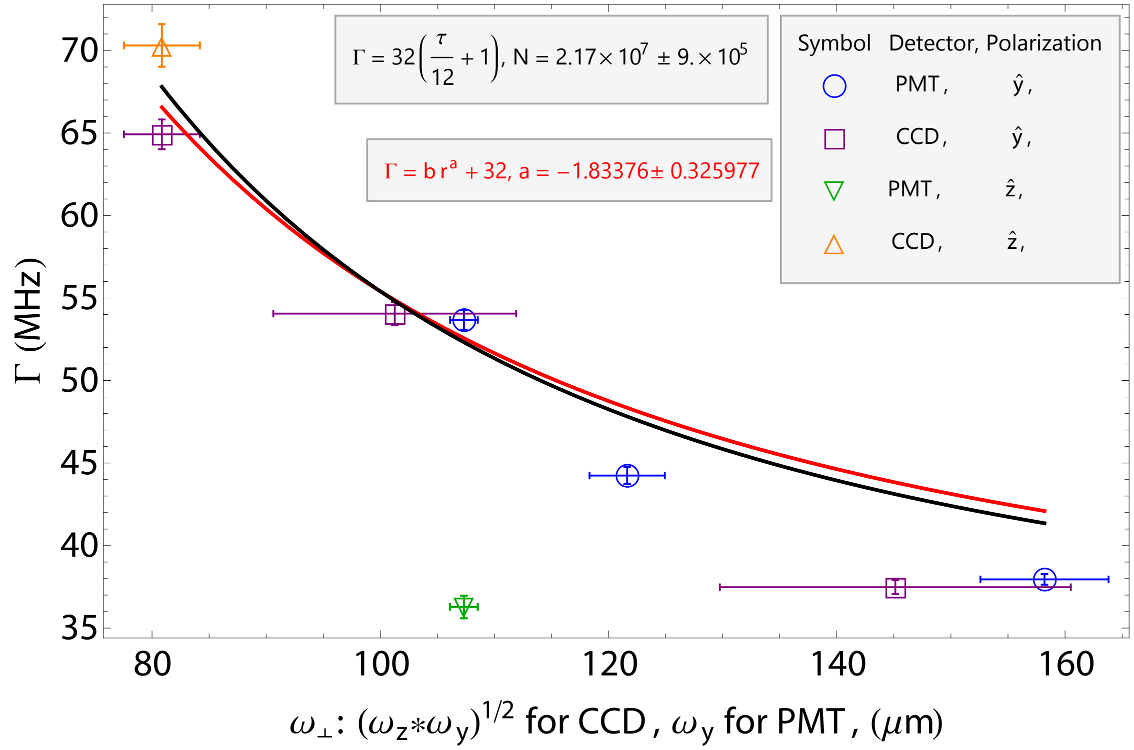

Figure 5.5: Measured linewidths of the blue transition versus $\sigma_\perp$. Blue points represent linewidths measured by the PMT for $\hat{y}$ polarized probe light. Purple points represent linewidths measured by the CCD for the very same experimental cycles (simultaneous with blue data). Similarly, the green point is the linewidth measured by the PMT for a $\hat{z}$ polarized probe beam and the orange point represents the simultaneously measured linewidth but from the view of the CCD. The red line represent a fit to the $\hat{y}$ polarized data of the form $\Gamma = b * r^a + \Gamma_0$. Γ_0 is held fixed to 32 MHz. If Γ_0, a, and b are all allowed to fit freely, the resulting numbers are unphysical (negative Γ_0 and $|a| < 1$). The black line represents a fit to Eqn. 5.1 where we let N fit freely to match the data.

a nano-thickness sapphire vapor cell [138], but never for atoms in free space, although theoretical models have predicted a shift that is proportional to atomic density [139, 140].

5.2.3 Preliminary measurements of broadening

We first turn our attention to the blue transition. Fig. 5.5 summarizes our measurements using a linearly polarized probe beam. We observe strong broadening in the PMT signal for probe polarization along $\hat{y}$ but no broadening when the probe is polarized along $\hat{z}$. With the CCD, we observe strong broadening for both $\hat{y}$ and $\hat{z}$ polarized probe beams. Since the atom cloud starts

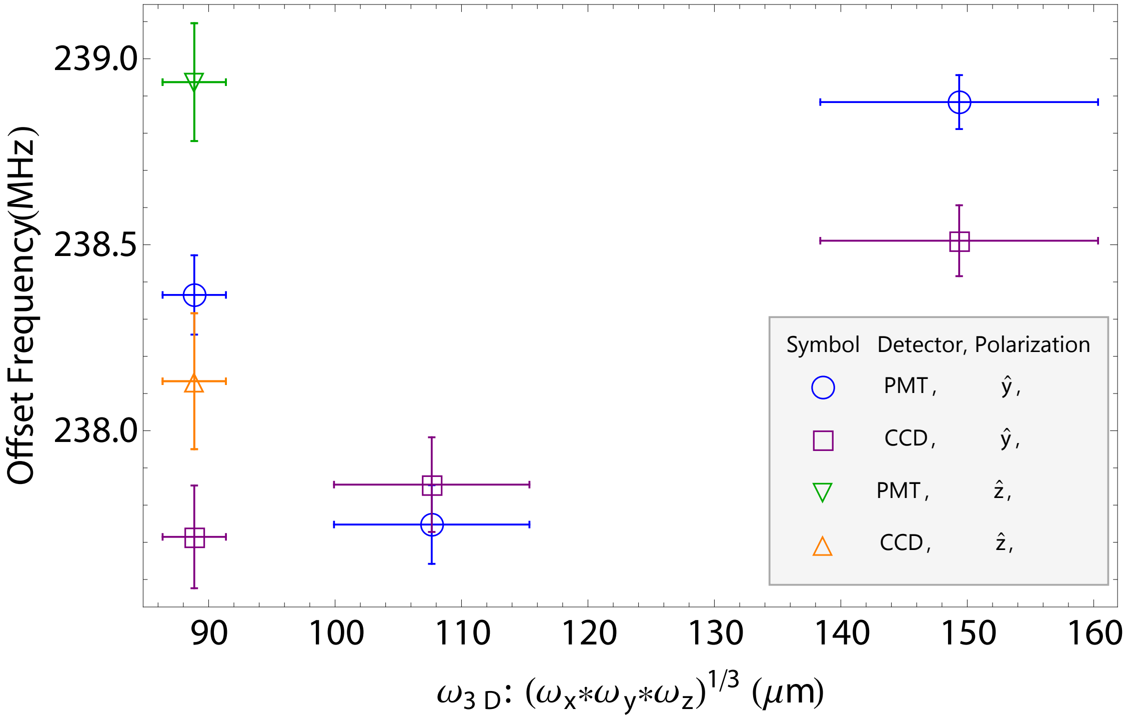

Figure 5.6: The measured transition center versus the geometrical mean of cloud radii. Line centers are derived from the Lorentzian fit. The experimental conditions here are the same as in Fig. 5.5.

with an asymmetric aspect ratio, linewidths measured in the PMT and CCD are quite different. Yet, when the data are plotted versus $\sigma_\perp$, the $\hat{y}$ polarized probe data from both detectors seem to lie on a single curve, supporting the OD dependence of the broadening. When we fit a power law dependent broadening to the $\hat{y}$ polarized data, letting only the amplitude and exponent fit freely, we get that the fitted curve gives a $\sigma_\perp^{-2}$ dependence. Using Eqn. 5.1 we fit out the atom number of the cloud to be 2×10^7 atoms, which is within a factor of 2 of our estimated value, 1.4×10^7, from the blue MOT population and transfer efficiencies.

We also look for frequency shifts of the transition center in this same data. Figure 5.6 shows the measured line centers versus the geometrical mean of the cloud radii. We see that when cloud is small and dense, there appears to be a negative shift of the line center, except for the measurement made by the PMT with a $\hat{z}$ polarized probe beam where no broadening was observed. Unfortunately, our data set is too small to draw any quantitative conclusions.

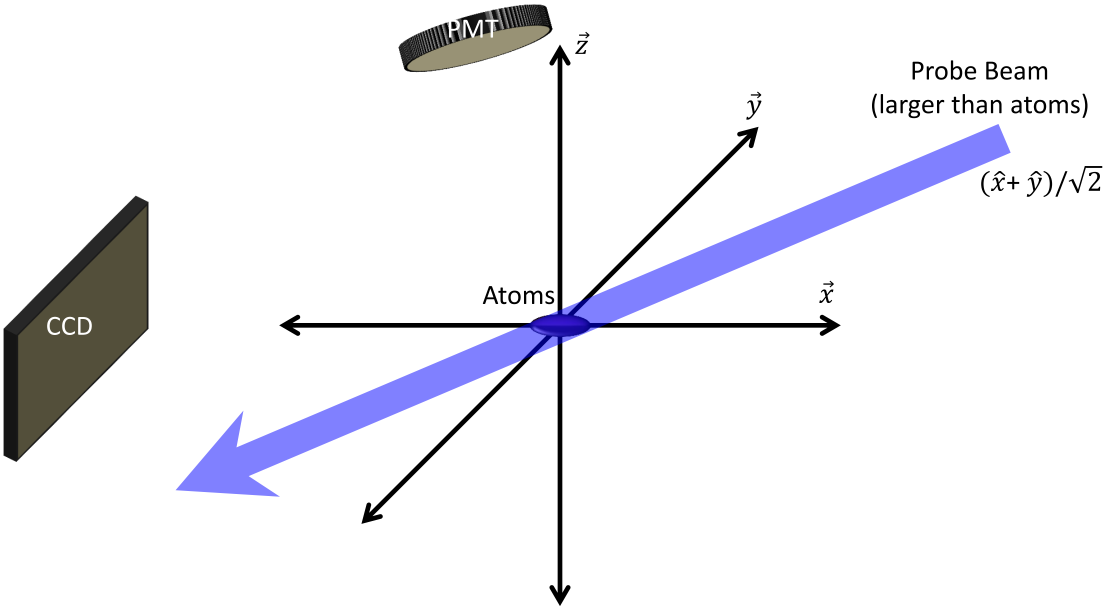

Figure 5.7: A diagram of an alternate probing scheme used with a circularly polarized probe beam. Here, the probe beam travels along the $(\hat{x}+\hat{y})/\sqrt{2}$ direction.

Moreover, the frequencies are referenced to a strontium discharge based spectrometer which is believed to demonstrate instabilities at the 1 MHz level. Additional data should illuminate the density dependence of this shift in the near future.

We have taken a much more extensive set of data using a circularly (σ) polarized probe beam traveling along a different path in the horizontal plane. Figure 5.7 demonstrates this alternate probing scheme. Although theory comparisons will inevitably be more difficult in this more complicated geometry, the large data set we have accumulated is illuminating.

If we look at the broadening in the fluorescence seen by the PMT and the CCD, we see that while the two detectors show a similar trend versus $\sigma_\perp$, there appears to be a static offset between the linewidths measured with the two detectors. Figure 5.8 shows the linewidths measured with

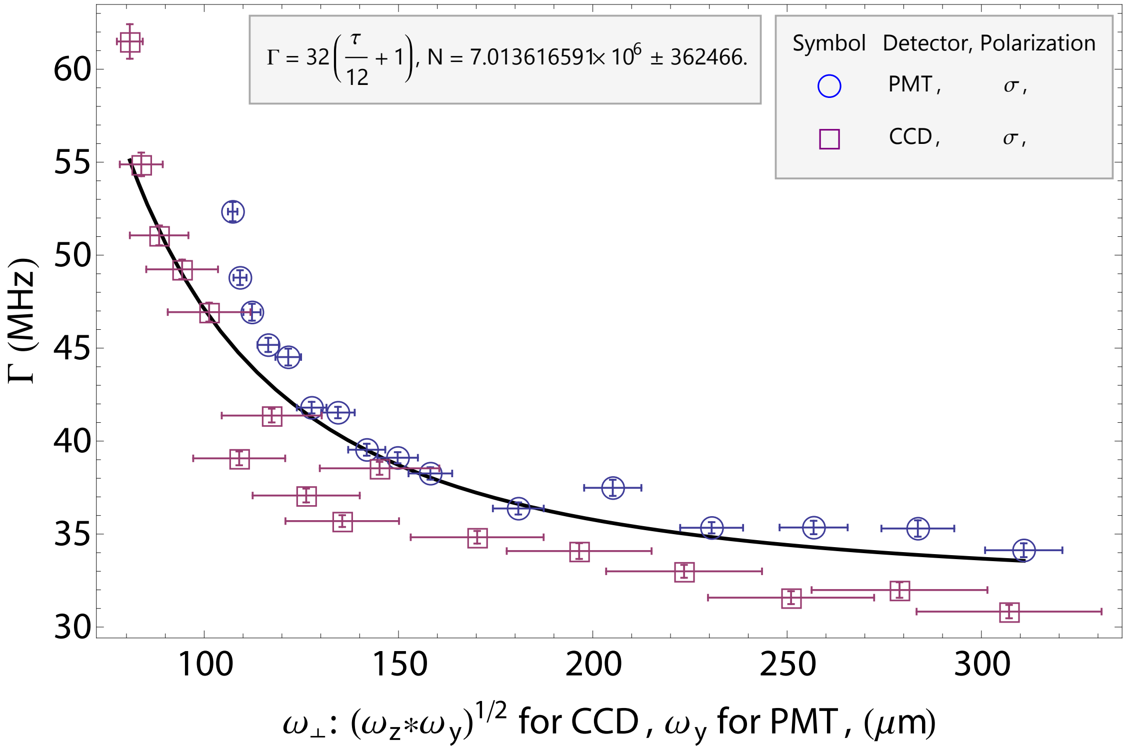

Figure 5.8: Measured linewidths versus $\sigma_\perp$ using the alternate probing geometry shown in Fig. 5.7 and a σ polarized probe beam. Blue circles correspond to linewidths measured with the PMT while purple squares correspond to measurements with the CCD.

the PMT and the CCD using this alternate probing scheme and a σ polarized probe. When we fit the atom number to both data sets simultaneously using Eqn. 5.1, we get that the atom number is 7×10^6, over a factor of 2 below the number fit from our linearly polarized probe scheme. It is important to note that the calibrated fluorescence level from the PMT is very similar between the linearly polarized probe data in Fig. 5.5 and the σ polarized probe data in Fig. 5.8, indicating that the atom number did not actually change. In fact, both data sets were acquired on the same day and under identical MOT loading conditions. Rather, it is likely that the broadening measured with the σ polarized probe is weaker due to the geometry used or the probe polarization (or both).

We also measure the line centers of the σ polarized probe data. This data shows an opposite trend as the linearly polarized probe data. As shown in Fig. 5.9(a), the line center shifts higher when the cloud is smallest. This higher frequency at large density is common to the PMT and the

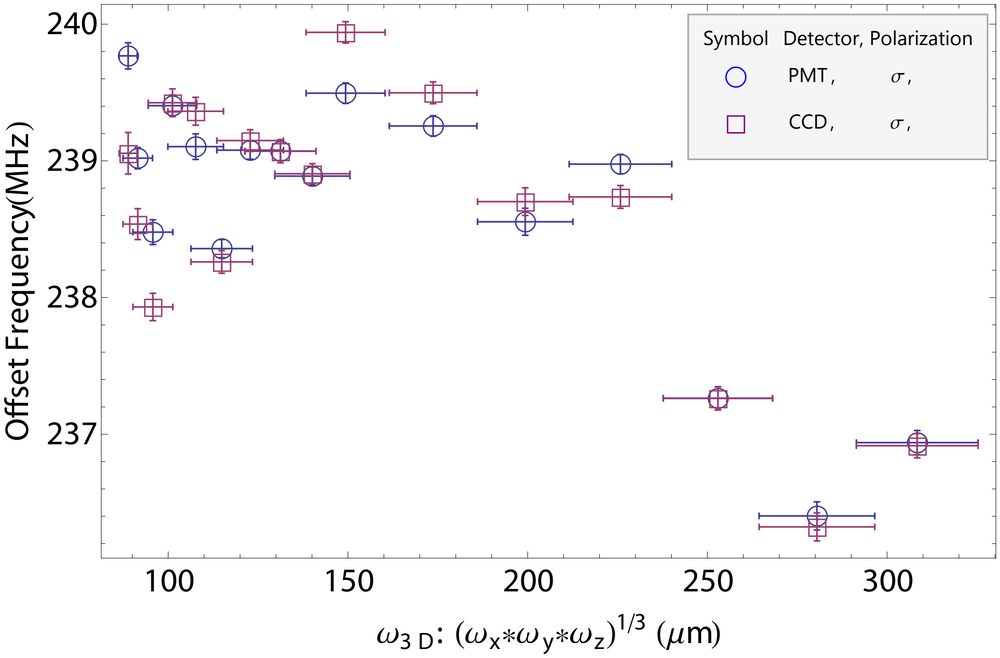

(a) Line Centers

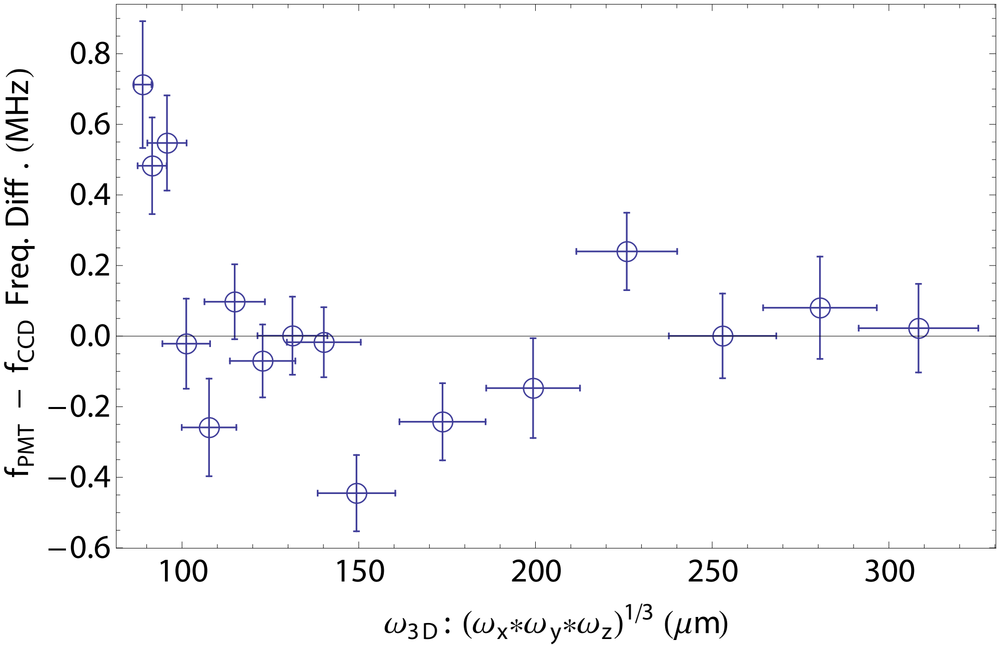

(b) PMT - CCD center difference

Figure 5.9: (a) Measured line centers versus the mean cloud radius for blue transition fluorescence as seen by the PMT and the CCD. (b) The difference between line centers measured by the two detectors versus mean cloud radius.

CCD and seems to remain constant until the mean cloud radius surpasses 250 μm. Once again we must be careful to draw conclusions from this data because the shift is still on the same level as fluctuations in our probe spectrometer. Figure 5.9(b) shows the difference between the linecenters measured by the PMT and the CCD. This quantity is immune to fluctuations of our probe laser spectrometer. The difference appears to start positive, decrease to zero, and become briefly negative between cloud radii of 150 and 200 μm before settling to zero. It will be interesting to see if theory reproduces this complicated behavior.

Moving to the red transition, we once again consider a linearly polarized probe beam traveling along the $-\hat{x}$ axis (Fig. 5.1). For this transition, we apply a 2 Gauss field in the $\hat{y}$ direction to separate the frequencies of the excited state magnetic sublevel transitions and only probe the field insensitive $m_J = 0$ to $m_J = 0$ transition. We measure fluorescence versus detuning for three different linear polarizations: along $\hat{y}$, along $\hat{z}$, and at 45° between these two axes (diagonal). For the red transition, the spectrometer used to lock the probe laser is known to have a long term drift. Moreover, motional effects contribute to the line center at the kHz level as well. Therefore, we do not consider the line center for this transition. The CCD is also not sensitive enough to detect red fluorescence so we only use the PMT. The broadening in this case is also complicated by Doppler broadening of the transition. While the natural linewidth of the red transition is 7.5 kHz, Doppler broadening at 1-2 μK is $30 - 50$ kHz. Therefore, we fit a Voigt profile to the measured line shapes. We take two approaches to this fit.

In the first approach, we let the Lorentzian and Gaussian widths of the fit vary freely (Fig. 5.10). In this case, both the $\hat{y}$ and $\hat{z}$ polarized probe line shapes do not initially show broadening of the fit Lorentzian linewith. While the $\hat{y}$ polarized probe data demonstrates nearly the same Lorentzian linewidth at all values of $\sigma_\perp$, the $\hat{z}$ polarized probe data shows a very quick increase in the fitted Lorentzian linewidth which does not decrease as $\sigma_\perp$ continues to increase. At values of $\sigma_\perp$ larger than ~ 225 μm, the $\hat{z}$ polarized probe data does not scatter enough light into the PMT for detection, as one might expect from a simple dipole radiation pattern. The diagonally polarized probe data demonstrates an initial broadening of the fitted Lorentzian linewidth which decreases

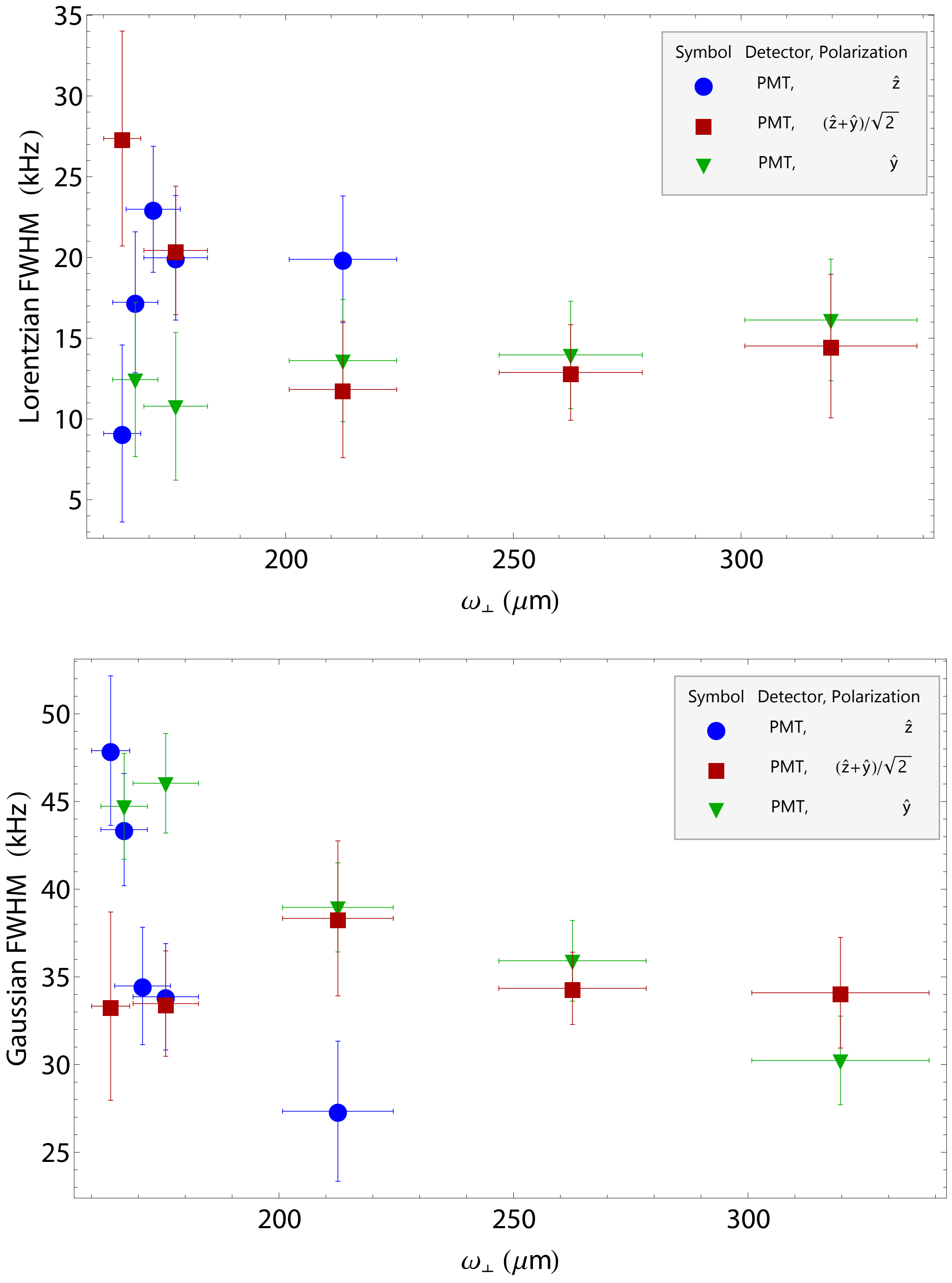

Figure 5.10: For the red transition we plot the fitted Lorentzian and Gaussian FWHM versus $\sigma_\perp$ for a Voigt profile where both linewidths are allowed to fit freely. Three probe beam polarizations are measured: $\hat{y}$ (green triangles), $\hat{z}$ (blue circles) and at 45° between $\hat{y}$ and $\hat{z}$ (red squares).

with increasing $\sigma_\perp$ until $\sigma_\perp \approx 200$ μm where the fitted linewidth is consistent with the $\hat{y}$ polarized probe data.

Surprisingly, the fitted Gaussian linewidths also demonstrate an $\sigma_\perp$ dependence that is different from that of the fitted Lorentzian linewidths. Both the $\hat{z}$ and $\hat{y}$ polarized probe data demonstrate a Gaussian linewidth that decreases with increasing $\sigma_\perp$, although the $\hat{z}$ polarized probe data decreases much faster. The diagonally polarized probe data demonstrate a nearly constant fitted Gaussian linewidth which is consistent with the ~ 1 μK temperature of the atoms and is consistent with the $\hat{y}$ polarized probe data at larger values of $\sigma_\perp$. Unfortunately, we observe a slight asymmetry in the measured line shapes (see Fig. 5.2(b)) that could systematically effect the fitted widths. In the future, a more simple scheme for applying our bias field in the $\hat{y}$ direction may eliminate this asymmetry if it is due to magnetic field misalignment. This scheme was successfully used in [141] to observe density dependent broadening without asymmetric line shapes.

With the asymmetry in mind, we can fix the Gaussian linewidth to be consistent with the 1.3 μK temperature that was measured for this data condition[a] . Figure 5.11 shows the fitted Lorentzian linewidths versus $\sigma_\perp$ for the three probe polarizations when the Gaussian linewidth is held fixed. In this case, the data show a consistent trend of decreasing linewidth with increasing $\sigma_\perp$. The three probe polarizations differentiate themselves by the rate at which the fitted linewidth decreases with the $\hat{z}$ polarized probe data decreasing the fastest and the $\hat{y}$ polarized probe data decreasing the slowest. This could be explained by a polarization independent, density-dependent broadening that dies out more quickly ($\propto (\sigma_x\sigma_y\sigma_z)^{-1}$) than the cooperative broadening ($\propto \sigma_\perp^{-2}$). Since we showed the cooperative broadening did not affect the linewidth for a $\hat{z}$ polarized probe in the blue transition, this would explain why broadening persists longer in the $\hat{y}$ polarized probe data which does experience cooperative broadening.

---

[a] It should be noted that later measurements of the temperature under identical conditions gave temperatures of about 2 μK, however, this temperature leads to fitted Lorentzian linewidths that are negative.

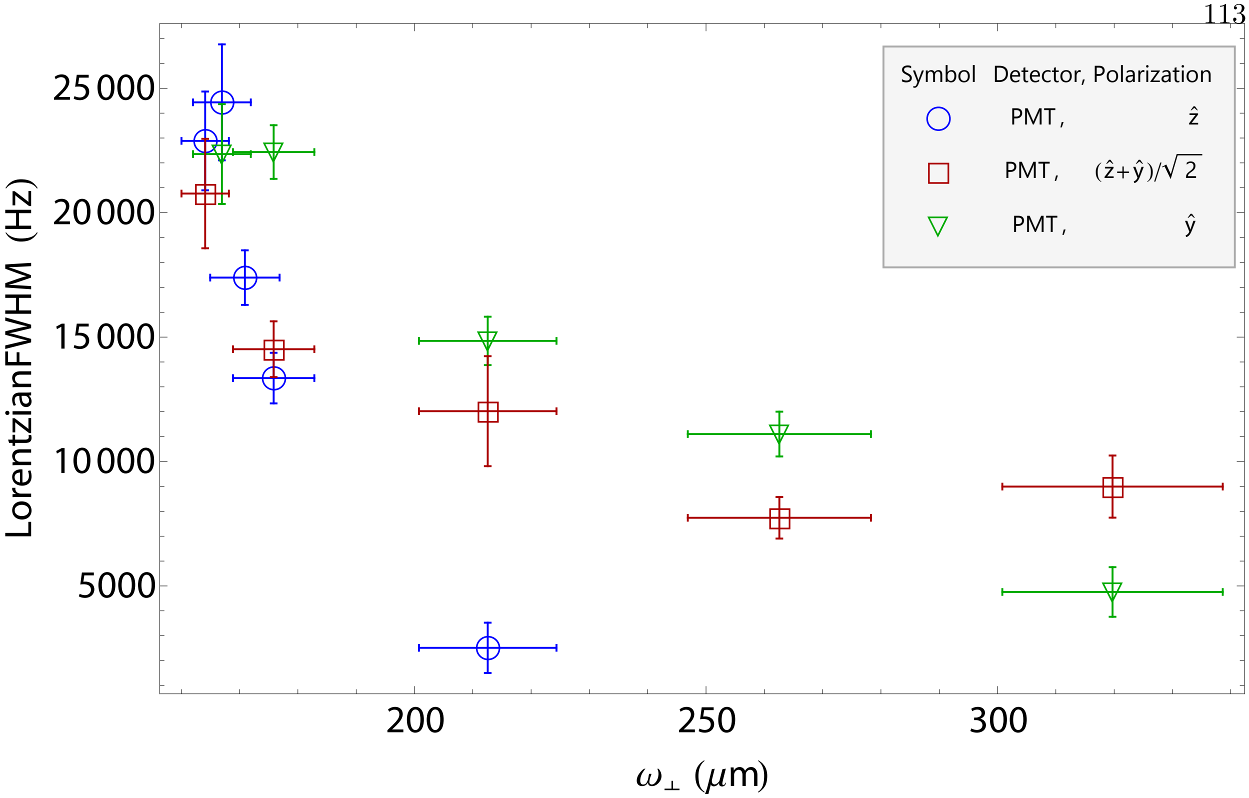

Figure 5.11: For the red transition we plot the fitted Lorentzian FWHM versus $\sigma_\perp$ for a Voigt profile where the Gaussian FWHM is held constant to 38kHz, corresponding to 1.3uK. Three probe beam polarizations are measured: $\hat{y}$ (green triangles), $\hat{z}$ (blue circles) and at 45° between $\hat{y}$ and $\hat{z}$ (red squares).

5.2.4 Conclusions for broadening in free atoms

Motivated by a previous observation of anomalously large natural linewidth broadening in the red transition [141], our experimental investigation aims to uncover the physical mechanism of this broadening. Our measurements of the blue and red transition have demonstrated that collective dipolar coupling is definitely contributing to the linewidth broadening because the effect scales with the transition linewidth and demonstrates a dependence on the optical depth of the atoms. Our current study provides unique insight into collective radiative coupling because we provide a very clean investigation of the underlying physical mechanism in the blue transition where collective effects dominate. Complimentary to this simple case, we can also provide measurements of collective broadening in the red transition where complications such as motional effects play a significant role in the observed fluorescence features. In alkali atoms is is much more difficult to disentangle these effects since they have similar contributions to the observed fluorescence features. The theoretical model that is being developed to explain our measurements could also provide insights into other collective dipolar systems such as Rydberg gases.

5.3 Strong Coupling to an optical cavity: future experiments with strontium

Ensembles of atoms coupled to optical cavity modes have the potential to demonstrate significant advances in precision measurement science via quantum non-demolition measurements [142, 143, 144, 145] and spin-squeezing [146, 147, 148, 143, 144, 149, 150, 151]. Furthermore, the non-classical states that are achievable in these systems could also lead to breakthroughs in quantum information and many-body physics [152, 153, 154, 155, 156, 157, 158, 159]. Experimental implementations of atom-cavity coupling have mostly been limited to alkali atoms. Although these atoms are extensively used in cold-atom-based sensors [160, 161, 162] and clocks [163, 24, 164], which could undoubtedly benefit from the increased spectroscopic sensitivity enabled by strong cavity coupling, alkaline-earth(-like) atoms, owing to their unique properties, are beginning to produce significant measurement improvements over their alkali counterparts. For example, while Cs based clocks have achieved 10^{-16} fractional systematic uncertainty and 10^{-13} fractional stability at 1 s, ^{87}Sr optical lattice clocks have achieved a fractional systematic uncertainty of 6×10^{-18} [2] and a fractional 1 s stability of 3×10^{-16} [1, 30]. Similarly, alkaline-earth(-like) atoms have also enabled a novel approach to studying many-body physics [4] and quantum magnetism [130, 5] and there are also multiple proposals to leverage the unique properties of these atoms for quantum computing and simulation [105, 103].

It is only natural, therefore, that we should aim to explore cavity quantum electrodynamics (cQED) with strontium atoms. This section will describe the experimental system we have designed for this purpose and calculate the expected performance of this system based on a simple model for coupling an atomic ensemble to an optical cavity [142].

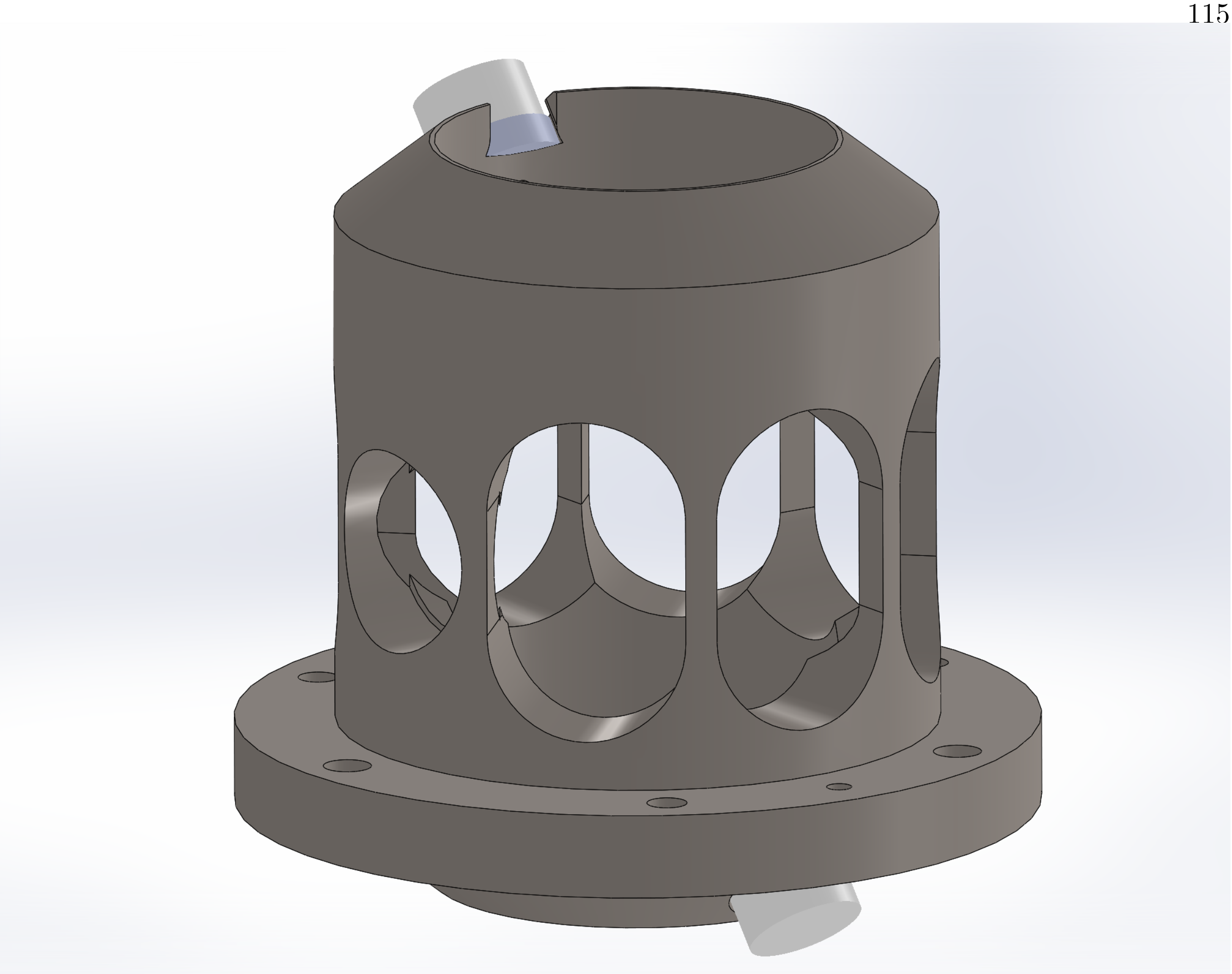

Figure 5.12: Drawing of the cavity mount to be used for strongly coupling strontium atoms to a high finesse optical cavity.

5.3.1 System Design

The primary goal in the design of our cavity is to achieve strong coupling to strontium atoms while not ruining the properties that make strontium so attractive for metrology. This presents a unique engineering challenge owing to a combination of many factors. Looking back on Chapter. 1, we will walk through the various components that make up our clock experiment and explain how the cavity spacer and mirrors that we plan to add to our experiment have been designed with the clock in mind.

Arguably the most important feature for a cQED system is to actually locate atoms within the cavity light field. Figure 5.12 shows the design of our cavity spacer. The oval shaped holes allow the atom beam, slowing light, and horizontal MOT beams to enter into the center of the spacer, where they intersect. The oval holes are roughly ~ 0.5 in by 1 in to allow large blue MOT beams to capture a large number of atoms. The top and bottom of the spacer also have large ~ 1 in openings for the vertical MOT beams. Once trapped and cooled to ~ 1 μK, the atoms need to be transfered into a magic wavelength optical lattice. To accommodate this, the cavity mirrors have high reflectivity at 813 nm and should achieve a finesse of about 1000 at this wavelength. Since the cavity coupling light will inevitably be at a different wavelength than the trapping light, the choice to use the cavity mirrors for both strong coupling and trapping leads to trapping sites that are non-commensurate with the cavity-coupling light field. Alternatively, one could interfere two trapping laser beams at an angle θ such that $\lambda_{\mathrm{trap}}/(2\sin[\theta/2]) = \lambda_c$ ($\sim 72^\circ$ for $= \lambda_c = 689$ nm coupling light), however, this adds complexity and alignment woes to an already complex experiment and we decided to go with the simplest geometry for our experiment.

With the atoms safely trapped at the center of the cavity, we now must be able to precisely and uniformly excite the clock transition at 698 nm. One inhibitor to achieving this is reflection from the cavity mirrors that cause unwanted interference patterns in the clock laser beam. Unfortunately, we will see in the following paragraph that the ideal atomic transition for cavity couping lies at 689 nm. Achieving high finesse at 689 nm and very low reflectivity at 698 nm is challenging for even today's most advanced coating technologies. The specifications for our cavity mirrors are for a finesse of $\sim$100,000 at 689 nm and reflectivity below 5 % at 698 nm. To estimate how much this will affect our measurements we calculate the worst-case variation in excited state fraction for 5% mirror reflectivity at 698 nm and perfect mode matching into the cavity. In terms of peak mean excitation fraction, this limits us to 94.2%, which doesn't sound too disastrous. However, if we consider the spread in excitation fraction for a $\pi/2$ pulse, As shown in Fig. 5.13, this results in a 34% peak-to-peak variation in excited state fraction corresponding to a standard deviation of 12%. This magnitude corresponds to the quantum projection noise (QPN) for approximately 18 atoms which scales inversely with the square root of atom number (see Eqn. C.3). Thus, if we

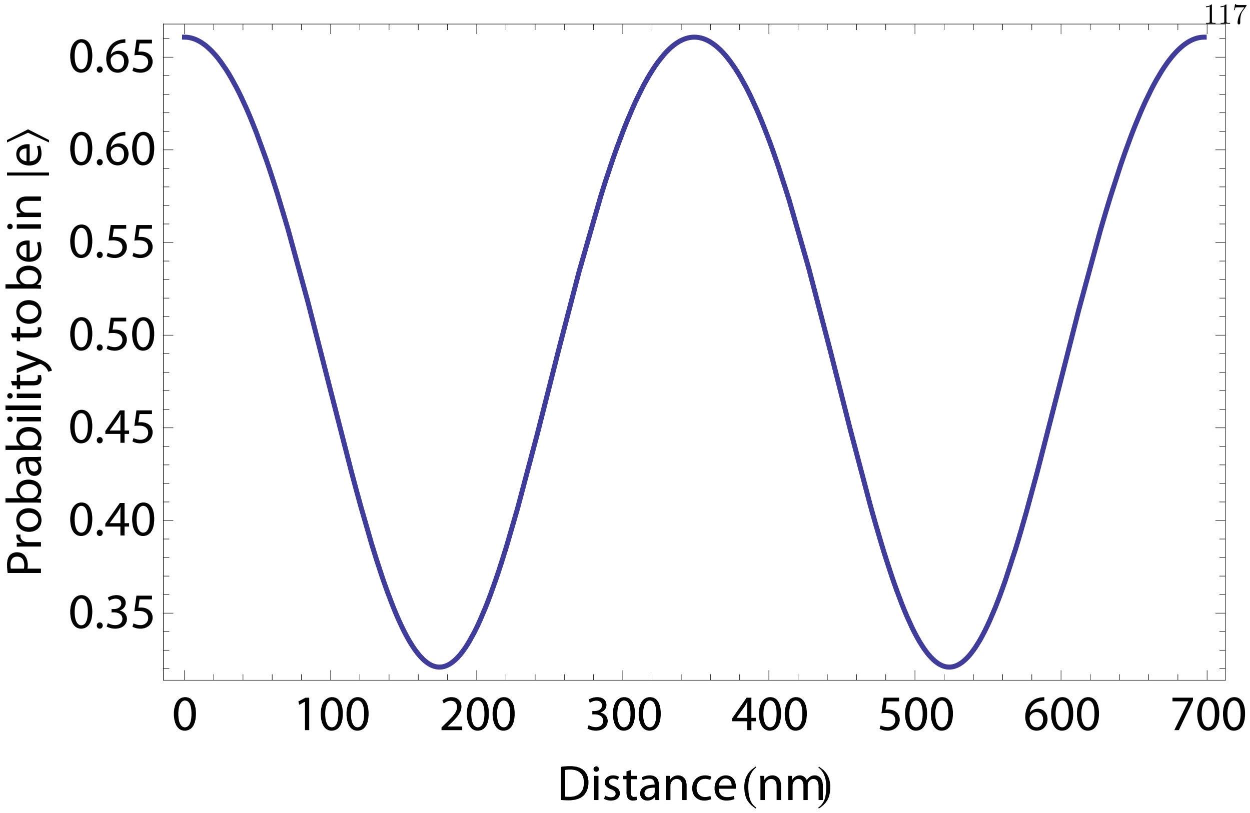

Figure 5.13: Calculation of variation in $|e\rangle$ excitation after $|g\rangle$ atoms are excited such that the mean probability to be in $|e\rangle$ is 1/2 ($\pi/2$ pulse). The calculated variation is due to cavity mirror reflectivity at 698 nm. We assume 5% reflectivity at 698 nm and perfect mode matching to the cavity mode.

want to make use of a large number of atoms in our cavity, care should be taken so that clock laser reflections from cavity mirrors do not make it back to the atoms. This could be achieved through slight intentional misalignment and beam shaping.

Finally, we must choose the atomic transition used for strong atom-cavity coupling. Our goal is to detect the population imbalance between ground, $^1\mathrm{S}_0$ F $= 9/2$ $\mathrm{m_F} = \pm 9/2$ ($|g\rangle$), and excited, $^3\mathrm{P}_0$ F $= 9/2$ $\mathrm{m_F} = \pm 9/2$ ($|e\rangle$), clock states. For this reason, a cycling transition from one of the clock states is ideal because any non-cycling transition would disturb the very state we wish to detect, causing decoherence. The only true cycling transition from either clock state is the $|g\rangle$ to $^3\mathrm{P}_1$ F $= 11/2$, $\mathrm{m_F} = \pm 11/2$ ($|d\rangle$) transition at 689 nm. Another option is to use the broad dipole allowed $|g\rangle$ to $^1\mathrm{P}_1$ transition, however, this transition has a small leak to the $^1\mathrm{D}_2$ state. Moreover,

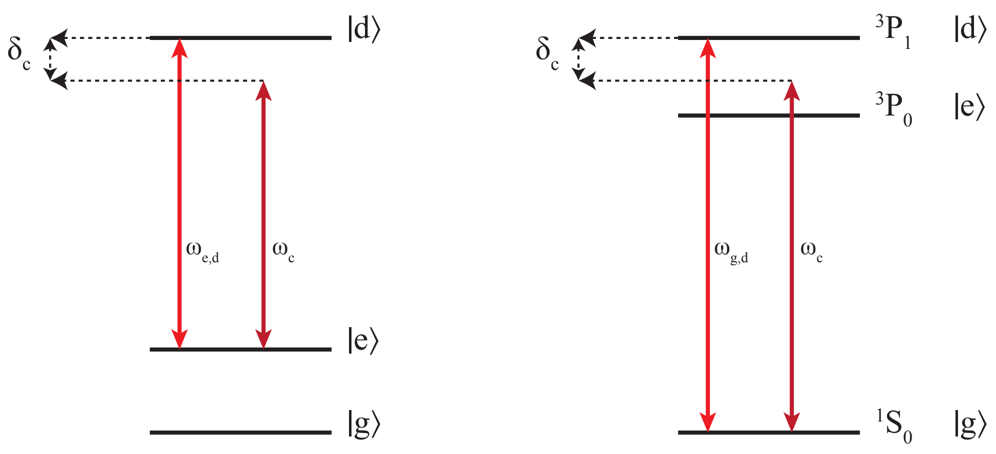

(a) Rb cavity coupling (b) Sr cavity coupling

Figure 5.14: Schematic diagrams (not to scale) for the relevant levels used in coupling atomic ensembles to optical cavities. Fig. 5.14(a) shows a common scheme used for Rb atoms where an optical cavity is tuned to the optical transition between $|e\rangle$ and $|d\rangle$. The coupling between the cavity and the atomic ensemble is used to probe the population difference between $|g\rangle$ and $|e\rangle$, which are separated by a microwave frequency. Fig. 5.14(b) shows the proposed cavity coupling scheme for ^{87}Sr. In this case, the clock states ($|g\rangle$ and $|e\rangle$) are separated by an optical frequency and we probe the population difference between these states using a cavity tuned to the $|g\rangle$ to $|d\rangle$ transition, which is also at an optical frequency.

in addition to being a true cycling transition, the $|g\rangle$ to $|d\rangle$ transition has a natural linewidth of $2\pi \times 7.5$ kHz, which allows us to selectively couple to the different hyperfine levels within the $^3\mathrm{P}_1$ manifold using a high finesse cavity with narrow linewidth. Figure 5.14 contrasts the proposed cavity-coupling scheme for ^{87}Sr with a common scheme used in Rb.

5.3.2 Calculating the peak single atom vacuum Rabi frequency

Table 5.1 lists the various design parameters for our cavity system. These values, along with the atomic properties of ^{87}Sr , will determine the coupling strength between cavity and atoms. Before going into detail about a model of the atom-cavity system, we can calculate the strength of the coupling from the dipole interaction of an atom and the vacuum field of a cavity mode that is tuned on resonance with the $|g\rangle$ to $|d\rangle$ transition. For an atom at the focus of the cavity mode and in an anti-node of the cavity, we define a frequency g_0, such that $\hbar g_0$ is equal to the electric dipole interaction energy $|\mu_{gd}\mathcal{E}_{\text{vac}}|$, where $\mu_{gd} = -e\langle g|\,\hat{x}\,|d\rangle$ (in this instance e is the electron charge) is the dipole matrix element of the $|g\rangle$ to $|d\rangle$ transition and $\mathcal{E}_{\text{vac}}$ is the amplitude of the vacuum field given by $\mathcal{E}_{\text{vac}} = \left(\frac{\hbar\omega_{g,d}}{2\epsilon_0 V_m}\right)^{1/2}$, with V_m the volume of the cavity mode and $\omega_{g,d}$ the $|g\rangle$ to $|d\rangle$ transition frequency. The quantity $2g_0$ is known as the vacuum Rabi frequency. Putting together the above relationships we get that g_0 is given by

$$g_0 = \left(\frac{\mu_{gd}^2\omega_{g,d}}{2\epsilon_0\hbar V_m}\right)^{1/2}. \tag{5.2}$$

For the TEM$_{00}$ cavity mode, $V_m = \frac{1}{4}\pi w_0^2 l$ where w_0 is the mode waist and l is the cavity length. Therefore, to calculate the coupling strength we now just need to calculate μ_{gd}. To accomplish this, we follow the procedure in [165] to relate the dipole matrix element $\mu_{gd} = -e\langle g|\,\hat{x}\,|d\rangle = -\langle F, m_F|\,e\hat{x}\,|F', m_{F'}\rangle$ to the reduced dipole matrix element, $\langle J|\,|e\hat{x}|\,|J'\rangle$ using the Wigner-Eckart theorem and addition rules for angular momenta [166]. This relationship is given by

$$\begin{aligned} &\langle F, m_F|\,e\hat{x}\,|F', m_{F'}\rangle = \\ &\langle J|\,|e\hat{x}|\,|J'\rangle\,(-1)^{F'+J+1+I}\sqrt{(2F'+1)(2J+1)}\begin{Bmatrix} J & J' & 1 \\ F' & F & I \end{Bmatrix} \\ &\times(-1)^{F'-1+m_F}\sqrt{2F+1}\begin{pmatrix} F' & 1 & F \\ m_{F'} & q & -m_F \end{pmatrix}. \end{aligned} \tag{5.3}$$

Here, () signifies a Wigner 3-j symbol, {} signifies a Wigner 6-j symbol, and $m_F = m_{F'} + q$. We can calculate the reduced matrix element $\langle J|\,|e\hat{x}|\,|J'\rangle$ from the linewidth of the $|g\rangle$ to $|d\rangle$ transition, Γ, as follows: [167]

$$\Gamma = \frac{\omega_{g,d}^3}{3\pi\epsilon_0\hbar c^3}\frac{2J+1}{2J'+1}\left|\langle J|\,|e\hat{x}|\,|J'\rangle\right|^2. \tag{5.4}$$

Putting in all the numbers from our cavity design and the $|g\rangle$ to $|d\rangle$ transition we get that the peak single atom vacuum Rabi frequency for our system is

$$2g_0 = 2\pi\times 19\,\text{kHz} \tag{5.5}$$

Table 5.1: A table of design parameters for our optical cavity

Parameter	Value
Cavity Length	5.16 cm
Free Spectral Range	$2\pi\times$ 2,900 MHz
Mirror Radius of Curvature	5 cm
Beam waist @ 689	74 μm
Cavity Finesse @ 689 nm	100,000
Cavity Linewidth @ 689 nm	$2\pi \times$ 29 kHz
Beam waist @ 813 nm	80 μm
Cavity Finesse @ 813 nm	1,000

5.3.3 Modeling the coupling between an atomic ensemble and an optical cavity

The most basic interaction between a cavity and an atomic ensemble is captured by the Tavis-Cummings model [168], which describes N two-level atoms coupled to a single cavity mode (this is the multi-atom extension of the Jaynes-Cummings model [169] for a single atom). Since we are only interested in the atom-cavity coupling we can even ignore $|e\rangle$ and focus entirely on $|g\rangle$ and $|d\rangle$. Neglecting constant terms and using the rotating wave approximation, the Hamiltonian for this model is given by

$$\hat{H}_{TC} = \hat{H}_{\text{field}} + \hat{H}_{\text{atoms}} + \hat{H}_{\text{int}} \tag{5.6}$$

where

$$\hat{H}_{\text{field}} = \hbar\omega_c \hat{c}^\dagger \hat{c}, \quad \hat{H}_{\text{atoms}} = \hbar\omega_{g,d}\hat{J}_z/2, \quad \textit{and} \quad \hat{H}_{\text{int}} = \hbar g(\hat{J}_-\hat{c}^\dagger + \hat{J}_+\hat{c})$$

where $\hat{J}_\alpha = \sum_i^N \hat{\sigma}_{i\alpha}$ with $\hat{\sigma}_{iz} = |d_i\rangle\langle d_i| - |g_i\rangle\langle g_i|$, $\hat{\sigma}_{i+} = |d_i\rangle\langle g_i|$, and $\hat{\sigma}_{i-} = |g_i\rangle\langle d_i|$, ω_c is the cavity frequency and $\hat{c}^{(\dagger)}$ is the photon annihilation(creation) operator for the cavity field. The atomic population in the $|\alpha\rangle$ state is given by the projection operator $\hat{N}_\alpha = \sum_i^N |\alpha_i\rangle\langle\alpha_i|$ whose expectation value is expressed as N_α. In the following section we will show how the effective single atom vacuum Rabi frequency, $2g$, and effective atom numbers N_g, N_e, and $N = N_g + N_e$ can be derived to account for the expected distribution of atoms within the cavity [146, 147, 149, 151].

For now, we can explore the behavior of this system in the limit where excitation to $|d\rangle$ is small, meaning $N_d/N \ll 1$. Following the procedure of [142], in this limit we use the Holstein-

Primakoff approximation [170] which replaces the collective spin operators with their approximate representation in terms of creation and annihilation operators. To understand this approximation, let us define the operator $\hat{\mathcal{N}} \equiv J + \hat{J}_z$ where $J = (N_g + N_d)/2$. The eigenvalue of $\hat{\mathcal{N}}$ for the state $|J, m_J\rangle$ is $\mathcal{N} = J + m_J$. In this representation, $|J, m_J = -J\rangle$ corresponds to all atoms in $|g\rangle$ and $|J, m_J = J\rangle$ corresponds to all atoms in $|d\rangle$. We can also represent the incremental increase(decrease) in spin projection with creation(annihilation) of bosons such that $|J, m_J = n - J\rangle \to \frac{1}{\sqrt{n!}}(\hat{a}^\dagger)^n |0\rangle$ and the number of bosons corresponds to the number of atoms excited to $|d\rangle$. Then we get that $\hat{\mathcal{N}} = \hat{a}^\dagger \hat{a}$, $\hat{J}_+ = \sqrt{2J}\hat{a}^\dagger \sqrt{1 - \frac{\hat{a}^\dagger \hat{a}}{2J}}$, and $\hat{J}_- = \sqrt{2J}\sqrt{1 - \frac{\hat{a}^\dagger \hat{a}}{2J}}\hat{a}$. For small $|d\rangle$ excitation, we can approximate $\sqrt{1 - \frac{\hat{a}^\dagger \hat{a}}{2J}} \approx 1$ since $\langle {}^{\hat{a}^\dagger \hat{a}}/{}_{2J} \rangle = {}^{N_d}/{}_{N_{\text{tot}}}$ is small. Now we get the approximations $\hat{J}_+ \approx \sqrt{N_g}\hat{a}^\dagger$ and $\hat{J}_- \approx \sqrt{N_g}\hat{a}$, where we have replaced $N_g + N_d$ with N_g since N_d is small.

Using this approximation, we can rewrite the Tavis-Cummings Hamiltonian in the frame rotating at the $|g\rangle$ to $|d\rangle$ transition frequency as [142]

$$\hat{H} = \hbar\delta_c \hat{c}^\dagger \hat{c} + \hbar\sqrt{N_g} g_0 (\hat{a}\hat{c}^\dagger + \hat{a}^\dagger \hat{c}), \tag{5.7}$$

where $\delta_c = \omega_c - \omega_{g,d}$. In the Heisenberg picture we get the coupled equations of motion

$$\frac{d\langle \hat{c} \rangle}{dt} = -i\delta_c \langle \hat{c} \rangle - i\sqrt{N_g} g_0 \langle \hat{a} \rangle, \tag{5.8}$$

$$\frac{d\langle \hat{a} \rangle}{dt} = i\sqrt{N_g} g_0 \langle \hat{c} \rangle \tag{5.9}$$

which give the eigenfrequencies of the system to be

$$\omega_\pm = \frac{\delta_c \pm \sqrt{\delta_c^2 + \Omega^2}}{2}, \tag{5.10}$$

where

$$\Omega \equiv \sqrt{N_g} 2g_0. \tag{5.11}$$

This demonstrates how the presence of $|g\rangle$ atoms in the cavity splits the cavity resonance into two resonances that are separated by $\sqrt{\delta_c^2 + \Omega^2}$. Ω is referred to as the vacuum Rabi splitting since the cavity resonances are split by Ω at zero detuning. Figure 5.15 shows the expected cavity resonance

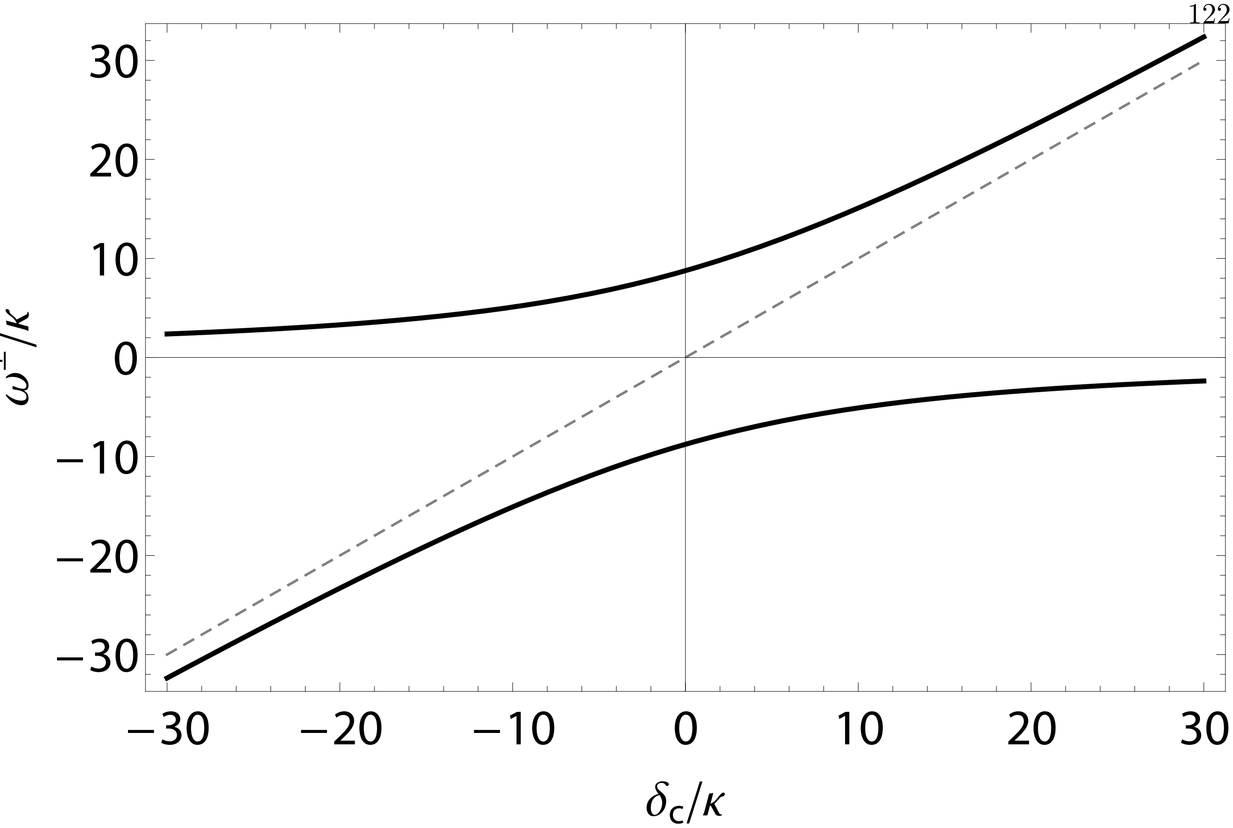

Figure 5.15: We plot the frequencies $\omega_{\pm}$ in thick black lines for an effective atom number of $N_g = 1000$ and a cavity finesse of 100,000. Frequencies are given in units of the cavity linewidth, $\kappa = 29kHz$ for this finesse. The dashed gray line represents the cavity resonance for an empty cavity.

locations normalized to the cavity linewidth for a modest N_g of 1,000 and the predicted finesse of 100,000. The cavity linewidth is given by $\kappa = \frac{\pi c}{l\mathcal{F}}$ with c the speed of light and $\mathcal{F}$ the cavity finesse. We see that for $N_g = 1000$, the resonances are split by $\sim 17\kappa$. At $N_g = 3$ the resonances are split by approximately κ.

5.3.4 Inhomogeneous cavity coupling: dealing with finite cloud size and non-commensurate cavity-lattice fields.

The true number of trapped atoms, N_{tot} are distributed in a lattice that is non-commensurate with the cavity field. Furthermore, the finite temperature of the atoms and the distribution of atoms along the longitudinal axis of the cavity can also degrade cavity coupling. To account for this we follow the procedure in [146, 147, 149, 151] and define an effective cavity coupling strength, g, and effective atom numbers N, N_g, and N_e such that the measured mean and variance of the cavity splitting are consistent with a sample of N atoms, N_g of which are in $|g\rangle$, all with uniform coupling strength g. Let's consider all atoms initially prepared in $(|e\rangle + |g\rangle)/\sqrt{2}$. Then we can relate the true magnitude of the splitting to the splitting in terms of effective values as

$$\left\langle \sum_{i=1}^{N_{\text{tot}}} \hat{P}_{g,i} [2g(\mathbf{r}_i)]^2 \right\rangle = \frac{N}{2}(2g)^2. \tag{5.12}$$

Here, $\hat{P}_{g,i} = |g_i\rangle\langle g_i|$, $g(\mathbf{r}_i)$ is the cavity coupling at the position of the i^{th} atom, $\mathbf{r}_i$, and we have used that $\langle \hat{N}_g \rangle = N/2$. Similarly, we relate the true variance of the splitting to the effective variance such that

$$\left\langle \left(\sum_{i=1}^{N_{\text{tot}}} P_{g,i} [2g(\mathbf{r}_i)]^2 \right)^2 \right\rangle - \left\langle \sum_{i=1}^{N_{\text{tot}}} P_{g,i} [2g(\mathbf{r}_i)]^2 \right\rangle^2 = \frac{N}{4}(2g)^4, \tag{5.13}$$

where we have used that $\Delta N_g^2 = N/4$. The angled brackets here denote an expectation value for $\hat{P}_{g,i}$ as well as a density weighted average over $g(\mathbf{r})$. To compute this average, we separate the contribution from the sinusoidal variation of $g(\mathbf{r})$ and the density $n(\mathbf{r})$ along $\hat{z}$, such that

$$g(\mathbf{r}) = g_{\text{Gauss}}(\mathbf{r}) \times \sin(2\pi z/\lambda_c) \quad where \quad g_{\text{Gauss}} = g_0 \frac{w_0}{w(z)} e^{-\frac{(x^2+y^2)}{w[z]^2}}. \tag{5.14}$$

Here, $w(z) = w_0\sqrt{1 + (z/z_r)^2}$ with $z_r = \pi w_0^2/\lambda_c$ the Rayleigh range and w_0 the beam waist of the cavity field. For the density, we estimate the Gaussian radial standard deviation of the clouds $\sigma_x = \sigma_y$ from the atom temperature using a harmonic approximation for a trap site (see Appendix A). We estimate the density variation across trap sites from the Gaussian standard deviation of the red MOT, L_z. To account for the lattice spacing that is non-commensurate with the cavity field we assume that the location of each trap site randomly samples the sinusoidal variation of the cavity field. Putting this all together we get that the density weighted average of $g(\mathbf{r})^n$ is given by

$$\langle g(\mathbf{r})^n \rangle = \int_{\infty}^{\infty} dxdydz g_{\text{Gauss}}(x, y, z)^n \frac{1}{\sqrt{2\pi}\sigma_x} e^{-\frac{x^2}{2\sigma_x^2}} \frac{1}{\sqrt{2\pi}\sigma_y} e^{-\frac{y^2}{2\sigma_y^2}} \frac{1}{\sqrt{2\pi}L_z} e^{-\frac{z^2}{2L_z^2}} \times \int_0^{2\pi} dz \sin^n(z)/(2\pi). \tag{5.15}$$

Combining equations 5.12, 5.13, and 5.15 we get that

$$2g = 0.972 \times \frac{\sqrt{3}}{2} 2g_0 = 2\pi \times 16\,\text{kHz} \quad and \quad N = 0.997 \times \frac{2}{3} N_{\text{tot}}, \tag{5.16}$$

Table 5.2: A table of predicted parameters for our cloud of ultracold ^{87}Sr atoms

Parameter	Value
Reference longitudinal trap frequency: ω_z	$2\pi \times 100$ kHz
Corresponding radial trap frequency: ω_r	$2\pi \times 229$ Hz
^{87}Sr typical atom temperature: T	2 μK
Standard deviation of radial cloud length: σ_r	9 μm
Standard deviation of longitudinal length of a single trap: σ_z	26 nm
Standard deviation of longitudinal length across all traps: L_z	30 μm

where the factors 0.972 and 0.997 come from the radial extent of the atoms and longitudinal extent of the atom distribution across lattices sites. The factors of $\sqrt{3}/2$ and 2/3 come from the non-commensurate cavity and trap fields. The properties of the atomic cloud that were used to compute these effective numbers are included in Table 5.2 and the relevant properties of the cavity are listed in Table 5.1. Another important parameter for our system is the collective cooperativity. The collective cooperativity is given by

$$N_g C = N_g \frac{g^2}{\kappa \Gamma}. \tag{5.17}$$

Using a conservative effective atom number of 1000, the predicted cavity finesse fo 10^5, and our calculated value of g, we get that NC=1200. The collective cooperativity can be thought of as the single pass optical depth of the atoms multiplied by the number of passes the light makes through the cloud.

5.3.5 A simple estimation of spin-squeezing

To estimate the performance of this cavity system we make a simple prediction for the spectroscopic enhancement ξ, that can be achieved by preparing a spin-squeezed state via non-demolition measurements. The enhancement is defined by

$$\xi = \left(\frac{\Delta J_z}{\Delta J_{z,CSS}} \right)^{-2} \widetilde{\mathcal{C}}, \tag{5.18}$$

where $\widetilde{\mathcal{C}}$ is the ratio of the contrast of the prepared state relative to the initial contrast, ΔJ_z is the actual standard deviation of J_z for the prepared state, and $\Delta J_{z,CSS}$ is the standard deviation of J_z

for a coherent spin state with N atoms, $|\Psi_{CSS}\rangle = \sum_{i=1}^{N}(|g_i\rangle + |e_i\rangle)/\sqrt{2}$. By including cavity and atomic dissipation through κ, the cavity linewidth, and Γ the linewidth of the $|g\rangle$ to $|d\rangle$ transition, the treatment in [142] was able to make a simple prediction for the spectroscopic enhancement. In the limit where one can neglect state changing transitions caused by the cavity light, the largest possible ξ is determined entirely by the number of photons one must scatter into free space per atom to achieve a projection limited measurement of the cavity splitting, m_s^{proj}. For ^{87}Sr , the limit of no probe induced state changes is a good approximation since the cavity transition is cycling and no transitions from $|e\rangle$ are close to 689 nm. In fact, the closest transition to one of the relevant states is a 688 nm transition from $|d\rangle$ to the $^3\mathrm{S}_1$ state. Proceeding with the simple estimation of ξ, we use that m_s^{proj} is given by,

$$m_s^{\text{proj}} = \frac{1}{4qN_gC}\left(\frac{\kappa'}{\kappa}\right)^2\left(1+\frac{\delta_c^2}{\Omega^2}\right)\frac{\Omega^2}{\omega^2}, \tag{5.19}$$

where q is the total quantum efficiency of detecting a photon that decays from the cavity mode, $C = {}^{(2g)^2}\!/_{\kappa\gamma}$ is the single atom cooperativity, and $\kappa' = \frac{\kappa+\left(\frac{\Omega}{2\omega}\right)^2\Gamma}{1+\left(\frac{\Omega}{2\omega}\right)^2}$ is the dressed cavity linewidth with $\omega = \omega_\pm$ when $|\omega_\pm| \geq |\omega_\mp|$. The main result is that,

$$\xi = \frac{m_s}{m_s^{\text{proj}}}e^{-2m_s}, \tag{5.20}$$

where m_s is the actual number of photons scattered into free space per atom and the exponential accounts for the reduction in contrast associated with scattering photons. The optimum value of m_s to maximize ξ is 1/2. In Fig. 5.16, we calculate the fundamental limit (quantum efficiency is set to 1) to spectroscopic enhancement versus effective atom number for various values of finesse and using the predicted cavity coupling, g.

It should be noted that this treatment relies on the assumption that N_d remains small, which for large single particle cooperativity, C, may not be the case because this value compares the vacuum Rabi frequency to the cavity and atomic linewidths. When C is large, either the field in the cavity is large, (corresponding to $\kappa \ll 2g$), the coupling of the atoms to the cavity field is stronger than the decay of $|d\rangle$ (corresponding to $\Gamma \ll 2g$), or both. This could result in a nontrivial

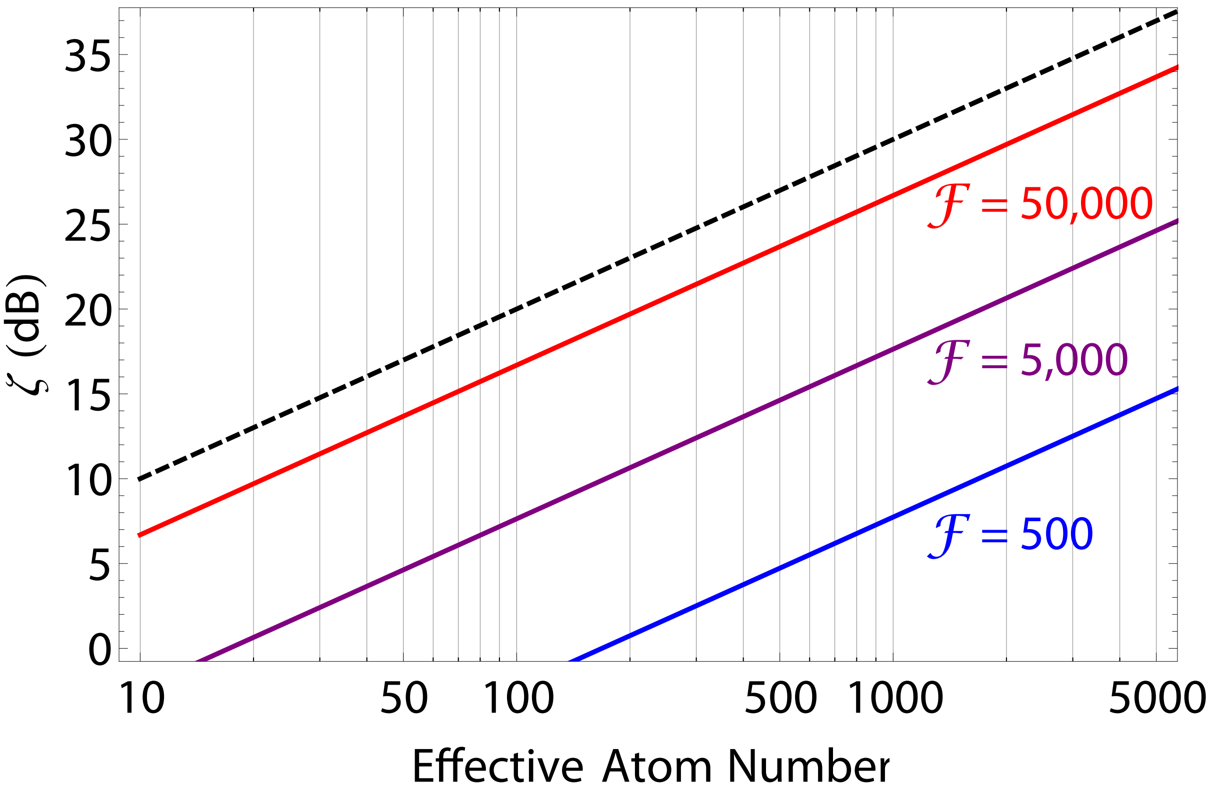

Figure 5.16: Calculations of fundamental limits to spectroscopic enhancement versus effective atom number for three example values of finesse. The red, purple, and blue lines correspond to a finesse of 50,000, 5,000, and 500, respectively. These upper limits on spectroscopic enhancement assume $q = 1$, $\delta_c = 0$ (detuning the cavity far from resonance only slightly increases ξ for these values of finesse), and use the predicted cavity coupling $2g = 2\pi \times 16$ kHz. The dashed black line represents the Heisenberg limit.

population of atoms in $|d\rangle$. For our predicted finesse of 100,000, this treatment already fails and predicts spectroscopic enhancement beyond the Heisenberg limit at large δ_c.

A more realistic prediction should take into account the major imperfections in our experimental system that will result in reduced spectroscopic enhancement and the actual quantum efficiency. One key example of this is two-body inelastic collisions in $|e\rangle$ [46], which we have neglected here entirely. Furthermore, birefringence of the cavity mirrors could distort the circular polarization needed to drive the cycling cavity transition. This could lead to cavity resonances for different linear polarizations that are separated in frequency. In this case, we would need to drive a

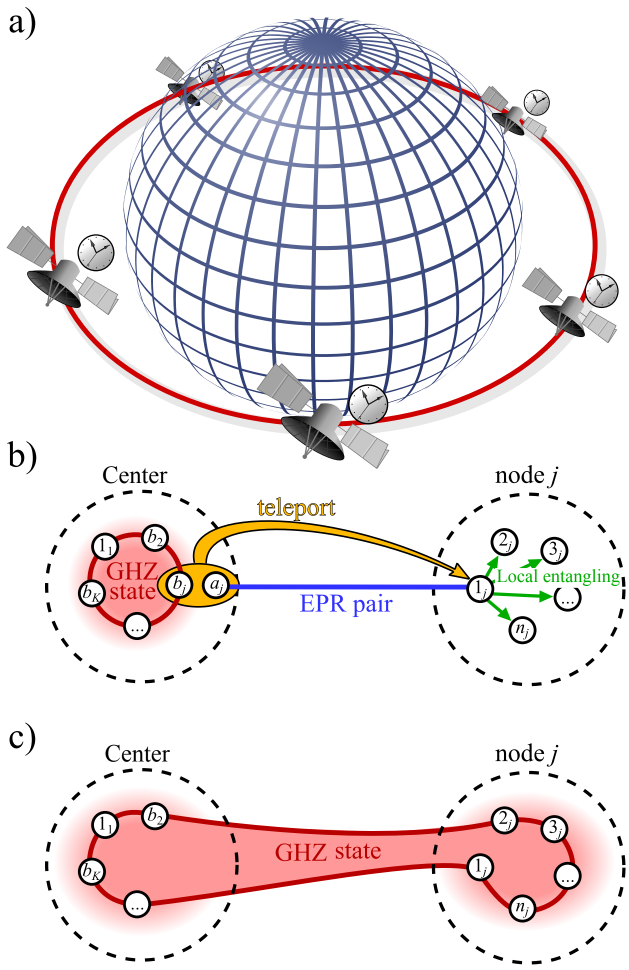

Figure 5.17: (a) a depiction of the clock network in which multiple clock satellites improve their collective clock performance by sharing entangled states. (b) a diagram illustrating how a locally entangled state can be spread to a nonlocal ensemble of atoms by creating an EPR pair and distributing the pair atoms across the two ensembles, then using quantum teleportation to transport the state of one of the entangled atoms to the nonlocal EPR pair atom. (c) a diagram depicting the final entangled state after entangling operations are performed at the nonlocal node. Here, all the atoms are part of the same GHZ state. To overcome noise from individual clock lasers, multiple such GHZ states of variable size will be transported and interrogated as described in [171].

π transition ($m_F = 9/2$ to $m_{F'} = 9/2$) that would allow for the potential for probe-induced nuclear spin decoherence.

5.4 Outlook

Certainly, this will be a challenging experiment to execute. The technical challenges associated with cavity mirror reflectivity at 698 nm and birefringence may be difficult hurdles to overcome. However, the potential to take the spectroscopic gains of spin squeezed states that have already been demonstrated in alkali atoms and apply them to the best clock in the world [2] is an alluring opportunity. This work is also just the first step in creating an ensemble of entangled atoms in a neutral atom based optical clock. Future systems could use optical cavities to create more exotic entangled quantum states to further improve clock performance or to spread entanglement across multiple clocks as we proposed in [171, 172]. In these works we outline a scheme for spreading entanglement between multiple independently operating clocks to use their resources most efficiently. Figure 5.17 demonstrates the general idea of this theoretical proposal which could be implemented in a network of satellites containing optical clocks (Fig. 5.17a). The proposal demonstrated that by spreading Greenberger-Horne-Zeilinger (GHZ) states across multiple clocks (Fig. 5.17b), the resulting entangled states (Fig. 5.17c) could provide stability approaching the Heisenberg limit. For neutral atoms, it may be plausible to spread entanglement locally by locating atoms in a high finesse cavity and performing quantum non-demolition measurements such as what we are proposing for our future experiment. While such a "quantum network of clocks" is still a long way off, it becomes more and more feasible every day with the exciting work being performed in the field of quantum information science and soon, our very own ^{87}Sr clock.

Bibliography

[1] T. L. Nicholson, M. J. Martin, J. R. Williams, B. J. Bloom, M. Bishof, M. D. Swallows, S. L. Campbell, and J. Ye, "Comparison of two independent Sr optical clocks with 1×10^{-17} stability at 10^3 s," Phys. Rev. Lett. **109**, 230801 (2012).

[2] B. J. Bloom, T. L. Nicholson, J. R. Williams, S. L. Campbell, M. Bishof, X. Zhang, W. Zhang, S. L. Bromley, and J. Ye, "An optical lattice clock with accuracy and stability at the 10^{-18} level," Nature **506**, 71–75 (2014).

[3] M. Bishof, X. Zhang, M. J. Martin, and J. Ye, "Optical spectrum analyzer with quantum-limited noise floor," Phys. Rev. Lett. **111**, 093604 (2013).

[4] M. J. Martin, M. Bishof, M. D. Swallows, X. Zhang, C. Benko, J. von Stecher, A. V. Gorshkov, A. M. Rey, and J. Ye, "A quantum many-body spin system in an optical lattice clock," Science **341**, 632–636 (2013).

[5] X. Zhang, M. Bishof, S. L. Bromley, C. V. Kraus, M. S. Safronova, P. Zoller, A. M. Rey, and J. Ye, "Spectroscopic observation of SU(N)-symmetric interactions in Sr orbital magnetism," Science (2014).

[6] M. M. Boyd, "High precision spectroscopy of strontium in an optical lattice: Towards a new standard for frequency and time," Ph.D. thesis, University of Colorado at Boulder (2007).

[7] A. D. Ludlow, "The strontium optical lattice clock: Optical spectroscopy with sub-hertz accuracy," Ph.D. thesis, University of Colorado at Boulder (2008).

[8] M. J. Martin, "Quantum metrology and many-body physics: Pushing the frontier of the optical lattice clock," Ph.D. thesis, University of Colorado at Boulder (2013).

[9] X. Xu, T. H. Loftus, J. L. Hall, A. Gallagher, and J. Ye, "Cooling and trapping of atomic strontium," J. Opt. Soc. Am. B **20**, 968–976 (2003).

[10] T. H. Loftus, T. Ido, M. M. Boyd, A. D. Ludlow, and J. Ye, "Narrow line cooling and momentum-space crystals," Phys. Rev. A **70**, 063413 (2004).

[11] A. Ludlow *et al.*, "Systematic study of the ^{87}Sr clock transition in an optical lattice," Phys. Rev. Lett. **96**, 033003 (2006).

[12] R. Grimm, M. Weidemüller, and Y. B. Ovchinnikov, "Optical dipole traps for neutral atoms," Adv. At. Mol. Opt. Phy. **42**, 95–170 (2000).

[13] M. V. Romalis and E. N. Fortson, "Zeeman frequency shifts in an optical dipole trap used to search for an electric-dipole moment," Phys. Rev. A **59**, 4547–4558 (1999).

[14] P. G. Westergaard, J. Lodewyck, L. Lorini, A. Lecallier, E. A. Burt, M. Zawada, J. Millo, and P. Lemonde, "Lattice-induced frequency shifts in sr optical lattice clocks at the 10^{-17} level," Phys. Rev. Lett. **106**, 210801 (2011).

[15] R. Le Targat, L. Lorini, Y. Le Coq, M. Zawada, J. Guéna, M. Abgrall, M. Gurov, P. Rosenbusch, D. Rovera, B. Nagórny *et al.*, "Experimental realization of an optical second with strontium lattice clocks," Nature communications **4** (2013).

[16] S. Blatt, J. W. Thomsen, G. K. Campbell, A. D. Ludlow, M. D. Swallows, M. J. Martin, M. M. Boyd, and J. Ye, "Rabi spectroscopy and excitation inhomogeneity in a one-dimensional optical lattice clock," Phys. Rev. A **80**, 052703 (2009).

[17] M. D. Swallows, M. Bishof, Y. Lin, S. Blatt, M. J. Martin, A. M. Rey, and J. Ye, "Suppression of collisional shifts in a strongly interacting lattice clock," Science **331**, 1043–1046 (2011).

[18] W. M. Itano, J. C. Bergquist, J. J. Bollinger, J. M. Gilligan, D. J. Heinzen, F. L. Moore, M. G. Raizen, and D. J. Wineland, "Quantum projection noise: Population fluctuations in two-level systems," Phys. Rev. A **47**, 3554–3570 (1993).

[19] P. Lemonde, P. Laurent, G. Santarelli, M. Abgrall, Y. Sortais, S. Bize, C. Nicolas, S. Zhang, A. Clairon, N. Dimarcq, P. Petit, A. Mann, A. Luiten, S. Chang, and C. Salomon, "Cold-atom clocks on earth and in space," in "Frequency Measurement and Control," , vol. 79 of *Topics in Applied Physics*, A. Luiten, ed. (Springer Berlin Heidelberg, 2001), pp. 131–153.

[20] G. J. Dick, in "Proceedings of the 19th PTTI Applications and Planning Meeting, 1987," (U.S. Naval Observatory, Washington, D.C., 1988), p. 133.

[21] G. Santarelli, C. Audoin, A. Makdissi, P. Laurent, G. J. Dick, and C. Clairon, "Frequency stability degradation of an oscillator slaved to a periodically interrogated atomic resonator," IEEE Trans. Ultrason. Ferroelectr. Freq. Control **45**, 887–894 (1998).

[22] A. Quessada, R. P. Kovacich, I. Courtillot, A. Clairon, G. Santarelli, and P. Lemonde, "The dick effect for an optical frequency standard," J. Opt. B **5**, S150 (2003).

[23] W. B. Dress, P. D. Miller, J. M. Pendlebury, P. Perrin, and N. F. Ramsey, "Search for an electric dipole moment of the neutron," Phys. Rev. D **15**, 921 (1977).

[24] T. P. Heavner *et al.*, "First accuracy evaluation of NIST-F2," Metrologia **51**, 174–182 (2014).

[25] A. D. Ludlow *et al.*, "Sr lattice clock at 1×10^{-16} fractional uncertainty by remote optical evaluation with a Ca clock," Science **319**, 1805–1808 (2008).

[26] B. J. Bloom, "Building a better atomic clock," Ph.D. thesis, University of Colorado at Boulder (2014).

[27] M. Swallows, M. Martin, M. Bishof, C. Benko, Y. Lin, S. Blatt, A. Rey, and J. Ye, "Operating a ^{87}Sr optical lattice clock with high precision and at high density," IEEE Trans. Ultrason. Ferroelectr. Freq. Control **59**, 416–425 (2012).

[28] A. D. Ludlow, X. Huang, M. Notcutt, T. Zanon-Willette, S. M. Foreman, M. M. Boyd, S. Blatt, and J. Ye, "Compact, thermal-noise-limited optical cavity for diode laser stabilization at 1×10^{-15}," Opt. Lett. **32**, 641–643 (2007).

[29] D. W. Allan, "Statistics of atomic frequency standards," Proc. IEEE **54**, 221–230 (1966).

[30] N. Hinkley, J. A. Sherman, N. B. Phillips, M. Schioppo, N. D. Lemke, K. Beloy, M. Pizzocaro, C. W. Oates, and A. D. Ludlow, "An atomic clock with 10^{-18} instability," Science **341**, 1215–1218 (2013).

[31] C. W. Chou, D. B. Hume, J. C. J. Koelemeij, D. J. Wineland, and T. Rosenband, "Frequency comparison of two high-accuracy Al^+ optical clocks," Phys. Rev. Lett. **104**, 070802 (2010).

[32] B. Young, F. Cruz, W. Itano, and J. Bergquist, "Visible Lasers with Subhertz Linewidths," Phys. Rev. Lett. **82**, 3799–3802 (1999).

[33] H. Stoehr, F. Mensing, J. Helmcke, and U. Sterr, "Diode laser with 1 Hz linewidth," Opt. Lett. **31**, 736–738 (2006).

[34] J. Alnis, A. Matveev, N. Kolachevsky, T. Udem, and T. W. Hänsch, "Subhertz linewidth diode lasers by stabilization to vibrationally and thermally compensated ultralow-expansion glass fabry-pérot cavities," Phys. Rev. A **77**, 053809 (2008).

[35] P. Dubé, A. Madej, J. Bernard, L. Marmet, and A. Shiner, "A narrow linewidth and frequency-stable probe laser source for the $^{88}\mathrm{Sr}^+$ single ion optical frequency standard," Appl. Phys. B **95**, 43–54 (2009).

[36] Y. Y. Jiang *et al.*, "Making optical atomic clocks more stable with 10^{-16}-level laser stabilization," Nat. Photonics **5**, 158–161 (2011).

[37] J. Rutman, "Characterization of phase and frequency instabilities in precision frequency sources: Fifteen years of progress," Proc. IEEE **66**, 1048–1075 (1978).

[38] Y. N. Zhao, J. Zhang, A. Stejskal, T. Liu, V. Elman, Z. H. Lu, and L. J. Wang, "A vibration-insensitive optical cavity and absolute determination of its ultrahigh stability," Opt. Express **17**, 8970–8982 (2009).

[39] T. Kessler *et al.*, "A sub-40-mHz-linewidth laser based on a silicon single-crystal optical cavity," Nat. Photonics **6**, 687–692 (2012).

[40] L. Cutler and C. Searle, "Some aspects of the theory and measurement of frequency fluctuations in frequency standards," Proc. IEEE **54**, 136–154 (1966).

[41] L. Viola, E. Knill, and S. Lloyd, "Dynamical decoupling of open quantum systems," Phys. Rev. Lett. **82**, 2417–2421 (1999).

[42] M. J. Biercuk, H. Uys, A. P. VanDevender, N. Shiga, W. M. Itano, and J. J. Bollinger, "Optimized dynamical decoupling in a model quantum memory," Nature **458**, 996–1000 (2009).

[43] S. Kotler, N. Akerman, Y. Glickman, A. Keselman, and R. Ozeri, "Single-ion quantum lock-in amplifier," Nature **473**, 61–65 (2011).

[44] J. Bylander, S. Gustavsson, F. Yan, F. Yoshihara, K. Harrabi, G. Fitch, D. G. Cory, Y. Nakamura, J.-S. Tsai, and W. D. Oliver, "Noise spectroscopy through dynamical decoupling with a superconducting flux qubit," Nat. Physics **7**, 565–570 (2011).

[45] Z. Chen, J. G. Bohnet, J. M. Weiner, and J. K. Thompson, "General formalism for evaluating the impact of phase noise on bloch vector rotations," Phys. Rev. A **86**, 032313 (2012).

[46] M. Bishof, M. J. Martin, M. D. Swallows, C. Benko, Y. Lin, G. Quéméner, A. M. Rey, and J. Ye, "Inelastic collisions and density-dependent excitation suppression in a ^{87}Sr optical lattice clock," Phys. Rev. A **84**, 052716 (2011).

[47] G. K. Campbell *et al.*, "The absolute frequency of the ^{87}Sr optical clock transition," Metrologia **45**, 539–548 (2008).

[48] J. Ye, H. J. Kimble, and H. Katori, "Quantum state engineering and precision metrology using state-insensitive light traps," Science **320**, 1734–1738 (2008).

[49] D. J. Wineland, C. Monroe, W. M. Itano, D. Leibfried, B. E. King, and D. M. Meekhof, "Experimental issues in coherent quantum-state manipulation of trapped atomic ions," J. Res. Natl. Inst. Stand. Technol. **103**, 259 (1998).

[50] D. S. Elliott, R. Roy, and S. J. Smith, "Extracavity laser band-shape and bandwidth modification," Phys. Rev. A **26**, 12–18 (1982).

[51] G. D. Domenico, S. Schilt, and P. Thomann, "Simple approach to the relation between laser frequency noise and laser line shape," Appl. Opt. **49**, 4801–4807 (2010).

[52] M. J. Martin, S. M. Foreman, T. R. Schibli, and J. Ye, "Testing ultrafast mode-locking at microhertz relative optical linewidth," Opt. Express **17**, 558–568 (2009).

[53] C. Hagemann, C. Grebing, T. Kessler, S. Falke, N. Lemke, C. Lisdat, H. Schnatz, F. Riehle, and U. Sterr, "Providing 10^{-16} short-term stability of a 1.5-μm laser to optical clocks," IEEE T. Instrumentation and Measurement **62**, 1556–1562 (2013).

[54] M. Greiner, O. Mandel, T. Esslinger, T. W. Hänsch, and I. Bloch, "Quantum phase transition from a superfluid to a Mott insulator in a gas of ultracold atoms." Nature **415**, 39–44 (2002).

[55] I. Bloch and W. Zwerger, "Many-body physics with ultracold gases," Rev. Mod. Phys. **80**, 885–964 (2008).

[56] Y.-J. Lin *et al.*, "Synthetic magnetic fields for ultracold neutral atoms," Nature **462**, 628–632 (2009).

[57] G. B. Jo *et al.*, "Itinerant ferromagnetism in a Fermi gas of ultracold atoms," Science **325**, 1521–1524 (2009).

[58] S. Will *et al.*, "Time-resolved observation of coherent multi-body interactions in quantum phase revivals," Nature **465**, 197–201 (2010).

[59] J. Simon *et al.*, "Quantum simulation of antiferromagnetic spin chains in an optical lattice." Nature **472**, 307–312 (2011).

[60] K. K. Ni *et al.*, “A high phase-space-density gas of polar molecules,” Science **322**, 231–235 (2008).

[61] M. H. G. de Miranda *et al.*, “Controlling the quantum stereodynamics of ultracold bimolecular reactions,” Nat. Phys. **7**, 502–507 (2011).

[62] A. Chotia *et al.*, “Long-lived dipolar molecules and Feshbach molecules in a 3D optical lattice,” Phys. Rev. Lett. **108**, 080405 (2012).

[63] K. Kim *et al.*, “Quantum simulation of frustrated Ising spins with trapped ions.” Nature **465**, 590–593 (2010).

[64] J. W. Britton *et al.*, “Engineered two-dimensional Ising interactions in a trapped-ion quantum simulator with hundreds of spins.” Nature **484**, 489–492 (2012).

[65] A. M. Rey, A. V. Gorshkov, and C. Rubbo, “Many-Body Treatment of the Collisional Frequency Shift in Fermionic Atoms,” Phys. Rev. Lett. **103**, 260402 (2009).

[66] A. Rey, A. Gorshkov, C. Kraus, M. Martin, M. Bishof, M. Swallows, X. Zhang, C. Benko, J. Ye, N. Lemke, and A. Ludlow”, “Probing many-body interactions in an optical lattice clock,” Ann. Phys. **340**, 311 – 351 (2014).

[67] A. P. Koller, M. Beverland, A. V. Gorshkov, and A. M. Rey, “Beyond the spin model approximation for ramsey spectroscopy,” Phys. Rev. Lett. **112**, 123001 (2014).

[68] D. J. Wineland and W. M. Itano, “Laser cooling of atoms,” Phys. Rev. A **20**, 1521 (1979).

[69] F. T. Arecchi, E. Courtens, R. Gilmore, and H. Thomas, “Atomic coherent states in quantum optics,” Phys. Rev. A **6**, 2211–2237 (1972).

[70] G. K. Campbell *et al.*, “Probing interactions between ultracold fermions,” Science **324**, 360–363 (2009).

[71] K. Gibble and B. J. Verhaar, “Eliminating cold-collision frequency shifts,” Phys. Rev. A **52**, 3370 (1995).

[72] S. Gupta *et al.*, “Radio-frequency spectroscopy of ultracold fermions,” Science **300**, 1723 (2003).

[73] M. W. Zwierlein, Z. Hadzibabic, S. Gupta, and W. Ketterle, “Spectroscopic insensitivity to cold collisions in a two-state mixture of fermions,” Phys. Rev. Lett. **91**, 250404 (2003).

[74] K. Gibble, “Decoherence and Collisional Frequency Shifts of Trapped Bosons and Fermions,” Phys. Rev. Lett. **103**, 113202 (2009).

[75] Z. H. Yu and C. J. Pethick, “Clock shifts of optical transitions in ultracold atomic gases,” Phys. Rev. Lett. **104**, 010801 (2010).

[76] M. Punk and W. Zwerger, “Theory of rf-Spectroscopy of strongly interacting fermions,” Phys. Rev. Lett. **99**, 170404 (2007).

[77] G. Baym, C. J. Pethick, Z. Yu, and M. W. Zwierlein, “Coherence and clock shifts in ultracold fermi gases with resonant interactions,” Phys. Rev. Lett. **99**, 190407 (2007).

[78] M. Girardeau, "Relationship between systems of impenetrable bosons and fermions in one dimension," J. Math. Phys. **1**, 516523 (1960).

[79] T. Kinoshita, T. Wenger, and D. S. Weiss, "Observation of a One-Dimensional Tonks-Girardeau gas," Science **305**, 11251128 (2004).

[80] B. Paredes, A. Widera, V. Murg, O. Mandel, S. Folling, I. Cirac, G. V. Shlyapnikov, T. W. Hansch, and I. Bloch, "Tonks-Girardeau gas of ultracold atoms in an optical lattice," Nature **429**, 277281 (2004).

[81] E. Haller, M. Gustavsson, M. J. Mark, J. G. Danzl, R. Hart, G. Pupillo, and H. Ngerl, "Realization of an excited, strongly correlated quantum gas phase," Science **325**, 1224 1227 (2009).

[82] N. Lemke *et al.*, "Spin-1/2 optical lattice clock," Phys. Rev. Lett. **103** (2009).

[83] M. Saffman, T. G. Walker, and K. Mlmer, "Quantum information with rydberg atoms," Rev. Mod. Phys. **82**, 2313 (2010).

[84] M. M. Boyd, T. Zelevinsky, A. D. Ludlow, S. Blatt, T. Zanon-Willette, S. M. Foreman, and J. Ye, "Nuclear spin effects in optical lattice clocks," Phys. Rev. A **76**, 022510 (2007).

[85] N. D. Lemke *et al.*, "*p*-Wave cold collisions in an optical lattice clock." Phys. Rev. Lett. **107**, 103902 (2011).

[86] A. Ludlow *et al.*, "Cold-collision-shift cancellation and inelastic scattering in a Yb optical lattice clock," Phys. Rev. A **84**, 052724 (2011).

[87] C. Lisdat, J. Winfred, T. Middelmann, F. RIEHLE, and U. STERR, "Collisional losses, decoherence, and frequency shifts in optical lattice clocks with bosons," Phys. Rev. Lett. **103** (2009).

[88] A. Traverso, R. Chakraborty, Y. N. Martinez de Escobar, P. G. Mickelson, S. B. Nagel, M. Yan, and T. C. Killian, "Inelastic and elastic collision rates for triplet states of ultracold strontium," Phys. Rev. A **79**, 060702 (2009).

[89] G. Quéméner and J. L. Bohn, "Strong dependence of ultracold chemical rates on electric dipole moments," Phys. Rev. A **81**, 022702 (2010).

[90] J. P. Burke, Jr., "Theoretical investigation of cold alkali atom," Ph.D. thesis, University of Colorado at Boulder (1999).

[91] Z. Idziaszek and P. S. Julienne, "Universal rate constants for reactive collisions of ultracold molecules," Phys. Rev. Lett. **104**, 113202 (2010).

[92] Z. Idziaszek, G. Quéméner, J. L. Bohn, and P. S. Julienne, "Simple quantum model of ultracold polar molecule collisions," Phys. Rev. A **82**, 020703 (2010).

[93] N. Boutassetta, A. R. Allouche, and M. Aubert-Frécon, "Theoretical study of the electronic structure of the Sr_2 molecule," Phys. Rev. A **53**, 3845–3852 (1996).

[94] E. Czuchaj, M. Kronicki, and H. Stoll, "Valence ab initio calculation of the potential energy curves for the Sr2 dimer," Chem. Phys. Lett. **371**, 401 – 409 (2003).

[95] S. Kotochigova, "Relativistic electronic structure of the Sr2 molecule," J. Chem. Phys. **128**, 024303 (2008).

[96] J. Mitroy and J. Zhang, "Dispersion and polarization interactions of the strontium atom," Mol. Phys. **108**, 1999–2006 (2010).

[97] R. Santra, K. V. Christ, and C. H. Greene, "Properties of metastable alkaline-earth-metal atoms calculated using an accurate effective core potential," Phys. Rev. A **69**, 042510 (2004).

[98] S. Ospelkaus, K.-K. Ni, D. Wang, M. H. G. de Miranda, B. Neyenhuis, G. Quéméner, P. S. Julienne, J. L. Bohn, D. S. Jin, and J. Ye, "Quantum-state controlled chemical reactions of ultracold potassium-rubidium molecules," Science **327**, 853–857 (2010).

[99] M. Kitagawa and M. Ueda, "Squeezed spin states." Phys. Rev. A **47**, 5138–5143 (1993).

[100] M. M. Boyd, T. Zelevinsky, A. D. Ludlow, S. M. Foreman, S. Blatt, T. Ido, and J. Ye, "Optical Atomic Coherence at the 1-Second Time Scale," Science **314**, 1430 (2006).

[101] C. Wu, J. Hu, and S. Zhang, "Exact SO(5) Symmetry in the Spin-3/2 Fermionic System," Phys. Rev. Lett. **91**, 186402 (2003).

[102] M. A. Cazalilla, A. F. Ho, and M. Ueda, "Ultracold gases of ytterbium: ferromagnetism and Mott states in an SU(6) Fermi system," New J. Phys. **11**, 103033 (2009).

[103] A. V. Gorshkov, M. Hermele, V. Gurarie, C. Xu, P. S. Julienne, J. Ye, P. Zoller, E. Demler, M. D. Lukin, and A. M. Rey, "Two-orbital *SU(N)* magnetism with ultracold alkaline-earth atoms," Nature Phys. **6**, 289 (2010).

[104] M. Hermele, V. Gurarie, and A. M. Rey, "Mott Insulators of Ultracold Fermionic Alkaline Earth Atoms: Underconstrained Magnetism and Chiral Spin Liquid," Phys. Rev. Lett. **103**, 135301 (2009).

[105] A. J. Daley, M. M. Boyd, J. Ye, and P. Zoller, "Quantum computing with alkaline-earth-metal atoms," Phys. Rev. Lett. **101**, 170504 (2008).

[106] A. J. Daley, "Quantum computing and quantum simulation with group-II atoms." Quantum Inf. Process **10**, 865 (2011).

[107] I. Reichenbach and I. H. Deutsch, "Sideband cooling while preserving coherences in the nuclear spin state in group-ii-like atoms," Phys. Rev. Lett. **99**, 123001 (2007).

[108] D. Banerjee, M. Bogli, M. Dalmonte, E. Rico, P. Stebler, U. J. Wiese, and P. Zoller, "Atomic Quantum Simulation of U(N) and SU(N) Non-Abelian Lattice Gauge Theories," Physical Rev. Lett. **110**, 125303 (2013).

[109] Y. Tokura and N. Nagaosa, "Orbital physics in transition-metal oxides," Science **288**, 462–468 (2000).

[110] X. G. Wen, F. Wilczek, and A. Zee, "Chiral spin states and superconductivity," Phys. Rev. B **39**, 11413–11423 (1989).

[111] S. Kraft, F. Vogt, O. Appel, F. Riehle, and U. Sterr, "Bose-Einstein Condensation of Alkaline Earth Atoms: ^{40}Ca," Phys. Rev. Lett. **103**, 130401 (2009).

[112] S. Stellmer, F. Schreck, and T. C. Killian, “Degenerate quantum gases of strontium,” ArXiv:1307.0601 (2013).

[113] Y. Takasu, K. Maki, K. Komori, T. Takano, K. Honda, M. Kumakura, T. Yabuzaki, and Y. Takahashi, “Spin-Singlet Bose-Einstein Condensation of Two-Electron Atoms,” Phys. Rev. Lett. **91**, 040404 (2003).

[114] S. Stellmer, R. Grimm, and F. Schreck, “Detection and manipulation of nuclear spin states in fermionic strontium,” Phys. Rev. A **84**, 043611 (2011).

[115] S. Blatt, T. L. Nicholson, B. J. Bloom, J. R. Williams, J. W. Thomsen, P. S. Julienne, and J. Ye, “Measurement of Optical Feshbach Resonances in an Ideal Gas,” Phys. Rev. Lett. **107**, 073202 (2011).

[116] R. Yamazaki, S. Taie, S. Sugawa, and Y. Takahashi, “Submicron Spatial Modulation of an Interatomic Interaction in a Bose-Einstein Condensate,” Phys. Rev. Lett. **105**, 050405 (2010).

[117] S. Taie, R. Yamazaki, S. Sugawa, and Y. Takahashi, “An SU(6) Mott insulator of an atomic Fermi gas realized by large-spin Pomeranchuk cooling,” Nature Phys. **8**, 825 (2012).

[118] G. Pagano, M. Mancini, G. Cappellini, P. Lombardi, F. Schafer, H. Hu, X.-J. Liu, J. Catani, C. Sias, M. Inguscio, and L. Fallani, “A one-dimensional liquid of fermions with tunable spin,” Nature Phys. **10**, 198 (2014).

[119] Y. N. Martinez de Escobar, P. G. Mickelson, P. Pellegrini, S. B. Nagel, A. Traverso, M. Yan, R. Côté, and T. C. Killian, “Two-photon photoassociative spectroscopy of ultracold ^{88}Sr,” Phys. Rev. A **78**, 062708 (2008).

[120] A. Stein, H. Knöckel, and E. Tiemann, “The ^{1}S+^{1}S asymptote of Sr$_2$ studied by Fourier-transform spectroscopy,” Eur. Phys. J. D **57**, 171 (2010).

[121] B. Yan, S. A. Moses, B. Gadway, J. P. Covey, K. R. A. Hazzard, A. M. Rey, D. S. Jin, and J. Ye, “Observation of dipolar spin-exchange interactions with lattice-confined polar molecules,” Nature **501**, 521 (2013).

[122] R. Islam, C. Senko, W. C. Campbell, S. Korenblit, J. Smith, A. Lee, E. E. Edwards, C.-C. J. Wang, J. K. Freericks, and C. Monroe, “Emergence and Frustration of Magnetism with Variable-Range Interactions in a Quantum Simulator,” Science **340**, 583 (2013).

[123] K. I. Kugel and D. I. Khomskii, “The Jahn-Teller effect and magnetism: transition metal compounds,” Sov. PHys. Usp. **25**, 231–256 (1982).

[124] P. Corboz, M. Lajkó, A. M. Läuchli, K. Penc, and F. Mila, “Spin-orbital quantum liquid on the honeycomb lattice,” Phys. Rev. X **2**, 041013 (2012).

[125] M. G. Kozlov, “Precision calculations of atoms with few valence electrons,” International Journal of Quantum Chemistry **100**, 336–342 (2004).

[126] M. S. Safronova, M. G. Kozlov, W. R. Johnson, and D. Jiang, “Development of a configuration-interaction plus all-order method for atomic calculations,” Phys. Rev. A **80**, 012516 (2009).

[127] M. S. Safronova, M. G. Kozlov, and C. W. Clark, "Precision calculation of blackbody radiation shifts for optical frequency metrology," Phys. Rev. Lett. **107**, 143006 (2011).

[128] K. R. A. Hazzard, M. van den Worm, M. Foss-Feig, S. R. Manmana, E. Dalla Torre, T. Pfau, M. Kastner, and A. M. Rey, "Quantum correlations and entanglement in far-from-equilibrium spin systems," ArXiv:1406.0937 (2014).

[129] K. R. A. Hazzard, B. Gadway, M. Foss-Feig, B. Yan, S. A. Moses, J. P. Covey, N. Y. Yao, M. D. Lukin, J. Ye, D. S. Jin, and A. M. Rey, "Many-body dynamics of dipolar molecules in an optical lattice," ArXiv:1402.2354 (2014).

[130] F. Scazza, C. Hofrichter, M. Höfer, P. C. De Groot, I. Bloch, and S. Fölling, "Observation of two-orbital spin-exchange interactions with ultracold SU(N)-symmetric fermions," ArXiv:1403.4761 (2014).

[131] G. Cappellini, M. Mancini, G. Pagano, P. Lombardi, L. Livi, M. Siciliani de Cumis, P. Cancio, M. Pizzocaro, D. Calonico, F. Levi, C. Sias, J. Catani, M. Inguscio, and L. Fallani, "Direct observation of coherent inter-orbital spin-exchange dynamics," ArXiv:1406.6642 (2014).

[132] M. Foss-Feig, M. Hermele, and A. M. Rey, "Probing the Kondo lattice model with alkaline-earth-metal atoms," Phys. Rev. A **81**, 051603(R) (2010).

[133] M. Hermele and V. Gurarie, "Topological liquids and valence cluster states in two-dimensional SU(N) magnets," Phys. Rev. B **84**, 174441 (2011).

[134] P. W. Courteille, S. Bux, E. Lucioni, K. Lauber, T. Bienaim, R. Kaiser, and N. Piovella, "Modification of radiation pressure due to cooperative scattering of light," Euro. Phys. J. D **58**, 69–73 (2010).

[135] T. Bienaim, M. Petruzzo, D. Bigerni, N. Piovella, and R. Kaiser, "Atom and photon measurement in cooperative scattering by cold atoms," J. Mod. Opt. **58**, 1942–1950 (2011).

[136] T. Bienaimé, S. Bux, E. Lucioni, P. W. Courteille, N. Piovella, and R. Kaiser, "Observation of a cooperative radiation force in the presence of disorder," Phys. Rev. Lett. **104**, 183602 (2010).

[137] R. Rhlsberger, K. Schlage, B. Sahoo, S. Couet, and R. Rffer, "Collective lamb shift in single-photon superradiance," Science **328**, 1248–1251 (2010).

[138] J. Keaveney, A. Sargsyan, U. Krohn, I. G. Hughes, D. Sarkisyan, and C. S. Adams, "Cooperative lamb shift in an atomic vapor layer of nanometer thickness," Phys. Rev. Lett. **108**, 173601 (2012).

[139] M. O. Scully, "Collective lamb shift in single photon dicke superradiance," Phys. Rev. Lett. **102**, 143601 (2009).

[140] R. Friedberg and J. T. Manassah, "Cooperative lamb shift and the cooperative decay rate for an initially detuned phased state," Phys. Rev. A **81**, 043845 (2010).

[141] T. Ido, T. H. Loftus, M. M. Boyd, A. D. Ludlow, K. W. Holman, and J. Ye, "Precision spectroscopy and density-dependent frequency shifts in ultracold Sr," Phys. Rev. Lett. **94**, 153001 (2005).

[142] Z. Chen, J. G. Bohnet, J. M. Weiner, and J. K. Thompson, “Cavity-aided non-demolition measuremments for atom counting and spin squeezing,” Phys. Rev. A **89**, 043837 (2014).

[143] A. Kuzmich, N. P. Bigelow, and L. Mandel, “Atomic quantum non-demolition measurements and squeezing,” Europhysics Letters **42**, 481–486 (1998).

[144] A. Kuzmich, L. Mandel, and N. P. Bigelow, “Generation of spin squeezing via continuous quantum nondemolition measurement,” Phys. Rev. Lett. **85**, 1594–1597 (2000).

[145] J. McKeever, J. R. Buck, A. D. Boozer, and H. J. Kimble, “Determination of the nuber of atoms trapped in an optical cavity,” Phys. Rev. Lett. **93**, 143601 (2004).

[146] J. Appel, P. J. Windpassinger, D. Oblak, U. B. Hoff, N. Kjærgaard, and E. S. Polzik, “Mesoscopic atomic entanglement for precision measurements beyond the standard quantum limit,” Proc. Natl. Acad. Sci. **106**, 10960–10965 (2009).

[147] Z. Chen, J. G. Bohnet, S. R. Sankar, J. Dai, and J. K. Thompson, “Conditional spin squeezing of a large ensemble via the vacuum rabi splitting,” Phys. Rev. Lett. **106**, 230501 (2011).

[148] C. Genes, P. R. Berman, and A. G. Rojo, “Spin squeezing via atom-cavity field coupling,” Phys. Rev. A **68**, 043809 (2003).

[149] I. D. Leroux, M. H. Schleier-Smith, and V. Vuletić, “Implementation of cavity squeezing of a collecive atomic spin,” Phys. Rev. Lett. **104**, 073602 (2010).

[150] M. H. Schleier-Smith, I. D. Leroux, and V. Vuletić, “Squeezing the collective spin of a dilute atomic ensemble by cavity feedback,” Phys. Rev. A **81**, 021804 (2010).

[151] M. H. Schleier-Smith, I. D. Leroux, and V. Vuletić, “States of an ensemble of two-level atoms with reduced quantum uncertainty,” Phys. Rev. Lett. **104**, 073604 (2010).

[152] A. T. Black, J. K. Thompson, and V. Vuletić, “On-demand superradiant conversion of quantized spin gratings into single photons with high efficiency,” Phys. Rev. Lett. **95**, 133601 (2003).

[153] I. B. Mekhov, C. Maschler, and H. Ritsch, “Cavity-enhanced light scattering in optical lattices to probe atomic quantum statistics,” Phys. Rev. Lett. **98**, 100402 (2007).

[154] I. B. Mekhov and H. Ritsch, “Quantum nondemolition measurements and state preparation in quantum gases by light detection,” Phys. Rev. Lett. **102**, 020403 (2009).

[155] I. B. Mekhov and H. Ritsch, “Quantum optics with quantum gases: controlled state reduction by designed light scattering,” Phys. Rev. A **80**, 013604 (2009).

[156] J. Simon, H. Tanji, S. Gosh, and V. Vuletić, “Single-photon bus connecting spin-wave quantum memories,” Nat. Physics **3**, 765 (2007).

[157] J. Simon, H. Tanji, J. K. Thompson, and V. Vuletić, “Interfacing collective atomic excitations and single photons,” Phys. Rev. Lett. **98**, 183601 (2007).

[158] H. Tanji, S. Gosh, J. Simon, B. Bloom, and V. Vuletić, “Heralded single-magnon quantum memory for photon polarization states,” Phys. Rev. Lett. **103**, 043601 (2009).

[159] J. K. Thompson, J. Simon, H.-Q. Loh, and V. Vuletić, "A high-brightness source of narrowband, identical-photon pairs," Science **313**, 74 (2006).

[160] D. S. Durfee, Y. K. Shaham, and M. A. Kasevich, "Long-term stability of an area-reversible atom-interferometer sagnac gyroscope," Phys. Rev. Lett. **97**, 240801 (2006).

[161] J. M. McGuirk, G. T. Foster, J. B. Fixler, M. J. Snadden, and M. A. Kasevich, "Sensitive absolute-gravity gradiometry using atom interferometry," Phys. Rev. A **65**, 033608 (2002).

[162] S. Wildermuth *et al.*, "Bose-Einstein condensates: Microscopic magnetic-field imaging," Nature **435**, 440 (2005).

[163] J. Guèna *et al.*, "Progress in atomic fountains at LNE-SYRTE," IEEE Trans. Ultrason. Ferroelectr. Freq. Control **59**, 391–410 (2012).

[164] S. R. Jefferts *et al.*, "Accuracy evaluation of NIST-F1," Metrologia **39**, 321–336 (2002).

[165] D. A. Steck, "Rubidium 87 d line data," available online at http://steck.us/alkalidata (revision 2.1.4, 23 December 2010).

[166] D. M. Brink and G. R. Satchler, *Angular Momentum* (Oxford, 1962).

[167] R. Loudon, *The quantum theory of light* (Oxford University Press, 1983), 2nd ed.

[168] M. Tavis and F. W. Cummings, "Exact solution for an N-molecule-radiation-field Hamiltonian," Phys. Rev. **170**, 379–384 (1968).

[169] E. T. Jaynes and F. W. Cummings, "Comparison of quantum and semiclassical radiation theories with application to the beam maser," Proc. IEEE **51**, 89 (1963).

[170] T. Holstein and H. Primakoff, "Field dependence of the intrinsic domain magnetization of a ferromagnet," Phys. Rev. **58**, 1098–1113 (1940).

[171] P. Kómár, E. M. Kessler, M. Bishof, L. Jiang, A. S. Sørensen, J. Ye, and M. D. Lukin, "A quantum network of clocks," Nat. Physics (2014).

[172] E. M. Kessler, P. Kómár, M. Bishof, L. Jiang, A. S. Sørensen, J. Ye, and M. D. Lukin, "Heisenberg-limited atom clocks based on entangled qubits," Phys. Rev. Lett. **112**, 190403 (2014).

Appendix A

Estimating the physical extent of our lattice trapped atoms

This appendix is based on a set of notes created by Pascal Naidon for the JILA strontium experiment in December of 2005. Here we approximate the size of our atoms clouds that are trapped in various trap sites along a one-dimensional (1D) lattice potential. The lattice is created from the standing wave interference pattern created by a retro-reflected Gaussian laser beam and the atoms are located at the focus. Since the extend of the atoms along direction of the trapping laser, determined by the Gaussian standard deviation of the magneto-optical trap cloud of 30 μm, is small compared to the Rayleigh range of a few millimeters, we neglect the variation in beam waste and describe the trapping potential as

$$V(x,y,z) = -V_0 \cos^2\left(\frac{2\pi z}{\lambda}\right) \exp\left(-2\frac{x^2+y^2}{w^2}\right), \tag{A.1}$$

where λ is the wavelength of the trap laser and w is its beam waist. Around the minimum of the n^{th} trap site, we can approximate the potential as

$$\begin{aligned} V(x,y,z) &\approx -V_0 + V_0\left(\frac{2\pi z}{\lambda} - \pi n\right)^2 + 2V_0\frac{x^2+y^2}{w^2} \\ &= -V_0 + \frac{1}{2}m\Omega_x^2 x^2 + \frac{1}{2}m\Omega_y^2 y^2 + \frac{1}{2}m\Omega_z^2\left(z - \frac{\lambda}{2}n\right)^2 \end{aligned} \tag{A.2}$$

where the trap frequencies are defined by $\Omega_x = \Omega_y = \frac{1}{w}\sqrt{\frac{4V_0}{m}}$ and $\Omega_z = \frac{2\pi}{\lambda}\sqrt{\frac{2V_0}{m}}$. The atoms therefore can be treated as three-dimensional harmonic oscillators, for which the eigenstates are known in terms of Hermite polynomials.

Assuming a Boltzmann thermal distribution of these eigenstates, the density profile is Gaussian and given by

$$n(x,y,z) = N \times \frac{1}{\sqrt{2\pi}\sigma_x} \exp\frac{x^2}{2\sigma_x^2} \times \frac{1}{\sqrt{2\pi}\sigma_y} \exp\frac{y^2}{2\sigma_y^2} \times \frac{1}{\sqrt{2\pi}\sigma_z} \exp\frac{z^2}{2\sigma_z^2}, \tag{A.3}$$

where N is the total number of atoms and σ_i is the standard deviation of the density distribution in the i^{th} dimension, given by

$$\sigma_i = \sqrt{\frac{\hbar}{m\Omega_i}} \times \sqrt{2\langle n_i\rangle_T + 1}, \tag{A.4}$$

where $\langle n_i\rangle_T = \left(\exp\frac{\hbar\Omega_i}{k_B T} - 1\right)^{-1}$ is the thermal average of the oscillator level occupation number in the i^{th} dimension and k_B is the Boltzmann constant.

Appendix B

Scattering lengths, and interaction matrix elements, and coupling constants... oh my!

B.1 Relationship between interaction matrix elements and scattering parameters

We consider atoms trapped in a harmonic oscillator potential such that the trap frequency in the $\hat{z}$ direction, ω_z is much larger than that of the other two directions, $\omega_x = \omega_y \equiv \omega_r$. This appendix will connect the fundamental scattering parameters a_η and b_η^3, to the interaction matrix elements $V^\eta_{\mathbf{n}_j,\mathbf{n}_{j'}}$, and $U^\eta_{\mathbf{n}_j,\mathbf{n}_{j'}}$, $\eta \in \{ee, gg, eg^+$ and $eg^-\}$, which determine the interaction energy for atoms that occupy oscillator levels $\mathbf{n}_j$ and $\mathbf{n}_{j'}$.

To accomplish this we make use of s- and p-wave coefficients that characterize the overlap of the harmonic oscillator modes. For two atoms that start in modes $\mathbf{n}$ and $\mathbf{n}'$ and end up in modes $\mathbf{n}''$ and $\mathbf{n}'''$ respectively these coefficients are defined as

$$S_{\mathbf{n}\mathbf{n}'\mathbf{n}''\mathbf{n}'''} = \frac{4\sqrt{2\pi}\sqrt{\omega_z\omega_r}}{a^r_{\text{ho}}}\left[s(n_x, n'_x, n''_x, n'''_x)s(n_y, n'_y, n''_y, n'''_y)\right], \tag{B.1}$$

and

$$P_{\mathbf{n}\mathbf{n}'\mathbf{n}''\mathbf{n}'''} = \frac{6\sqrt{2\pi}\sqrt{\omega_z\omega_r}}{{a^r_{\text{ho}}}^3}\left[s(n_x, n'_x, n''_x, n'''_x)p(n_y, n'_y, n''_y, n'''_y) + p(n_x, n'_x, n''_x, n'''_x)s(n_y, n'_y, n''_y, n'''_y)\right], \tag{B.2}$$

where $a^r_{\text{ho}} = \sqrt{\frac{\hbar}{\omega_r m}}$ is the harmonic oscillator length in the weakly confined dimensions and

$$s(n, n', n'', n''') = \frac{\int d\xi e^{-2\xi^2} H_n(\xi)H_{n'}(\xi)H_{n''}(\xi)H_{n'''}(\xi)}{\pi\sqrt{2^{n+n'+n''+n'''}n!n'!n''!n'''!}}, \tag{B.3}$$

$$p(n,n',n'',n''') = \frac{\int d\xi e^{-2\xi^2}\left[\left(\frac{d}{d\xi}H_n(\xi)\right)H_{n'}(\xi) - H_n(\xi)\left(\frac{d}{d\xi}H_{n'}(\xi)\right)\right]\left[\left(\frac{d}{d\xi}H_{n''}(\xi)\right)H_{n'''}(\xi) - H_{n''}(\xi)\left(\frac{d}{d\xi}H_{n'''}(\xi)\right)\right]}{\pi\sqrt{2^{n+n'+n''+n'''}n!n'!n''!n'''!}}. \tag{B.4}$$

Here, $H_n(\xi)$ are Hermite polynomials. Fig. B.1 plots the mode dependence of $s(n,n',n',n)$ and $p(n,n',n',n)$, which represents our assumption that collisions do not change the mode of the atoms. These coefficients obey the exchange (anti-symmetry)symmetry of (p-)s-wave interactions such that $S_{\mathbf{nn'n''n'''}} = S_{\mathbf{n'nn''n'''}} = S_{\mathbf{nn'n'''n''}}$ and $P_{\mathbf{nn'n''n'''}} = -P_{\mathbf{n'nn''n'''}} = -P_{\mathbf{nn'n'''n''}}$.

Since we neglect collisions that change the mode of the atoms, we can finally connect our interaction matrix elements to the fundamental scattering parameters with the following equations:

$$V^{\eta}_{\mathbf{n}_j,\mathbf{n}_{j'}} = b^3_\eta P_{\mathbf{nn'nn'}} \equiv b^3_\eta P_{\mathbf{nn'}}, \tag{B.5}$$

and

$$U^{\eta}_{\mathbf{n}_j,\mathbf{n}_{j'}} = a_\eta S_{\mathbf{nn'nn'}} \equiv a_\eta S_{\mathbf{nn'}}. \tag{B.6}$$

B.2 Definition of coupling constants

The coupling constants from Eqn. 3.3 in Ch. 3 (+ values) and Eqn. 4.2 in Ch. 4 are defined as,

$$\begin{aligned}
J^{\pm}_{\mathbf{n}_j,\mathbf{n}_{j'}} &= \frac{(\zeta^{+}_{eg} - \Upsilon^{-}_{eg})_{\mathbf{n}_j,\mathbf{n}_{j'}}}{2}, \\
C^{\pm}_{\mathbf{n}_j,\mathbf{n}_{j'}} &= \frac{(\zeta_{ee} - \zeta_{gg})_{\mathbf{n}_j,\mathbf{n}_{j'}}}{2}, \\
\chi^{\pm}_{\mathbf{n}_j,\mathbf{n}_{j'}} &= \frac{(\zeta_{ee} + \zeta_{gg} - 2\zeta^{+}_{eg})_{\mathbf{n}_j,\mathbf{n}_{j'}}}{2} \\
K^{\pm}_{\mathbf{n}_j,\mathbf{n}_{j'}} &= \frac{(\zeta_{ee} + \zeta_{gg} + \zeta^{+}_{eg} + \Upsilon^{-}_{eg})_{\mathbf{n}_j,\mathbf{n}_{j'}}}{8}, \\
&where \quad \Upsilon = U, \zeta = V \quad for +, \qquad and \qquad \Upsilon = V, \zeta = U \quad for - .
\end{aligned} \tag{B.7}$$

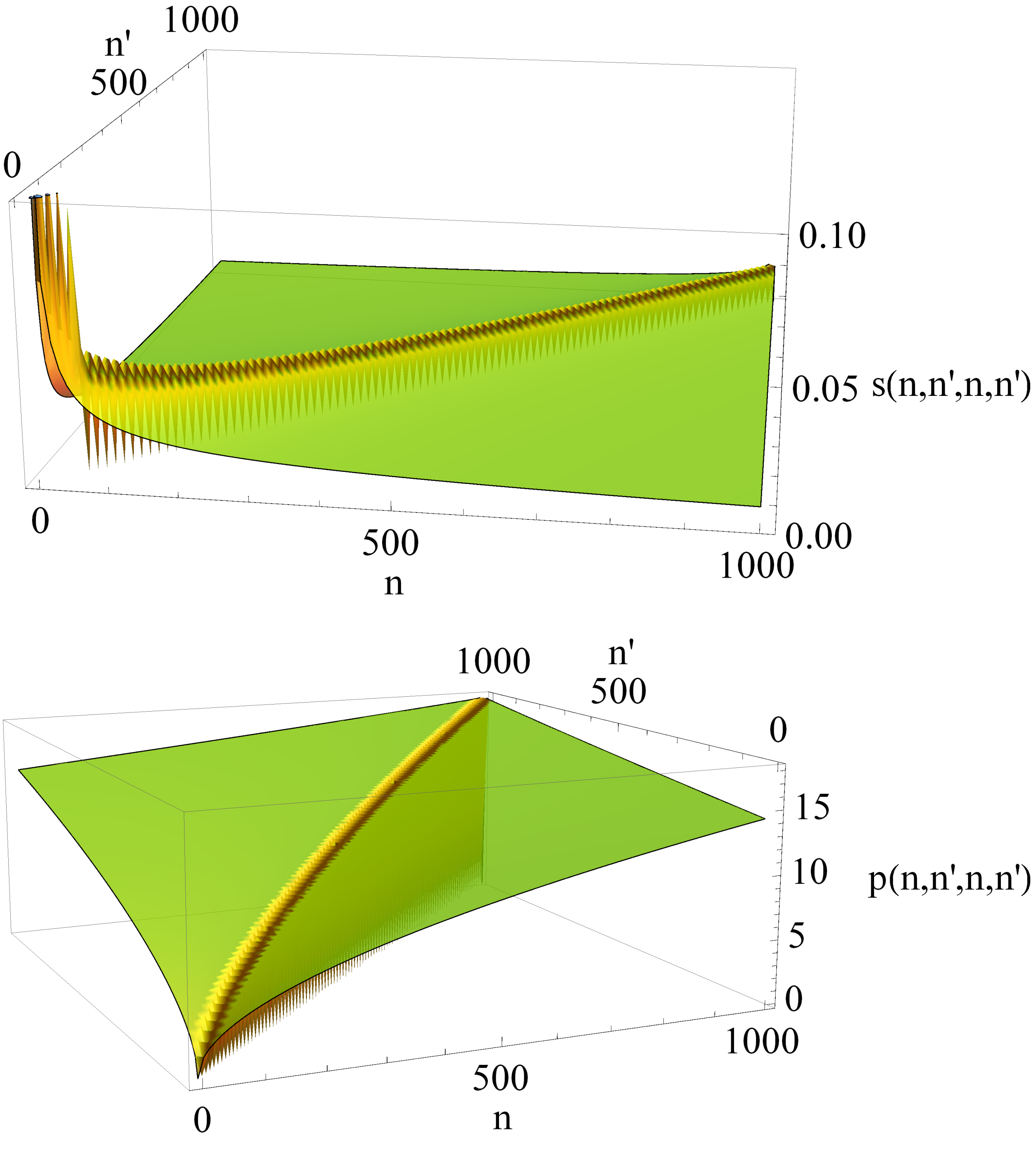

Figure B.1: Mode dependence of the functions $s(n, n', n, n')$ and $p(n, n', n, n')$.

Appendix C

Data analysis for spin noise measurement

During the course of these measurements, we typically observe slow, systematic fluctuations of the atom number on the order of ±10% as we operate the experiment and measure spin noise over the course of ~10 hours. In most instances, these fluctuations are negligible due to the normalization techniques we employ. However, the atomic spin noise depends directly on the atom number, and a slowly varying atom number could result in unintended systematic biases. Specifically, spin noise for the coherent spin state typically considered in optical clocks scales as $1/\sqrt{N_{\text{tot}}}$. Thus, the deviations in atom number can cause variations on the order of ±5% in the measured spin noise. Ideally, these fluctuations are randomly distributed and should not result in interpretation as a false-positive for non-trivial spin-noise correlations. In the unlikely possibility that these fluctuations were correlated with a specific measurement quadrature, they could cause a spurious phase shift in the spin noise minimum. We thus take care to analyze the data in a way that is immune to this potential bias.

A given measurement of $\langle \hat{S}^z_{\text{tot}} \rangle / N_{\text{tot}}$ is accomplished by independently measuring $N_{e(g)}$, the number of atoms in the excited (ground) state after a single Ramsey experimental sequence, using standard electron shelving techniques. We determine its i^{th} value, $\langle \hat{S}^z_{\text{tot}} \rangle_i / N^i_{\text{tot}}$, by measuring the ith value of $N_{e(g)}$ (which we denote as $N^i_{e(g)}$) and obtain

$$\langle \hat{S}^z_{\text{tot}} \rangle_i / N^i_{\text{tot}} = \frac{N^i_e}{N^i_e + N^i_g} - 1/2. \tag{C.1}$$

From the j^{th} set of measurements of $\langle \hat{S}^z_{\text{tot}} \rangle$, denoted $\{\langle \hat{S}^z_{\text{tot}} \rangle_1, \ldots, \langle \hat{S}^z_{\text{tot}} \rangle_i, \ldots \langle \hat{S}^z_{\text{tot}} \rangle_{n_j}\}_j$, we estimate

$\sigma_j^2 \equiv \langle (S^z_{\text{tot}})^2 \rangle / N^2_{\text{tot}} - \langle \hat{S}^z_{\text{tot}} \rangle^2 / N^2_{\text{tot}}$ using a pair variance, such that

$$\sigma_j^2 = \frac{1}{2\,(n_j - 1)} \sum_{i=1}^{i=n_j} \left(\langle \hat{S}^z_{\text{tot}} \rangle_{i+1} - \langle \hat{S}^z_{\text{tot}} \rangle_i \right)^2 . \tag{C.2}$$

For white noise, the pair variance is a good estimator for the standard deviation [37], while remaining insensitive to noise processes that only manifest themselves on long time scales. The number of measurements in a set, n_j, was typically $n_j \simeq 80$. For a given measurement quadrature, we average the results of many such measurement sets to produce one experimental data point (*i.e.*, a data point in Fig. 3.13).

In order to maintain insensitivity to slow fluctuations in atom number between sets j and j', we consider the standard expression for quantum noise for the case of a coherent spin state, σ_{sql}, which is expected in the absence of many-body interactions. The explicit goal is to remove any mechanism by which the trivial case—where the spin noise is described by σ_{sql}—can mimic the many-body effect we predict from the theory. We calculate the jth value of σ_{sql} as

$$\left(\sigma^j_{\text{sql}} \right)^2 = p_j \left(1 - p_j \right) / N^j_{\text{tot}}, \tag{C.3}$$

where $p_j = \text{Mean}\left[\{ N^1_e / \left(N^1_e + N^1_g \right), \ldots, N^i_e / \left(N^i_e + N^i_g \right), \ldots, N^{n_j}_e / \left(N^{n_j}_e + N^{n_j}_g \right) \}_j \right]$. We additionally consider a technical noise term, which represents the effect of intrinsic technical detection noise, given by Δs_j. This noise is characterized by a separate measurement. The detection noise accounts for 10% of the observed noise at typical low atom numbers, while at high atom number it is only $\sim 1\%$ of the observed noise, and is therefore negligible. It is quadrature-independent in all cases. From the σ_j^2, we subtract the atom-number-dependent $\left(\sigma^j_{\text{sql}} \right)^2$ such that

$$\tilde{\sigma_j}^2 = \sigma_j^2 - \left(\sigma^j_{\text{sql}} \right)^2 - \Delta s_j^2 . \tag{C.4}$$

Here, $\tilde{\sigma_j}^2$ represents only the effects of non-trivial spin noise and laser noise.

The many-body theory for a given measurement condition is calculated at fixed atom number. To facilitate comparison with the many body theory, we add a noise term back to $\tilde{\sigma_j}^2$ that corresponds to σ^2_{sql} for the mean atom number over the entire data set, $\overline{\sigma^2_{\text{sql}}}$. We emphasize that

$\overline{\sigma_{\mathrm{sql}}^2}$ is a constant number, with no quadrature dependence. The many-body theoretical prediction is calculated based upon the same mean atom number used to calculate $\overline{\sigma_{\mathrm{sql}}^2}$. Ultimately, the net effect of this process is to remove the variability due to slow fluctuations in atom number, but to retain the part of the noise that departs from σ_{sql} due to both laser noise and many-body effects. As discussed in the text, we observe a phase shift of the minimum of the phase noise that is consistent with the many-body theory and indicative of correlated spin noise of the atom ensemble.